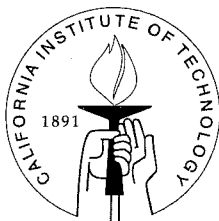


Optical Nanocavities in Two-Dimensional Photonic Crystal Planar Waveguides

Thesis by
Oskar J. Painter

In Partial Fulfillment of the Requirements
for the Degree of
Doctor of Philosophy



California Institute of Technology
Pasadena, California

2001

(Submitted November 10, 2000)

For Joe Buck

© 2001

Oskar J. Painter

All Rights Reserved

Acknowledgements

I would first like to thank my advisor, Axel Scherer, for his support. I am extremely grateful to Axel for the freedom that he extended to me during my thesis work. I am thankful to have worked in an environment in which new paths could be explored and new ideas brought to fruition.

Much of the inspiration for the theoretical work in this thesis came from a two semester course I took during my second year at Caltech that was taught by Professor Kerry Vahala. It was in this class that I was first introduced to group theory, not just as an abstract set of mathematical axioms, but as a powerful tool for analyzing physical systems. I am truly indebted to Kerry for his time and mentorship throughout my graduate career.

I am also grateful to Professor Amnon Yariv who took the time, and had the patience, to discuss my many strange and often ill-posed questions. Having come from an electrical engineering background, the physical picture which came through in Amnon's teaching was crucial for me as I started out.

While at Caltech I was fortunate to work alongside a group of talented people. My office mates Ali Husain, David Barsic, Marko Loncar, Tomoyuki Yoshie, Jelena Vuckovic, Dr. Joyce Wong, and Dr. Chuan-Cheng Cheng provided an exciting and fun atmosphere in which to work. I will miss their comradeship. To all of them I wish the best.

A special thanks goes to Chuan-Cheng who built many of the machines used to fabricate the photonic crystal structures for this thesis, and to Jelena who helped in the design and simulation of these structures. I must also thank Brian D'Urso and Oliver Dial, two undergraduates who did SURF projects while at Caltech. Brian wrote a finite-difference time-domain simulator and Oliver developed an electron-beam writing software package, both of which were instrumental to my thesis work.

I also feel fortunate to have met and worked with Professor John O'Brien. I thank

John for his early guidance, his partnership in collaborative work, and his friendship. I thank Professor Dan Dapkus and his research group at USC for the design and growth of semiconductor wafers. Specifically, I would like to acknowledge the help of Dr. In Kim, Dr. Denis Tishinin, Dr. David Lin, and Dr. Aaron Bond.

I would also like to acknowledge two of my undergraduate teachers at the University of British Columbia who provided much of my early inspiration to undertake my graduate studies. Professor David Pulfrey introduced me to semiconductor physics, and Professor Lon Rosen taught me mathematics while I was at UBC. Their superb teaching abilities and generosity of time were vital in providing me with the direction I needed.

I gratefully acknowledge the financial support of the Canadian government in the form of an NSERC scholarship during my first four years at Caltech.

Finally, I would like to thank three very important people to me. I thank my wife Joy, who showed Herculean patience while I was writing this thesis (a two year period), and without whose love and support none of this would matter. I also thank my mother and father who have been, and continue to be, hugely inspirational to me. I thank them for their love and their guidance.

Abstract

One of the most fundamental properties of a physical system is its energy-momentum dispersion. The electronic dispersion present in semiconductor crystals results in energy gaps which play an extremely important role in the physics of many of the electronic and optical devices we use today. A similar dispersion for electromagnetic waves can be found in periodic dielectric structures. Owing to their strong dispersion, these “photonic crystals” can be used to manipulate light at sub-wavelength scales. The majority of this thesis is concerned with the design and implementation of optical resonant cavities formed by introducing small local imperfections into a periodically perforated slab waveguide. Light becomes localized to these “defect” regions, forming optical cavities with modal volumes approaching the theoretical limit of a cubic half-wavelength.

The resonant cavities studied in this thesis are fabricated using electron-beam lithography, anisotropic dry etching, and selective wet etching. These methods are used to create a two-dimensional array of cylindrical air holes in a free-standing waveguide structure. A multi-quantum-well Indium Gallium Arsenide Phosphide (In-GaAsP) active region is epitaxially grown within the waveguide in order to provide light emission in the $1.5\ \mu\text{m}$ band. Optical pumping of the active region is then used to probe the resonant structure of the photonic crystal cavities.

Numerical finite-difference time-domain simulations and qualitative predictions based on symmetry arguments are used to label the different resonant modes present in the cavity photoluminescence spectra. It is found that both donor and acceptor type modes are localized within the defect cavities. Pulsed lasing action is observed in cavity modes with modal volumes as small as $2(\lambda/2n)^3$. Lithographic adjustments in the scale and symmetry of the cavity geometry are also used to tune the resonant mode wavelength, split mode degeneracies, and adjust the emission pattern and polarization of the defect modes.

Contents

Acknowledgements	iii
Abstract	v
1 Introduction	1
2 Spontaneous Emission in Semiconductor Optical Microcavities	7
2.1 Canonical Quantization Method of the Electromagnetic Field in a Dielectric Material	8
2.1.1 Photon Modes of a Uniform Dielectric	13
2.1.2 Quasi-Modes, Leaky Modes, and Multi-mode Fields: Counting Photons in a Microcavity	15
2.2 Quantization of the Electron Field	19
2.2.1 Electrons and Holes	21
2.2.2 Electronic Envelope Approximation	23
2.2.3 Quantum-Well States in a III-V Semiconductor	24
2.3 Electron-Photon Coupling	29
2.3.1 Spontaneous Emission of Light	35
2.3.2 Spontaneous Emission Rate from a QW Active Region in the Absence of Microcavity Effects	43
2.3.3 Spontaneous Emission from a Quantum-Well Active Region Embedded in a Single Mode Microcavity	51
2.3.4 Spontaneous Emission Enhancement and the Purcell Factor	56
2.3.5 Gain, Lasing, and Super-luminescence in a Microcavity	62
3 Group Theory and the Analysis of Periodic Electromagnetic Structures	69

3.1	Introduction	69
3.2	Symmetries of Classical and Quantum Systems	70
3.3	Macroscopic Maxwell's Equations and Symmetry	73
3.3.1	Electric and Magnetic Field Master Equations	78
3.3.2	The Bloch Equation: A Prelude to Space Groups	82
3.4	Space Groups	83
3.4.1	Translation Group, \mathbb{T}	85
3.4.2	★ of \mathbf{k}	90
3.4.3	The Little Group, $\mathcal{G}_{\mathbf{k}}$	90
3.4.4	Time Reversal Symmetry and Space Groups	94
3.5	Localized Defect Modes: Point Groups	98
3.5.1	X-point	103
3.5.2	J-point	105
3.5.3	Conduction Band Donor Modes	107
3.5.4	Valence Band Acceptor Modes	108
4	Numerical Electromagnetic Design of Photonic Crystal Defect Cav-	
	ities	110
4.1	Effective 2D Photonic Crystal Waveguide Analysis	110
4.2	3D FDTD Bandstructure Calculations of 2D Photonic Crystal Wave-	
	guide Structures	116
4.3	3D FDTD Analysis of Localized Defect Resonances	121
4.3.1	Degeneracy Splitting of the Dipole Modes	132
4.4	FDTD Simulation of Reduced Symmetry Defect Cavities	136
4.4.1	Symmetric (S) Cavity	136
4.4.2	X-Split (X) Cavity	143
4.4.3	Y-Split (Y) Cavity	147
5	Fabrication	151

6	Photoluminescence Measurements	165
6.1	S-Defect Cavity	168
6.2	Lithographic Wavelength Tuning	179
6.3	X-Defect Cavity	184
6.4	Y-Defect Cavity	188
6.5	Polarization of (x,y) Dipole Modes	195
6.6	Low Temperature Lasing of the X-Dipole Mode	199
7	Summary	207
	Bibliography	209

List of Figures

1.1	Cross-section through the middle of the photonic crystal microcavity. Photons are localized to the defect region by TIR at the air/slab interface and by Bragg reflection from the 2D photonic crystal.	4
1.2	In-plane bandstructure of the triangular lattice of air holes for the TE-like (even) modes in an optically thin high-index slab. The parameters used in this calculation are: $r/a=0.32$, $d/a=0.409$, $n_{slab} = 3.4$, and $n_{clad} = 1$. The TE-like guided mode band-gap extends between the lowest frequency band (“valence” band) and the next higher frequency band (“conduction” band). The band-gap covers a normalized frequency range of roughly 0.28-0.36, or 25% of the midgap frequency.	5
2.1	Illustration showing the approximate band-structure of a III-V semiconductor in the vicinity of the zone center Γ -point. Each energy band is doubly degenerate in this case. Δ is the spin-orbit splitting energy and σ is the heavy-hole and light-hole splitting due to strain.	26
2.2	A map of the typical time scales of different processes in semiconductor optical cavities at room temperature.	29
2.3	The four distinct length scales associated with opto-electronic processes in semiconductor optical cavities.	30
3.1	Bravais and Reciprocal lattice of a 2D hexagonal photonic crystal. . .	89
3.2	IBZ of the hexagonal lattice showing the indexing used to identify the different X and J points.	101

- 4.1 Intensity plot of the fundamental TE guided mode at $1.55 \mu\text{m}$ for a 211 nm dielectric slab of refractive index 3.4 surrounded by air cladding. The fundamental TE mode effective index (2.67) is used in the 2D bandstructure calculations for TE polarized light. 112
- 4.2 Intensity plot of the fundamental TM guided mode at $1.55 \mu\text{m}$ for a 211 nm dielectric slab of refractive index 3.4 surrounded by air cladding. The fundamental TM mode effective index (1.415) is used in 2D bandstructure calculations for TM polarized light. 113
- 4.3 Band diagram for TE polarized light (E-field polarized in plane). The holes have a refractive index, $n_{air} = 1$. The dielectric has an index, $n_{eff}^{TE} = 2.65$, representing the fundamental TE mode effective index of an air clad 211 nm slab waveguide at a wavelength of $1.55 \mu\text{m}$. The radius of the holes is defined by the ratio $r/a=0.3$. The resulting in-plane TE band-gap extends between a normalized frequency, $\Delta\omega_{gap} = a/\lambda_o = 0.28 - 0.35$. The air (cladding) light line is also shown as a solid black line. 114
- 4.4 Band diagram for TM polarized light (E-field polarized in \hat{z} -direction). The dielectric has an index, $n_{eff}^{TM} = 1.415$, representing the fundamental TM mode effective index of an air clad 211 nm slab waveguide at a wavelength of $1.55 \mu\text{m}$. In this case the index contrast and r/a are not large enough to open a full 2D band-gap between the first (“valence”) and second (“conduction”) bands. The air (cladding) light line is also shown as a solid black line. 115
- 4.5 In-plane bandstructure of the triangular lattice of air holes in an optically thin high-index slab for (a) the TE-like (even) modes and (b) the TM-like (odd) modes. The parameters used in this calculation are: $r/a=0.32$, $d/a=0.409$, $n_{slab} = 3.4$, and $n_{clad} = 1$ 118
- 4.6 Plot of the “conduction” (“air”) and “valence” (“dielectric”) band-edges as a function of slab thickness. The mid-gap frequency is also plotted as a dashed line (- -). 120

4.7	Plot of the frequency gap between the “conduction” and “valence” bands versus slab thickness.	120
4.8	Schematic of a 2D slice through the middle of the patterned high index slab. The center hole has a larger refractive index than air, n_d , forming a defect in the hexagonal lattice of air holes.	122
4.9	Plot of the normalized frequency versus defect refractive index of the degenerate defect mode. The radius of the defect hole was kept constant at $0.3a$ while the refractive index was varied.	123
4.10	2D slice through the middle of the slab showing the x and y dipole mode electric field amplitudes (degenerate case).	124
4.11	Plot of the quality factor versus normalized frequency of the x -dipole mode.	126
4.12	Plot of the effective in-plane quality factor, $Q_{ }$, versus normalized frequency.	127
4.13	Plot of the effective quality factor in the vertical direction, Q_{\perp} , versus normalized frequency.	128
4.14	In-plane radiation losses of the x and y dipole mode (degenerate case) are shown in (a) and (b), respectively. The vertical radiation pattern of the x -dipole mode is given in (c). In each plot the electric field amplitude has been saturated so as to highlight the losses.	129
4.15	Plot of the different radiation loss components (Q_T , $Q_{ }$, and Q_{\perp}) of the x -dipole mode versus the number of periods of the photonic crystal surrounding the defect ($d = 0.4a$).	130
4.16	Plot of the quality factor versus normalized frequency of the x -dipole mode for a photonic crystal cavity with a seven period photonic crystal mirror surrounding the defect ($d = 0.4a$).	131

4.17	Cavity geometry for splitting of the dipole mode degeneracy. Only the nearest neighbor holes of the defect are shown. The two nearest holes in the \hat{x} direction have been enlarged. The central hole has been filled in and has a dielectric constant equal to that of the slab. Notice that the two enlarged holes have also been moved inwards towards the central hole so as to preserve the spacing between holes in the \hat{x} -direction.	132
4.18	Calculated Q and normalized frequency of the y -dipole as a function of the degeneracy-splitting defect, r'/a .	133
4.19	Fourier spectrum of an initial field chosen to excite both the x and y dipole modes. $r'/a = 0.35$ in this case. For larger r'/a ratios the splitting of the x and y dipoles is strong enough to push the y dipole frequency out of the band-gap. The y -dipole, on the other hand, is still highly localized and its frequency is only moderately changed [cf. Figure 4.18].	134
4.20	Schematic of a symmetric defect cavity with a single hole removed.	137
4.21	FDTD simulation of the resonant modes in a symmetric defect cavity ($r/a = 0.34$, $d/a = 0.409$, $n_{slab} = 3.4$, $p = 5$).	138
4.22	FDTD simulation of the resonant modes in a symmetric (S) defect cavity with r/a graded (center outwards) from 0.38–0.34 ($d/a = 0.409$, $n_{slab} = 3.4$, $p = 5$).	141
4.23	Schematic of an X-split defect cavity. The degree of splitting is measured by Δy , the distance which the four nearest neighbors on top and bottom of the defect region are moved together.	143
4.24	FDTD simulation of the resonant modes in an X-split defect cavity with $r/a = 0.34$, $d/a = 0.409$, $n_{slab} = 3.4$, and $\Delta y = 0.15a$.	144
4.25	Schematic of a Y-split defect cavity. The degree of splitting is measured by r'/r , the scaling factor of the radius of the two nearest neighbor holes along the \hat{x} -direction.	147
4.26	FDTD simulation of the resonant modes in a Y-split defect cavity with $r/a = 0.34$, $r'/a = 0.51$, $d/a = 0.409$, and $n_{slab} = 3.4$.	148

5.1	InGaAsP-InP epitaxy for the defect lasers. The active region consists of four 0.85% compressively strained InGaAsP quantum-wells. The InP buffer layer is used as a sacrificial layer which is removed by a selective HCl etch in order to free the membrane from the substrate. The total thickness of the membrane after processing is 211 nm. . . .	152
5.2	Suspended membrane photonic crystal waveguide processing steps. . .	153
5.3	SEM micrograph of a defect cavity taken at an angle of 30° . After the HCl etch the etched surfaces appear smooth down to a scale of 5 nm (SEM resolution). The sidewalls of the holes are sloped at 10° from vertical, which can be reduced by optimizing the temperature and gas flow during the chemically-assisted ion-beam etch.	157
5.4	Illustration of the shape of the etch pits resulting from the crystallographic dependence of the HCl wet etch. Notice that the size of the “V-grooves” formed are dependent upon the depth of the CAIBE etch.	159
5.5	SEM images of a partially undercut photonic crystal waveguide structure showing the formation of $\{111\}$ In crystal plane facets. A cross-section in the $(01\bar{1})$ plane is shown in (a), and a top view (30° tilt) is shown in (b).	159
5.6	SEM images of the wet etch structure formed from photonic crystal patterns with different orientations relative to the InP crystal lattice. In (a) the ΓJ direction of the hexagonal photonic crystal lattice is aligned with the $[01\bar{1}]$ direction of the InP lattice. In (b) the ΓX direction is aligned with the $[01\bar{1}]$ direction.	160
5.7	Top view of a microfabricated 2D hexagonal array of air holes with a single central hole missing. The inter-hole spacing, a , is 500nm, and the radius of the holes are approximately 160nm.	161

5.8	Cross-section through the patterned membrane structure. The slab is 211 nm thick after processing. The use of an InGaAs etch stop layer results in a smooth bottom interface below the membrane. For membranes larger than 10 μm a significant bowing occurs and for devices greater than 15 μm the membrane collapses onto the InGaAs etch stop layer.	162
5.9	SEM image showing how the under-cutting of the patterned waveguide proceeds from the center, where the holes are largest, towards the edge of the patterned area.	164
6.1	Photoluminescence measurement set-up used to characterize the photonic crystal defect cavities.	166
6.2	PL from an unprocessed area is shown for three different pumping conditions (4 μm pump spot size). The bottom plot corresponds to 20 μW CW pumping. In the middle plot the peak pump power is 170 μW with a 50% duty cycle. The PL in the top plot was taken using 10 ns pulses with a 3 μs period at a peak pump power of 7 mW (duty cycle $\sim 0.3\%$).	167
6.3	Near-threshold photoluminescence from a symmetric defect cavity with $a = 515$ nm, $r/a \approx 0.34$, and $d/a = 0.409$. The two resonance peaks correspond to the degenerate DD S-B ₁₀ and S-B ₂₁ modes(x,y dipole-like modes, respectively), and the SA S-B ₂₀ cavity mode.	169
6.4	PL from a series of S defect cavities with lattice spacing equal to 570, 515, and 480 nm ($d/a = 0.3721 - 0.4416$). The porosity of the cavities were nearly identical (as measured by SEM) with an r/a ratio of 0.325.	170
6.5	SA S-B ₂₀ laser mode in a symmetric defect cavity with dimensions $a = 515$ nm, $r/a = 0.351$, and $d/a = 0.409$	172
6.6	Estimated external lasing threshold optical pump power vs. mode Q for 1,2,3, and 4 QW active regions at room temperature using parameters in Table 6.1.	177

6.7	Estimated threshold current and carrier density vs. mode Q for a four QW active region at room temperature (see Table 6.1).	178
6.8	SEM micrograph of the photonic crystal laser array. The lattice spacing varies with row number, and the hole radius varies with column number. An expanded view of an individual defect cavity is also shown on the right.	181
6.9	Tuning of the laser wavelength versus r/a . The lattice spacing in this case is fixed at 490 nm, while the radius of the air holes is tuned from 165 nm to 150 nm [$r/a = 0.38 - 0.32$].	183
6.10	Plot of the SA laser peak (\diamond) and the DD peak (\square) for different photonic crystal lattice spacings. On the left the wavelength is plotted versus lattice spacing, and on the right the normalized frequency is plotted versus the normalized slab thickness. The solid lines correspond to FDTD simulations of the DD and SA cavity mode tuning. .	183
6.11	Photoluminescence spectra from an X-split defect cavity with $a = 515$ nm, $r/a = 0.35$, $\Delta y = 0.05a$, and $d/a = 0.409$. The peak external pump power is 7.16 mW with pulses of width 10 ns and a pulse period of 3 μ s.	185
6.12	Plot of the peak collected power at the wavelength of the SA X-B ₂₀ defect mode wavelength (1560 nm) vs. external peak pump power (10 ns pulses with 3% duty cycle).	186
6.13	Plot of the peak collected power at the wavelength of the SA X-A ₂₀ defect mode wavelength (1573 nm) vs. external peak pump power (10 ns pulses with 3% duty cycle).	187
6.14	Photoluminescence spectra from a Y-split defect cavity with $a = 515$ nm, $r/a = 0.35$, $r'/a = 0.52$, and $d/a = 0.409$. The peak external pump power is 7.16 mW with pulses of width 10 ns and a pulse period of 3 μ s.	189
6.15	Selective mode excitation with varying pump beam profile in a Y-split cavity ($a = 490$ nm, $r/a = 0.315$, $r'/a = 0.45$, $d/a = 0.409$).	190

6.16	Y-A1 ₀ (VB) and Y-A2 ₀ lasing lines in the Y-split defect cavity of Figure 6.14. The peak external pump power is 4.3 mW with pulses of width 10 ns and a pulse period of 3 μ s.	191
6.17	Light-in vs. Light-out curve for a localized DA Y-A2 ₁ mode. The Y-split defect cavity has dimensions: $a = 515$ nm, $r/a = 0.316$, $r'/a = 0.45$, and $d/a = 0.409$	192
6.18	Light-in vs. Light-out curve for a localized DA Y-B2 ₀ mode. The Y-split defect cavity has dimensions: $a = 515$ nm, $r/a = 0.325$, $r'/a = 0.50$, and $d/a = 0.409$	193
6.19	Electric field patterns of the (x,y) dipole modes in the middle of the slab waveguide.	195
6.20	PX and PY polarizer angle projected on the top surface of a defect cavity as mounted in the PL set-up.	196
6.21	Polarization filtered (no polarizer (NP), X-polarized (PX), and Y-polarized (PY)) photoluminescence spectra for the three cavity geometries (S , X , Y) showing the polarization characteristics of the deep donor modes.	198
6.22	Top view of a microfabricated Y-split cavity. The inter-hole spacing is 515 nm, and the radius of the holes are approximately 180 nm. The two enlarged holes, which are used to split the dipole mode degeneracy, have a radius of 240 nm. The InGaAsP membrane is 220 nm in thickness.	200
6.23	2D slice through the middle of the slab showing the electric field amplitude of the x -dipole mode. The defect mode has a large overlap with the gain region due to the anti-node at the center of the defect. The enlarged air holes serve two functions: the first is to tune the x -dipole mode frequency so as to maximize the Q; the second is to push the y -dipole mode frequency out of the band-gap of the photonic crystal resulting in a single mode cavity.	201

6.24	Spectrum of the laser line just above threshold. The linewidth is approximately 0.2nm, limited by the resolution of the spectrometer. The spontaneous emission well below threshold is shown in the inset. . . .	204
6.25	L-L curve showing the power at the laser wavelength versus the incident pump power. The sample was cooled to 143K and pumped with 10 ns pulses (4% duty cycle).	205

List of Tables

3.1	D_{6h} character table.	100
3.2	C_{2v} character table.	101
3.3	C_{3v} character table.	102
3.4	C_{6v} character table	102
4.1	Magnetic field amplitude patterns of the resonant modes in a symmetric cavity ($r/a = 0.34$, $d/a = 0.409$, $n_{slab} = 3.4$, $p = 5$).	139
4.2	Symmetric cavity resonant mode characteristics ($r/a = 0.34$, $d/a = 0.409$, $n_{slab} = 3.4$, $p = 5$).	140
4.3	Field amplitudes of the SA modes of a symmetric cavity with r/a linearly graded from 0.38 – 0.34 ($d/a = 0.409$, $n_{slab} = 3.4$, $p = 8$). . .	142
4.4	Characteristics of shallow acceptor modes in a symmetric cavity with different gradings of the hole radius ($d/a = 0.409$, $n_{slab} = 3.4$, $p = 8$). . .	142
4.5	Magnetic field (amplitude) patterns of the resonant modes in an X-split cavity ($r/a = 0.34$, $d/a = 0.409$, $n_{slab} = 3.4$, $\Delta y = 0.15a$, $p = 5$). . . .	145
4.6	X-split cavity resonant mode characteristics ($r/a = 0.34$, $d/a = 0.409$, $n_{slab} = 3.4$, $\Delta y = 0.15a$, $p = 5$).	146
4.7	Field amplitude patterns of the resonant modes in a Y-split cavity ($r/a = 0.34$, $r'/a = 0.51$, $d/a = 0.409$, $n_{slab} = 3.4$, $p = 8$).	149
4.8	Y-split cavity resonant mode characteristics ($r/a = 0.34$, $r'/a = 0.51$, $d/a = 0.409$, $n_{slab} = 3.4$, $p = 8$).	150
6.1	Parameters used to estimate the threshold pump power of localized defect modes in the MQW InGaAsP perforated membrane.	176

Chapter 1 Introduction

The work presented in this thesis is grounded largely upon two concepts of microwave theory discovered around the time of World War II. In 1946 [1] Edward Purcell wrote a short abstract discussing the spontaneous emission properties of atoms located in microwave cavities with dimensions on the order of the wavelength of the emitted radiation. This was the first hint that the electromagnetic environment of an atom could significantly alter its emission properties. About the same time work on traveling wave amplifiers and linear accelerators was being carried out in which microwave radiation signals are converted to electronic signals [2]. Efficient energy transfer required phase matching of the two signals. In order to match the momentum of the microwave radiation to the electrical currents, periodic waveguides were used to create electromagnetic dispersion [3].

Both of these physical phenomena can also be used for optical devices as was put forth more than 40 years later by Daniel Kleppner in 1981 [4] and Eli Yablonovitch in 1987 [5]. Due to the inherent size scale, initial work focused on periodic structures for microwave devices [6,7]. Even before the concept of photonic band-gaps, however, periodic dielectric structures were already being used for distributed Bragg reflection of optical waves. In the 1970's Yeh, et al. [8] were designing "Bragg fibers" in which a cylindrical fiber formed from layered media could be used to guide light in new and interesting ways. Another example is that of the Distributed Feedback (DFB) laser [9]. Developed in the 70's as well, the DFB laser utilizes the coherent Bragg reflection from a spatially periodic dielectric to provide the feedback necessary for lasing action. It wasn't until the 1980's, with the advent of highly anisotropic dry etching techniques [10] of semiconductor materials that high-index contrast multi-dimensional periodic dielectric structures became feasible.

During the 1990's there was extensive work done on the fabrication of two and three-dimensional optical photonic crystals using a myriad of different materials and

methods [11–22]. Although three-dimensional photonic crystals are required in order to form a full frequency band-gap covering all directions of light propagation, the fabrication of such structures remains rather difficult [17] limiting the ability of devices to take full advantage of all three dimensions. Presently, a technologically more appealing method of manipulating light is to effectively reduce space to two dimensions by using a vertical waveguiding structure. By quantizing the modes in a waveguide, one sacrifices the third direction normal to the waveguide [15], however many of the salient features of three-dimensional photonic crystals carry over into the quasi-two-dimensional system [23–26].

Two-dimensional photonic crystal waveguides can be used to efficiently trap light in all three directions [27–29], guide light around sharp corners [18], and to diffract light over large angles [19,30]. Nano-optic structures formed from planar two-dimensional photonic crystals hold a great deal of promise due to the flexibility in their geometries. Lithographic methods may be employed to alter the photonic crystal geometry to tune device characteristics. An array of densely packed photonic crystal waveguides [18], prisms [19], and light sources [31] integrated on a single monolithic chip may thus be envisioned.

The focus of this thesis is on one aspect of this vision, the formation of ultra-small volume high-Q optical cavities. Historically, the Vertical Cavity Surface Emitting Laser [32] (VCSEL), in which light is confined between two epitaxially grown distributed Bragg reflectors, was one of the first semiconductor cavities with dimensions on the order of the wavelength of light. Another microcavity laser, the “thumbtack” or microdisk laser [33–35], uses total internal reflection at the edge of a high refractive index disk to form low-loss whispering gallery type modes [36]. More recently, there has been work done by several groups on photonic wire/waveguide structures using a one-dimensional in-plane photonic crystal [37–39]. The work here borrows attributes from all of these structures to form a low-loss cavity with a volume approaching a cubic half-wavelength.

An illustration of the two-dimensional photonic crystal defect cavity laser studied in this thesis is shown in Figure 1.1. Light is contained inside the microcavity using

two different mechanisms. First, a $\lambda/2$ high-index slab is used to trap photons in the vertical direction by way of total internal reflection (TIR) at the air-slab interface. Second, the light is localized in-plane using a micro-fabricated 2D photonic crystal consisting of a hexagonal array of air holes etched into the slab. The periodic variation in the refractive index gives rise to Bragg scattering of photons, which opens up forbidden energy gaps in the in-plane photon dispersion relation [40] (see Figure 1.2). The photonic crystal thus provides an energy barrier for the propagation of guided electromagnetic waves with frequencies that lie within the band-gap. In the simplest structure a single hole is removed in the photonic crystal, similar to a phase-slip in a distributed feedback laser, forming a resonant cavity. The resonant mode is highly localized to the defect region, and photons can only escape by either tunneling through the 2D photonic crystal, or by impinging on the air-slab interface at a high enough angle to leak out in the vertical direction.

The advantage of using a photonic crystal to form the optical cavity is the inherent flexibility in geometry which allows one to fine-tune the defect mode emission wavelength, as well as its radiation pattern [27]. The compact size and high spontaneous emission coupling factor (β) of the defect microcavity [41] also make it interesting for high modulation rate light-emitting diodes [42], or as a low-noise [43], low-threshold [44] light source. In addition, microcavities based upon nanofabricated photonic crystals may be useful where crystal growth of high-index contrast mirrors are limited, such as in long wavelength VCSELs or blue/green gallium nitride based devices [45].

Thesis Outline

Chapter 2 begins by analyzing how the spontaneous emission of light within semiconductor materials is modified by the presence of optical microcavities. The focus here is on the interaction of light and matter in the weak coupling limit, as is appropriate in semiconductor active regions at room temperature. In chapter 3 the symmetries of periodic dielectric structures are studied in order to develop a qualitative feel for the resonant modes present in photonic crystal resonators with different

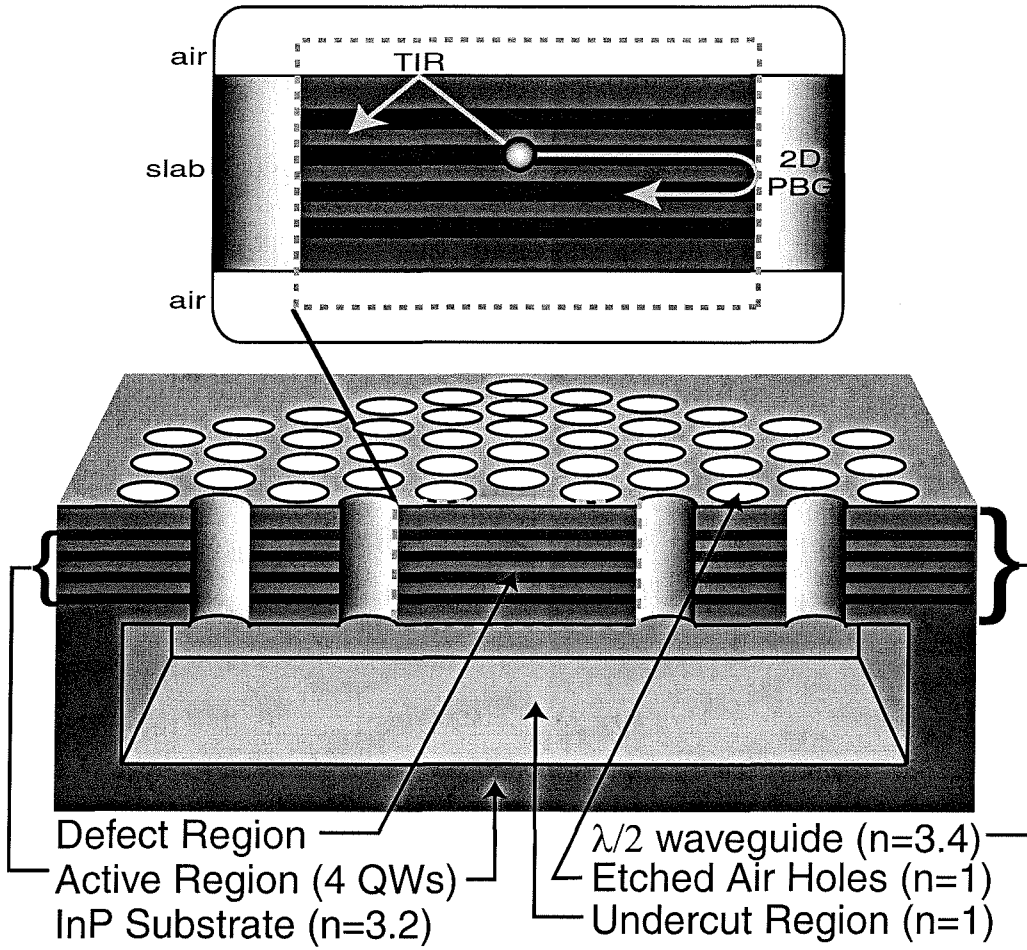


Figure 1.1: Cross-section through the middle of the photonic crystal microcavity. Photons are localized to the defect region by TIR at the air/slab interface and by Bragg reflection from the 2D photonic crystal.

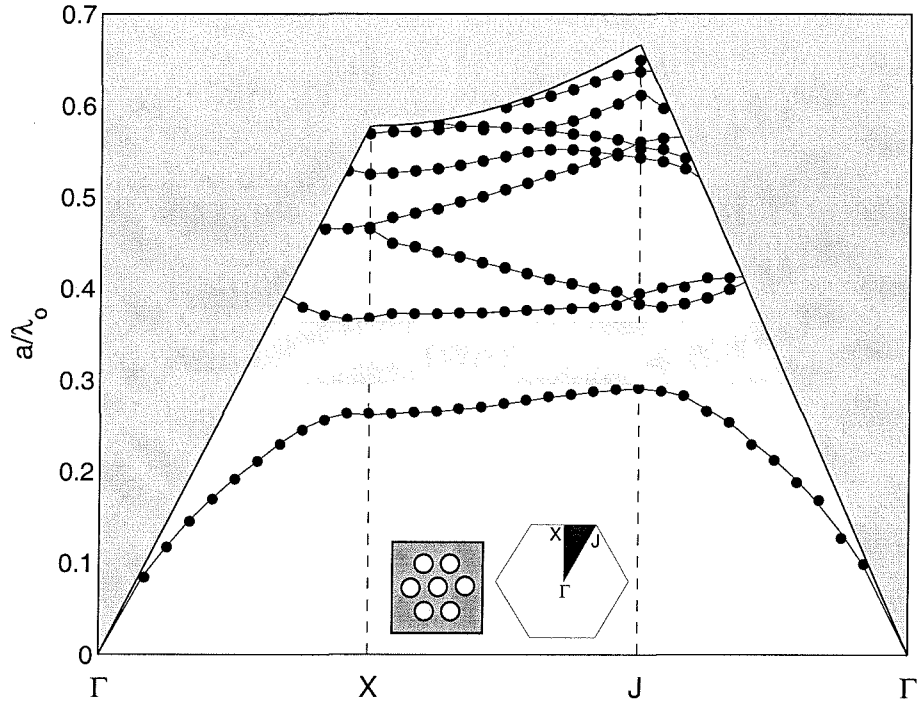


Figure 1.2: In-plane bandstructure of the triangular lattice of air holes for the TE-like (even) modes in an optically thin high-index slab. The parameters used in this calculation are: $r/a=0.32$, $d/a=0.409$, $n_{slab} = 3.4$, and $n_{clad} = 1$. The TE-like guided mode band-gap extends between the lowest frequency band (“valence” band) and the next higher frequency band (“conduction” band). The band-gap covers a normalized frequency range of roughly 0.28-0.36, or 25% of the midgap frequency.

geometries. Numerical methods are then used in chapter 4 to study the optical losses in two-dimensional photonic crystal defect cavities, and to accurately design the resonator geometry for light emission at $1.5\text{ }\mu\text{m}$. Chapter 5 details the techniques used to fabricate the defect cavities, and in chapter 6, results from photoluminescence measurements of several different cavity geometries are presented. Finally, a brief summary is given in chapter 7.

Chapter 2 Spontaneous Emission in Semiconductor Optical Microcavities

It has been known for some time now [1] that the interaction between photons and the electronic states of matter can be significantly altered by modifying the environment in which the interaction takes place¹. In this chapter we would like to determine how the boundary conditions enforced by a given electromagnetic cavity affects the emission of light. We will narrow our focus to optical processes pertinent to semiconductor materials near room temperature. This will limit our discussion to rather weak matter-radiation coupling in which perturbative methods can be accurately employed².

Spontaneous emission is the process by which an excited state of matter relaxes back to a lower lying energy state, and in the process emits a quanta of electromagnetic energy. This is different from the stimulated process by which an existing field “coerces” the relaxation process. There are several physical pictures that can be used to describe the spontaneous emission process of an excited electronic state. Each can be inferred from the same mathematical (quantum mechanical) model. Here we will use a more physically intuitive picture, one that does not require discussion of mysterious entities such as vacuum field fluctuations (VFF). In this picture one starts from the viewpoint that the true “field” is the coupled electron + photon system. Energy located entirely in the electron field then naturally diffuses out into the electromagnetic field. The irreversible process of spontaneous emission can then be attributed

¹This is only true for interactions which take place over time scales which are much longer than the time it takes light to “sense” its environment [46]. This is usually taken as the round-trip time for a photon in an electromagnetic cavity.

²In this chapter we will be concerned with dephasing affects which happen on a much faster time scale ($\tau_d \approx 0.1ps$ [47]) than the spontaneous lifetime or the coherent Rabi oscillation period. This allows us to make certain simplifying assumptions resulting in a closed form for the spontaneous emission rate.

to the large phase space of the electromagnetic field (continuum of modes)³ or to dephasing effects which break the electron + field coherence, spilling the energy into one system or the other.

The coupled field equations, however, are non-linear in the uncoupled fields. This makes an exact closed form solution of the coupled field theory very difficult in most cases, and impossible in general. One must resort then to breaking the complete field into different parts which are linear in the field variables, and then perturbatively coupling all the parts. A Hamiltonian for the combined system can be written as:

$$H = H_{e-} + H_{em} + H_{int}, \quad (2.1)$$

where H_{e-} is the free electron field energy, H_{em} is the free electromagnetic field energy, and H_{int} is an electron-photon interaction term. We will first consider the free electromagnetic field.

2.1 Canonical Quantization Method of the Electromagnetic Field in a Dielectric Material

In this section we make the judicious choice of considering the stable, bound states of atoms (electrons, protons, neutrons, and coulombic field (longitudinal photons)) as one system representing the bulk material, and that of the free radiation field representing another. One can then consider different excitations of the bulk material such as phonons, plasmons, magnons, etc. as separate fields. The main point is that we have separated the free electromagnetic field and the bulk material with all of its associated charges and local coulombic fields. If we consider a test “atom” which is situated somewhere within our bulk material, and we would like to figure out how it radiates electromagnetic energy we must take into account the response of all the

³The energy diffuses out in phase space and does not coherently return until a time proportional to the inverse of the frequency spacing of electromagnetic modes.

atoms in the bulk material to the radiated field, and the subsequent effects on the radiative properties of our test “atom” in a self-consistent manner.

This separation of matter and radiation turns out to be a little extreme. A major simplification can be made by including in the radiation field excitations that part of the dielectric material response (polarization) which is linear in the electromagnetic field strength and frequency independent. These two conditions are generally met for far-off resonance deep core electrons in atoms⁴. We now consider not the free radiation field, but the excitations of the combined material polarization and free field through the use of the dielectric function, $\epsilon(\mathbf{r}, t)$. The resulting field excitations take into account, in a self-consistent manner, the interactions of the atomic dipoles and the free electromagnetic field. We will from now on consider these compound excitations as our fundamental particles and quantize them.

In order to go from the classical electromagnetic field⁵ to a quantum field, the classical fields must be modified to include quantum mechanical operators. Dynamics of the field are then governed by linear transformations by these operators on a Hilbert space of vectors. The canonical quantization method used here is one “recipe” for introducing such operators into a classical field. If the equations of motion of the classical field theory are linear in the fields then they can be expanded as a superposition of harmonic modes⁶:

$$\mathbf{E}(\mathbf{r}, t) = \sum_m \left[a_m(t) \mathbf{E}_m(\mathbf{r}) + a_m^\dagger(t) \mathbf{E}_m^*(\mathbf{r}) \right], \quad (2.2)$$

where the electric field harmonic mode profiles, $\mathbf{E}_m(\mathbf{r})$, are obtained by solving Maxwell’s equations of motion (eq. 3.44). Classically, the field Fourier coefficients,

⁴Resonant phenomena such as spontaneous and stimulated emission, and non-linear processes must be folded in in a different manner.

⁵Discussed in the next chapter.

⁶The superposition in most practical situations contains both discrete and continuous spectra. A discrete sum has been used here for simplicity. In the case of a continuous spectra the normalization of modes is slightly different utilizing the Dirac-delta function.

a_m and a_m^\dagger , evolve as $e^{\pm i(\omega_m t)}$ ⁷:

$$a_m^\dagger(t) = a_m^\dagger(0)e^{i\omega_m t}, \quad (2.3)$$

$$a_m(t) = a_m(0)e^{-i\omega_m t}. \quad (2.4)$$

In quantum mechanics, energy is quantized into units of $\hbar\omega_m$, and a_m and a_m^\dagger are upgraded from complex numbers to operators which annihilate and create a single quanta of energy⁸. The electric field operator⁹ is then,

$$\hat{\mathbf{E}}(\mathbf{r}, t) = \sum_m \left[\hat{a}_m(t) \mathbf{E}_m(\mathbf{r}) + \hat{a}_m^\dagger(t) \mathbf{E}_m^*(\mathbf{r}) \right]. \quad (2.5)$$

In the canonical quantization method the (equal-time) commutation relations between the annihilation and creation operators are¹⁰

$$[\hat{a}_m(t), \hat{a}_{n_\lambda}^\dagger(t)] \equiv \hat{a}_{n_\lambda}(t) \hat{a}_{n_\lambda}^\dagger(t) - \hat{a}_{n_\lambda}^\dagger(t) \hat{a}_{n_\lambda}(t) = \delta_{mn_\lambda}, \quad (2.6)$$

$$[\hat{a}_m(t), \hat{a}_{n_\lambda}(t)] = [\hat{a}_m^\dagger(t), \hat{a}_{n_\lambda}^\dagger(t)] = 0. \quad (2.7)$$

In order to associate \hat{a}_m (\hat{a}_m^\dagger) with single photon annihilation (creation) operators the classical mode profiles must be distinct (orthogonal), and one must determine what amplitude constitutes a single quantum of energy¹¹. As discussed in chap-

⁷Compare with eq. 3.89 of sub-section 3.4.4.

⁸The creation operator is chosen to carry positive energy ($+\omega_m$)

⁹In order to differentiate quantum operators from complex fields a $\hat{}$ will be used above each operator.

¹⁰One can start from these relations, or in a Lagrangian approach from the commutation relations of the canonically conjugate field operators.

¹¹One other implicit condition is that the time evolution of a_m and a_m^\dagger be consistent with that of the time evolution of the classical harmonic modes. In the Heisenberg picture of quantum mechanics the time evolution of an operator is governed by its commutation with the Hamiltonian operator. The trick of the canonical quantization method is that the classical time evolution of a and a^\dagger turn out to be consistent with the time evolution determined in the Heisenberg picture. In the approach taken here this consistency seems rather accidental. For a more rigorous analysis starting from the

ter 3 the classical mode profiles, $\mathbf{E}_m(\mathbf{r})$, satisfy an (energy) orthogonality relation. This ensures proper energy partitioning amongst the modes, and thus proper photon counting. It should be noted that it is possible to define a generalized set of annihilation and creation operators which annihilate and create an arbitrary vector field distribution. However, if different field configurations are not power orthogonal then one must consider correlations between modes when counting photons [49]. The time evolution of such operators is also not as simple as the harmonic oscillation of the standard \hat{a}_m and \hat{a}_m^\dagger operators.

To determine the correct normalization for the vector mode profiles we start with the Hamiltonian density for the electromagnetic field in a dielectric material,

$$\hat{h}_{em}(\mathbf{r}) = \frac{1}{2}\epsilon(\mathbf{r})\hat{\mathbf{E}} \cdot \hat{\mathbf{E}}^* + \frac{1}{2\mu}\hat{\mathbf{H}} \cdot \hat{\mathbf{H}}^*. \quad (2.8)$$

The energy stored in the electromagnetic system (including the polarization) is given by the Hamiltonian, $\hat{H}_{em} = \int_V d^3r \hat{h}_{em}(\mathbf{r})$. Deriving $\hat{\mathbf{H}}$ from $\hat{\mathbf{E}}$ using Maxwell's equations, and integrating the Hamiltonian density over all space, one finds that the Hamiltonian operator can be expressed as

$$\hat{H}_{em} = \sum_m 2\bar{E}_m(\hat{a}_m^\dagger \hat{a}_m + 1/2). \quad (2.9)$$

where \bar{E}_m is equal to,

$$\bar{E}_m = \int_V d^3r \epsilon(\mathbf{r})\mathbf{E}_m(\mathbf{r}) \cdot \mathbf{E}_m^*(\mathbf{r}). \quad (2.10)$$

The eigenvalues of the operator $\hat{a}_m^\dagger \hat{a}_m$ count the number of photons in the m th field mode. For this reason $\hat{n}_m = \hat{a}_m^\dagger \hat{a}_m$ is called the photon number operator. The 1/2 in

field Lagrangian see reference [48].

the $\hat{n}_m + 1/2$ term represents energy stored in the ground state of the electromagnetic field. Although arbitrary in value, it's presence is essential as it is responsible for spontaneous emission [50]. It is a place holder for the ground state in interactions with other fields.

The eigenvalues of the Hamiltonian operator are then equal to

$$\mathcal{H}_{em,m} = 2\bar{E}_m(n_m + 1/2). \quad (2.11)$$

As n_m is the number of photons in mode m , $2\bar{E}_m$ must equal the quanta of energy for mode m ,

$$\int_V d^3r \epsilon(\mathbf{r}) \mathbf{E}_m(\mathbf{r}) \cdot \mathbf{E}_m^*(\mathbf{r}) = \frac{\hbar\omega_m}{2}. \quad (2.12)$$

It will also be important to have an expression for the electromagnetic vector field operator. The generalized Coulomb gauge (radiation gauge) for a spatially varying dielectric is used,

$$\nabla \cdot (\epsilon \mathbf{A}) = 0. \quad (2.13)$$

This allows us to write the scalar potential, V , as a function of the free charge, ρ . In the absence of free charge (such as is the case for the free-field) the scalar potential (coulomb field) is 0. Thus the electric field can be written in terms of the vector potential alone,

$$\hat{\mathbf{E}} = -\dot{\hat{\mathbf{A}}} = \sum_m \left[\hat{a}_m(t)(i\omega_m \mathbf{A}_m(\mathbf{r})) + \hat{a}_m^\dagger(t)(i\omega_m \mathbf{A}_m(\mathbf{r}))^* \right]. \quad (2.14)$$

The vector potential (normalized) field profiles for the free field can now be related

to those of the electric field,

$$\mathbf{E}_m(\mathbf{r}) = i\omega_m \mathbf{A}_m(\mathbf{r}). \quad (2.15)$$

In this gauge, it is possible to show [51] that the energy associated with electromagnetic radiation is contained in that part of the electric field satisfying eq. (2.14), and the coulomb energy is contained in an instantaneous coulomb potential depending on the distribution of free charges. It is then possible to quantize only the radiating part of the electric field, which is what we have implicitly done above. The coulomb energy term must then be incorporated as part of the quantization scheme of the charged particles¹².

With the orthonormality conditions in hand for both the vector potential and the electric field mode profiles inside a spatially varying dielectric material, along with their corresponding photon creation and annihilation operators, we can now proceed to quantize the system of free charges (electrons).

2.1.1 Photon Modes of a Uniform Dielectric

The transverse (radiation) electric field eigenmodes of a uniform dielectric material consists of plane waves:

$$\mathbf{E}_{\mathbf{k}_p, \sigma} = \bar{\mathbf{e}}_\sigma \sqrt{\frac{\hbar \omega_{\mathbf{k}_p}}{2\epsilon V_{box}}} e^{-i(\mathbf{k}_p \cdot \mathbf{r})}, \quad (2.16)$$

where \mathbf{k}_p labels the photon momentum, $\omega_{\mathbf{k}_p}$ is the photon angular frequency, ϵ is the dielectric constant, V_{box} is the normalization volume, $\bar{\mathbf{e}}_\sigma$ is a unit vector, and $\sigma \in \{1, 2\}$ labels the polarization state. Owing to the transversality of the electric field in a uniform dielectric, $\bar{\mathbf{e}}_\sigma \cdot \mathbf{k}_p = 0$. Also, as one can check, the modes of eq.

¹²It is usually perturbatively incorporated into a free field theory [47, 52] using the Hartree-Fock approximations.

(2.16) are normalized such that they satisfy the orthogonality conditions as dictated by eq. (2.12).

Using the standard “big box” with periodic boundary conditions we quantize the photon momentum:

$$\mathbf{k}_p^{l,m,n} = (lK_x, mK_y, nK_z), \quad (2.17)$$

where $K_i = 2\pi/L_i$ for $i \in \{x, y, z\}$ and $V_{box} = L_x L_y L_z$. Letting the sides of the “big box” grow towards infinity, sums over photon momentum states can be replaced by integrals:

$$\sum_{\mathbf{k}_p} = \frac{1}{K_x K_y K_z} \left(\sum_{l,m,n} K_x K_y K_z \right) \approx \frac{V_{box}}{(2\pi)^3} \int d^3k. \quad (2.18)$$

The density of photon states in momentum space, including a factor of two for polarization, is

$$\rho_p(\mathbf{k}) = 2 \frac{V_{box}}{(2\pi)^3}. \quad (2.19)$$

Typically, the required integrations are over energy or frequency, and thus one would like to know the spectral density of modes. In a homogeneous dielectric material $\omega_{\mathbf{k}_p} = \frac{c}{n} |\mathbf{k}_p|$, where $n = \sqrt{\epsilon/\epsilon_o}$ is the refractive index. The integral over \mathbf{k} can be written as¹³

¹³Integrating over θ and ϕ gives the density (per unit volume) of photon modes per unit angular frequency in a homogeneous dielectric material

$$\rho_\omega^o = \frac{\omega^2 n^3}{\pi^2 c^3}. \quad (2.20)$$

$$\int d^3k = \int d|\mathbf{k}| d\theta d\phi |\mathbf{k}|^2 \sin(\theta) = \int d\omega d\theta d\phi \frac{\omega^2 n^3}{c^3} \sin(\theta). \quad (2.21)$$

The sum over optical modes can now be replaced by a sum over polarization states and an integral over \mathbf{k} -space:

$$\sum_{\mathbf{k}_p, \sigma} = \frac{V_{box}}{(2\pi)^3} \sum_{\sigma} \int d\omega d\theta d\phi \frac{\omega^2 n^3}{c^3} \sin(\theta). \quad (2.22)$$

2.1.2 Quasi-Modes, Leaky Modes, and Multi-mode Fields: Counting Photons in a Microcavity

Many times the term optical *mode* is used in place of the more accurate term *resonance*. In classical optics there is rarely a problem with inter-mixing these two terms, however, in quantum mechanics extra care must be taken in partitioning the electromagnetic radiation amongst different modes. The special orthonormality¹⁴ conditions placed upon the optical mode profiles in eq. (2.12), and the corresponding equal-time commutators in eq. (2.3) satisfied by the creation and annihilation operators, ensure that the photon energy quanta are correctly accounted for. Although the (lossless) eigenmodes are extremely beneficial from a photon accounting standpoint, in many cases the natural resonances of an optical system can provide an easier attack on a problem.

All practical resonators support resonances¹⁵ which have a finite linewidth, and thus do not qualify as true photon eigenmodes. These resonances are formed from a continuum of photon modes; they are quasi-modes or leaky modes. All laser cavities and laser *modes* fall into this category as well. Many interesting, and often bewildering, properties of laser radiation can be attributed to the fact that the laser supports resonances, not photon modes. A good example is that of the Petermann

¹⁴The photon modes are energy (power for transverse waveguide modes) orthogonal.

¹⁵Resonances are still eigenmodes of the system, they just have complex eigenvalues.

factor [53–55] which describes the enhancement of the laser linewidth in gain-guided or anti-guided laser cavities. Although the laser linewidth enhancement at first glance seems to contradict the famous Einstein relation between spontaneous emission rate and stimulated emission rate, in fact it is the non-power-orthogonality of the leaky laser cavity modes and resulting photon correlations¹⁶ which cause the Petermann effect [49, 54]. Besides the non-orthogonality issue of resonator quasi-modes, there is also the problem of normalization. Quasi-modes are in general not energy (power) normalizable [56].

As the quality of a resonator increases, the quasi-mode resonances approach that of proper modes and it is possible to define creation and annihilation operators for the quasi-modes. An excellent discussion of the limits of validity of the quasi-mode approach and its relation to reservoir damping theory and the Quantum Langevin formalism is given by Vogel and Welsch [48] in their book, “Lectures on Quantum Optics.” In this approach the local field of the resonator is described by a reduced set of quasi-modes which are then coupled to a reservoir of radiation modes outside the resonator. Vogel and Welsch show that in the limit that the resonator is of high enough quality¹⁷ and the time in which events of interest occur is much larger than the cavity round trip time, then the quasi mode approach is valid. These conditions are satisfied if the following relations between the required resolution in time $\Delta\tau$, the cavity round trip time τ_{cav} , and the cavity photon lifetime τ_{ph} are met:

¹⁶The Petermann factor can also be thought of as a result of the fact that some of the excited state electrons in the gain media do not participate in amplifying the laser mode but still participate in spontaneous emission into the laser mode. Physically this is possible if spontaneous emission from gain media located outside of the internal laser field pattern contributes to the total laser output. This can happen for non-power-orthogonal modes.

¹⁷The cavity finesse, \mathcal{F} , ironically is usually a better gauge of the *quality* of a resonator as opposed to the quality factor, Q . This is because the finesse describes the ability to spectrally resolve the resonant structure of a resonator, whereas the Q describes only the spectral width of each individual resonance. \mathcal{F} and Q are approximately related by the formula: $Q \approx \mathcal{F} \frac{L}{\lambda_o/n_g}$. The Q quantifies the loss per optical cycle whereas the finesse quantifies the loss per round trip [57].

$$\Delta\tau \ll \tau_{cav}, \quad (2.23)$$

$$\Delta\tau \ll \tau_{ph}, \quad (2.24)$$

$$\mathcal{F} \approx 2\pi(\tau_{ph}/\tau_{cav}) \gg 1, \quad (2.25)$$

$$\Rightarrow \tau_{cav} \ll \Delta\tau \ll \tau_{ph}. \quad (2.26)$$

These limits are dependent not only on the characteristics of the optical cavity but also on the electron-photon interaction which one would like to investigate. For example, $\Delta\tau$ must be much less than the spontaneous emission lifetime in order to accurately describe spontaneous emission within the cavity. The spontaneous emission lifetime then sets the time-scale and the limits of validity of the quasi-mode approach. If the cavity walls were separated by a great distance then spontaneous emission from excited atoms within the cavity would not reach the cavity walls before the spontaneous emission event was already over. The effects of the cavity walls are negligible and the cavity itself and its quasi-modes play no role. Similarly, if the cavity is so lossy (finesse small) that individual resonances spectrally “bleed” together¹⁸, then correlations amongst the different quasi-modes must be included. The local density of states approaches that of vacuum and the concept of a resonant cavity fades away.

As shown by Vogel and Welsch [48], if the above limits of validity are met (over a given frequency bandwidth), then one can define quasi-modes, m , with creation and annihilation operators which satisfy the standard equal-time commutation relations of eq. (2.6). In the time evolution of the quasi-mode creation and annihilation operators given in eq. (2.3) one must include fluctuation terms from the radiation mode reservoir external to the cavity in order to maintain the equal-time commutation relationships¹⁹. The quasi-modes are defined and normalized only over the region of the cavity, which can be operationally defined as the volume outside of which no

¹⁸Spatial orthogonality amongst the different quasi-modes can no longer be assumed as well.

¹⁹There is decay present since the quasi-modes have a finite-linewidth, and thus a complex frequency. It is this decay that the fluctuations counteract to maintain unitarity.

feedback occurs²⁰. As discussed by Deutsch, et al. [49], the above limits described in eq. (2.23) assure that orthogonality amongst the quasi-modes is approximately maintained over the cavity volume²¹.

With regard to the quasi-modes of the photonic crystal cavities studied in this thesis, the cavity round trip time is only a few optical cycles as the cavities are on the order of a cubic wavelength in size. Since the Q factors are on the order of 10^3 , the short cavity length results in an equally small loss per round trip (large finesse). Therefore, in the weak-coupling limit in which spontaneous emission (or Rabi flopping) occurs over many optical cycles, the quasi-mode approach in these cavities is valid.

²⁰In this case radiation generated by an internal cavity source, once past the cavity boundary, continues to radiate outwards and does not get fed-back, by reflections or other processes, into the cavity. Optical feedback from external sources (including the vacuum) are then incorporated through coupling to the reservoir of radiation modes outside of the cavity.

²¹The quasi-modes are not orthogonal to the radiation modes of the reservoir external to the cavity, which allows for output and input coupling from the cavity. This is the source of the fluctuation and dissipation in the equations of motion of the quasi-modes.

2.2 Quantization of the Electron Field

The spatial dependence of the electronic states play an equal role to the electromagnetic field patterns in determining the electron-photon coupling. Similar to the canonical quantization method described above for the electromagnetic field, we write the (non-relativistic) electron field operator as,

$$\hat{\phi}_{e-} = \sum_n \hat{e}_n(t) \phi_n(\mathbf{r}), \quad (2.27)$$

where $\hat{e}_n(t)$ are the electron annihilation operators of the (uncoupled) electronic states, n , with energy eigenmode profile $\phi_n(\mathbf{r})$.²² For now the $\phi_n(\mathbf{r})$ do not need to be explicitly defined and we simply assume they represent the spatial dependence of quantized energy excitations of the electronic system uncoupled from the radiation field²³. In making the transition between the classical and the quantum pictures the electron annihilation and creation must satisfy the following equal-time anti-commutation relations (Fermi statistics):

$$\{\hat{e}_n(t), \hat{e}_m^\dagger(t)\} \equiv \hat{e}_n(t) \hat{e}_m^\dagger(t) + \hat{e}_m^\dagger(t) \hat{e}_n(t) = \delta_{mn}, \quad (2.28)$$

$$\{\hat{e}_n(t), \hat{e}_m(t)\} = \{\hat{e}_n^\dagger(t), \hat{e}_m^\dagger(t)\} = 0. \quad (2.29)$$

Assuming for now a discrete electronic mode density (and a hermitian Hamiltonian), the following orthonormality conditions are satisfied by the single particle energy eigenstates²⁴:

²²For instance, in a periodic structure $n = n(m, s, \mathbf{k})$, where m labels the electronic band, s labels any degeneracies that may be present in the band (spin, etc.), and \mathbf{k} represents the plane wave propagation vector.

²³Later we will need to make some assumptions as to what electron interactions we include in our electron field theory and this will determine what form the Hamiltonian will take.

²⁴Again, in the case of a continuum of modes the Kröencker delta must be replaced by the Dirac-delta function.

$$\hat{H}_s \phi_m(\mathbf{r}) = \varepsilon_m \phi_m(\mathbf{r}), \quad (2.30)$$

$$\int_V \phi_n^*(\mathbf{r}) \phi_m(\mathbf{r}) d^3r = \delta_{mn}, \quad (2.31)$$

where \hat{H}_s is the single particle electron Hamiltonian²⁵, and V represents the physical extent of the semiconductor crystal. The multi-particle Hamiltonian (second quantized) can be obtained from the single-particle Hamiltonian using the transformation,

$$\hat{H}_{e-} = \int_V d^3r \hat{\phi}_{e-}^\dagger(\mathbf{r}) \hat{H}_s \hat{\phi}_{e-}(\mathbf{r}) \quad (2.32)$$

$$= \sum_m \varepsilon_m \hat{e}_m^\dagger \hat{e}_m, \quad (2.33)$$

which, from the Heisenberg equations of motion, yields the correct time dependence for the annihilation and creation operators of energy excitations:

$$\dot{\hat{e}}_m = \frac{i}{\hbar} \{ \hat{e}_m, \hat{H}_{e-} \} = -\frac{i\varepsilon_m}{\hbar} \hat{e}_m \quad (2.34)$$

$$\Rightarrow \hat{e}_m(t) = \hat{e}_m(0) e^{-i(\varepsilon_m/\hbar)t}, \quad (2.35)$$

$$\dot{\hat{e}}_m^\dagger = \frac{i}{\hbar} \{ \hat{e}_m^\dagger, \hat{H}_{e-} \} = \frac{i\varepsilon_m}{\hbar} \hat{e}_m^\dagger \quad (2.36)$$

$$\Rightarrow \hat{e}_m^\dagger(t) = \hat{e}_m^\dagger(0) e^{i(\varepsilon_m/\hbar)t}. \quad (2.37)$$

Two important operators which will be needed in the second quantized picture are the position operator, $\hat{\mathbf{r}}$, and the momentum operator, $\hat{\mathbf{p}}$. The second quantized operators can be written in terms of the single electron position ($\hat{\mathbf{r}}_s$) and momentum ($\hat{\mathbf{p}}_s$) operators as was done for the Hamiltonian:

²⁵In this case the Schrödinger equation.

$$\begin{aligned}
\hat{\mathbf{r}} &= \int_V d^3r \hat{\phi}_{e-}^\dagger \hat{\mathbf{r}}_s \hat{\phi}_{e-} \\
&= \sum_{m,n} \hat{e}_m^\dagger \hat{e}_n \langle \phi_m | \hat{\mathbf{r}}_s | \phi_n \rangle,
\end{aligned} \tag{2.38}$$

$$\begin{aligned}
\hat{\mathbf{p}} &= \int_V d^3r \hat{\phi}_{e-}^\dagger \hat{\mathbf{p}}_s \hat{\phi}_{e-} \\
&= \sum_{m,n} \hat{e}_m^\dagger \hat{e}_n \langle \phi_m | \hat{\mathbf{p}}_s | \phi_n \rangle,
\end{aligned} \tag{2.39}$$

where the Dirac bra (\langle) ket (\rangle) notation has been used to represent the inner product of functions (vectors). In the position basis, $\hat{\mathbf{r}}_s = \mathbf{r}$ and $\hat{\mathbf{p}}_s = -i\hbar\partial/\partial\mathbf{r}$.

2.2.1 Electrons and Holes

In a (intrinsic) semiconductor and insulator there are just enough valence electrons to completely fill the valence band at 0 K temperature²⁶. A metal, on the other hand, will generally have a half-filled valence band at 0 K. At finite temperature some of the valence band electrons are excited and populate the higher lying bands, or conduction bands. Conduction in crystalline materials requires an energy band that is populated enough to get sufficient current; however, overpopulation tends to stifle the electrons ability move²⁷. The difference between an insulator and semiconductor is the size of the energy gap between valence and conduction bands. An insulator can become semi-conducting if the temperature is raised to a suitable level. Semiconductors can also be made conductive by doping with impurities which add electrons to the system (donors) and tend to fill the conduction band, or by doping with impurities which remove electrons from the valence band (acceptors) and thus open ‘holes’ in the

²⁶The valence band can be defined as the highest energy band that has occupied electronic states at a temperature of 0 Kelvin.

²⁷This is most easily visualized in momentum space where a full band has electrons with equal +ve and -ve momentum which tend to cancel each other out. Under the influence of a force, electrons cannot build up a net momentum as all momentum states are full [58].

valence band.

To help in the book keeping of particles that are involved in inter-band interactions we introduce “hole” particles in the valence band. The annihilation of an electron in the valence band with charge e , mass m_e , and quantum numbers λ_v ²⁸ corresponds to the creation of a hole in the electron “sea” of the valence band with charge $-e$, mass $-m_e$, and quantum numbers $-\lambda_v$. A similar relation in which the charge, mass, and quantum numbers reverse sign holds true between the creation of a valence band electron and the annihilation of a valence band hole. The creation and annihilation of holes thus have the following one-to-one relation to valence band electron operators:

$$\hat{h}_{-\lambda_v}^\dagger = \hat{e}_{\lambda_v}, \quad (2.40)$$

$$\hat{h}_{-\lambda_v} = \hat{e}_{\lambda_v}^\dagger. \quad (2.41)$$

With the above relationship between hole and electron operators, the commutation relationships for the hole operators are:

$$\{\hat{h}_{-\lambda_v}^\dagger(t), \hat{h}_{-\lambda'_v}(t)\} = \delta_{\lambda_v \lambda'_v}, \quad (2.42)$$

$$\{\hat{h}_{-\lambda_v}(t), \hat{h}_{-\lambda'_v}(t)\} = \{\hat{h}_{-\lambda_v}^\dagger(t), \hat{h}_{-\lambda'_v}^\dagger(t)\} = 0. \quad (2.43)$$

The time evolution of “free” hole states follows from eq. (2.40) and eqs. (2.34-2.36):

$$\hat{h}_{-\lambda_v}(t) = \hat{h}_{-\lambda_v}(0)e^{+i(\varepsilon_{\lambda_v}/\hbar)t}, \quad (2.44)$$

$$\hat{h}_{-\lambda_v}^\dagger(t) = \hat{h}_{-\lambda_v}^\dagger(0)e^{-i(\varepsilon_{\lambda_v}/\hbar)t}. \quad (2.45)$$

One can also define a hole number operator which counts the number of holes in a particular electronic state (0 or 1),

²⁸Including such attributes as the electron energy, momentum, and spin for instance.

$$\hat{n}_{-\lambda_v}^h = \hat{h}_{-\lambda_v}^\dagger \hat{h}_{-\lambda_v} = 1 - \hat{e}_{\lambda_v}^\dagger \hat{e}_{\lambda_v} = 1 - \hat{n}_{\lambda_v}, \quad (2.46)$$

where we have used the superscript h to represent a hole number operator as opposed to an electron number operator.

2.2.2 Electronic Envelope Approximation

There are in general two length scales in the electron wavefunction in crystalline materials such as semiconductors. There is the periodic Bloch part of the wavefunction which is localized to each lattice point in the Bravais lattice of the semiconductor crystal, and then there is a slowly varying envelope which describes the distribution of the electron wavefunction over many lattice periods:

$$\phi_{\lambda_n, l}(\mathbf{r}) \approx F_l^{\lambda_n}(\mathbf{r}) u_{\lambda_n}(\mathbf{r}), \quad (2.47)$$

where $F_l^{\lambda_n}$ is an envelope function and u_{λ_n} is the periodic Bloch function. The separation of the envelope and Bloch function, which is not strictly valid, is a good approximation only for slowly varying envelope functions²⁹. Normalization of the Bloch and envelope parts of electronic wavefunction follows from the normalization of the overall electron wavefunction given in eq. (2.30):

$$\begin{aligned} \int_V d^3r \phi_{\lambda_n, l}^* \phi_{\lambda_m, p} &\approx \left(\sum_{i=1}^N (F_l^{\lambda_n})^*(\mathbf{R}_i) F_p^{\lambda_m}(\mathbf{R}_i) \right) \int_\nu d^3r u_{\lambda_n}^*(\mathbf{r}) u_{\lambda_m}(\mathbf{r}) \\ &\approx \left(\int_V d^3R (F_l^{\lambda_n})^*(\mathbf{R}) F_p^{\lambda_m}(\mathbf{R}) \right) \left(\frac{1}{\nu} \int_\nu d^3r u_{\lambda_n}^*(\mathbf{r}) u_{\lambda_m}(\mathbf{r}) \right), \end{aligned} \quad (2.48)$$

where \mathbf{R}_i is the position vector of the i th lattice point, ν is the unit cell volume of

²⁹One which is formed from \mathbf{k} -components which are localized in \mathbf{k} -space, relative to the extent of the IBZ.

the crystalline lattice, and V is the volume of the entire crystal. In the envelope approximation the envelope and Bloch parts of the wavefunction satisfy their own orthonormality relations:

$$\frac{1}{V} \int_V d^3r u_{\lambda_n}^* u_{\lambda_m} = \delta_{nm}, \quad (2.49)$$

$$\int_V d^3r (F_l^{\lambda_n})^* F_p^{\lambda_m} = \Gamma_m^n \delta_{lp}, \quad (2.50)$$

where Γ_m^n is an overlap factor between the localized envelope functions ($\Gamma_n^n = 1$). The envelope approximation will be used to simplify expressions for the electronic states of a quantum-well in the calculation of transition matrix elements described below.

2.2.3 Quantum-Well States in a III-V Semiconductor

The envelope function of a bound state of the quantum-well consists of a plane-wave in the plane of the quantum-well and one of a discrete set of localized envelope functions in the direction normal to the quantum-well. The quantum-well states are labelled by a Bloch index m , the bound state integer n_z , and the in-plane momentum \mathbf{k}_\perp :

$$\phi_{m(n_z, \mathbf{k}_\perp)}(\mathbf{r}) \approx \frac{e^{-i\mathbf{k}_\perp \cdot \mathbf{r}_\perp} F_{n_z}^m(z)}{\sqrt{V_X}} u_{m(n_z, \mathbf{k}_\perp)}(\mathbf{r}), \quad (2.51)$$

where $u_{m(n_z, \mathbf{k}_\perp)}(\mathbf{r})$ is the periodic Bloch function of electron band m_{n_z} of the quantum-well, \mathbf{k}_\perp labels the momentum state in the plane of the quantum-well, $F_{n_z}^m$ is the quantized envelope function in the direction normal to the quantum-well, and V_X is the volume of the crystal. The electron spin has been implicitly included in the periodic Bloch function. The direction normal to the quantum-well is chosen as the \mathbf{z} -direction, and the plane of the quantum-well is taken to lie in the (\mathbf{x}, \mathbf{y}) -plane. The notation \mathbf{r}_\perp has been used for the in-plane coordinates.

The normalization of the envelope function is obtained from the orthonormality condition of eq. (2.49):

$$\begin{aligned}
\int_{V_X} d^3r \frac{e^{-i(\mathbf{k}_\perp - \mathbf{k}_\perp') \cdot \mathbf{r}_\perp} F_{n_z}^m(z) (F_{n_z'}^{m'}(z))^*}{V_X} &= \frac{A_\perp \delta_{\mathbf{k}_\perp, \mathbf{k}_\perp'}}{V_X} \int_{L_z} dz F_{n_z}^m (F_{n_z'}^{m'})^* \\
&= \frac{\delta_{\mathbf{k}_\perp, \mathbf{k}_\perp'}}{L_z} \int_{L_z} dz F_{n_z}^m (F_{n_z'}^{m'})^*.
\end{aligned} \tag{2.52}$$

A_\perp and L_z are the in-plane area and the vertical height of the semiconductor crystal, respectively. The orthonormality conditions for the quantized envelope functions, $F_{n_z}^m$, are then

$$\int_{L_z} dz F_{n_z}^m F_{n_z'}^{m'} = \Gamma_{m'}^m \delta_{n_z, n_z'} L_z, \tag{2.53}$$

where $\Gamma_{m'}^m$ is an overlap factor between the localized envelope functions of different bands. In a bulk III-V semiconductor [47, 59] the conduction band states are formed from a pair of degenerate spin states ($s = 1/2$) with a Bloch function of s-orbital symmetry ($l = 0$). The valence band states are given by three doubly degenerate bands: the heavy-hole (hh), light-hole (lh), and split-off (so) bands. The band-diagram of a strained bulk III-V semiconductor is given in Figure 2.1. The labels heavy and light-hole correspond to the relative size of the effective masses of each band (m_{hh}^*, m_{lh}^*). The Bloch functions of these states are linear combinations of wavefunctions with p-orbital symmetry ($l = 1$) and spin one-half ($s = 1/2$). The light and heavy-hole Bloch functions are formed from the $j = 3/2$ total angular momentum basis. The so valence band ($j = 1/2$)³⁰ can be neglected as the spin-orbit splitting energy is quite significant ($\sim 0.1 - 0.3\text{eV}$).

In a strained quantum-well the Bloch function eigenmodes of the lowest energy (for holes) valence band states are approximately given by linear superpositions of the light and heavy-holes, the exact mixture of which depends on the in-plane momentum \mathbf{k}_\perp . Here we neglect the \mathbf{k}_\perp -dependence and use the Bloch functions at the zone center

³⁰ j is the quantum number for total angular momentum of the Bloch state, spin and orbital momentum.

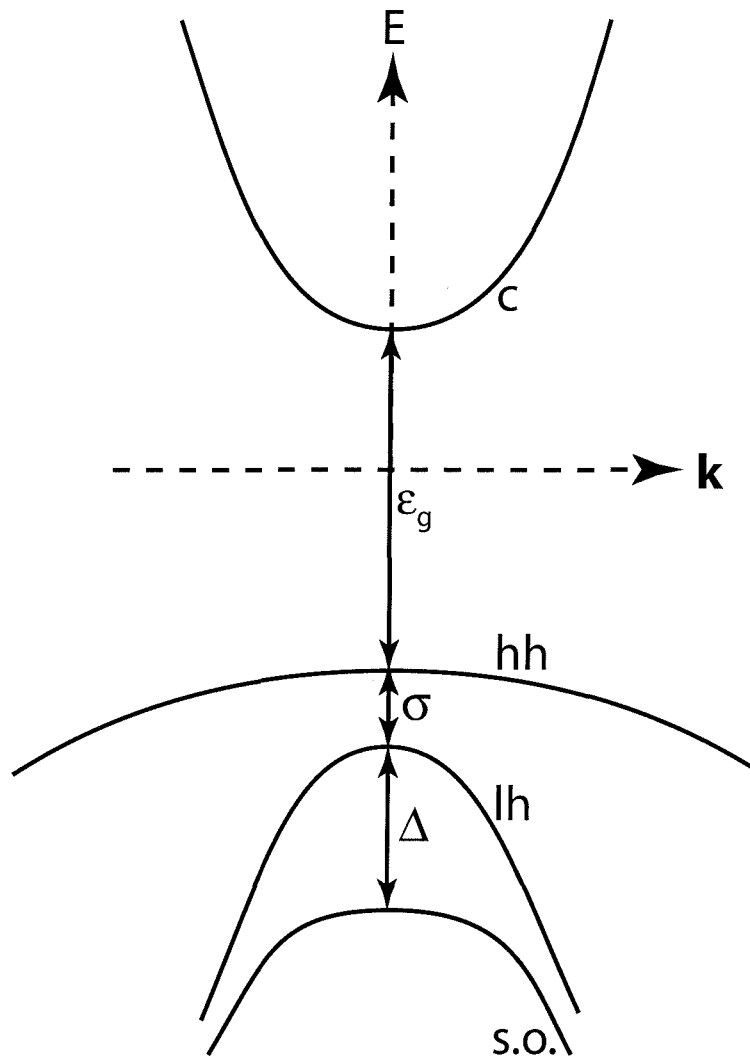


Figure 2.1: Illustration showing the approximate band-structure of a III-V semiconductor in the vicinity of the zone center Γ -point. Each energy band is doubly degenerate in this case. Δ is the spin-orbit splitting energy and σ is the heavy-hole and light-hole splitting due to strain.

(Γ -point)³¹. For an excellent treatment of the valence band states in quantum-wells the reader is referred to references [47, 59]. Although split by quantum confinement and strain, the Bloch states of a quantum-well near the zone center still approximately separate into the degenerate heavy and light-hole bands. The effective mass of the valence band states in the plane of the quantum-well is quite different than it is normal to the quantum-well though. As in reference [47] the label “heavy” will correspond to the states with the largest effective mass in the \mathbf{z} -direction normal to the quantum-well. The in-plane and out-of-plane hh and lh effective masses are written as $m_{(hh,lh)\perp}^*$ and $m_{(hh,lh)z}^*$, respectively.

At the zone center the light and heavy-hole Bloch functions of the quantum-well both consist of a pair of degenerate states which have the following symmetry basis [59]:

$$u_{hh} = \frac{-1}{\sqrt{2}}(u_x + iu_y), \quad (2.54)$$

$$\bar{u}_{hh} = \frac{1}{\sqrt{2}}(\bar{u}_x - i\bar{u}_y), \quad (2.55)$$

$$u_{lh} = \frac{-1}{\sqrt{6}}(\bar{u}_x + i\bar{u}_y - 2u_z), \quad (2.56)$$

$$\bar{u}_{lh} = \frac{1}{\sqrt{6}}(u_x - iu_y + 2\bar{u}_z), \quad (2.57)$$

where $u_{x,y,z}$ are functions with $p_{x,y,z}$ -orbital symmetry, and $\bar{u}_{x,y,z}$ is the spin-flipped state. The $u_{x,y,z}$ are taken to be normalized such that $\langle u_i | u_j \rangle_\nu = \delta_{i,j}$.

The conduction band Bloch states are approximately given by the spin pair u_c and \bar{u}_c , which have s-orbital symmetry. Of particular interest for calculating the strength of optical transitions is the momentum matrix element between the underlying Bloch states. The momentum matrix element between u_c and $u_{x,y,z}$ can be simply evaluated due to the symmetry of the states:

³¹This is the envelope approximation of the previous sub-section.

$$\langle u_c | \hat{p}_i | u_j \rangle_\nu = M \delta_{i,j}, \quad (2.58)$$

$$\langle u_c | \hat{p}_i | \bar{u}_j \rangle_\nu = 0, \quad (2.59)$$

where $i, j \in \{x, y, z\}$ and $M \equiv$ transition matrix element. Using eq. (2.54) we can now calculate transition matrix vectors for the conduction band to hh and lh transitions³²:

$$\mathbf{M}_{c \rightarrow hh} \equiv \langle u_c | \hat{\mathbf{p}}_s | u_{hh} \rangle_\nu = \frac{-M}{\sqrt{2}} (\mathbf{x} + i\mathbf{y}), \quad (2.60)$$

$$\mathbf{M}_{c \rightarrow \bar{h}h} \equiv \langle u_c | \hat{\mathbf{p}}_s | \bar{u}_{hh} \rangle_\nu = 0, \quad (2.61)$$

$$\mathbf{M}_{\bar{c} \rightarrow hh} \equiv \langle \bar{u}_c | \hat{\mathbf{p}}_s | u_{hh} \rangle_\nu = 0, \quad (2.62)$$

$$\mathbf{M}_{\bar{c} \rightarrow \bar{h}h} \equiv \langle \bar{u}_c | \hat{\mathbf{p}}_s | \bar{u}_{hh} \rangle_\nu = \frac{M}{\sqrt{2}} (\bar{\mathbf{x}} - i\bar{\mathbf{y}}), \quad (2.63)$$

$$\mathbf{M}_{c \rightarrow lh} \equiv \langle u_c | \hat{\mathbf{p}}_s | u_{lh} \rangle_\nu = \frac{2M}{\sqrt{6}} \mathbf{z}, \quad (2.64)$$

$$\mathbf{M}_{c \rightarrow \bar{l}h} \equiv \langle u_c | \hat{\mathbf{p}}_s | \bar{u}_{lh} \rangle_\nu = \frac{M}{\sqrt{6}} (\bar{\mathbf{x}} - i\bar{\mathbf{y}}), \quad (2.65)$$

$$\mathbf{M}_{\bar{c} \rightarrow lh} \equiv \langle \bar{u}_c | \hat{\mathbf{p}}_s | u_{lh} \rangle_\nu = \frac{-M}{\sqrt{6}} (\mathbf{x} + i\mathbf{y}), \quad (2.66)$$

$$\mathbf{M}_{\bar{c} \rightarrow \bar{l}h} \equiv \langle \bar{u}_c | \hat{\mathbf{p}}_s | \bar{u}_{lh} \rangle_\nu = \frac{2M}{\sqrt{6}} \mathbf{z}. \quad (2.67)$$

The above list highlights the fact that we are dealing with eight different transitions from two different conduction band states into four different valence band states. These transition matrix vectors will be used to determine the strength of the electron-photon coupling between different states of the quantum-well in sub-section 2.3.2.

³²The $\bar{\mathbf{x}}$ and $\bar{\mathbf{y}}$ are unit vectors.

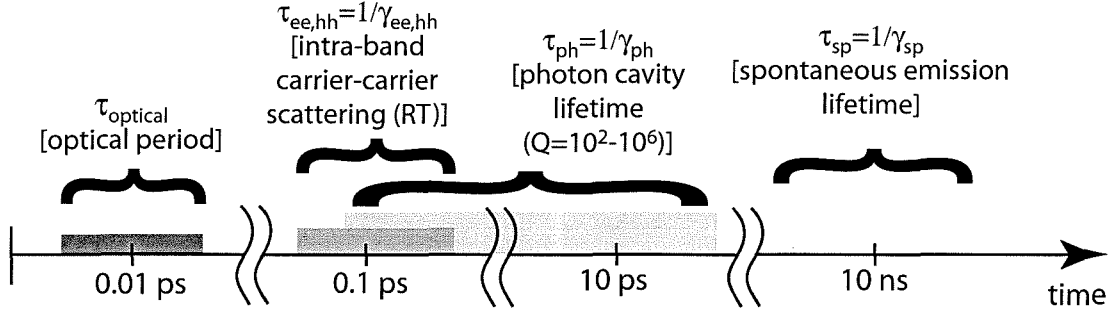


Figure 2.2: A map of the typical time scales of different processes in semiconductor optical cavities at room temperature.

2.3 Electron-Photon Coupling

As discussed in section 2.1, although the background (far off-resonance) electron-photon coupling has been incorporated into the radiation field as a material dielectric function, in order to study energy converting processes such as spontaneous emission we must include the near resonant transitions. These transitions are associated with light in the visible and near infrared wavelength ranges for direct band-gap (in order to conserve momentum) III-V semiconductor materials, and occur between electrons in the conduction and valence bands.

In order to greatly simplify our analysis we will take advantage of the fact that in most semiconductor materials at room temperature, and for reasonable light field intensities³³, the coupling between electrons and optical photons is weak relative to other scattering processes [60]. A map of the different time scales³⁴ involved in the electron-photon coupling is given in Figure 2.3. In the weak-coupling limit the spontaneous emission lifetime is much longer than the photon lifetime, carrier-carrier scattering of electrons, and the period of an optical cycle.

Along with different time scales, there are corresponding different length or spatial scales. The length scales relevant to opto-electronic processes in semiconductor

³³Here our goal is to study spontaneous emission which involves very small light fields, namely the vacuum or ground state electromagnetic field.

³⁴One can also think of the different energies associated with each process.

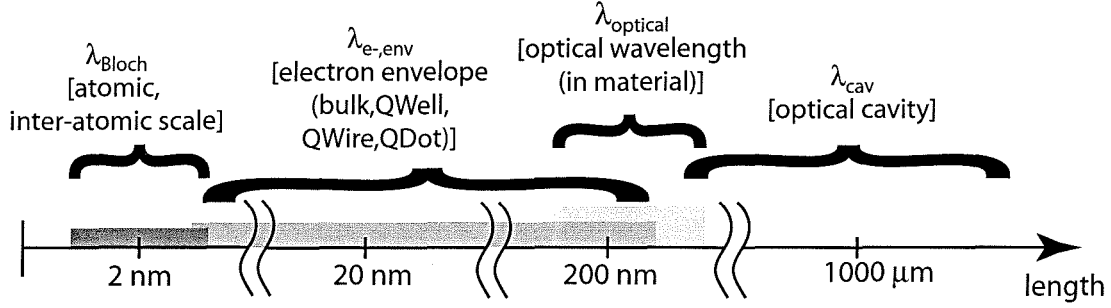


Figure 2.3: The four distinct length scales associated with opto-electronic processes in semiconductor optical cavities.

electromagnetic cavities is outlined in Figure 2.3. The electron wavefunction has two different length scales: one corresponding to the atomic and inter-atomic scale (Bloch function), and another associated with the distribution of the electron over many lattice sites (an envelope function). There are two length scales for the photon as well: the optical wavelength of the light, and the size of the optical cavity used to “store” the light. It is this disparity in length and time scales which allows us to make several simplifying approximations below³⁵.

In the dipole approximation³⁶ the energy associated with the coupling of charged particles to the electric field is given by:

$$\hat{H}_{int} = \int_V d^3r (-\hat{\mathbf{P}} \cdot \hat{\mathbf{E}}), \quad (2.68)$$

where $\hat{\mathbf{P}}(\mathbf{r}, t)$ is the polarization density operator related to dipoles formed between the near resonant conduction and valence band states. The polarization density of these dipoles can be written as,

³⁵As the size of the optical cavity is scaled further and further down towards that of the wavelength of light, and more importantly towards the scale of the electronic wavefunction (or at least its envelope), one must be careful to ensure self-consistency of approximations bearing in mind the different time and length scales in Figures 2.3 and 2.3.

³⁶We are talking here of coupling to the electric field and to electric dipoles. We are neglecting the energy resulting from magnetic dipoles and electron spin interaction with the magnetic field.

$$\mathbf{P}(\mathbf{r}, t) = Q\mathbf{d}(\mathbf{r}, t). \quad (2.69)$$

Q is the electron charge ³⁷ per unit volume and \mathbf{d} is the dipole vector. Equivalently, in second quantized quantum field theory the polarization density operator is given as:

$$\hat{\mathbf{P}}(\mathbf{r}, t) = e \sum_{\lambda_c, \lambda_v} \left(\hat{e}_{\lambda_c}^\dagger \phi_{\lambda_c}^*(\mathbf{r}) \right) \hat{\mathbf{r}}_s \left(\hat{e}_{\lambda_v} \phi_{\lambda_v}(\mathbf{r}) \right) + h.a., \quad (2.70)$$

where λ_c and λ_v label the conduction and valence band states, respectively.

Substituting $\hat{\mathbf{P}}$ from eq. (2.70) and $\hat{\mathbf{E}}$ from eq. (2.5) into eq. (2.68) we find for the dipole coupling energy,

$$\begin{aligned} \hat{H}_{int} = - \sum_{m, \lambda_c, \lambda_v} & \left(\hat{a}_m^\dagger \hat{e}_{\lambda_v}^\dagger \hat{e}_{\lambda_c} \int_V d^3r \phi_{\lambda_v}^* (\mathbf{E}_m^* \cdot e\hat{\mathbf{r}}_s) \phi_{\lambda_c} \right. \\ & \left. + \hat{a}_m \hat{e}_{\lambda_c}^\dagger \hat{e}_{\lambda_v} \int_V d^3r \phi_{\lambda_c}^* (\mathbf{E}_m \cdot e\hat{\mathbf{r}}_s) \phi_{\lambda_v} \right) + h.a. \end{aligned} \quad (2.71)$$

In the above equation there are four different terms formed from products of two electron operators and one photon operator with harmonic unperturbed (free field) time dependencies. In the weak coupling limit the field operators have a time dependence which is the product of a slowly varying envelope function and a rapidly oscillating optical harmonic function. Terms in which energy is not conserved oscillate at optical frequencies, and to a good approximation average out to zero after many optical cycles³⁸. Thus, in the rotating wave approximation, only the first two terms in which energy is conserved (realizing that conduction band electrons are more energetic than

³⁷This is the dipole charge density associated with electrons in the conduction and valence bands.

³⁸This is the time scale appropriate to spontaneous emission and other physical phenomena in the weak coupling limit. We are equivalently only keeping terms to first order in the interaction when considering emission or absorption processes.

valence band electrons) are kept in the interaction Hamiltonian:

$$\begin{aligned} \hat{H}_{int} \approx - \sum_{m, \lambda_c, \lambda_v} & \left(\hat{a}_m^\dagger \hat{e}_{\lambda_v}^\dagger \hat{e}_{\lambda_c} \int_V d^3r \phi_{\lambda_v}^* (\mathbf{E}_m^* \cdot e \hat{\mathbf{r}}_s) \phi_{\lambda_c} \right. \\ & \left. + \hat{a}_m \hat{e}_{\lambda_c}^\dagger \hat{e}_{\lambda_v} \int_V d^3r \phi_{\lambda_c}^* (\mathbf{E}_m \cdot e \hat{\mathbf{r}}_s) \phi_{\lambda_v} \right). \end{aligned} \quad (2.72)$$

An electron-photon coupling factor, $g_{m, \lambda_c, \lambda_v}$, can then be defined,

$$\begin{aligned} \hat{H}_{int} \approx - \sum_{m, \lambda_c, \lambda_v} & \left(\hat{a}_m^\dagger \hat{e}_{\lambda_v}^\dagger \hat{e}_{\lambda_c} g_{m, \lambda_v, \lambda_c}^* \right. \\ & \left. + \hat{a}_m \hat{e}_{\lambda_c}^\dagger \hat{e}_{\lambda_v} g_{m, \lambda_v, \lambda_c} \right), \end{aligned} \quad (2.73)$$

where $g_{m, \lambda_c, \lambda_v}$ is equal to the (spatially averaged) dot product of the conduction-valence band dipole moment and the electric field,

$$g_{m, \lambda_c, \lambda_v} = \int_V d^3r \hat{\mathbf{d}}_{\lambda_c, \lambda_v} \cdot \mathbf{E}_m, \quad (2.74)$$

$$\hat{\mathbf{d}}_{\lambda_c, \lambda_v}(\mathbf{r}) = e \phi_{\lambda_c}^* \hat{\mathbf{r}}_s \phi_{\lambda_v}. \quad (2.75)$$

$\hat{\mathbf{d}}_{\lambda_c, \lambda_v}(\mathbf{r})$ is the operator of the electric dipole moment for the conduction-valence band transition.

Although this result is intuitively satisfying, another approach to deriving $g_{m, \lambda_c, \lambda_v}$, utilizing the vector potential $\hat{\mathbf{A}}$, is useful as fewer approximations are made from the outset than in the dipole approximation above and the electronic matrix elements determining the optical transitions are momentum matrix elements rather than position matrix elements. Looking forward, the electronic states of a crystalline semiconductor material will have eigenstates which are Bloch states. As it is rather simple to describe the Bloch states in momentum space, calculations and approximations³⁹ to

³⁹Specifically the dispersion of $g_{m, \lambda_c, \lambda_v}$.

$g_{m,\lambda_e,\lambda_v}$ are usually more easily performed in momentum space as well.

Starting from a Lagrangian appropriate⁴⁰ for non-relativistic particles [50, 51], it can be shown that the coupling of the electron field to the photon field can be found by making the substitution $\hat{\mathbf{p}}_s \rightarrow \hat{\mathbf{p}}_s - \frac{e}{c}\hat{\mathbf{A}}$ in the Hamiltonian for the physical electron momentum operator,⁴¹

$$\hat{H}_{free,e^-} = \int_V d^3r \hat{\phi}_{e^-}^\dagger \left(\frac{\hat{\mathbf{p}}_s^2}{2m_e} \right) \hat{\phi}_{e^-} + h.a. \rightarrow \int_V d^3r \hat{\phi}_{e^-}^\dagger \left(\frac{(\hat{\mathbf{p}}_s - \frac{e}{c}\hat{\mathbf{A}})^2}{2m_e} \right) \hat{\phi}_{e^-}, \quad (2.76)$$

which gives for the interaction Hamiltonian,

$$\hat{H}_{int} = \int_V d^3r \hat{\phi}_{e^-}^\dagger \left(\frac{e}{2m_e} (\hat{\mathbf{A}} \cdot \hat{\mathbf{p}}_s - \hat{\mathbf{p}}_s \cdot \hat{\mathbf{A}}) + \frac{e^2}{2m_e^2} \hat{\mathbf{A}}^2 \right) \hat{\phi}_{e^-}, \quad (2.77)$$

where m_e is the rest mass of the electron. In the above equations we have implicitly assumed that we are working in the generalized coulomb gauge of eq. (2.13). In this gauge $\hat{\mathbf{A}} \cdot \hat{\mathbf{p}}_s \neq \hat{\mathbf{p}}_s \cdot \hat{\mathbf{A}}$, and

$$(\hat{\mathbf{p}}_s \cdot \hat{\mathbf{A}}) \hat{\phi}_{e^-} \sim (\hat{\mathbf{A}} \cdot \mathbf{k}_\lambda + \hat{\mathbf{A}} \cdot \hat{\mathbf{p}}_s) \hat{\phi}_{e^-}. \quad (2.78)$$

Also, $\hat{\mathbf{p}}_s \hat{\phi}_{e^-} \sim \frac{1}{\lambda_{Bloch}} \hat{\phi}_{e^-}$. Thus, due to the scale difference between optical waves and electron waves ($\lambda_{optical}/\lambda_{Bloch} \ll 1$), at optical frequencies $\hat{\mathbf{p}}_s \cdot \hat{\mathbf{A}} \approx \hat{\mathbf{A}} \cdot \hat{\mathbf{p}}_s$. For the same reason the $\hat{\mathbf{A}}^2$ term in eq. (2.77) can be neglected⁴². The electron-photon interaction Hamiltonian is now,

⁴⁰In the sense that it correctly derives the Lorentz force law given in eq. (3.13).

⁴¹In the presence of an electromagnetic field the canonically conjugate momentum, $\hat{\mathbf{p}}_s$, to the position operator, $\hat{\mathbf{r}}_s$, now contains momentum of electromagnetic field as well as the electron. In calculating the kinetic energy of the electron we must subtract from $\hat{\mathbf{p}}_s$ that part of the momentum associated with the electromagnetic field.

⁴²This is true only for optical fields with a limited intensity [61]. For very intense fields this term must be included in the interaction.

$$\hat{H}_{int} \approx \int_V d^3r \hat{\phi}_{e-}^\dagger \left(\frac{e}{m_e} (\hat{\mathbf{A}} \cdot \hat{\mathbf{p}}_s) \right) \hat{\phi}_{e-}. \quad (2.79)$$

In the interaction Hamiltonian we have neglected the electron spin coupling to the magnetic field as to lowest order it is also a factor of λ/r_{atom} smaller than the $\hat{\mathbf{A}} \cdot \hat{\mathbf{p}}_s$ term [51]. This series of approximations falls under the broad envelope of the electric dipole approximation as it leads to an interaction Hamiltonian which is equivalent⁴³ to that given by the electric dipole interaction term of eq. (2.72). Substituting the annihilation and creation operators and mode profiles for $\hat{\mathbf{A}}$, $\hat{\phi}_{e-}$, and $\hat{\phi}_{e-}^\dagger$ into eq. (2.79) we get the following relation for the interaction Hamiltonian⁴⁴:

$$\begin{aligned} \hat{H}_{int} \approx \sum_{m, \lambda_c, \lambda_v} & \left(\hat{a}_m^\dagger \hat{e}_{\lambda_v}^\dagger \hat{e}_{\lambda_c} \int_V d^3r \phi_{\lambda_v}^* \left(\frac{e}{m_e} (\mathbf{A}_m^* \cdot \hat{\mathbf{p}}_s) \right) \phi_{\lambda_c} \right. \\ & \left. + \hat{a}_m \hat{e}_{\lambda_c}^\dagger \hat{e}_{\lambda_v} \int_V d^3r \phi_{\lambda_c}^* \left(\frac{e}{m_e} (\mathbf{A}_m \cdot \hat{\mathbf{p}}_s) \right) \phi_{\lambda_v} \right). \end{aligned} \quad (2.80)$$

The electron-photon coupling factor is now given as,

$$g_{m, \lambda_c, \lambda_v} = \left(\frac{e}{m_e} \right) \int_V d^3r \mathbf{A}_m \cdot (\phi_{\lambda_c}^* \hat{\mathbf{p}}_s \phi_{\lambda_v}). \quad (2.81)$$

Substituting into eq. (2.81) the relation between the normalized vector potential and electric field⁴⁵ mode profiles found in eq. (2.15) allows us to write for the electron-photon coupling factor,

$$g_{m, \lambda_c, \lambda_v} = \left(\frac{-ie}{\omega_m m_e} \right) \int_V d^3r \mathbf{E}_m \cdot (\phi_{\lambda_c}^* \hat{\mathbf{p}}_s \phi_{\lambda_v}), \quad (2.82)$$

⁴³The momentum space version of the real space dipole.

⁴⁴Making use of the rotating wave approximation once again, and keeping only those terms which conserve energy in the uncoupled system.

⁴⁵The radiation component of the electric field (ie. not including the instantaneous coulomb field).

which depends on the momentum matrix elements between electronic states. Depending on the geometry of the problem, either of eq. (2.82) or eq. (2.74) can be used to calculate the coupling factor g within the electric dipole approximation.

The full Hamiltonian including interaction terms now looks as follows:

$$H = \sum_{\lambda_n} \varepsilon_{\lambda_n} \hat{e}_{\lambda_n}^\dagger \hat{e}_{\lambda_n} + \sum_m \hbar \omega_m (\hat{a}_m^\dagger \hat{a}_m + 1/2) - \sum_{r_\lambda, \lambda_s, \lambda_t} \left(\hat{a}_{r_\lambda}^\dagger \hat{e}_{\lambda_s}^\dagger \hat{e}_{\lambda_t} g_{r_\lambda, \lambda_s, \lambda_t}^* + \hat{a}_{r_\lambda} \hat{e}_{\lambda_t}^\dagger \hat{e}_{\lambda_s} g_{r_\lambda, \lambda_s, \lambda_t} \right), \quad (2.83)$$

where it has been implicitly assumed in the interaction terms that $\varepsilon_{\lambda_t} > \varepsilon_{\lambda_s}$, consistent with the rotating wave approximation. In many cases we are only interested in interactions and transitions between two different bands, the valence and conduction bands, in a semiconductor. Equation (2.83) can be re-written in terms of electron operators of the conduction band and hole operators of the valence band⁴⁶:

$$H = \sum_{\lambda_c} \varepsilon_{\lambda_c} \hat{e}_{\lambda_c}^\dagger \hat{e}_{\lambda_c} - \sum_{\lambda_v} \varepsilon_{\lambda_v} \hat{h}_{-\lambda_v}^\dagger \hat{h}_{-\lambda_v} + \sum_m \hbar \omega_m (\hat{a}_m^\dagger \hat{a}_m + 1/2) - \sum_{m, \lambda_v, \lambda_c} \left(\hat{a}_m^\dagger \hat{h}_{-\lambda_v} \hat{e}_{\lambda_c} g_{m, \lambda_v, \lambda_c}^* + \hat{a}_m \hat{e}_{\lambda_c}^\dagger \hat{h}_{-\lambda_v}^\dagger g_{m, \lambda_v, \lambda_c} \right). \quad (2.84)$$

This results in a rather pleasing picture where the interaction terms represent either a creation of a photon combined with the annihilation of an electron-hole pair, or the annihilation of a photon along with the creation of an electron-hole pair.

2.3.1 Spontaneous Emission of Light

The simplest *inter*-band optical transitions in semiconductors involve an occupied electron state in one band and an empty electron state, or hole state, in another band. A third particle involved in the interaction is the photon. There are emis-

⁴⁶Note that the zero of energy has been shifted in eq. (2.84), which is fine, and now ground state represents a full valence band.

sion processes in which a photon is generated, and absorption processes in which a photon is destroyed. Spontaneous emission occurs in the absence of any photons (electromagnetic field in its ground state), and as the name indicates, only occurs for an emission process. There is no spontaneous absorption process. In a spontaneous emission event, an excited electronic state drops down to a lower energy (ground) state, emitting a photon in the process. Here we will take the excited state to be an electron in the conduction band⁴⁷.

In the Heisenberg picture, the excited conduction band state is represented as a number operator for that state,

$$\hat{n}_{\lambda_c} = \hat{e}_{\lambda_c}^\dagger \hat{e}_{\lambda_c}. \quad (2.85)$$

To determine the spontaneous emission rate (spontaneous decay rate) we must analyze the time evolution of the excited state number operator in the presence of a photon vacuum or ground state. Using the Heisenberg equations of motion, with the interaction Hamiltonian derived in the previous sub-section, the time derivative of the excited state operator is

$$\begin{aligned} \frac{d}{dt} \hat{n}_{\lambda_c} &= \frac{i}{\hbar} [H, \hat{n}_{\lambda_c}] \\ &= \frac{-i}{\hbar} \sum_{m, \lambda'_v} (g_{m, \lambda'_v, \lambda_c}^* \hat{a}_m^\dagger \hat{h}_{-\lambda'_v} \hat{e}_{\lambda_c} - g_{m, \lambda'_v, \lambda_c} \hat{a}_m \hat{e}_{\lambda_c}^\dagger \hat{h}_{-\lambda'_v}^\dagger). \end{aligned} \quad (2.86)$$

The sum over valence band states can be collapsed in many instances⁴⁸, leaving a sum over all electromagnetic modes.

In eq. (2.86), the terms which drive the time evolution of the excited state are the polarization operators, $\hat{a}_m^\dagger \hat{h}_{-\lambda'_v} \hat{e}_{\lambda_c}$ and its adjoint. There are many other electron-

⁴⁷Another definition for the excited state may be that of an electron-hole pair, or exciton. Since for the interaction Hamiltonian derived above $\frac{d}{dt} \hat{n}_{\lambda_c} = \frac{d}{dt} \hat{n}_{\lambda_c} \hat{n}_{-\lambda_v}^h$, either excited state has the same spontaneous decay rate.

⁴⁸This is due to momentum conservation, or the conservation of some other quantum number for the electron-hole-photon system.

electron and electron-phonon interactions which have been left out of H_{int} that also drive the time evolution of the excited state. Referring to Figure 2.3, these interactions occur at a much faster rate than spontaneous emission in semiconductors at room temperature. From the time perspective of spontaneous emission, the churning sea of electrons within each energy band looks to evolve smoothly, the only indication of the underlying turmoil being phenomenologically added decay terms. In the approximations described below, a clear separation is made between the fast *intra*-band processes, and the slower *inter*-band photon emission and absorption processes.

Following the formalism of Chow, Koch, and Sargent III [47], the discrepancy in time scales allows us to close the loop of coupled operators and solve for the approximate spontaneous emission decay rate of the excited state. We start with the total time derivative of the semiconductor polarization,

$$\begin{aligned} \frac{d}{dt} \hat{a}_m^\dagger \hat{h}_{-\lambda_v} \hat{e}_{\lambda_c} &= \frac{i}{\hbar} (\hbar\omega_m - (\varepsilon_{\lambda_c} - \varepsilon_{\lambda_v})) \hat{a}_m^\dagger \hat{h}_{-\lambda_v} \hat{e}_{\lambda_c} \\ &+ \frac{-i}{\hbar} \sum_{m', \lambda'_v, \lambda'_c} g_{m', \lambda'_v, \lambda'_c} (\delta_{m, m'} \hat{e}_{\lambda'_c}^\dagger \hat{e}_{\lambda_c} \hat{h}_{-\lambda'_v}^\dagger \hat{h}_{-\lambda_v} \\ &+ \hat{a}_m^\dagger \hat{a}_{m'} (\hat{e}_{\lambda'_c}^\dagger \hat{e}_{\lambda_c} \delta_{\lambda_v, \lambda'_v} + \hat{h}_{-\lambda'_v}^\dagger \hat{h}_{-\lambda_v} \delta_{\lambda_c, \lambda'_c} - \delta_{\lambda_c, \lambda'_c} \delta_{\lambda_v, \lambda'_v})) \end{aligned} \quad (2.87)$$

A number of simplifications can be made in eq. (2.87) by taking the expectation value of all the operators under the assumption that the electrons (and holes) within a given energy band have been driven approximately into equilibrium by *intra*-band and lattice scattering. In this quasi-equilibrium⁴⁹ approximation, at the time scales of the *inter*-band photon coupling, the density operator ($\hat{\rho}$) describing the electrons within each band is diagonal in the number (Fock) state representation⁵⁰. All correlations between different number states of a given energy band are washed out on the time scale of spontaneous emission by the fast *intra*-band scattering processes.

⁴⁹We use the term “quasi” as equilibrium has only been established between carriers within a given energy band; we have not assumed inter-band equilibrium such as between the electrons in the conduction band and electrons in the valence band.

⁵⁰Here we are talking about multi-particle states formed from direct products of individual electron number states: $|Fock\rangle = |n_1\rangle \times |n_2\rangle \times |n_3\rangle \cdots \times |n_N\rangle$.

In the density matrix formalism the expectation of an operator is given by [47],

$$\langle \hat{A} \rangle = \text{Tr}(\hat{\rho} \hat{A}) \quad (2.88)$$

In the scenario of quasi-equilibrium, $\hat{\rho}_e$ is diagonal in each of the valence and conduction band Fock spaces:

$$\hat{\rho}_c = \frac{1}{Z_c} \exp \left[-\beta \sum_{\lambda_c} (\varepsilon_{\lambda_c} - \mu_c) \hat{e}_{\lambda_c}^\dagger \hat{e}_{\lambda_c} \right] = \text{Tr}_v(\hat{\rho}_e) \quad (2.89)$$

$$\hat{\rho}_v = \frac{1}{Z_v} \exp \left[-\beta \sum_{\lambda_v} (\varepsilon_{\lambda_v} - \mu_v) \hat{e}_{\lambda_v}^\dagger \hat{e}_{\lambda_v} \right] = \text{Tr}_c(\hat{\rho}_e) \quad (2.90)$$

$$\hat{\rho}_e = \hat{\rho}_c \times \hat{\rho}_v \quad (2.91)$$

where the partition function is $Z_n = \text{Tr}_n(\exp[-\beta \sum_{\lambda_n} (\varepsilon_{\lambda_n} - \mu_n) \hat{e}_{\lambda_n}^\dagger \hat{e}_{\lambda_n}])$, $n \in \{v, c\}$ labels the electron energy band, Tr_n traces over the Fock states of the n th band, μ_n is the chemical potential of the n th band, and $\beta = 1/k_B T$. The quasi-equilibrium approximation still allows for the full density operator to include *inter*-band correlations such as those of the semiconductor polarization, and can be written formally as⁵¹:

$$\hat{\rho} \approx (\hat{\rho}_c \times \hat{\rho}_v) \times \hat{\rho}_m + \hat{\rho}_{e-h-\gamma} \quad (2.92)$$

where $\hat{\rho}_m$ is the density operator for the radiation field after tracing out the conduction and valence band states, and $\hat{\rho}_{e-h-\gamma}$ represents off-diagonal electron-hole-photon correlations.

⁵¹In this density operator we neglect any conduction and valence band correlations in which the photon number does not change. In other words, we have not included any *inter*-band interactions, which in the absence of the radiation field, would drive the two different bands into equilibrium with each other. These additional interactions would include electron-phonon interactions for instance.

Taking the expectation of eq. (2.87), with a density operator of the form given in eq. (2.87), the time derivative of the semiconductor polarization becomes:

$$\begin{aligned} \frac{d}{dt} \langle \hat{a}_m^\dagger \hat{e}_{\lambda_v}^\dagger \hat{e}_{\lambda_c} \rangle = & -[(\gamma_{\lambda_c, \lambda_v} + \frac{1}{2}\gamma_m) + i(\frac{(\varepsilon_{\lambda_c} - \varepsilon_{\lambda_v})}{\hbar} - \omega_m)] \langle \hat{a}_m^\dagger \hat{e}_{\lambda_v}^\dagger \hat{e}_{\lambda_c} \rangle \\ & + \frac{i}{\hbar} \sum_{m'} g_{m', \lambda_v, \lambda_c} (\langle \hat{a}_m^\dagger \hat{a}_{m'} (1 - \hat{e}_{\lambda_c}^\dagger \hat{e}_{\lambda_c} - \hat{h}_{-\lambda_v}^\dagger \hat{h}_{-\lambda_v}) \rangle \\ & - \delta_{m, m'} \langle \hat{e}_{\lambda_c}^\dagger \hat{e}_{\lambda_c} \hat{h}_{-\lambda_v}^\dagger \hat{h}_{-\lambda_v} \rangle) \end{aligned} \quad (2.93)$$

where carrier-carrier scattering resulting in polarization dephasing has been added phenomenologically through $\gamma_{\lambda_c, \lambda_v}$, and the optical losses in mode m have been included in the term γ_m ⁵². In the Hartree-Fock approximation [47],

$$\langle \hat{e}_{\lambda_c}^\dagger \hat{e}_{\lambda_c} \hat{h}_{-\lambda_v}^\dagger \hat{h}_{-\lambda_v} \rangle \approx \langle \hat{e}_{\lambda_c}^\dagger \hat{e}_{\lambda_c} \rangle \langle \hat{h}_{-\lambda_v}^\dagger \hat{h}_{-\lambda_v} \rangle \quad (2.94)$$

where we have neglected terms with bilinear operator expectations which are not diagonal in Fock space⁵³. This allows us to write for the equation of motion of the semiconductor polarization:

$$\begin{aligned} \frac{d}{dt} \langle \hat{a}_m^\dagger \hat{e}_{\lambda_v}^\dagger \hat{e}_{\lambda_c} \rangle = & -[(\gamma_{\lambda_c, \lambda_v} + \frac{1}{2}\gamma_m) + i(\frac{(\varepsilon_{\lambda_c} - \varepsilon_{\lambda_v})}{\hbar} - \omega_m)] \langle \hat{a}_m^\dagger \hat{e}_{\lambda_v}^\dagger \hat{e}_{\lambda_c} \rangle \\ & + \frac{i}{\hbar} \sum_{m'} g_{m', \lambda_v, \lambda_c} (\langle \hat{a}_m^\dagger \hat{a}_{m'} (1 - \hat{e}_{\lambda_c}^\dagger \hat{e}_{\lambda_c} - \hat{h}_{-\lambda_v}^\dagger \hat{h}_{-\lambda_v}) \rangle \\ & - \delta_{m, m'} \langle \hat{e}_{\lambda_c}^\dagger \hat{e}_{\lambda_c} \rangle \langle \hat{h}_{-\lambda_v}^\dagger \hat{h}_{-\lambda_v} \rangle) \end{aligned} \quad (2.95)$$

Since the *intra*-band electron-electron scattering happens at such a rapid rate it quickly drives the polarization to a steady-state value. The steady-state value of $\langle \hat{a}_m^\dagger \hat{e}_{\lambda_v}^\dagger \hat{e}_{\lambda_c} \rangle$ can then be used in calculating spontaneous emission which occurs over a much larger time scale. Setting the time derivative to zero in eq. (2.93), one finds

⁵²We use $\frac{1}{2}\gamma_m$ in eq. (2.93) as γ_m is the *energy* decay constant; a_m^\dagger and a_m decay as $\frac{1}{2}\gamma_m$. The implications of the single photon operator decay, and its validity are discussed in sub-section 2.1.2.

⁵³i.e., number operators.

for the steady-state value of the polarization:

$$\begin{aligned} \langle \hat{a}_m^\dagger \hat{e}_{\lambda_v}^\dagger \hat{e}_{\lambda_c} \rangle_{ss} = & \sum_{m'} \frac{\frac{i}{\hbar} g_{m', \lambda_v, \lambda_c}}{(\gamma_{\lambda_c, \lambda_v} + \frac{1}{2} \gamma_m) + i \left(\frac{(\varepsilon_{\lambda_c} - \varepsilon_{\lambda_v})}{\hbar} - \omega_m \right)} \\ & \times \left(\langle \hat{a}_m^\dagger \hat{a}_{m'} (1 - \hat{n}_{-\lambda_v}^h - \hat{n}_{\lambda_c}) \rangle - \delta_{m, m'} \langle \hat{n}_{\lambda_c} \rangle \langle \hat{n}_{-\lambda_v}^h \rangle \right) \end{aligned} \quad (2.96)$$

Taking the vacuum expectation value of the equation of motion for the excited state in eq. (2.86), and adding an *intra*-band scattering term [47] gives for the time derivative of the excited state in the presence of no photons,

$$\frac{d}{dt} \langle \hat{n}_{\lambda_c} \rangle_{vac} = \frac{d}{dt} \langle \hat{n}_{\lambda_c} \rangle_{vac} \Big|_{col} - \frac{1}{\hbar} \sum_{m, \lambda'_v} (i g_{m, \lambda'_v, \lambda_c}^* \langle \hat{a}_m^\dagger \hat{h}_{-\lambda'_v} \hat{e}_{\lambda_c} \rangle_{vac} + adj.) \quad (2.97)$$

In order to obtain a closed form for the spontaneous decay rate of the excited state operator we must solve for the steady-state polarization expectation value with the electromagnetic field in its ground state (vacuum), which from eq. (2.96) is

$$\langle \hat{a}_m^\dagger \hat{e}_{\lambda_v}^\dagger \hat{e}_{\lambda_c} \rangle_{ss, vac} = \frac{-\frac{i}{\hbar} g_{m, \lambda_c, \lambda_v} \langle \hat{n}_{\lambda_c} \rangle \langle \hat{n}_{-\lambda_v}^h \rangle}{(\gamma_{\lambda_c, \lambda_v} + \frac{1}{2} \gamma_m) + i \left(\frac{(\varepsilon_{\lambda_c} - \varepsilon_{\lambda_v})}{\hbar} - \omega_m \right)} \quad (2.98)$$

Substituting this value for the polarization into eq. (2.97) gives,

$$\begin{aligned}
\frac{d}{dt}\langle\hat{n}_{\lambda_c}\rangle_{vac} &\approx \frac{d}{dt}\langle\hat{n}_{\lambda_c}\rangle_{vac} \big|_{col} \\
&- \frac{1}{\hbar} \sum_{m,\lambda'_v} (ig_{m,\lambda'_v,\lambda_c}^* \left(\frac{-\frac{i}{\hbar} g_{m,\lambda'_v,\lambda_c} \langle\hat{n}_{\lambda_c}\rangle_{vac} \langle\hat{n}_{-\lambda'_v}^h\rangle_{vac}}{(\gamma_{\lambda_c,\lambda'_v} + \frac{1}{2}\gamma_m) + i((\varepsilon_{\lambda_c} - \varepsilon_{\lambda'_v})/\hbar - \omega_m)} \right) + adj.) \\
&= \frac{d}{dt}\langle\hat{n}_{\lambda_c}\rangle_{vac} \big|_{col} \\
&- \sum_{m,\lambda'_v} \frac{2(\gamma_{\lambda_c,\lambda'_v} + \frac{1}{2}\gamma_m) |\frac{1}{\hbar} g_{m,\lambda'_v,\lambda_c}|^2 \langle\hat{n}_{-\lambda'_v}^h\rangle_{vac}}{(\gamma_{\lambda_c,\lambda'_v} + \frac{1}{2}\gamma_m)^2 + ((\varepsilon_{\lambda_c} - \varepsilon_{\lambda'_v})/\hbar - \omega_m)^2} \langle\hat{n}_{\lambda_c}\rangle_{vac}
\end{aligned} \tag{2.99}$$

The spontaneous decay constant, $\gamma_{\lambda_c}^{sp}$, for the λ_c conduction band electron is then given by:

$$\gamma_{\lambda_c}^{sp} = \sum_{m,\lambda'_v} \frac{2(\gamma_{\lambda_c,\lambda'_v} + \frac{1}{2}\gamma_m) |\frac{1}{\hbar} g_{m,\lambda'_v,\lambda_c}|^2 \langle\hat{n}_{-\lambda'_v}^h\rangle_{vac}}{(\gamma_{\lambda_c,\lambda'_v} + \frac{1}{2}\gamma_m)^2 + ((\varepsilon_{\lambda_c} - \varepsilon_{\lambda'_v})/\hbar - \omega_m)^2} \tag{2.100}$$

Equating the (radiative) decay rate of the conduction electron in the presence of a vacuum electromagnetic field to the emission rate of photons, we find for the spontaneous emission rate per unit volume into mode m from conduction electron λ_c :

$$W_{m,\lambda_c}^{sp} = \frac{1}{V} \sum_{\lambda'_v} A_{m,\lambda_c,\lambda'_v}^{sp} \langle\hat{n}_{\lambda_c}\rangle_{vac} \langle\hat{n}_{-\lambda'_v}^h\rangle_{vac} \tag{2.101}$$

with the spontaneous emission coefficient for mode m between electron states λ_c and λ_v given by

$$A_{m,\lambda_c,\lambda_v}^{sp} = \frac{2(\gamma_{\lambda_c,\lambda_v} + \frac{1}{2}\gamma_m) |\frac{1}{\hbar} g_{m,\lambda_v,\lambda_c}|^2}{(\gamma_{\lambda_c,\lambda_v} + \frac{1}{2}\gamma_m)^2 + ((\varepsilon_{\lambda_c} - \varepsilon_{\lambda_v})/\hbar - \omega_m)^2} \tag{2.102}$$

The total spontaneous emission rate per unit volume into all modes from all excited state conduction band electrons is

$$W^{sp} = \frac{1}{V} \sum_m \sum_{\lambda_c} \sum_{\lambda'_v} A_{m,\lambda_c,\lambda'_v}^{sp} \langle \hat{n}_{\lambda_c} \rangle_{vac} \langle \hat{n}_{-\lambda'_v}^h \rangle_{vac} \quad (2.103)$$

In eq. (2.96), if instead of taking the electromagnetic field in the ground state we had assumed that mode m contained n_m photons and was in the number state $|n_m\rangle$, we find a stimulated emission rate per unit volume from the electron transition $\lambda_c \rightarrow \lambda_v$:

$$W_{m,\lambda_c \rightarrow \lambda_v}^{st} = \frac{1}{V} B_{m,\lambda_c,\lambda_v}^{st} (\langle \hat{n}_{\lambda_c} \rangle - \langle \hat{n}_{\lambda_v} \rangle) \quad (2.104)$$

where the stimulated emission coefficient is

$$B_{m,\lambda_c,\lambda_v}^{st} = \frac{2(\gamma_{\lambda_c,\lambda_v} + \frac{1}{2}\gamma_m) |\frac{1}{\hbar} g_{m,\lambda_v,\lambda_c}|^2 (n_m)}{(\gamma_{\lambda_c,\lambda_v} + \frac{1}{2}\gamma_m)^2 + ((\varepsilon_{\lambda_c} - \varepsilon_{\lambda_v})/\hbar - \omega_m)^2} \quad (2.105)$$

In eq. (2.104) the stimulated emission rate is proportional to the difference in the conduction band electron density (excited state density) and the valence band electron density (ground state density)⁵⁴. Since $\hat{n}_{\lambda_c} - \hat{n}_{\lambda_v} = \hat{n}_{\lambda_c}(1 - \hat{n}_{\lambda_v}) - \hat{n}_{\lambda_v}(1 - \hat{n}_{\lambda_c})$, we see that the total stimulated emission rate in eq. (2.104) is the net sum of emission minus absorption. We also have the physically pleasing result, first derived by Einstein, that the ratio of stimulated emission to spontaneous emission into a given optical mode is equal to the number of photons in that mode:

$$\frac{B_{m,\lambda_c,\lambda_v}^{st}}{A_{m,\lambda_c,\lambda_v}^{sp}} = n_m \quad (2.106)$$

⁵⁴This is the semiconductor inversion.

2.3.2 Spontaneous Emission Rate from a QW Active Region in the Absence of Microcavity Effects

The spontaneous emission rate depends upon the strength of the spatial and spectral overlap of the electron and photon normalized field modes. We consider here only the transitions between lowest electron energy conduction band and lowest hole energy valence band in the quantum-well as they are first to be filled by electrons and holes, respectively. This limits us to the $n_z = 1$ fundamental bound states (for both electron and holes) of the quantum-well. The InGaAsP/InP quantum-well material used in the devices studied in this thesis are compressively strained (see chapter 5). As discussed in reference [47] the lowest energy hole states are in the $(m = hh, n_z = 1)$ degenerate band for compressively strained quantum-wells in this material system. This allows us to focus on the following electronic transitions when considering spontaneous emission in the quantum-well (see sub-section 2.2.3 for notation):

$$\begin{aligned}
(c, n_z = 1, \mathbf{k}_\perp) &\longrightarrow (hh, n_z = 1, \mathbf{k}'_\perp), \\
(c, n_z = 1, \mathbf{k}_\perp) &\longrightarrow (\overline{hh}, n_z = 1, \mathbf{k}'_\perp), \\
(\bar{c}, n_z = 1, \mathbf{k}_\perp) &\longrightarrow (hh, n_z = 1, \mathbf{k}'_\perp), \\
(\bar{c}, n_z = 1, \mathbf{k}_\perp) &\longrightarrow (\overline{hh}, n_z = 1, \mathbf{k}'_\perp).
\end{aligned} \tag{2.107}$$

The total spontaneous emission rate per unit volume from the quantum-well is then given by (see eq. (2.103)):

$$\begin{aligned}
W^{sp} = \frac{1}{V_{QW}} \sum_m \sum_{\mathbf{k}_\perp, \mathbf{k}'_\perp} &\left(A_{m, (c, 1, \mathbf{k}_\perp), (hh, 1, \mathbf{k}'_\perp)}^{sp} + A_{m, (c, 1, \mathbf{k}_\perp), (\overline{hh}, 1, \mathbf{k}'_\perp)}^{sp} \right. \\
&\left. + A_{m, (\bar{c}, 1, \mathbf{k}_\perp), (hh, 1, \mathbf{k}'_\perp)}^{sp} + A_{m, (\bar{c}, 1, \mathbf{k}_\perp), (\overline{hh}, 1, \mathbf{k}'_\perp)}^{sp} \right) \langle \hat{n}_{(c, 1, \mathbf{k}_\perp)} \rangle_{vac} \langle \hat{n}_{(hh, 1, -\mathbf{k}'_\perp)}^h \rangle_{vac},
\end{aligned} \tag{2.108}$$

where we have assumed that the degenerate $(c, \bar{c})|_{n_z=1}$ and the degenerate $(hh, \overline{hh})|_{n_z=1}$ states are equally populated. The quantum-well volume is $V_{QW} = A_\perp L_{QW}$, where

A_{\perp} is the in-plane area of the quantum-well and L_{QW} is the quantum-well width. The spontaneous emission coefficients depend on the square of the coupling factor. Consider the coupling factor between the $(c, 1, \mathbf{k}_{\perp})$ and $(hh, 1, \mathbf{k}'_{\perp})$ states near the zone center:

$$g_{m,(c,1,\mathbf{k}_{\perp}), (hh,1,\mathbf{k}'_{\perp})} \approx \left(\frac{-ie}{\omega_m m_e} \right) \int_{V_{QW}} d^3r \left(\frac{e^{-i(\mathbf{k}'_{\perp} - \mathbf{k}_{\perp}) \cdot \mathbf{r}_{\perp}}}{V_{QW}} \right) F_1^{hh} (F_1^c)^* \mathbf{E}_m \cdot \langle u_c | \hat{\mathbf{p}}_s | u_{hh} \rangle_{\nu}. \quad (2.109)$$

At optical frequencies we can assume that the photon the field is approximately constant over the width of the quantum-well. This allows us integrate over \mathbf{z} -direction in eq. (2.109):

$$g_{m,(c,1,\mathbf{k}_{\perp}), (hh,1,\mathbf{k}'_{\perp})} \approx \left(\frac{-ie\Gamma_{hh1}^{c1}}{\omega_m m_e} \right) \int_{A_{\perp}} d^2r \left(\frac{e^{-i(\mathbf{k}'_{\perp} - \mathbf{k}_{\perp}) \cdot \mathbf{r}_{\perp}}}{A_{\perp}} \right) \mathbf{E}_m(\mathbf{r}_{\perp}, z_o) \cdot \langle u_c | \hat{\mathbf{p}}_s | u_{hh} \rangle_{\nu}, \quad (2.110)$$

where z_o is the position of the quantum-well and Γ_{hh1}^{c1} is the overlap factor between the lowest order bound envelope functions of the conduction and heavy-hole bands. Since the wavelength of the optical field is much larger than the inter-atomic spacing in a semiconductor crystal, the photon momentum is tremendously small on the scale of the IBZ of electronic lattice, which allows us to also take $\mathbf{k}'_{\perp} = \mathbf{k}_{\perp,ph} + \mathbf{k}_{\perp} \approx \mathbf{k}_{\perp}$. Here we are effectively assuming that the electron wavefunction has some width in \mathbf{k}_{\perp} -space, small in relation to the size of the IBZ, which localizes the electron in the plane of the quantum-well to an area much smaller than the wavelength of light⁵⁵:

⁵⁵This wavefunction is a better representation of the states of the electrons in the quantum-well as electron-electron and electron-phonon scattering cause the electron to be localized in space, although still over many lattice periods. For a nice discussion of electron wave-packets in semiconductors see reference [62]. Note that this approximation comes into serious question for low-temperature semiconductors, as well as at higher frequency light. In the defect cavities studied in this thesis we are working mostly at room-temperature and the wavelength of light is quite long at 1.5 μm in vacuum (500 nm in the material).

$$g_{m,(c,1,\mathbf{k}_\perp),(hh,1,\mathbf{k}'_\perp)} \approx \left(\frac{-ie\Gamma_{hh1}^{c1}\delta_{\mathbf{k}_\perp,\mathbf{k}'_\perp}}{\omega_m m_e} \right) \langle u_c | \hat{\mathbf{p}}_s | u_{hh} \rangle_\nu \cdot \mathbf{E}_m(\bar{\mathbf{r}}_\perp, z_o), \quad (2.111)$$

where $\bar{\mathbf{r}}_\perp$ is an arbitrary position of an electron-hole pair within the plane of the quantum-well active region.

Substituting the transition momentum matrix elements derived in sub-section 2.2.3 gives for the coupling factors of the optical transitions in eq. (2.107):

$$\begin{aligned} g_{m,(c,1,\mathbf{k}_\perp),(hh,1,\mathbf{k}'_\perp)} &\approx \left(\frac{-ie\Gamma_{hh1}^{c1}\delta_{\mathbf{k}_\perp,\mathbf{k}'_\perp}}{\omega_m m_e} \right) \frac{-M}{\sqrt{2}} (\bar{\mathbf{x}} + i\bar{\mathbf{y}}) \cdot \mathbf{E}_m(\bar{\mathbf{r}}_\perp, z_o), \\ g_{m,(\bar{c},1,\mathbf{k}_\perp),(\bar{h}\bar{h},1,\mathbf{k}'_\perp)} &\approx \left(\frac{-ie\Gamma_{hh1}^{c1}\delta_{\mathbf{k}_\perp,\mathbf{k}'_\perp}}{\omega_m m_e} \right)^2 \frac{M}{\sqrt{2}} (\bar{\mathbf{x}} - i\bar{\mathbf{y}}) \cdot \mathbf{E}_m(\bar{\mathbf{r}}_\perp, z_o), \\ g_{m,(c,1,\mathbf{k}_\perp),(\bar{h}\bar{h},1,\mathbf{k}'_\perp)} &\approx 0, \\ g_{m,(\bar{c},1,\mathbf{k}_\perp),(hh,1,\mathbf{k}'_\perp)} &\approx 0. \end{aligned} \quad (2.112)$$

Note that the only TE-like fields which are polarized in the plane of the quantum-well couple to the conduction band to heavy-hole transition⁵⁶.

Using eq. (2.102), and averaging over the active region volume, we find for the average spontaneous emission coefficients within the quantum-well active region:

$$\begin{aligned} \bar{A}_{m,(c,1,\mathbf{k}_\perp),(hh,1,\mathbf{k}_\perp)}^{sp} &= \left(\frac{e\Gamma_{hh1}^{c1}|M|}{\hbar\omega_m m_e} \right)^2 \frac{1}{V_{QW}} \int_{V_{QW}} d^3r \left| \frac{(\bar{\mathbf{x}} + i\bar{\mathbf{y}})}{\sqrt{2}} \cdot \mathbf{E}_m(\mathbf{r}_\perp, z) \right|^2 \\ &\quad \times \frac{2(\gamma_{c,hh} + \frac{1}{2}\gamma_m)}{(\gamma_{c,hh} + \frac{1}{2}\gamma_m)^2 + (\omega_{\mathbf{k}_\perp} - \omega_m)^2}, \end{aligned} \quad (2.113)$$

and

⁵⁶This is why the photonic crystal cavity is designed to support defect modes which are TE-like in nature.

$$\begin{aligned} \bar{A}_{m,(\bar{c},1,\mathbf{k}_\perp),(\bar{h}h,1,\mathbf{k}_\perp)}^{sp} &= \left(\frac{e\Gamma_{hh1}^{c1}|M|}{\hbar\omega_m m_e} \right)^2 \frac{1}{V_{QW}} \int_{V_{QW}} d^3r \left| \frac{(\bar{\mathbf{x}} - i\bar{\mathbf{y}})}{\sqrt{2}} \cdot \mathbf{E}_m(\mathbf{r}_\perp, z) \right|^2 \\ &\times \frac{2(\gamma_{c,hh} + \frac{1}{2}\gamma_m)}{(\gamma_{c,hh} + \frac{1}{2}\gamma_m)^2 + (\omega_{\mathbf{k}_\perp} - \omega_m)^2}, \end{aligned} \quad (2.114)$$

where $\omega_{\mathbf{k}_\perp} \equiv (\varepsilon_{c,1,\mathbf{k}_\perp} - \varepsilon_{hh,1,\mathbf{k}_\perp})/\hbar$.

Substituting the average spontaneous emission coefficients into eq. (2.108) gives for the average spontaneous emission rate in the active region per unit volume

$$\begin{aligned} \bar{W}^{sp} &= \frac{1}{V_{QW}} \sum_m \sum_{\mathbf{k}_\perp} \left(\frac{e\Gamma_{hh1}^{c1}|M|}{\hbar\omega_m m_e} \right)^2 \left(\frac{1}{V_{QW}} \int_{V_{QW}} d^3r \left(\left| \frac{(\bar{\mathbf{x}} + i\bar{\mathbf{y}})}{\sqrt{2}} \cdot \mathbf{E}_m(\mathbf{r}_\perp, z) \right|^2 \right. \right. \\ &\quad \left. \left. + \left| \frac{(\bar{\mathbf{x}} - i\bar{\mathbf{y}})}{\sqrt{2}} \cdot \mathbf{E}_m(\mathbf{r}_\perp, z) \right|^2 \right) \right) \frac{2(\gamma_{c,hh} + \frac{1}{2}\gamma_m) \langle \hat{n}_{(c,1,\mathbf{k}_\perp)} \rangle_{vac} \langle \hat{n}_{(hh,1,-\mathbf{k}_\perp)}^h \rangle_{vac}}{(\gamma_{c,hh} + \frac{1}{2}\gamma_m)^2 + (\omega_{\mathbf{k}_\perp} - \omega_m)^2}. \end{aligned} \quad (2.115)$$

Taking the zero of energy to be at the band-edge for each band, the energy of the electrons in the first conduction band and the holes in the first heavy-hole band are approximately:

$$\varepsilon_{c,1,\mathbf{k}_\perp} \approx \frac{\hbar^2 |\mathbf{k}_\perp|^2}{2m_{c_\perp}^*}, \quad (2.116)$$

$$\varepsilon_{hh,1,-\mathbf{k}_\perp}^h \approx \frac{\hbar^2 |\mathbf{k}_\perp|^2}{2m_{hh_\perp}^*}, \quad (2.117)$$

where $m_{c_\perp}^*$ is the effective mass of the first conduction band in the plane of the quantum-well, and $m_{hh_\perp}^*$ is the in-plane effective mass of the holes in the first heavy-hole band⁵⁷. The energy difference between the conduction and valence band states is then [47],

⁵⁷The valence band holes have a positive effective mass typically, as the valence band has a negative electron effective mass at the band-edge (negative curvature).

$$\hbar\omega_{\mathbf{k}_\perp} = \bar{\varepsilon}_g + \varepsilon_{c,1,\mathbf{k}_\perp} + \varepsilon_{hh,1,-\mathbf{k}_\perp}^h \approx \bar{\varepsilon}_g + \frac{\hbar^2|\mathbf{k}_\perp|^2}{2m_{(c,hh)\perp}^*}, \quad (2.118)$$

where $\bar{\varepsilon}_g$ is the renormalized band-gap energy including the energy due to quantum confinement⁵⁸, and $m_{(c,hh)\perp}^*$ is an effective mass for the electron-hole pair,

$$\frac{1}{m_{(c,hh)\perp}^*} \equiv \frac{1}{m_{c\perp}^*} + \frac{1}{m_{hh\perp}^*}. \quad (2.119)$$

In the quasi-equilibrium approximation the electron and hole state populations are given by Fermi-Dirac energy distributions. The Fermi-Dirac distribution for the electrons in the first conduction band level and the holes in the first heavy-hole valence band level, written as a function of the transition energy, is:

$$f_\alpha^{e,h}(\omega_{\mathbf{k}_\perp}) = \frac{1}{e^{\frac{1}{k_B T}((\hbar\omega_{\mathbf{k}_\perp} - \bar{\varepsilon}_g)(m_{(c,hh)\perp}^*/m_\alpha^*) - \mu_\alpha)} + 1}. \quad (2.120)$$

In eq. (2.120) the chemical potential of the α energy band is μ_α , and $k_B T$ is the thermal energy. A superscript e is used to label an electron Fermi-Dirac distribution and a superscript h is used to label a hole distribution. The probability of the electron-hole pair being occupied within the quasi-equilibrium approximation is

$$\langle \hat{n}_{(c,1,\mathbf{k}_\perp)} \rangle_{vac} \langle \hat{n}_{(hh,1,-\mathbf{k}_\perp)}^h \rangle_{vac} \approx f_{c,1}^e(\omega_{\mathbf{k}_\perp}) f_{hh,1}^h(\omega_{\mathbf{k}_\perp}). \quad (2.121)$$

The sum over in-plane momentum in eq. (2.115) can also be transformed into an integral over the transition frequency⁵⁹,

⁵⁸A renormalized band-gap is usually used to take into account coulomb interactions of the charged particles [47].

⁵⁹Throughout this analysis we have assumed that the energy bands of the conduction and heavy-holes are cylindrically symmetric in the plane of the quantum-well. This allows the angular depen-

$$\sum_{\mathbf{k}_\perp} \approx \frac{A_\perp}{(2\pi)^2} \int_0^\infty d|\mathbf{k}_\perp| \int_0^{2\pi} d\theta |\mathbf{k}_\perp| = A_\perp \int_{\frac{\varepsilon_g}{\hbar}}^\infty d\omega_{\mathbf{k}_\perp} \frac{m_{(c, hh)_\perp}^*}{2\pi\hbar}, \quad (2.122)$$

which yields for the spontaneous emission rate per unit volume in the quantum-well,

$$\begin{aligned} \overline{W}^{sp} = \frac{1}{L_{QW}} \sum_m \left(\frac{e\Gamma_{hh1}^{cl} |M| (m_{(c, hh)_\perp}^*)^{1/2}}{2^{1/2} \hbar^{3/2} \omega_m m_e} \right)^2 & \left(\frac{1}{V_{QW}} \int_{V_{QW}} d^3r \left(\left| \frac{(\bar{\mathbf{x}} + i\bar{\mathbf{y}})}{\sqrt{2}} \cdot \mathbf{E}_m(\mathbf{r}_\perp, z) \right|^2 \right. \right. \\ & \left. \left. + \left| \frac{(\bar{\mathbf{x}} - i\bar{\mathbf{y}})}{\sqrt{2}} \cdot \mathbf{E}_m(\mathbf{r}_\perp, z) \right|^2 \right) \right) \mathcal{D}(\omega_m), \end{aligned} \quad (2.123)$$

where

$$\mathcal{D}(\omega_m) \equiv \int_{\frac{\varepsilon_g}{\hbar}}^\infty d\omega_{\mathbf{k}_\perp} \frac{2(\gamma_{c, hh} + \frac{1}{2}\gamma_m) f_{c,1}^e(\omega_{\mathbf{k}_\perp}) f_{hh,1}^h(\omega_{\mathbf{k}_\perp})}{(\gamma_{c, hh} + \frac{1}{2}\gamma_m)^2 + (\omega_{\mathbf{k}_\perp} - \omega_m)^2}. \quad (2.124)$$

Inserting the normalized electric field modes for a uniform dielectric material from eq. (2.16) into the above equation gives

$$\begin{aligned} \overline{W}_{fs}^{sp} = \frac{1}{L_{QW}} \sum_{\mathbf{k}_p, \sigma} \left(\frac{e\Gamma_{hh1}^{cl} |M| (m_{(c, hh)_\perp}^*)^{1/2}}{2^{1/2} \hbar^{3/2} \omega_{\mathbf{k}_p} m_e} \right)^2 \\ \times \left(\frac{1}{V_{QW}} \int_{V_{QW}} d^3r \left(\left| \frac{(\bar{\mathbf{x}} + i\bar{\mathbf{y}}) \cdot \bar{\mathbf{e}}_\sigma}{\sqrt{2}} \sqrt{\frac{\hbar\omega_{\mathbf{k}_p}}{2\epsilon V_{box}}} e^{-i(\mathbf{k}_p \cdot (\mathbf{r}_\perp, z_o))} \right|^2 \right. \right. \\ \left. \left. + \left| \frac{(\bar{\mathbf{x}} - i\bar{\mathbf{y}}) \cdot \bar{\mathbf{e}}_\sigma}{\sqrt{2}} \sqrt{\frac{\hbar\omega_{\mathbf{k}_p}}{2\epsilon V_{box}}} e^{-i(\mathbf{k}_p \cdot (\mathbf{r}_\perp, z_o))} \right|^2 \right) \right) \mathcal{D}(\omega_{\mathbf{k}_p})|_{\gamma_{\mathbf{k}_p}=0}. \end{aligned} \quad (2.125)$$

Since the amplitude of the free-space modes is unity this collapses to

dence to be integrated out.

$$\begin{aligned} \overline{W}_{fs}^{sp} = \frac{1}{L_{QW}} \sum_{\mathbf{k}_p, \sigma} \left(\frac{e\Gamma_{hh1}^{c1} |M| (m_{(c, hh)\perp}^*)^{1/2}}{2^{1/2} \hbar^{3/2} \omega_{\mathbf{k}_p} m_e} \right)^2 \left(\frac{\hbar \omega_{\mathbf{k}_p}}{2\epsilon V_{box}} \right) \\ \left(\left| \frac{(\bar{\mathbf{x}} + i\bar{\mathbf{y}})}{\sqrt{2}} \cdot \bar{\mathbf{e}}_\sigma \right|^2 + \left| \frac{(\bar{\mathbf{x}} - i\bar{\mathbf{y}})}{\sqrt{2}} \cdot \bar{\mathbf{e}}_\sigma \right|^2 \right) \mathcal{D}(\omega_{\mathbf{k}_p})|_{\gamma_{\mathbf{k}_p}=0}. \end{aligned} \quad (2.126)$$

Replacing the sum over photon momentum in eq. (2.126) by the integral expression of eq. (2.22)) yields

$$\begin{aligned} \overline{W}_{fs}^{sp} = \frac{1}{L_{QW}} \left(\frac{e\Gamma_{hh1}^{c1} |M| (m_{(c, hh)\perp}^*)^{1/2}}{2^{1/2} \hbar m_e} \right)^2 \sum_{\sigma} \int d\omega_{\mathbf{k}_p} d\theta d\phi \sin(\theta) \frac{\omega_{\mathbf{k}_p} n}{2(2\pi)^3 c^3 \epsilon_o} \\ \left(\left| \frac{(\bar{\mathbf{x}} + i\bar{\mathbf{y}})}{\sqrt{2}} \cdot \bar{\mathbf{e}}_\sigma \right|^2 + \left| \frac{(\bar{\mathbf{x}} - i\bar{\mathbf{y}})}{\sqrt{2}} \cdot \bar{\mathbf{e}}_\sigma \right|^2 \right) \mathcal{D}(\omega_{\mathbf{k}_p})|_{\gamma_{\mathbf{k}_p}=0}. \end{aligned} \quad (2.127)$$

Without loss of generality, we can take the Bloch momentum matrix element to be along the \mathbf{z}' -direction ($\theta = 0$). Then for every photon momentum direction we can choose the $\sigma = 1$ polarization to be orthogonal to the Bloch momentum matrix element, and the $\sigma = 2$ polarization to have a projection equal to $\sin(\theta)$ on the \mathbf{z}' -axis [63]. Integrating over θ and ϕ in eq. (2.127) gives,

$$\begin{aligned} \overline{W}_{fs}^{sp} = \frac{1}{L_{QW}} \left(\frac{e\Gamma_{hh1}^{c1} |M| (m_{(c, hh)\perp}^*)^{1/2}}{2^{1/2} \hbar m_e} \right)^2 \int d\omega_{\mathbf{k}_p} d\theta \sin^3(\theta) \frac{\omega_{\mathbf{k}_p} n}{(2\pi)^2 c^3 \epsilon_o} \mathcal{D}(\omega_{\mathbf{k}_p})|_{\gamma_{\mathbf{k}_p}=0} \\ = \frac{1}{L_{QW}} \left(\frac{e\Gamma_{hh1}^{c1} |M| (m_{(c, hh)\perp}^*)^{1/2}}{2^{1/2} \hbar m_e} \right)^2 \int d\omega_{\mathbf{k}_p} \frac{\omega_{\mathbf{k}_p} n}{3\pi^2 c^3 \epsilon_o} \mathcal{D}(\omega_{\mathbf{k}_p})|_{\gamma_{\mathbf{k}_p}=0}. \end{aligned} \quad (2.128)$$

In evaluating $\mathcal{D}(\omega_{\mathbf{k}_p})|_{\gamma_{\mathbf{k}_p}=0}$ we can assume that for reasonable pumping levels the inhomogeneous linewidth defined by the Fermi-Dirac distributions is much broader than the homogeneous linewidth, $\gamma_{c, hh}$, and the occupation probabilities can be moved through the integral over the transition frequency:

$$\begin{aligned} \mathcal{D}(\omega_{\mathbf{k}_p})|_{\gamma_{\mathbf{k}_p}=0} &\approx f_{c,1}^e(\omega_{\mathbf{k}_p})f_{hh,1}^h(\omega_{\mathbf{k}_p}) \int_{\frac{\bar{\epsilon}_g}{\hbar}}^{\infty} d\omega_{\mathbf{k}_\perp} \frac{2(\gamma_{c,hh})}{\gamma_{c,hh}^2 + (\omega_{\mathbf{k}_\perp} - \omega_{\mathbf{k}_p})^2} \\ &\approx \begin{cases} 0 & ; \text{ if } \omega_{\mathbf{k}_p} < \bar{\epsilon}_g/\hbar, \\ 2\pi f_{c,1}^e(\omega_{\mathbf{k}_p})f_{hh,1}^h(\omega_{\mathbf{k}_p}) & ; \text{ otherwise.} \end{cases} \end{aligned} \quad (2.129)$$

In evaluating the average spontaneous emission rate, the integral of $\omega f_{c,1}^e(\omega)f_{hh,1}^h(\omega)$ over optical frequencies above the re-normalized band-gap must be evaluated, which for moderate pumping levels can be approximately given as⁶⁰:

$$\int_{\frac{\bar{\epsilon}_g}{\hbar}}^{\infty} d\omega_{\mathbf{k}_p} (\omega_{\mathbf{k}_p}) f_{c,1}^e(\omega_{\mathbf{k}_p}) f_{hh,1}^h(\omega_{\mathbf{k}_p}) \approx \left(\frac{\bar{\epsilon}_g}{\hbar}\right) \left(\frac{k_B T}{\hbar}\right) \left(e^{\frac{1}{k_B T}(\mu_{c1} + \mu_{hh1})}\right). \quad (2.130)$$

Finally, under non-degenerate pumping conditions of the quantum-well levels, the approximate average spontaneous emission rate per unit volume in the quantum-well active region is,

$$\bar{W}_{fs}^{sp} \approx \frac{1}{L_{QW}} \left(\frac{e\Gamma_{hh1}^{c1} |M| (m_{(c,hh)\perp}^*)^{1/2}}{2^{1/2} \hbar m_e} \right)^2 \left(\frac{2n\omega_g^2}{3\pi c^3 \epsilon_o \bar{Q}} \right) \left(e^{\frac{1}{k_B T}(\mu_{c1} + \mu_{hh1})} \right), \quad (2.131)$$

where \bar{Q} is the ratio of the band-gap energy to thermal energy⁶¹, and ω_g is the angular frequency corresponding to the band-gap energy. More generally, \bar{Q} represents the degree of inhomogeneous broadening present in the active region, the narrower the emission spectrum the higher the value of \bar{Q} . For higher carrier densities then,

$$\frac{1}{\bar{Q}} \approx \frac{\Delta\lambda_{sp}}{\lambda_o}, \quad (2.132)$$

⁶⁰Moderate meaning that the conduction and heavy-hole distributions are not degenerate and can be approximated by Maxwell-Boltzmann distributions, i.e., $\mu_{c1}, \mu_{hh1} < 0$ where energy is referenced to the each respective band-edge.

⁶¹At room temperature $\bar{Q} \sim 30$.

where λ_o is spontaneous emission peak wavelength and $\Delta\lambda_{sp}/\lambda_o$ is the normalized inhomogeneous spontaneous emission linewidth.

2.3.3 Spontaneous Emission from a Quantum-Well Active Region Embedded in a Single Mode Microcavity

Starting from eq. (2.123) we have for the average spontaneous emission rate into mode m per unit volume in a quantum-well active region ($c1 \rightarrow hh1$):

$$\begin{aligned} \overline{W}_m^{sp} = & \frac{1}{L_{QW}} \left(\frac{e\Gamma_{hh1}^{c1} |M| (m_{(c, hh)\perp}^*)^{1/2}}{2^{1/2} \hbar^{3/2} \omega_m m_e} \right)^2 \left(\frac{1}{V_{QW}} \int_{V_{QW}} d^3r \left(\left| \frac{(\bar{\mathbf{x}} + i\bar{\mathbf{y}})}{\sqrt{2}} \cdot \mathbf{E}_m(\mathbf{r}_\perp, z) \right|^2 \right. \right. \\ & \left. \left. + \left| \frac{(\bar{\mathbf{x}} - i\bar{\mathbf{y}})}{\sqrt{2}} \cdot \mathbf{E}_m(\mathbf{r}_\perp, z) \right|^2 \right) \right) \mathcal{D}(\omega_m). \end{aligned} \quad (2.133)$$

In evaluating $\mathcal{D}(\omega_m)$ we must include the optical loss rate of the quasi-mode m . However, for cavity modes with relatively high- Q , $\gamma_{c, hh} \gg \omega_m/2Q$. The inhomogeneous linewidth of the quantum-well active region (as defined by the quasi-Fermi distributions) is also significantly broader than the linewidth of a high- Q optical cavity⁶².

Thus, for a reasonable cavity mode Q -factor (> 100), $\mathcal{D}(\omega_m)$ is given by eq. (2.129). If the cavity mode is well aligned with the gain peak of the active region (close to the band-gap frequency), the average spontaneous emission rate per unit volume into mode m is then,

⁶²At room temperature and optical wavelengths ($1.5\mu\text{m}$) a Q of roughly 60 is equivalent to the homogeneous linewidth in a semiconductor ($\gamma_{c, hh} \sim (0.1\text{ps})^{-1}$). For a reasonable quantum-well inhomogeneous linewidth of 100 nm, the corresponding Q is 15. In the defect cavities studied in this thesis the defect mode quality factors are on the order of 10^3 which results in an optical linewidth much narrower than either the homogeneous or inhomogeneous linewidths of a semiconductor quantum-well active region at room temperature.

$$\begin{aligned} \overline{W}_m^{sp} = & \frac{1}{L_{QW}} \left(\frac{e\Gamma_{hh1}^{c1} |M| (m_{(c,hh)\perp}^*)^{1/2}}{2^{1/2} \hbar^{3/2} \omega_m m_e} \right)^2 \left(\frac{1}{V_{QW}} \int_{V_{QW}} d^3r \left(\left| \frac{(\bar{\mathbf{x}} + i\bar{\mathbf{y}})}{\sqrt{2}} \cdot \mathbf{E}_m(\mathbf{r}_\perp, z) \right|^2 \right. \right. \\ & \left. \left. + \left| \frac{(\bar{\mathbf{x}} - i\bar{\mathbf{y}})}{\sqrt{2}} \cdot \mathbf{E}_m(\mathbf{r}_\perp, z) \right|^2 \right) \right) 2\pi \left(e^{\frac{1}{k_B T} (\mu_{c1} + \mu_{hh1})} \right), \end{aligned} \quad (2.134)$$

where $\omega_m \approx \omega_g$. The cavity enhancement due to the Q of the cavity mode, as predicted by the standard Purcell factor⁶³, has been washed out by the homogeneous and inhomogeneous broadening in the semiconductor quantum-well active region. There still exists, however, a cavity enhancement to the spontaneous emission rate due to the increased energy density per photon in the cavity.

Assuming the cavity mode is polarized in the plane of the quantum-well, the average spontaneous emission rate is found by averaging the normalized cavity mode electric field intensity over the active region volume. The integral of the cavity mode electric field intensity over the entire cavity volume is,

$$\int_{V_c} d^3r |\mathbf{E}_m(\mathbf{r}_\perp, z)|^2 \approx \frac{\hbar\omega_m}{2\bar{\epsilon}}, \quad (2.135)$$

where $\bar{\epsilon}$ is the average (weighted by the electric field intensity) dielectric constant within the cavity, and V_c is the cavity volume. The average electric field intensity over the active region is then,

$$\int_{V_a} d^3r |\mathbf{E}_m(\mathbf{r}_\perp, z)|^2 = \Gamma_{m,a}^{sp} \frac{\hbar\omega_m}{2\bar{\epsilon}}, \quad (2.136)$$

where the confinement factor of mode m is defined as,

⁶³See the next sub-section.

$$\Gamma_{m,a}^{sp} \equiv \frac{\int_{V_a} d^3r |\mathbf{E}_m(\mathbf{r}_\perp, z)|^2}{\int_{V_c} d^3r |\mathbf{E}_m(\mathbf{r}_\perp, z)|^2}. \quad (2.137)$$

Using the above notation, the average spontaneous emission rate over the active region per unit volume is

$$\begin{aligned} \overline{W}_m^{sp} &\approx \frac{1}{L_{QW}} \left(\frac{e\Gamma_{hh1}^{c1} |M| (m_{(c,hh)\perp}^*)^{1/2}}{2^{1/2} \hbar^{3/2} \omega_m m_e} \right)^2 \left(\frac{2\pi \Gamma_{m,a}^{sp} \frac{\hbar \omega_m}{2\bar{\epsilon}}}{V_a} \right) \left(e^{\frac{1}{k_B T} (\mu_{c1} + \mu_{hh1})} \right) \\ &= \frac{1}{L_{QW}} \left(\frac{e\Gamma_{hh1}^{c1} |M| (m_{(c,hh)\perp}^*)^{1/2}}{2^{1/2} \hbar m_e} \right)^2 \left(\frac{\pi}{\bar{\epsilon} \omega_m V_{eff,m}^a} \right) \left(e^{\frac{1}{k_B T} (\mu_{c1} + \mu_{hh1})} \right), \end{aligned} \quad (2.138)$$

where the cavity mode is assumed to be polarized entirely in the plane of the quantum-well. The effective cavity mode volume, dependent upon the position and size of the active region, is defined as

$$V_{eff,m}^a \equiv \frac{\Gamma_{m,a}^{sp}}{V_a}. \quad (2.139)$$

The Purcell enhancement factor for a microcavity supporting the single mode m (within the spectral bandwidth of the the quantum-well active region) is given by the ratio of \overline{W}_m^{sp} to \overline{W}_{fs}^{sp} :

$$P_{m,a} \approx \frac{\frac{\pi}{\bar{\epsilon} \omega_m V_{eff,m}^a}}{\frac{2n\omega_g^2}{3\pi c^3 \epsilon_o \bar{Q}}} = \frac{3\pi^2 c^3 \epsilon_o \bar{Q}}{2n\bar{\epsilon} \omega_m \omega_g^2 V_{eff,m}^a}. \quad (2.140)$$

Taking $\bar{\epsilon} \sim n^2 \epsilon_o$ and $\omega_g \approx \omega_m$ gives for the Purcell factor,

$$\begin{aligned}
P_{m,a} &\approx \frac{3\pi^2}{2} \left(\frac{c^3}{n^3 \omega_m^3 V_{eff,m}^a} \right) \left(\bar{Q} \right) \\
&= \frac{3}{2\pi} \left(\frac{(\lambda_m/2n)^3}{V_{eff,m}^a} \right) \left(\bar{Q} \right) = \frac{3}{2\pi} \left(\frac{1}{\bar{V}_{eff,m}^a} \right) \left(\bar{Q} \right),
\end{aligned} \tag{2.141}$$

where $\bar{V}_{eff,m}^a$ is the normalized effective mode volume in units of cubic half-wavelengths. The Purcell factor is thus a product of the spatial density given by the inverse of the effective cavity mode volume and a spectral density which in the semiconductor is dominated by the inhomogeneous linewidth.

Consider, for instance, one of the localized dipole-like defect modes of the photonic crystal cavities studied in chapter 4. The polarization of these modes lies nearly completely in the plane of the quantum-well for quantum-wells positioned near the middle of the perforated waveguide. The Purcell enhancement for spontaneous emission into either of the dipole-like photonic crystal modes can then be estimated using eq. (2.141). The dipole-like modes of sub-section 4.4.1 have roughly half of there energy stored in a modal volume (V_d) which is $2.5(\lambda_o/2n)^3$, λ_o being the free space wavelength of the mode. The vertical confinement factor (Γ_z) per quantum-well is roughly 6%⁶⁴, and assuming that the quantum-well is only pumped over the area intersected by V_d in the plane of the quantum-well⁶⁵, the in-plane confinement factor (Γ_{xy}) is 50%. For such a pumping scheme the active region volume is,

$$V_a \approx L_{QW}(V_d)^{2/3}, \tag{2.142}$$

the implicit assumption being that the cavity mode has equal extent in each dimension. For a 10 nm wide quantum-well, such as those in the tested devices (see chapter 6), the width of the quantum-well is approximately 0.04 half-wavelengths in the di-

⁶⁴See section 6.1.

⁶⁵We are assuming here that the active region within the quantum-well only extends over the effective cavity volume. This also means that there is no absorption or gain outside of this area.

electric material ($n \sim 3.4$). The normalized effective volume for the dipole-like mode of the photonic crystal cavity is then

$$\bar{V}_{eff,d}^a \approx \frac{(0.04)(2.5)^{2/3}}{\Gamma_z \Gamma_{xy}} \approx 2.25. \quad (2.143)$$

For a normalized spontaneous emission linewidth of 10% which is typical for a semiconductor quantum-well⁶⁶,

$$P_{d,a} = \frac{3}{2\pi} \left(\frac{1}{2.25} \right) \left(\frac{1}{0.1} \right) \approx 2 \quad (2.144)$$

One of the most important parameters in determining the performance of a laser is the spontaneous emission coupling coefficient, or β -factor. For a symmetric photonic crystal defect cavity with only the two degenerate dipole-like modes resonant with the quantum-well active region, an estimate of the β -factor for either of the two defect modes can be made by including that part of the free-space (radiation) mode spectrum that is not captured by the photonic crystal waveguide. With reference to the TE-like band-diagram of Figure 4.5, since the defect mode frequencies lie within the guided mode band-gap of the photonic crystal slab, the only other modes that can be excited by electrons in the quantum-well (which is embedded in the slab) are those that lie above the light-line of the cladding. This corresponds to the angular region in photon momentum space that is within the critical angle of the slab-air interface. Using an average slab index of 3.4 gives $\theta_{crit.} = 17^\circ = 0.095\pi$ radians. The total angular region accessible by the quantum-well active region is then four times this value, or 20% of the total available free-space modes.

Neglecting any resonances within the radiation mode spectrum (which there are), the ratio of the spontaneous emission rate into either of the two dipole-like modes to

⁶⁶For quantum-wells which are displaced from the center of the photonic crystal waveguide, or for pumping geometries which extend out past the central anti-node of the dipole-like modes, the Purcell factor decreases.

the total spontaneous emission rate is approximately:

$$\beta_{d,a} = \frac{W_{d,a}^{sp}}{W_{x,a}^{sp} + W_{y,a}^{sp} + W_{rad}^{sp}} \approx \frac{1}{1 + 1 + \frac{0.20}{P_{d,a}}} \approx 47.6\%, \quad (2.145)$$

where $W_{x,a}^{sp}$ and $W_{y,a}^{sp}$ are the (equal) spontaneous emission rates into the degenerate x and y dipole-like modes, respectively. If the cavity were made single mode by splitting the dipole-like mode degeneracy as is done in chapter 4, then the β -factor is theoretically as high as 91%. For a more accurate calculation using the finite-difference time-domain method to simulate the coupling to radiation modes the reader is referred to reference [41].

2.3.4 Spontaneous Emission Enhancement and the Purcell Factor

The analysis of the previous two sections is rather tedious due to the complex nature of the semiconductor medium. In 1946 Edward Purcell [1], in working with a much simpler (and ideal) atomic medium, was able to derive a simple expression for the enhancement of the spontaneous emission rate in a generic microcavity. The method used to derive this result is very insightful and is presented below.

The local spontaneous emission rate of an atom, regardless of the cavity geometry, is proportional to the product of the spatial electric field intensity and spectral energy density; the local density of modes. We know from the analysis in sub-section 2.1.1 that the average spatial electric field intensity⁶⁷ of a given mode is inversely proportional to volume, and that the spectral density of modes is directly proportional to volume. Therefore, the average (in both space and frequency) local mode density remains approximately constant as cavity walls are brought inwards and the volume shrinks. This leads to the conclusion that the average emitter within the cavity will see an average local density of modes which is the same as that in free-space.

⁶⁷Here we assume that within the cavity volume the dielectric function is constant, i.e., the cavity consists of a uniform dielectric material surrounded by mirrors.

Cavity enhancement of spontaneous emission is a result of the fact that the (non-averaged) local mode density is neither homogeneous in space or frequency. If the emitters are placed inside the cavity at anti-nodes of a cavity resonance, or if a cavity resonance aligns spectrally with an atomic transition, then an enhanced spontaneous emission rate over that in free-space is possible. Following the analysis of Purcell [1] and Kleppner [4] we can find an approximate formula for the cavity enhanced spontaneous emission rate of an active material source embedded in a microcavity. In order to make connection to the work of Purcell, consider the active material to be independent, identical, randomly oriented atoms⁶⁸ which have an optically active transition centered at ω_a with a line-shape much narrower than the optical cavity resonance linewidth:

$$\Delta\omega_a \ll \Delta\omega_m \quad (2.146)$$

where $\Delta\omega_a$ is the atomic linewidth and $\Delta\omega_m$ is the linewidth of the m th cavity resonance.

In the absence of a cavity, the electric field intensity is uniform and each atom has a spontaneous emission rate given by:

$$R_{sp,a}^o \propto \int U^{e,o} \rho_{ph}^o \rho_a d\omega \approx U^{e,o}(\omega_a) \rho_{ph}^o(\omega_a) \quad (2.147)$$

where ρ_a is the narrow atomic line-shape, $U^{e,o}$ is the spatial electric field intensity per mode, ρ_{ph}^o is the mode density per unit frequency in a homogeneous dielectric material (free-space) of refractive index n . The local mode density is $\theta_{ph}^o = U^{e,o} \rho_{ph}^o$.

Now consider a cavity resonant mode with an average spatial electric field intensity \bar{U}_m^e , center frequency aligned with ω_a , and linewidth $\Delta\omega_m$. The average spectral density of the cavity is approximately given by the product of the cavity volume and

⁶⁸This allows us to assume that the atoms couple to different field polarizations equally on average.

the free-space mode density per unit frequency per unit volume,

$$\bar{\rho}_{ph}^c \approx V_c \left(\frac{\omega_a^2 n^3}{\pi^2 c^3} \right). \quad (2.148)$$

The average local mode density for the cavity in the vicinity of the atomic line frequency is then

$$\bar{\theta}_{ph}^c \equiv \bar{U}_m^e \bar{\rho}_{ph}^c \approx \bar{U}_m^e V_c \left(\frac{\omega_a^2 n^3}{\pi^2 c^3} \right) \quad (2.149)$$

Equating $\bar{\theta}_{ph}^c$ and θ_{ph}^o we can solve for the average electric field intensity in mode m :

$$\bar{U}_m^e \approx \frac{U^{e,o} \rho_{ph}^o}{V_c \left(\frac{\omega_a^2 n^3}{\pi^2 c^3} \right)} \quad (2.150)$$

The spontaneous emission rate of the average atom in the microcavity, assuming the atoms are uniformly distributed throughout the entire cavity, is

$$\bar{R}_{sp,a}^c \propto \int_{\omega} \bar{U}_m^e \rho_m \rho_a d\omega \approx \bar{U}_m^e \rho_m(\omega_a), \quad (2.151)$$

where $\rho_m(\omega)$ is the Lorentzian line-shape of the cavity mode m , normalized such that $\int_0^\infty \rho_m(\omega) d\omega = 1$. Substituting the value of \bar{U}_{em} given in eq. (2.150) into eq. (2.151), and taking the ratio of the cavity spontaneous emission rate to that in free-space one finds:

$$P = \frac{R_{sp,a}^c}{R_{sp,a}^o} \approx \frac{\pi^2 c^3 \rho_m(\omega_a)}{V_c \omega_a^2 n^3}. \quad (2.152)$$

where P is the Purcell enhancement factor. If the atomic line is exactly centered with the m th cavity resonance then $\rho_m(\omega_a) \approx 1/(\pi\Delta\omega_m) = Q_m/(\pi\omega_a)$, and

$$P \approx \frac{1}{\pi^2} \frac{Q_m}{V_c/(\lambda_o/2n)^3}, \quad (2.153)$$

where λ_o is the optical wavelength of the emitted light in vacuum. The Purcell enhancement factor is the product of a normalized spectral density Q_m , and a normalized spatial density $1/\bar{V}_c$, where $\bar{V}_c = V_c/(\lambda_o/2n)^3$ is the cavity volume in units of cubic half-wavelengths in the material. If the atoms were not distributed uniformly within the cavity mode, but were selectively positioned at an anti-node of the cavity mode standing wave, then the average atom would see an electric field intensity larger than \bar{U}_m^e . In general the average electric field intensity seen by the atoms within the active region volume, V_a , is:

$$\bar{U}_m^{e,a} = \frac{1}{V_a} \int_{V_a} |\mathbf{E}_m|^2 d^3r \quad (2.154)$$

$$= \bar{U}_m^e \left(\frac{V_c}{V_a} \right) \left(\frac{\int_{V_a} |\mathbf{E}_m|^2 d^3r}{\int_{V_c} |\mathbf{E}_m|^2 d^3r} \right). \quad (2.155)$$

The Purcell factor for the average atom is then given by

$$P \approx \frac{1}{\pi^2} \frac{Q_m}{\bar{V}_{eff,m}}, \quad (2.156)$$

where the normalized effective volume for mode m is

$$\bar{V}_{eff,m} = \left(\frac{V_a}{(\lambda_o/2n)^3} \right) \left(\frac{\int_{V_c} |\mathbf{E}_m|^2 d^3r}{\int_{V_a} |\mathbf{E}_m|^2 d^3r} \right). \quad (2.157)$$

When considering the effects of the active material distribution within the cavity,

it is helpful to define a spontaneous emission confinement factor, Γ_m^{sp} , between the active material and the m th cavity mode⁶⁹:

$$\Gamma_m^{sp} = \frac{\int_{V_a} |\mathbf{E}_m|^2 d^3r}{\int_{V_c} |\mathbf{E}_m|^2 d^3r}. \quad (2.158)$$

In terms of the confinement factor,

$$\bar{V}_{eff,m} = \frac{1}{\Gamma_m^{sp}} \left(\frac{V_a}{(\lambda_o/2n)^3} \right), \quad (2.159)$$

and the spontaneous emission rate for the average atom in the active region is,

$$\bar{R}_{sp,a}^c \propto \frac{\Gamma_m^{sp} Q_m}{V_a}. \quad (2.160)$$

Comparing eq. (2.156) and (2.141) we see that the major modification to Purcell's original formula for the cavity enhanced spontaneous emission rate is to replace the cavity Q with the effective Q of the entire system of electrons and photons:

⁶⁹The confinement factor defined above is different than the confinement factor typically used to calculate waveguide modal gain. The difference stems from the fact that the modal gain for a waveguide is typically written as a gain per unit length and the dispersive properties of the waveguide must be taken into account [64]. What we are effectively considering in this section is the average gain per unit time, $\langle g_t^o(x, y, z) \rangle$, for which the confinement factor defined above is correct. Unfortunately, what can be more directly measured in semiconductor amplifiers, and thus is typically referenced, is the local material gain per unit length, $g_l^o(x, y, z)$. For example, take $g_l^o(x, y, z)$ to be the (local) material gain per unit length (no waveguide) in a non-dispersive material with index n . The group velocity in this case is c/n , and the gain per unit length can be written in terms of the local gain per unit time: $g_l^o = (n/c)g_t^o$. Now if the field is propagating in a waveguide with an effective index of propagation for the guided mode of \bar{n} , then the group velocity (due to waveguide dispersion only) is $v_g^{wg} = c/(n^2/\bar{n})$. This gives for the waveguide local gain per unit length: $g_l^{wg} = (n/\bar{n})(n/c)g_t^o$. The local gain per unit length of the waveguide in terms of the local material gain per unit length is then, $g_l^{wg}(x, y, z) = (n(x, y, z)/\bar{n})g_l^o(x, y, z)$. As described in this section, the average gain per unit time, $\langle g_t^o \rangle$, can be calculated by averaging $g_t^o(x, y, z)$ using the electric field intensity as a weighting function. To calculate the average gain per unit length of a waveguide mode then $g_l^{wg}(x, y, z) = (n(x, y, z)/\bar{n})g_l^o(x, y, z)$ must be averaged using the electric field intensity as a weighting function, not $g_l^o(x, y, z)$. This is the source of the difference in the confinement factor definitions.

$$\frac{1}{\bar{Q}} \approx \frac{1}{Q_m} + \frac{1}{Q_{hom.}} + \frac{1}{Q_{inhom.}}, \quad (2.161)$$

where Q_m represents the cavity mode losses, $Q_{hom.}$ the homogeneous broadening, and $Q_{inhom.}$ the inhomogeneous broadening of the excited state levels.

2.3.5 Gain, Lasing, and Super-luminescence in a Microcavity

In sub-section 2.3.4 we looked at the spontaneous emission properties of an active material which is embedded in a microcavity. Here we investigate how semiconductor laser mode gain and laser threshold current are also effected by the presence of a microcavity. In order to streamline the analysis and focus on the microcavity effects we will use a simple rate equation to describe the dynamics of the laser system⁷⁰. In this analysis the laser system is defined by the following parameters:

$n_e \equiv$ density of excited state electrons in the active region,

$n_o \equiv$ density of excited state electrons at which transparency is reached,

$R_{sp} \equiv$ average spontaneous emission rate of excited state electrons,

$\beta_m \equiv$ fraction of total spontaneous emission which enters the laser cavity mode m ,

$G_m \equiv$ differential gain, or average stimulated emission rate into mode m ,

$R_{nr} \equiv$ average non-radiative decay rate of excited state electrons in the active region,

$p_m \equiv$ number of photons in laser cavity mode m ,

$V_c \equiv$ volume of the optical cavity,

$V_a \equiv$ effective volume of the active region.

The spontaneous emission rate of an average excited state electron in the active region into cavity mode m is given by,

$$R_{sp}^m = \beta_m R_{sp}. \quad (2.162)$$

For laser cavities which support power orthogonal eigenmodes⁷¹, excited state electrons in the active region provide stimulated photons into cavity mode m at a rate of

⁷⁰We consider only the dynamics of an average electron, where the averaging is performed both spatially and spectrally.

⁷¹See sub-section 2.1.2 for a discussion.

p_m times the spontaneous rate into that mode (eq. (2.106)). The differential gain of mode m is then,

$$G_m \equiv R_{sp}^m = \beta_m R_{sp}. \quad (2.163)$$

The coupled rate equations for the (average) excited state electron density and the photon number in mode m are⁷²:

$$\frac{dn_e}{dt} = \eta \frac{J}{q} - n_e(R_{sp} + R_{nr}) - G_m(n_e - n_o)p_m + \text{noise}, \quad (2.164)$$

$$\frac{dp_m}{dt} = -(\gamma_m - G_m(n_e - n_o)V_a)p_m + \text{noise}, \quad (2.165)$$

where J is electron current density, η is the pumping efficiency of the excited state, and γ_m is the photon decay rate in mode m . In the rate equation for photon number we have lumped spontaneous emission in as a noise term due to its random phase.

Although the principle of laser action is quite simple, depending on the laser cavity under study, the definition of a lasing threshold can become quite blurred. For example, the classic definition that lasing action occurs when the number of photons in the laser mode is equal to one, breaks down for long resonators with very lossy end mirrors. In this case the photon loss rate is non-uniform throughout the cavity (highly localized to the mirrors) and the round-trip gain may be less than the loss even though the average photon number within the cavity is greater than one. This results in super-luminescent emission, not true lasing action. Defining the lasing threshold to occur when photon gain equals photon loss ($g_m = \gamma_m$) is problematic as well as spontaneous emission (noise) into the laser mode causes the average photon number to be indeterminate as it will rise until gain saturation kicks in.

A more robust definition of lasing threshold can be obtained by combining the

⁷²The spontaneous emission and stimulated emission rates have also been linearized in carrier density, which means that the spontaneous emission coefficient is a function of carrier density.

two definitions. The threshold photon number is taken to be one under the constraint that photon gain equals photon loss. Solving for the threshold carrier density and threshold current under steady-state conditions gives:

$$n_e^{th} = n_o + \frac{\gamma_m}{V_a G_m}, \quad (2.166)$$

and

$$I_{th} = J_{th} V_a = \frac{q}{\eta} \left(n_o V_a (R_{sp} + R_{nr}) + \frac{\gamma_m}{\beta_m} ((1 + R_{nr}/R_{sp}) + \beta_m) \right). \quad (2.167)$$

The threshold current consists of two distinct components. The first term in eq. (2.164) represents the current needed to reach transparency. The second term is the current needed to overcome the optical loss in mode m . The geometry of the optical cavity obviously affects the loss rate, however, it is not obvious what role the cavity volume plays in determining the threshold current.

As the volume shrinks the free-spectral range between modes increases and the number of modes accessible by the active medium rapidly approaches one for cavities several cubic wavelengths in dimension. This effectively suppresses unwanted spontaneous emission into the non-lasing modes and drives the threshold current down by reducing the current needed to overcome the optical losses in the lasing mode. In this microcavity limit, $\beta_m \sim 1$ and R_{sp} is dominated by the spontaneous emission into mode m :

$$I_{th}^{\beta_m \sim 1} \approx \frac{q}{\eta} \left(n_o V_a (R_{sp}^m + R_{nr}) + \gamma_m \left(2 + \frac{R_{nr}}{R_{sp}^m} \right) \right). \quad (2.168)$$

From eq. (2.160), the spontaneous emission rate into a cavity mode is proportional

to $V_c \approx \Gamma_m/V_a$ ⁷³, where V_c is the cavity volume and Γ_m is the confinement factor of mode m to the active region within the cavity. The spontaneous emission rate is then approximately,

$$R_{sp}^m \approx C_{sp} V_c \approx C_{sp} \frac{\Gamma_m}{V_a}, \quad (2.169)$$

where C_{sp} is some reference spontaneous emission rate. This yields for the microcavity laser threshold current,

$$I_{th} \Big|_{\beta_m \sim 1} \approx \frac{q}{\eta} \left(n_o (V_a R_{nr} + C_{sp} \Gamma_m) + \gamma_m \left(2 + \frac{R_{nr}}{C_{sp} V_c} \right) \right). \quad (2.170)$$

The two components of the threshold current behave differently as the volume of the cavity is changed. The transparency current increases linearly with Γ_m , whereas the non-radiative component of the current associated with the losses of the optical mode decreases as $1/V_c$. If non-radiative recombination dominates the sub-threshold inter-band dynamics, or if the active region is reduced coincidentally with cavity volume to keep Γ_m constant, then shrinking the mode volume will tend to reduce the lasing threshold current. This is a result of the increased efficiency of the radiative process over that of the non-radiative process. If, however, non-radiative effects play a minor role, then simply reducing the cavity volume without adjusting the active region volume will tend to increase the threshold current due to an increase in transparency current (i.e., it becomes harder to maintain a given excited state population as the spontaneous emission rate increases).

From a measurement standpoint, the onset of lasing action will become apparent as the linewidth of the laser mode narrows and the differential efficiency of the collected laser mode power versus the input current (power) increases (threshold “knee”).

⁷³This assumes that the enhancement due to the Q of the mode is negligible, which is the case in most high-Q semiconductor resonators.

The linewidth narrowing is a result of the reduced loss suffered by the cavity mode due to gain. The change in differential efficiency can be attributed to a number of different phenomena. If the active region is coupled to a large number of different optical modes ($\beta_m \ll 1$), then upon lasing the increase in photon number in mode m causes the emission efficiency into mode m to jump due to stimulated emission. In a microcavity in which only a single mode is supported within the active region bandwidth a threshold “knee” will still be evident as an increase in the differential efficiency stems from the increased efficiency of the radiative process which is in competition with non-radiative processes. A “thresholdless” microcavity laser is possible only in the absence of non-radiative effects.

In experimentally determining the threshold of a laser it is important to differentiation between true lasing action and super-luminescent emission⁷⁴. In laser cavities in which gain and loss are uniformly distributed one will see narrowing of the cavity mode linewidth prior to lasing as the gain increases; however, the change in differential efficiency will be negligible prior to lasing as the spontaneous emission is not amplified (p_m remains close to zero) and the stimulated rate remains much less than the spontaneous rate throughout the cavity. In the case of distributed loss and gain then, lasing coincides with a change in the differential efficiency which can be measured as a “knee” in a curve of the collected laser mode power versus input power or current.

The situation becomes more clouded for optical cavities which have highly non-distributed loss or gain. The total cavity round-trip loss can be greater than the round-trip gain, while still having local regions within the cavity that have net gain. A good example is that of an anti-reflection coated semiconductor amplifier. The gain experienced by an electromagnetic wave as it passes through cavity can be substantial, but due to the negligible feedback afforded by the anti-reflection coated facets, the round-trip gain can be less than one. Amplified spontaneous emission within the gain regions increases the radiative efficiency, and can also increase the effective beta factor

⁷⁴Super-luminescence is stimulated emission without lasing.

if the high gain regions have a preferential overlap with the laser mode. This results in a noticeable “knee” in the collected laser mode power versus input power curve even though lasing may not yet have been reached. Assuming that all the losses are localized to the mirror facets and that the non-radiative recombination rate is much larger than the spontaneous emission rate⁷⁵, a slope change (A) of two in efficiency requires a single-pass gain (G) of roughly two ($G \approx A$). The required average material gain per unit length, \bar{g}^{sl} , for a factor A increase in slope efficiency change is:

$$\bar{g}_A^{sl} = \frac{1}{L} \ln A, \quad (2.171)$$

where L is the single-pass cavity length.

For a cavity mode with finesse \mathcal{F} , the net round-trip gain is roughly $G(1 - 2\pi/\mathcal{F})$. This puts a limit on the maximum possible value of A before lasing occurs⁷⁶,

$$A^{sl} \lesssim \frac{\mathcal{F}}{\mathcal{F} - 2\pi}. \quad (2.172)$$

A more accurate relation for small finesse cavity modes is,

$$A^{sl} \lesssim e^{\frac{2\pi n_g (L/\lambda_o)}{Q}}, \quad (2.173)$$

where n_g is the group index, L is the effective single-pass cavity length, Q is the quality factor, and λ_o is the free-space wavelength of the cavity mode.

For microcavities which have a length scale comparable to that of the wavelength

⁷⁵The slope efficiency is proportional to $\eta_i = \frac{R_{sp} + R_{st}}{R_{sp} + R_{st} + R_{nr}}$. Assuming G photons are created for every one spontaneously emitted photon then $\eta_i = \frac{G}{G + R_{nr}/R_{sp}}$. If η_i^o is the efficiency with no stimulated emission ($G=1$), then $\eta_i/\eta_i^o \approx G$ for $R_{nr}/R_{sp} \gg 1$. If $R_{sp}/R_{nr} \gg 1$ then there will be little change in efficiency with the addition of stimulated emission as the radiative efficiency is already very high.

⁷⁶This relation is only valid for finesse much larger than one.

of light, the required material gain per unit length to see significant slope efficiency changes from super-luminescence is enormously high. For instance, in the photonic crystal defect cavities studied in this thesis the effective cavity length (gain region) is roughly $2\mu\text{m}$. The required material gain per unit length to a see factor of two increase in slope efficiency is roughly $5 \times 10^5 \text{ cm}^{-1}$, well beyond the ability of a semiconductor active material. Also, assuming a conservative Q value of 500, we see from eq. (2.167) that $A^{sl} \lesssim e^{\frac{1}{10}} \approx 1.1$. The threshold “knee” and linewidth narrowing seen in the photoluminescence data from the photonic crystal defect cavities analyzed in chapter 6 can not be explained by super-luminescence. In order to observe these effects in such a tiny cavity volume, the defect mode must be lasing and the cavity mode photon number must be much greater than one.

Chapter 3 Group Theory and the Analysis of Periodic Electromagnetic Structures

3.1 Introduction

In analyzing and designing photonic crystals one first looks to the plethora of work done in the field of solid-state physics and the analysis of electrons in crystalline structures. We know from solid-state physics that the periodicity in the coulombic crystal potential opens up band-gaps in the electron dispersion relation. The engineering of electronic bands in semiconductors plays a central role in much of the technology we see today, from transistors in electronics, to lasers in optical telecommunications. Group theory has been the key to unraveling much of the complexity of such periodic structures, allowing one to sort and catalog many of the electronic states.

The analogous “potential” for photons in the optical regime is the macroscopic dielectric function, ϵ . As in the electronic states of crystals, group theory is a powerful tool for analyzing photonic crystals. In the electromagnetic problem, however, there is the added complexity of the vector nature of the fields. In this short chapter I will describe the symmetries present in Maxwell’s equations and how group theory can be used to label photonic bands, describe mode coupling (“selection rules”), and predict the degeneracies and symmetries of localized “defect” modes of a photonic crystal. Particular emphasis will be given to the two-dimensional triangular lattice as this is the geometry used in the actual fabricated laser cavities described in subsequent chapters.

3.2 Symmetries of Classical and Quantum Systems

What is a symmetry? We all know from everyday experience that the symmetries of an object correspond to those vantage points from which the object looks identical. Similarly, the symmetries of a physical system can be described as the group of observation points from which the underlying structure of a system “looks” identical. Mathematically, symmetries describe a set of reference frames¹ in which the governing equations of motion of the dynamical variables are identical. As the state of the system is the same for all observers, the symmetries then constrain the possible solutions of the dynamical variables². These constraints can lead to conservation laws (conserved currents)³, and to degeneracies (in frequency or energy) of the different states of the system. Symmetry plays a very important role in physics. It is an active role. In many cases physicists are led to new theories by postulating a required symmetry of nature⁴.

The representation of a symmetry may take different forms depending upon the model used to describe the system. This can be a source of much confusion, and one must remember that the form of a symmetry transformation is only valid in context. This is most evident in quantum theory in which a symmetry is represented as an operator on a Hilbert space which commutes with the Hamiltonian operator. In the following a brief description of the dynamics for classical and quantum theories is given, and an attempt is made to relate the different representations of symmetry transformations.

In classical mechanics one deals with particles localized in space and time. The dynamical variables (degrees of freedom) are the position ($q_i(t)$) and velocity ($\dot{q}_i(t)$) of each particle. The dynamics of the system are found by extremizing (usually minimizing) the “action” of the paths taken by the particles. The action, S , is the

¹Here we mean reference frame in the most general sense, not just coordinate transformations but also transformations of the fields or particles.

²Of course no more than the equations of motion do themselves.

³This is the basis of Noether’s theorem.

⁴Take for example Einstein and his Special Theory of Relativity in which each observer in an inertial reference frame must be using the same physics (equations of motion) to describe nature.

integral along the path⁵ of the Lagrangian, $L(q_i(t), \dot{q}_i(t))$. An equivalent formulation is possible in which a change of variables is made and the system is described by the particle's position and canonical momentum, $p^i(t) = \partial L / \partial(\dot{q}_i)$. The dynamics of the system can then be defined in terms of the Hamiltonian, $H(q_i, p^i) \equiv p^i \dot{q}_i - L$.

In classical field theory every point in space-time⁶ is considered to be an independent degree of freedom. The fields are defined as (scalar, vector, spinor, etc.) functions on the space-time manifold. Take for example a scalar field in space-time, $\phi(x_\mu)$. The Lagrangian is now an integral over space of a Lagrangian density, $\mathcal{L}(\phi(x_\mu), \partial_\mu \phi(x_\mu))$. The action, S , is then the integral of the Lagrangian over a path parametrized by time, t :

$$S = \int_{t_o}^{t_o+T} dt L(t) = \int_{t_o}^{t_o+T} dt \int_{space} d^3x \mathcal{L}(\phi, \partial_\mu \phi). \quad (3.1)$$

S is a functional which measures the “length” of a path that can be taken by the dynamical variables. The classical path, as described by the classical equations of motion, is then determined by extremizing the action S . The symmetries of the system are transformations which leave the equations of motion invariant. More generally, symmetries are transformations which leave the action invariant up to a surface term⁷, or equivalently the Lagrangian density invariant up to a 4-divergence $\partial_\mu \mathcal{J}^\mu(x)$ ⁸.

In quantum mechanics the picture is much different. The system is described by a Hilbert space. The dynamical evolution of the Hilbert space states is governed by the Hamiltonian operator which is proportional to the generator of time translations. Focusing on the Hilbert space states as the fundamental objects, we then qualify symmetries as those operators which commute with the Hamiltonian operator (i.e., leave the equations of motion of the Hilbert states unchanged). The transformation

⁵A path in this case is defined by the evolution in time of the particles.

⁶Or whatever manifold the system lives on.

⁷An integral over the boundary of the space-time volume in eq. (3.1).

⁸See [65].

of the Hamiltonian from a function of the dynamical variables to an operator on a Hilbert space may be regarded as simple mathematical trickery. The quantum picture and the classical picture of the symmetries of a system are reconciled by use of the Feynman path integral method as described below.

Feynman⁹ believed in the concept that all paths are responsible for the dynamics of a system. He used this idea to formulate the Feynman path integral approach. In the Feynman path integral method, all paths are to be treated as equal participants in the system evolution and their “length” is measured (as in classical mechanics) by the action, S . The full dynamics of the system is then governed by the interference pattern formed by all the paths evolving together and is described mathematically as follows:

$$U([\phi_a(\mathbf{x}); t_o], [\phi_b(\mathbf{x}); t_o + T]) = \sum_{paths} e^{iS/\hbar} = \sum_{paths} e^{i\frac{1}{\hbar} \int_{t_o, \phi_a(\mathbf{x})}^{t_o+T, \phi_b(\mathbf{x})} d^4x \mathcal{L}(\phi, \partial_\mu \phi)}, \quad (3.2)$$

$$P([\phi_a(\mathbf{x}); t_o] \rightarrow [\phi_b(\mathbf{x}); t_o + T]) = |U([\phi_a(\mathbf{x}); t_o], [\phi_b(\mathbf{x}); t_o + T])|^2, \quad (3.3)$$

where $\phi(x)|_{t_o} = \phi_a(\mathbf{x})$ is the initial field distribution, $\phi(x)|_{t_o+T} = \phi_b(\mathbf{x})$ is the final field distribution, $U([\phi_a(\mathbf{x}); t_o], [\phi_b(\mathbf{x}); t_o + T])$ is the time evolution functional, and $P([\phi_a(\mathbf{x}); t_o] \rightarrow [\phi_b(\mathbf{x}); t_o + T])$ is the probability that the system will evolve from $\phi_a(\mathbf{x}) \rightarrow \phi_b(\mathbf{x})$ as $t = t_o \rightarrow t_o + T$. In the Feynman path integral, the evolution of the system asymptotically approaches classical motion for large scale systems ($\hbar \rightarrow 0$). A symmetry transformation within this framework is then found to be equivalent to the invariance of the action up to a surface term as in the classical case. One can also show that the Hamiltonian, defined as a function of the dynamical variables, satisfies the following relationship: $i\hbar \frac{\partial}{\partial T} U(\phi(x_a), \phi(x_b); T) = H U(\phi(x_a), \phi(x_b); T)$. It is in this sense that one can treat the Hamiltonian (H) equivalently as a linear operator responsible for time translation on an underlying vector (Hilbert) space. Symmetry operators on this underlying Hilbert space are then those operators which commute

⁹This was based on an earlier idea of Dirac's.

with the Hamiltonian operator. The two pictures, although mathematically different, are nonetheless equivalent in their predictions.

In the next section we will study the symmetries of a (classical) electromagnetic field in a macroscopic dielectric. The symmetries of the system will correspond to those transformations of the fields which leave Maxwell's equations, the equations of motion, invariant.

3.3 Macroscopic Maxwell's Equations and Symmetry

In a given observer's reference frame, electromagnetic phenomena can be described by two coupled fields, the electric field ($\mathbf{E}(\mathbf{r}, t)$) and the magnetic field ($\mathbf{B}(\mathbf{r}, t)$). The following Maxwell's equations¹⁰ couple the electric and magnetic time varying vector fields in vacuum,

$$\nabla \times \mathbf{E}(\mathbf{r}, t) = -\frac{\partial \mathbf{B}(\mathbf{r}, t)}{\partial t}, \quad (3.4)$$

$$\nabla \times \mathbf{B}(\mathbf{r}, t) = \mu_o \epsilon_o \frac{\partial \mathbf{E}(\mathbf{r}, t)}{\partial t}, \quad (3.5)$$

$$\nabla \cdot \mathbf{E}(\mathbf{r}, t) = 0, \quad (3.6)$$

$$\nabla \cdot \mathbf{B}(\mathbf{r}, t) = 0, \quad (3.7)$$

where ϵ_o and μ_o are the electric and magnetic permeabilities of free-space ("vacuum")¹¹. The product $\epsilon_o \mu_o$ is related to the speed of light in free-space, $c^2 = 1/(\epsilon_o \mu_o)$.

In free-space (uncoupled to matter) the electromagnetic field equations are symmetric in \mathbf{E} and \mathbf{B} (apart from a sign change and a multiplicative factor). In the pres-

¹⁰Throughout this thesis the rationalized MKSA system of units is used [66].

¹¹The term "vacuum" is typically used to describe the electromagnetic field in free-space; however, this is rather misleading as indeed the electromagnetic field itself represents "something." Even in the absence of real photons, there still exists an infrastructure for the electromagnetic field as represented by the two permeability values. The term "ground state" is much more descriptive.

ence of matter, which carries charge and conducts current, we must modify Maxwell's equations. A set of macroscopic field equations can then be derived in which the graininess of matter is neglected and all the field quantities are averaged on a scale much larger than the atom:

$$\nabla \times \mathbf{E} = -\frac{\partial \mathbf{B}}{\partial t}, \quad (3.8)$$

$$\nabla \times \mathbf{B} = \mu_o(\epsilon_o \frac{\partial \mathbf{E}}{\partial t} + \frac{\partial \mathbf{P}}{\partial t} + \nabla \times \mathbf{M} + \mathbf{J}_{free}), \quad (3.9)$$

$$\nabla \cdot \mathbf{E} = \frac{1}{\epsilon_o}(\rho_{bound} + \rho_{free}), \quad (3.10)$$

$$\nabla \cdot \mathbf{B} = 0, \quad (3.11)$$

$$\nabla \cdot \mathbf{P} = -\rho_{bound}, \quad (3.12)$$

where \mathbf{P} is the electric dipole moment density or the polarization of the material, \mathbf{M} is the magnetic dipole moment density or magnetization of the material, \mathbf{J}_{free} is the conduction current due to free charges, ρ_{bound} is the trapped or bound charge density, and ρ_{free} is the density of charge which can move freely (conduct macroscopic currents) in response to electric and magnetic forces. The asymmetry between the electric and magnetic fields within matter stems from the fact that there is no observable “magnetic” charge ($\nabla \cdot \mathbf{B} = 0$), or “magnetic” current.

Equations (3.8)-(3.11) are still rather awkward and incomplete in the sense that the charge within a material not only acts as a source for the electromagnetic field but also responds to the electromagnetic field:

$$\mathbf{F}_{em} = q(\mathbf{E} + \mathbf{v} \times \mathbf{B}), \quad (3.13)$$

where \mathbf{F}_{em} is the force on a particle of charge q moving with velocity \mathbf{v} . The position and movement of charge within matter both produces an electromagnetic field, and is produced by the electromagnetic field. A more general theory (QED) which treats

charge (electrons) and the electromagnetic field on a more equal footing requires a quantum theory of the electron. We will be satisfied here to find a self-consistent solution for the electromagnetic field and the charge and current within matter. In order to reduce the number of unknowns a number of simplifying (empirical) relations must be made which are based upon intuition and experience.

Polarization is due to charge separation and thus can be induced by an electric field. Magnetization, on the other hand, is due to current loops formed from the orbital motion of electrons in molecules or the intrinsic electron spin, both of which energetically favor alignment with an applied magnetic field. Also, the force law in eq. (3.13) shows that free charge will be accelerated by an electric field (steady-state is reached due to electron scattering in the material) thus forming a conduction current (we assume the electron velocity in the current is much slower than the speed of light and therefore the force of the magnetic field on the electrons is neglected in comparison to the electric field). With the above observations we are led to the following relations:

$$\mathbf{P} = \epsilon_o \chi_e \mathbf{E}, \quad (3.14)$$

$$\mathbf{M} = \chi_m \mathbf{B}, \quad (3.15)$$

$$\mathbf{J}_{free} = \sigma \mathbf{E}, \quad (3.16)$$

where χ_e is the electric susceptibility, χ_m the magnetic susceptibility¹², and σ the conductance of a given material. We have neglected any anisotropy in the material which would make the three parameters second rank tensors as opposed to scalars. All three relations are approximate in nature and the three quantities (χ_e, χ_m, σ) must be empirically determined. Apart from ferro-electric and ferro-magnetic materials, these

¹²The traditional definition of the magnetic susceptibility is $\mathbf{M} = \chi_m \mathbf{H}$, where \mathbf{H} is defined below. Since the magnetic field in matter which induces the magnetization is the \mathbf{B} field, we will use the more physical, but non-standard definition. This does not lead to any physical differences in the theory for if \mathbf{M} is proportional to \mathbf{B} , then it is also proportional to \mathbf{H} , and vice versa. In fact, the two definitions are nearly equivalent for $\chi_m \ll 1$.

relations can be quite linear, at least for small field values, and thus quite useful. Substituting relations (3.14)-(3.16) into Maxwell's equations,

$$\nabla \times \mathbf{E} = -\frac{\partial \mathbf{B}}{\partial t}, \quad (3.17)$$

$$\nabla \times (1 - \mu_o \chi_m) \mathbf{B} = \mu_o (\epsilon_o (1 + \chi_e) \frac{\partial \mathbf{E}}{\partial t} + \sigma \mathbf{E}), \quad (3.18)$$

$$\nabla \cdot \mathbf{E} = \frac{1}{\epsilon_o} (\rho_{bound} + \rho_{free}), \quad (3.19)$$

$$\nabla \cdot \chi_e \mathbf{E} = -\rho_{bound}, \quad (3.20)$$

$$\nabla \cdot \mathbf{B} = 0. \quad (3.21)$$

The fields in matter are \mathbf{E} and \mathbf{B} ; however, for traditional (and some practical) reasons we introduce the displacement field \mathbf{D} and the vector field \mathbf{H} :

$$\mathbf{D} = \epsilon_o \mathbf{E} + \mathbf{P} = \epsilon_o (1 + \chi_e) \mathbf{E}, \quad (3.22)$$

$$\mathbf{H} = \frac{1}{\mu_o} \mathbf{B} - \mathbf{M} = \frac{1}{\mu_o} (1 - \chi_m) \mathbf{B}, \quad (3.23)$$

$$\nabla \cdot \mathbf{D} = \rho_{free}, \quad (3.24)$$

$$\nabla \times \mathbf{H} = \frac{\partial \mathbf{D}}{\partial t} + \mathbf{J}_{free}. \quad (3.25)$$

The practical reasons are now apparent as the sources for \mathbf{D} and \mathbf{H} are free charges and currents which one can externally control and measure, as opposed to the internal bound current and charge¹³.

Dielectric and magnetic materials are usually described by their electric and magnetic permeabilities rather than their susceptibilities, thus we make one last simplification,

¹³This is actually only true of the current; the free charge cannot be easily separated from the bound charge and thus the introduction of \mathbf{D} is still rather cumbersome [67].

$$\epsilon = \epsilon_o(1 + \chi_e), \quad (3.26)$$

$$\mu = \mu_o(1 - \chi_m)^{-1}. \quad (3.27)$$

where for $\chi_m \ll 1$, $\mu \approx \mu_o(1 + \chi_m)$, which is the standard definition of the magnetic permeability. Maxwell's equations in matter finally take the following form in terms of four macroscopic (volume averaged) field quantities ($\mathbf{E}, \mathbf{B}, \mathbf{D}, \mathbf{H}$), two source terms ($\rho_{free}, \mathbf{J}_{free}$), and three empirically determined parameters (ϵ, μ, σ):

$$\nabla \times \mathbf{E} = -\frac{\partial \mathbf{B}}{\partial t}, \quad (3.28)$$

$$\nabla \times \mathbf{H} = \frac{\partial \mathbf{D}}{\partial t} + \sigma \mathbf{E}, \quad (3.29)$$

$$\nabla \cdot \mathbf{D} = \rho_{free}, \quad (3.30)$$

$$\nabla \cdot \mathbf{B} = 0, \quad (3.31)$$

$$\mathbf{D} = \epsilon \mathbf{E}, \quad (3.32)$$

$$\mathbf{B} = \mu \mathbf{H}, \quad (3.33)$$

$$\mathbf{J}_{free} = \sigma \mathbf{E}. \quad (3.34)$$

In this thesis we will consider only an idealized dielectric material in which no free currents or free charges exist. We will also neglect the magnetic response of the material ($\mu \approx \mu_o$). All other “non-ideal” properties of the material can be added as perturbations to this simplified theory:

$$\nabla \times \mathbf{E} = -\frac{\partial \mathbf{B}}{\partial t}, \quad (3.35)$$

$$\nabla \times \mathbf{B} = \mu_o \frac{\partial}{\partial t} \mathbf{D}, \quad (3.36)$$

$$\nabla \cdot \epsilon \mathbf{E} = 0, \quad (3.37)$$

$$\nabla \cdot \mathbf{B} = 0, \quad (3.38)$$

$$\mathbf{D}(\omega, \mathbf{r}) \equiv \epsilon(\omega, \mathbf{r}) \mathbf{E}(\omega, \mathbf{r}). \quad (3.39)$$

In general $\epsilon = \epsilon(\mathbf{k}, \omega, |\mathbf{E}|)$ is a function of the magnitude and frequency (in both space and time) of the forcing field. We will consider only the linear response of the polarization and neglect the field dependence of ϵ . We also assume that the dielectric function acts locally in space and time (constant in frequency).

3.3.1 Electric and Magnetic Field Master Equations

The first symmetry that we will invoke is that of the homogeneity of time (time invariance), which results in the energy of the system being conserved. The generator for time translations¹⁴ is the vector $\partial/\partial t$. The eigenvalue and eigenfunction of the time generator operator are the angular frequency ω and the harmonic function $e^{i\omega t}$, respectively. Since we have assumed linearity in the field response, time invariance allows us to classify the fields of the system by their angular frequency¹⁵. As we will be dealing with spatially varying dielectric material, we do not have homogeneity of space and thus the spatial harmonics are no longer the preferred basis for describing the electromagnetic fields. For this reason we will retain only the Fourier transform in time in order to define the field eigen-equations:

¹⁴In quantum field theory the Hamiltonian of the system is also related to the generator of time translations, $H = -i\hbar\partial/\partial t$.

¹⁵We have yet to mention an eigen-equation; however, for the energy eigen-equation at least the eigenmodes will be the harmonics. More generally, any eigen-equation which commutes with the time shift generator will have the harmonics as their eigen-basis.

$$\mathbf{E}(\mathbf{r}, t) = \int \frac{d\omega}{2\pi} \mathbf{E}(\omega, \mathbf{r}) e^{i(\omega t)}, \quad (3.40)$$

$$\mathbf{B}(\mathbf{r}, t) = \int \frac{d\omega}{2\pi} \mathbf{B}(\omega, \mathbf{r}) e^{i(\omega t)}, \quad (3.41)$$

$$\mathbf{D}(\omega, \mathbf{r}) \equiv \epsilon(\omega, \mathbf{r}) \mathbf{E}(\omega, \mathbf{r}), \quad (3.42)$$

where $\mathbf{E}(\omega, \mathbf{r})$ and $\mathbf{B}(\omega, \mathbf{r})$ are the complex spatial field patterns with angular frequency ω . A physically observable field is a real quantity, thus the total field must be written as a special expansion of positive and negative frequency harmonics. This requires $\mathbf{E}(-\omega, \mathbf{r}) = \mathbf{E}^*(\omega, \mathbf{r})$ (and similarly for the magnetic field). With this restriction, we can then proceed to work with the complex harmonic field modes.

From Maxwell's equations in a dielectric material (with no free charge or current present), we can form two separate eigen-equations for time harmonic (ω) electric and magnetic complex spatial fields:

$$\frac{1}{n^2(\mathbf{r})} \nabla \times \nabla \times \mathbf{E}(\omega, \mathbf{r}) = \left(\frac{\omega}{c} \right)^2 \mathbf{E}(\omega, \mathbf{r}), \quad (3.43)$$

$$\nabla \times \frac{1}{n^2(\mathbf{r})} \nabla \times \mathbf{H}(\omega, \mathbf{r}) = \left(\frac{\omega}{c} \right)^2 \mathbf{H}(\omega, \mathbf{r}), \quad (3.44)$$

where $n(\mathbf{r})$ is the spatially varying refractive index and $\epsilon \equiv n^2 \epsilon_0$. Using the vector identity $\nabla \cdot (\mathbf{F} \times \mathbf{G}) = \mathbf{F} \cdot \nabla \times \mathbf{G} - \mathbf{G} \cdot \nabla \times \mathbf{F}$, Gauss' theorem, and the principle that physical fields must go to zero or are periodic at the boundary of the spatial domain, one can show that the magnetic field eigen-operator is Hermitian¹⁶ with the following vector field inner product definition:

¹⁶A Hermitian operator, \hat{A} , is equal to its adjoint, \hat{A}^\dagger , which is defined by the relation $(\hat{A}\mathbf{F})^* = \mathbf{F}^* \hat{A}^\dagger$. A Hermitian operator \hat{A} must then satisfy the following relation for all \mathbf{F}, \mathbf{G} : $\int d^3r (\hat{A}\mathbf{F})^* \cdot \mathbf{G} = \int d^3r \mathbf{F}^* \cdot \hat{A}\mathbf{G}$.

$$\langle \mathbf{F}, \mathbf{G} \rangle \equiv \int d^3r \mathbf{F}^* \cdot \mathbf{G}. \quad (3.45)$$

The electric field operator is not Hermitian in a spatially varying dielectric with the above inner product definition. Of course this is not that surprising as the electric field does not carry all the energy of the free field + dielectric system, one must include the energy of the polarization¹⁷. The electric field energy density of a given harmonic mode is given by $\epsilon \mathbf{E} \cdot \mathbf{E}^*$. In order to account for the extra energy stored in the polarization of the dielectric material the integration measure in eq. (3.45) must be modified from d^3r to $d^3r \epsilon(\mathbf{r})$. Alternatively, we can define a new field, $n(\mathbf{r})\mathbf{E}$. The electric field energy density is now given by the square of the amplitude of this new field. $n(\mathbf{r})\mathbf{E}$ represents the energy excitations of the harmonic field and one can easily check that its eigen-operator is Hermitian with respect to the inner product of eq. (3.45)¹⁸. The eigen-equations for the two fields are:

$$\Theta_E(n\mathbf{E}) = \left(\frac{\omega}{c}\right)^2 (n\mathbf{E}), \quad (3.46)$$

$$\Theta_E \equiv \frac{1}{n} \nabla \times \nabla \times \frac{1}{n}, \quad (3.47)$$

$$\Theta_B(\mathbf{H}) = \left(\frac{\omega}{c}\right)^2 (\mathbf{H}), \quad (3.48)$$

$$\Theta_B \equiv \nabla \times \frac{1}{n^2} \nabla \times . \quad (3.49)$$

The fields are only fully defined once we apply the divergence relations in equations (3.37) and (3.38). The field $n(\mathbf{r})\mathbf{E}$ is not in general transverse which is the

¹⁷The magnetic field on the other hand carries all the magnetic field energy as we have assumed a non-magnetic material.

¹⁸We expect this as the Hamiltonian should be Hermitian.

reason we choose to work with the magnetic field in most cases. The spectrum of a Hermitian operator has special properties. The eigenvalues are all real and the eigenfunctions with different eigenvalues are orthogonal ($\langle \mathbf{H}_\lambda, \mathbf{H}_{\lambda'} \rangle = \delta_{\lambda, \lambda'}$). Also, since the dielectric function is assumed real and positive, the eigenvalues must be positive¹⁹. This restricts ω to the real line.

In analyzing Θ_E and Θ_B we see that the spatial symmetries of the system are limited by the symmetries present in the dielectric function ($\epsilon(\mathbf{r})$), as well as the transformation properties of the curl operator ($\nabla \times$). The curl operator is a second rank tensor field defined on a Cartesian basis in a three-dimensional Euclidean space [68]. The curl operator is invariant under coordinate transformations among different Cartesian basis²⁰. These transformations preserve the metric tensor field, $\eta_{ij} = \delta_{ij}$ ²¹. This limits the allowable coordinate transformations to rotary-reflections and shifts of the origin, elements of the Euclidean symmetry group E_3 . The symmetry of the dielectric function (assumed scalar here) further reduces the rotational and translational symmetries of the system. All Cartesian coordinate transformations which leave the dielectric function invariant, $\epsilon(\mathbf{r}) \rightarrow \epsilon(\mathbf{r}')$, are symmetry operations of the electric field operator Θ_E .

Periodic dielectric structures form a Bravais lattice which has an infinite set of translational symmetries and a finite set of rotary-reflection symmetries. Since rotational and translational symmetries do not commute in general, the analysis of the full symmetry group cannot be reduced to analyzing rotations and translations separately. A simplification is possible, based on the fact that the translations are an invariant subgroup of the full symmetry group, that allows one to simply analyze the spectrum of eigenmodes of a periodic structure, albeit within a limited region of the global mode spectrum.

¹⁹The proof follows a similar line of reasoning to the proof of hermiticity.

²⁰Transformations which are not symmetries of the curl operator and of Maxwell's equations are ones which scale the coordinate axes such $x \rightarrow ax$, where $|a| \neq 1$. Therefore, the electric field modes of a dielectric media which is periodic in the radial direction, for instance, do not transform among a degenerate set of modes under radial shifts, even though this is a symmetry of the dielectric.

²¹The metric tensor only takes this form in a Cartesian basis.

3.3.2 The Bloch Equation: A Prelude to Space Groups

From Bloch's theorem, for a periodic dielectric lattice, we can write the electric and magnetic eigen-fields as products of a periodic function and a plane wave:

$$\mathbf{E}_{Bloch}(\mathbf{r}) = \mathbf{U}_{\mathbf{k}}(\mathbf{r})e^{i\mathbf{k}\cdot\mathbf{r}}, \quad (3.50)$$

where $\mathbf{U}_{\mathbf{k}}(\mathbf{r})$ is a Bloch function which is invariant under all translational symmetry operations of the dielectric lattice, and \mathbf{k} is the plane wave momentum. The \mathbf{k} -vector labels the irreducible representation (IRREP) of the translations, and must be restricted to the first Brillouin Zone (IBZ) so as not to over count the IRREPs (see section 3.4). Substituting this form of the electric field into Θ_E gives

$$\begin{aligned} \Theta_E(n\mathbf{E}_{Bloch}) &= \frac{1}{n}\nabla \times \nabla \times \mathbf{U}_{\mathbf{k}}e^{i\mathbf{k}\cdot\mathbf{r}} \\ &= \frac{\omega_{\mathbf{k}}^2}{c^2}(n\mathbf{U}_{\mathbf{k}}e^{i\mathbf{k}\cdot\mathbf{r}}), \end{aligned} \quad (3.51)$$

which when simplified yields an eigenvalue equation for $\mathbf{U}_{\mathbf{k}}$:

$$\begin{aligned} \frac{1}{n}(i\mathbf{k} + \nabla \times)(i\mathbf{k} + \nabla \times)\frac{1}{n}(n\mathbf{U}_{\mathbf{k}}) &= \Phi_{\mathbf{k}}(n\mathbf{U}_{\mathbf{k}}) \\ &= \frac{\omega_{\mathbf{k}}^2}{c^2}(n\mathbf{U}_{\mathbf{k}}), \end{aligned} \quad (3.52)$$

where $\Phi_{\mathbf{k}}$ is the master operator for the Bloch eigen-equation.

We now have a new eigen-equation for the Bloch functions, in which translational symmetries have been eliminated through the introduction of a \mathbf{k} -vector label. It now suffices to analyze the rotary-reflection symmetries of the $\Phi_{\mathbf{k}}$ operator. Since the \mathbf{k} label transforms as a vector under $O(3)$, the symmetry operations of eq. (3.52) are those point group operations which conserve \mathbf{k} modulo a reciprocal lattice vector, \mathbf{G}_n . This set of symmetry operations is called the group of the wave vector, and is

labelled $\mathcal{G}_{0\mathbf{k}}$.

The Bloch equation and $\mathcal{G}_{0\mathbf{k}}$ provide a local description of the eigenmodes of a periodic system, limited to a sub-region of the IBZ called the irreducible Brillouin zone. Additional degeneracies between each of these sub-regions within the IBZ, which is important for the study of modes which form in the presence of defects in the lattice, requires a global view of the IBZ. The mathematical machinery needed to study the IRREPs of the full space group of a periodic dielectric lattice is rather complex. An introduction is given below.

3.4 Space Groups

Composite objects formed from the arrangement of smaller identical objects in a periodic fashion take on new and interesting properties which are intrinsic to the geometry of the arrangement and distinct from the characteristics of the individual smaller elements. It is for this reason that the geometry of a crystal lattice plays such an important role in determining the chemical, vibrational, electronic, and optical properties of a crystalline material formed from the regular bonding of atoms. At a larger scale the same is true for periodic dielectric structures (photonic crystals) in which the photon dispersion relation can be strongly affected by the geometry of the dielectric “lattice.” Group theory is the mathematical tool designed to characterize and extract information about the properties of these composite periodic structures.

The fundamental elements of group theory are the symmetry *operations* which form a closed set or group under a multiplication rule²². More concretely, operations are the generalization of the concept of the rotation of an object or the shifting from one position to another within a structure. Of most interest to us are space groups, which encapsulate all the spatial symmetry content of periodic structures. Periodic (infinite) structures are defined by a Bravais lattice, with a “unit” cell and associated “primitive” lattice vectors, \mathbf{a}_i :

²²These operations must also satisfy the special properties of a group such as closure, inclusion of an identity element, and associativity.

$$\mathbf{R}^h = h^i \mathbf{a}_i, \quad h^i \in \mathbb{Z}, \quad (3.53)$$

where \mathbf{R}^h is the position coordinate of a vertex of the lattice. The unit cell is the smallest volume²³ which when tiled in space generates the entire periodic structure. The space group, \mathcal{R} , is a set of operations which transform the periodic structure back into itself. \mathcal{R} is composed of translation operations and point symmetry operations. The pure translation group, \mathbb{T} , is composed of those translations given by the unit cell coordinates, \mathbf{R}^h . The pure point symmetry group, \mathcal{G} , contains all the rotary-reflection operations which, when performed on the periodic structure, leave it unchanged. \mathcal{R} can also contain operations which are mixtures of non-primitive translations and rotary-reflections²⁴. In order to simplify the discussion here we will consider symmorphic space groups in which all symmetry operations are products of elements in \mathcal{G} and \mathbb{T} . A detailed analysis of symmorphic and non-symmorphic groups can be found in the study text by Ludwig and Falter [69].

The space group operations will be labelled as follows:

$$\{d|\mathbf{t}\} \in \mathcal{R}, \quad (3.54)$$

where d represents a point group operation and \mathbf{t} a translation²⁵. The operation of $\{d|\mathbf{t}\}$ can be defined by its transformation of the coordinate system:

$$\mathbf{x}' = \{d|\mathbf{t}\} \cdot \mathbf{x} \equiv d\mathbf{x} + \mathbf{t}. \quad (3.55)$$

The following is a list of group properties that can be derived from the operator

²³Depending on the dimension of the structure, this could also be an area or a length.

²⁴This would be operations such as a screw axis or glide plane.

²⁵For symmorphic space groups $d \in \mathcal{G}$ and $\mathbf{t} \in \mathbb{T}$; however, for non-symmorphic space groups this need not be the case.

definitions:

$$\text{identity: } \{e|\mathbf{0}\}, \quad (3.56)$$

$$\text{translation: } \{e|\mathbf{t}\}, \quad (3.57)$$

$$\text{rotation: } \{d|\mathbf{0}\}, \quad (3.58)$$

$$\text{multiplication: } \{d_2|\mathbf{t}_2\} \cdot \{d_1|\mathbf{t}_1\} = \{d_2d_1|\mathbf{t}_2 + d_2\mathbf{t}_1\}, \quad (3.59)$$

$$\text{inverse: } \{d|\mathbf{t}\}^{-1} = \{d^{-1}|-d^{-1}\mathbf{t}\}. \quad (3.60)$$

Since rotational and translational symmetries do not in general commute, the analysis of the full symmetry group cannot be reduced to analyzing rotations and translations separately. However, by careful analysis one can “induce” the representations of the space group from the representations of \mathbb{T} and \mathcal{G} .

3.4.1 Translation Group, \mathbb{T}

The translation group, \mathbb{T} , plays a special role in that it is an invariant subgroup²⁶ of \mathcal{R} . The quotient group, \mathcal{R}/\mathbb{T} , is isomorphic to \mathcal{G} ,

$$\mathcal{R} = \sum_{d \in \mathcal{G}} \{d|\mathbf{s}(d)\} \cdot \mathbb{T}. \quad (3.61)$$

When all $\mathbf{s}(d)$ can be chosen to be $\mathbf{0}$, then $\mathcal{G} \subset \mathcal{R}$ and \mathcal{R} is symmorphic.

\mathbb{T} is also an Abelian group²⁷. Restricting ourselves to translations in three dimensions, we can write the elements of the translation group as products of translations along Cartesian axes,

²⁶An invariant subgroup is one in which its left and right cosets are identical, and thus it is formed from complete classes of operations. Invariant subgroups play the role of an identity operation in a homomorphism.

²⁷All elements commute with each other.

$$\begin{aligned}
\mathbb{T} &= \{e|\mathbf{R}^{\mathbf{h}}\} = \{e|h^i \mathbf{a}_i\} \\
&= \{e|\mathbf{a}_1\}^{h^1} \cdot \{e|\mathbf{a}_2\}^{h^2} \cdot \{e|\mathbf{a}_3\}^{h^3},
\end{aligned} \tag{3.62}$$

where $h^i \in \mathbb{Z}$. We can then write the translation group as an outer direct product of translations along each different axis, $\mathbb{T} = \mathbb{T}_1 \times \mathbb{T}_2 \times \mathbb{T}_3$.

\mathbb{T} and \mathbb{T}_i are infinite groups for a Bravais lattice and in order to simplify our analysis we apply periodic boundary conditions, forming a super-cell,

$$\{e|\mathbf{a}_i\}^Q = \{e|Q\mathbf{a}_i\} = \{e|\mathbf{0}\}, \quad Q \in \mathbb{Z}, \tag{3.63}$$

where Q can be taken to be as large as we wish. This is equivalent to introducing a super translation group, \mathbb{T}_s :

$$\mathbb{T}_s = \{e|Q\mathbf{a}_i\}^{n_i}, \quad n_i \in \mathbb{Z}. \tag{3.64}$$

The quotient group, \mathbb{T}/\mathbb{T}_s , is equivalent to the finite group formed by assuming periodic boundary conditions. We now define $\mathbb{T}'_{finite} = \mathbb{T}/\mathbb{T}_s$, and drop the $'_{finite}$ for convenience.

\mathbb{T}_i is thus now a cyclic group of order Q with one-dimensional (1D) irreducible representations (IRREPs), the number of which is Q ,

$$D^{(m_i)}(\{e|\mathbf{a}_i\}) = e^{-i2\pi m_i/Q}, \quad m_i = 1, 2, 3, \dots, Q, \tag{3.65}$$

where m_i now labels the IRREP. Since \mathbb{T} is an outer direct product of the \mathbb{T}_i , and the IRREPs of \mathbb{T}_i are 1-D, the IRREPs of \mathbb{T} are formed from powers of $D^{(m_i)}$:

$$D^{(\mathbf{m})}(\{e|\mathbf{R}^{\mathbf{h}}\}) = e^{-i2\pi m_i h^i/Q}. \quad (3.66)$$

The triple integer label, \mathbf{m} , has Q^3 different possible values equaling the number of inequivalent IRREPs for the finite group \mathbb{T} .

Instead of using \mathbf{m} to label the IRREPs of \mathbb{T} , one usually uses \mathbf{k} which are vectors in the reciprocal, dual, or momentum space. One can define primitive reciprocal lattice vectors (\mathbf{b}^i) in terms of the primitive lattice vectors (\mathbf{a}_i) in real space,

$$\mathbf{b}^i \cdot \mathbf{a}_j = 2\pi\delta_j^i, \quad (3.67)$$

where the 2π normalization was chosen to simplify equations that are to follow. We will label reciprocal lattice vectors as $\mathbf{G}_{\mathbf{g}}$:

$$\mathbf{G}_{\mathbf{g}} \equiv g_i \cdot \mathbf{b}^i, \quad g_i \in \mathbb{Z}. \quad (3.68)$$

The primitive reciprocal lattice vectors (PRLV) then form a basis for the dual space. We then have the following definition for the IRREPs of \mathbb{T} ,

$$D^{(\mathbf{k})}(\{e|\mathbf{R}^{\mathbf{h}}\}) = e^{-i\mathbf{k} \cdot \mathbf{R}^{\mathbf{h}}}, \quad (3.69)$$

where $\mathbf{k} = m_i \mathbf{b}^i/Q$. One can see now why the IRREP label \mathbf{k} is used as it represents the momentum of a wave in free-space²⁸.

With the above definition, and the range of the m_i used, \mathbf{k} ranges over the simplest possible unit cell of the reciprocal lattice. It is more convenient to use an alternate

²⁸Here we are using the fact that the curvature of a wave through space is its momentum. For more complex systems one must distinguish between conjugate momentum (dual) and the physical momentum carried by a wave.

definition²⁹, one in which \mathbf{k} ranges over the first Brillouin zone (IBZ). The IBZ is equivalent to the Weiner-Seitz cell in real space, except now constructed in reciprocal space.

An illustration showing the real space and reciprocal space of a 2D hexagonal photonic crystal lattice is given in Figure 3.1. The PLVs and PRLVs of a hexagonal lattice are:

$$\begin{aligned} \mathbf{a}_1 &= (a, 0) & \mathbf{a}_2 &= \left(\frac{a}{2}, \frac{\sqrt{3}a}{2}\right) \\ \mathbf{b}_1 &= \left(0, \frac{4\pi}{\sqrt{3}a}\right) & \mathbf{b}_2 &= \left(\frac{2\pi}{a}, \frac{2\pi}{\sqrt{3}a}\right) \end{aligned} \quad (3.70)$$

where a is the center to center distance between nearest neighbor holes. The high symmetry points of the IBZ are the Γ , X , and J points (see Figure 3.1(b)). The high symmetry points of the IBZ play an especially important role in defining the photonic band-gaps of periodic dielectric structures (see section 3.5).

The basis functions of the IRREPs of \mathbb{T} are called Bloch functions and will be labelled as $\psi^{(\mathbf{k})}(\mathbf{x})$,

$$P(\{e|\mathbf{R}^h\})\psi^{(\mathbf{k})}(\mathbf{x}) = \psi^{(\mathbf{k})}(\mathbf{x} - \mathbf{R}^h) = e^{-i\mathbf{k}\cdot\mathbf{R}^h}\psi^{(\mathbf{k})}(\mathbf{x}), \quad (3.71)$$

where $P(\{e|\mathbf{R}^h\})$ represents the physical operation of translation. The projection operator [70] can then be used to project an arbitrary wave function onto the Bloch functions:

$$\mathcal{P}^{(\mathbf{k})} \equiv \frac{1}{N} \sum_{\mathbf{h}} e^{+i\mathbf{k}\cdot\mathbf{R}^h} P(\{e|\mathbf{R}^h\}), \quad (3.72)$$

where $\mathcal{P}^{(\mathbf{k})}$ represents the projection operator for the \mathbf{k} -th IRREP and $N \equiv Q^3$.

²⁹ Any region which contains the same number of \mathbf{k} -vectors can be used as it conserves the number of IRREPs.

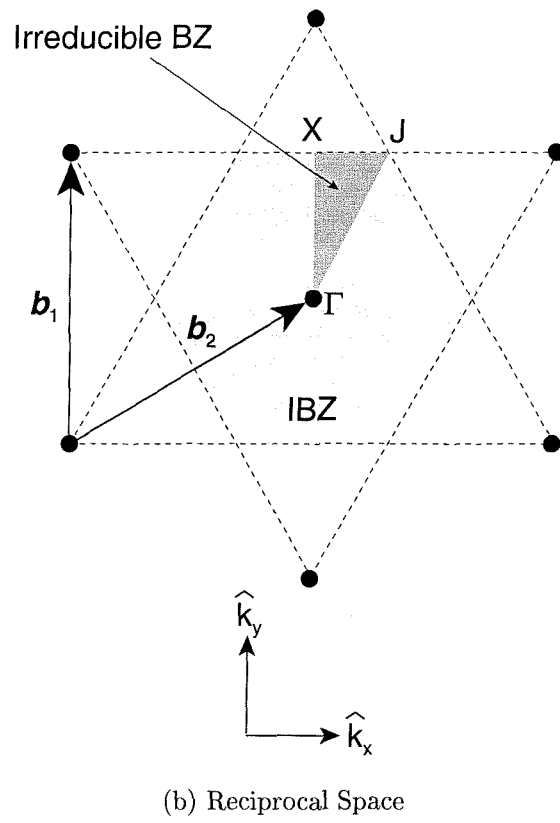
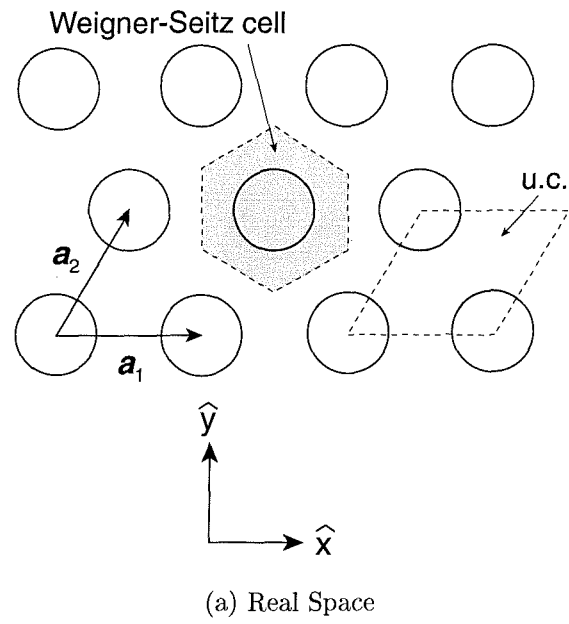


Figure 3.1: Bravais and Reciprocal lattice of a 2D hexagonal photonic crystal.

3.4.2 ★ of \mathbf{k}

In group theory one defines conjugate group elements as those elements which perform the same operation, just in different reference frames. Mathematically, if b and c are group elements of an arbitrary group \mathcal{A} , then c is conjugate to b if $c = a^{-1}ba$ for some $a \in \mathcal{G}$. One can also define a type of conjugacy amongst different representations (REPs). Specifically, if D is a REP of an invariant subgroup $\mathcal{N} \subset \mathcal{A}$, then D_a is said to be the conjugate REP to D for $D_a(b) \equiv D(a^{-1}ba)$, where $a \in \mathcal{A}$, $b \in \mathcal{N}$. Since \mathcal{N} is an invariant subgroup, D_a is also a REP of \mathcal{N} .

In our case, for space groups, $\mathcal{N} = \mathbb{T}$, $\mathcal{A} = \mathcal{R}$, and $D = D^{(\mathbf{k})}$. The REP $D_{\{d|\mathbf{t}\}}^{(\mathbf{k})}$, conjugate to $D^{(\mathbf{k})}$, has the following value:

$$\begin{aligned} D_{\{d|\mathbf{t}\}}^{(\mathbf{k})}(e|\mathbf{R}^h) &\equiv D^{(\mathbf{k})}(e|d^{-1}\mathbf{R}^h) = e^{-i\mathbf{k} \cdot (d^{-1}\mathbf{R}^h)} \\ &= e^{-i(d\mathbf{k}) \cdot \mathbf{R}^h} \\ &= e^{-i(d\mathbf{k} + \mathbf{G}_g) \cdot \mathbf{R}^h} \triangleq D^{(\mathbf{k}')} (e|\mathbf{R}^h), \end{aligned} \tag{3.73}$$

where $\mathbf{k}' = d\mathbf{k} \bmod \mathbf{G}_g$, such that $\mathbf{k}' \in \text{IBZ}$. An “orbit” of \mathbb{T} with respect to \mathcal{R} is a maximal set of inequivalent conjugate IRREPs of \mathbb{T} . The ★ of \mathbf{k} (★ \mathbf{k}) is a pictorial representation of a given orbit of \mathbb{T} , and contains all the \mathbf{k} -vectors labelling the IRREPs of the orbit:

$$\star\mathbf{k} = \{\mathbf{k}' | \mathbf{k}' = d\mathbf{k} + \mathbf{G}; d \in \mathcal{G}, \mathbf{G} \in \{\mathbf{G}_g\}\}. \tag{3.74}$$

3.4.3 The Little Group, $\mathcal{G}_\mathbf{k}$

The little group, $\mathcal{G}_\mathbf{k}$, is a subgroup of \mathcal{R} which consists of those symmetry operations which conserve $\mathbf{k} \bmod \mathbf{G}_g$:

$$\mathcal{G}_\mathbf{k} = \{\{d|\mathbf{t}\} | d\mathbf{k} = \mathbf{k} + \mathbf{G}; \{d|\mathbf{t}\} \in \mathcal{R}, \mathbf{G} \in \{\mathbf{G}_g\}\}. \tag{3.75}$$

The elements of $\mathcal{G}_{\mathbf{k}}$ yield a number of equivalent IRREPs assigned to $D^{(\mathbf{k})}$ of \mathbb{T} . The full space group can be decomposed in terms of cosets of the little group,

$$\mathcal{R} = \mathcal{G}_{\mathbf{k}} + \{d_2|\mathbf{s}_2\}\mathcal{G}_{\mathbf{k}} + \cdots + \{d_s|\mathbf{s}_s\}\mathcal{G}_{\mathbf{k}}, \quad (3.76)$$

where $\{d'_\nu|\mathbf{s}'_\nu\}$ generate the $\star\mathbf{k}$. Note that for a symmorphic group the \mathbf{s}_ν can be chosen as $\mathbf{0}$.

Group of the Wave Vector, $\mathcal{G}_{0\mathbf{k}}$

The group of the wave vector, $\mathcal{G}_{0\mathbf{k}}$, is by definition the quotient group of the little group and the invariant subgroup of translations,

$$\mathcal{G}_{0\mathbf{k}} \equiv \mathcal{G}_{\mathbf{k}}/\mathbb{T}. \quad (3.77)$$

$\mathcal{G}_{0\mathbf{k}}$ is a point symmetry group and its IRREPs ($D^{(0\mathbf{k},\alpha)}$) can be constructed from its character table³⁰.

IRREPs of $\mathcal{G}_{\mathbf{k}}$, $D^{(\mathbf{k},\alpha)}$

For symmorphic space groups \mathcal{G} and $\mathcal{G}_{0\mathbf{k}}$ are subgroups of \mathcal{R} , and thus the following semi-direct products can be formed with the invariant subgroup \mathbb{T} ,

$$\begin{aligned} \mathcal{R} &= \mathbb{T} \otimes \mathcal{G}, \\ \mathcal{G}_{\mathbf{k}} &= \mathbb{T} \otimes \mathcal{G}_{0\mathbf{k}}. \end{aligned}$$

To generate the IRREPs of $\mathcal{G}_{\mathbf{k}}$ ($D^{(\mathbf{k},\alpha)}$) we can then take the outer direct product of

³⁰See section 3.5.

the IRREPs of \mathbb{T} and $\mathcal{G}_{0\mathbf{k}}$, which since $D^{(\mathbf{k})}$ is 1-D is simply:

$$D^{(\mathbf{k},\alpha)}(d|\mathbf{R}^h) = e^{-i\mathbf{k}\cdot\mathbf{R}^h} \mathbf{1}_\alpha D^{(0\mathbf{k},\alpha)}(d), \quad (3.81)$$

where α is the dimension of the IRREP of the point group $\mathcal{G}_{0\mathbf{k}}$.

The basis functions of $D^{(\mathbf{k},\alpha)}$ are Bloch functions ($\psi^{(\mathbf{k})}(\mathbf{x})$) which consist of a plane wave component and a periodic component $\mathbf{u}_{\mathbf{k}}(\mathbf{x})$:

$$\psi^{(\mathbf{k})}(\mathbf{x}) = e^{-i\mathbf{k}\cdot\mathbf{x}} \mathbf{u}_{\mathbf{k}}(\mathbf{x}). \quad (3.82)$$

The action of the IRREP $D^{(\mathbf{k},\alpha)}(d|\mathbf{R}^h)$ on the Bloch functions can be broken down into $D^{(0\mathbf{k},\alpha)}(d)$ which rearranges the set of periodic functions $\left[\mathbf{u}_{\mathbf{k}_\alpha}(\mathbf{x})\right]$ and $e^{-i\mathbf{k}\cdot\mathbf{R}^h}$ which applies a uniform phase factor to each periodic function.

IRREPs of \mathcal{R} , $D^{(\star\mathbf{k},\alpha)}$

The IRREPs of $\mathcal{G}_{\mathbf{k}}$ only contain information about one point in the $\star\mathbf{k}$. An IRREP of \mathcal{R} involves all of the points of the $\star\mathbf{k}$ as the coset generating symmetry operations ($\{d'_\nu|s'_{nu}\}$) mix the different $\star\mathbf{k}$ points amongst each other. In order to find the IRREPs of \mathcal{R} we will use a constructive approach starting by subducing these REPs onto \mathbb{T} . This subduction takes a rather simple form reducing to s diagonal blocks of dimension α (equal to the dimension of the IRREP of $\mathcal{G}_{0\mathbf{k}}$), each with a phase factor corresponding to one point on the $\star\mathbf{k}$:

$$D^{(\star\mathbf{k},\alpha)}(e|\mathbf{R}^h) = \begin{bmatrix} \mathbf{1}_{\alpha_1} e^{-i\mathbf{k}_1\cdot\mathbf{R}^h} & & & \\ & \mathbf{1}_{\alpha_2} e^{-i\mathbf{k}_2\cdot\mathbf{R}^h} & & \\ & & \ddots & \\ & & & \mathbf{1}_{\alpha_s} e^{-i\mathbf{k}_s\cdot\mathbf{R}^h} \end{bmatrix}$$

where $\mathbf{k}_1 \equiv \mathbf{k}$, $\mathbf{k}_\nu = d'_\nu \mathbf{k}$, and $\alpha_1 = \alpha_2 = \cdots = \alpha_s =$ the dimension of the IRREP of $\mathcal{G}_{0\mathbf{k}}$. The basis functions of $D^{(\star\mathbf{k},\alpha)}$ also separate into s blocks of α Bloch functions:

$$\begin{bmatrix} \left[\begin{matrix} \psi_1^{(\mathbf{k}_1, \alpha)} \\ \vdots \\ \psi_\alpha^{(\mathbf{k}_1, \alpha)} \end{matrix} \right] \\ \left[\begin{matrix} \psi_1^{(\mathbf{k}_2, \alpha)} \\ \vdots \\ \psi_\alpha^{(\mathbf{k}_2, \alpha)} \end{matrix} \right] \\ \vdots \\ \left[\begin{matrix} \psi_1^{(\mathbf{k}_s, \alpha)} \\ \vdots \\ \psi_\alpha^{(\mathbf{k}_s, \alpha)} \end{matrix} \right] \end{bmatrix}$$

The $\{d'_\nu | \mathbf{s}'_\nu\}$ rearrange the s different blocks, and the elements of $\mathcal{G}_{\mathbf{k}}$ rearrange the elements within each block. Using these two principles we can write a simple formula for the IRREPs of \mathcal{R} :

$$D_{\mu j, \nu i}^{(\star\mathbf{k}, \alpha)}(a) = \begin{cases} D_{ji}^{(\mathbf{k}, \alpha)}(b) & \text{if } b = d'_\mu{}^{-1} a d'_\nu \in \mathcal{G}_{\mathbf{k}}, \\ 0 & \text{otherwise,} \end{cases} \quad (3.83)$$

where a is any symmetry operation of \mathcal{R} and $(\{d'_\mu | \mathbf{s}'_\mu\}, \{d'_\nu | \mathbf{s}'_\nu\})$ are the coset generators which transform \mathbf{k} within the $\star\mathbf{k}$ as follows:

$$\begin{aligned} d'_\mu \mathbf{k} &= \mathbf{k}_\mu, \\ d'_\nu \mathbf{k} &= \mathbf{k}_\nu. \end{aligned} \quad (3.84)$$

In this notation (μ, ν) label the row and column of the different $\alpha \times \alpha$ blocks within

$D^{(\star\mathbf{k},\alpha)}$, and (j, i) label the row and column within each block.

An example may help clarify this notation. Consider an arbitrary \mathbf{k} -point in the IBZ³¹. Assuming for simplicity that the point group contained within \mathcal{R} is C_2 , the $\star\mathbf{k}$ then consists of $\{\pm\mathbf{k}\}$. In this case $\mathcal{R} = \mathbb{T} \otimes \{e, C_2\}$ and $\mathcal{G}_{\mathbf{k}} = \mathbb{T} \otimes \{e\} = \mathbb{T} = \{e|\mathbf{R}^h\}$. Thus, the only possible IRREP of $\mathcal{G}_{0\mathbf{k}}$ is the identity REP (A). Since the $\star\mathbf{k}$ consists of $\pm\mathbf{k}$, the identity REPs come in pairs which have their spaces coupled through the only coset generator ($C_2|0$):

$$D^{(\star\mathbf{k},A)}(e|\mathbf{R}^h) = \begin{bmatrix} 1 \cdot e^{-i\mathbf{k} \cdot \mathbf{R}^h} & 0 \\ 0 & 1 \cdot e^{-i(-\mathbf{k}) \cdot \mathbf{R}^h} \end{bmatrix} \quad (3.85)$$

$$D^{(\star\mathbf{k},A)}(C_2|\mathbf{R}^h) = \begin{bmatrix} 0 & 1 \cdot e^{-i(\mathbf{k}) \cdot \mathbf{R}^h} \\ 1 \cdot e^{-i\mathbf{k} \cdot (-\mathbf{R}^h)} & 0 \end{bmatrix}. \quad (3.86)$$

3.4.4 Time Reversal Symmetry and Space Groups

Although the space group contains all the information regarding the spatial symmetry of a periodic structure, there are other intrinsic symmetries present in physical systems (and their mathematical theories). We have thus far neglected any possible symmetries present in time. Non-relativistic theories assume that time is independent of space, and thus the full symmetry group of the system is an outer direct product of the space group and the symmetry group of the time coordinate.³² In this picture time is homogeneous and thus translationally invariant. The resulting IRREPs of time translations are the time harmonics, $e^{i\omega t}$, where ω labels the IRREP and corresponds to the angular frequency of the field. Apart from time translations there is one other symmetry operation that one might expect to be present, that being time inversion, T [71].

³¹i.e., $\mathcal{G}_{0\mathbf{k}} = \{e\}$

³²Of course Einstein showed that time and space do not live in isolated worlds, but rather are tied together in a Minkowski space-time manifold. Relativistic systems are described by the Poincare group which contains time and space translations, spatial and temporal rotary-reflections, and a new type of operation best described as a velocity boost.

Time reversal symmetry can best be described physically as a reversal of motion [72]: if one records the dynamical evolution of a field (particle, object, etc.), and then replays the recording backwards, the resulting motion can also be described by the same set of dynamical equations. From a (scientific) observer's standpoint, both playbacks of the recording (in forward or reverse) would seem equally as physical. Mathematically one is performing an inversion in the time dimension ($t \rightarrow -t$). In order to fully understand time reversal symmetry in the context of Maxwell's equations, we must first determine how the electric and magnetic fields transform.

The transformation properties of the electric and magnetic field are formally determined by the transformation properties of the electromagnetic 4-vector potential A_μ [73]³³. Based on physical intuition alone, however, we expect under time reversal symmetry charge density to remain unchanged and current density (movement of charge) to reverse direction. Considering the effects of time reversal symmetry on an electric and magnetic dipole, we then expect the electric field to be even under time reversal and the magnetic field to be odd [66]:

$$T\mathbf{E}(\mathbf{x}, t) = \mathbf{E}(\mathbf{x}, -t), \quad (3.87)$$

$$T\mathbf{B}(\mathbf{x}, t) = -\mathbf{B}(\mathbf{x}, -t). \quad (3.88)$$

This is the representation of T on the classical real fields. The full spectrum of eigenfunctions permitted by Maxwell's equations includes complex field amplitudes from which the real fields are a special linear combination. The representation of T on the complex fields is a little more difficult to motivate, however, is essential as most spectra of the electromagnetic fields are computed using complex fields in order to take advantage of the fact that the harmonic functions are the IRREPs of

³³To describe light relativistically, one must use the concept of an electromagnetic 4-vector potential A_μ and an electromagnetic stress-energy tensor $F_{\mu\nu}$. Our analysis is done in "3+1"-space so to speak. One may question whether or not we will miss some symmetries (within our single inertial frame) because of the narrower scope of our analysis. The answer is undoubtedly yes; however, for our purposes a non-relativistic picture will be adequate.

time translations, as well as to help bridge the gap from classical to quantum fields. Consider the electric field for example³⁴:

$$\mathbf{E}(\mathbf{r}, t) = \int_0^\infty \frac{d\omega}{2\pi} \sum_{m(\omega)} \left[c_m \mathbf{E}_m(\mathbf{r}) e^{-i\omega t} + c_m^* \mathbf{E}_m^*(\mathbf{r}) e^{i\omega t} \right], \quad (3.89)$$

where $m(\omega)$ is an index into the degenerate space of modes for each frequency, and the positive and negative frequency components are combined such that E is real. The $c_{m(\omega)}$ are complex constants in the context of the classical fields; however, in quantum field theory these coefficients are upgraded to operators which act upon a Hilbert space representing the quantum states of the field. The complex spatial fields $\mathbf{E}_m(\mathbf{r}, \omega)$ are eigenfunctions of Θ_E in eq. (3.47) with eigenvalue $\lambda = (\omega/c)^2$.

As discussed earlier λ must be real and positive. It follows that the frequency ω must be real. However, the spectrum of Θ_E permits both positive and negative frequencies, $\omega = \pm c\sqrt{\lambda}$. Furthermore, since Maxwell's equations are real for real $\epsilon(\mathbf{r}, t)$, $\mathbf{E}_m(\mathbf{r}, \omega)^*$ is also an eigenfunction with frequency $\pm c\sqrt{\lambda_m}$ ³⁵. The degeneracy of \mathbf{E}_m and \mathbf{E}_m^* is a consequence of the time reversal symmetry embedded in Maxwell's equations, and is present regardless of the space group of $\epsilon(\mathbf{r})$.

The representation of the action of T on the complex spatial fields is that of complex conjugation (up to a multiplicative phase factor)³⁶:

$$T\mathbf{E}_m(\mathbf{r}) = \mathbf{E}_m^*(\mathbf{r}). \quad (3.90)$$

With this definition the action of T on the real classical fields and the action of T on

³⁴The magnetic field has a slightly different form, $\mathbf{B}(\mathbf{r}, t) = \int_0^\infty \frac{d\omega}{2\pi} \sum_{m(\omega)} -i \left[d_m \mathbf{B}_m(\mathbf{r}) e^{-i\omega t} - d_m^* \mathbf{B}_m^*(\mathbf{r}) e^{i\omega t} \right]$, in order to satisfy the time reversal relation in eq. (3.88). This makes intuitive sense as the $\text{curl}(\mathbf{B})$ is proportional to the derivative of \mathbf{E} .

³⁵To see this simply take the complex conjugate of eq. (3.47).

³⁶Similarly for the complex spatial magnetic fields.

the complex spatial fields are consistent. The consequences are also the same, namely that \mathbf{E}_m and \mathbf{E}_m^* are degenerate in frequency. Also, consider the operation of T on a plane wave:

$$T e^{-i(\mathbf{k} \cdot \mathbf{x})} = e^{-i(-\mathbf{k} \cdot \mathbf{x})}. \quad (3.91)$$

We see that the direction of motion of the plane wave has indeed been reversed ($\mathbf{k} \rightarrow -\mathbf{k}$), which is physically satisfying as we expect time reversal to correspond to a reversal of motion. However, the action of complex conjugation not only reverses the direction of each individual plane wave but also reverses the phase relationship between different plane waves³⁷. The operation of T is now nonlinear on the complex spatial fields. It is what is called anti-linear or anti-unitary [65,72,74,75]. As described below this complicates the group theoretical analysis of such a system³⁸.

In order to analyze a symmetry group which includes anti-linear operators such as complex conjugation requires the use of corepresentation theory [69,72,76]. It can be shown that the corepresentations are completely defined in terms of the normal space group representations. A simple criterion can then be used on the normal representation in order to determine any additional degeneracies that may appear in the photonic bandstructure [69]:

$$\sum_d \chi^{(\mathbf{k}, \alpha)}(\{d|\mathbf{s}\}^2) = \begin{cases} g_{o\mathbf{k}}, \\ -g_{o\mathbf{k}}, \\ 0, \end{cases} \quad (3.92)$$

³⁷The simple replacement of \mathbf{k} with $-\mathbf{k}$ actually corresponds to the parity operation, or spatial inversion.

³⁸Why do we need the added complication of complex conjugation? The answer lies in the underpinnings of quantum mechanics, and experimental verification of such a symmetry. It was E. P. Wigner who first attributed the added degeneracy present in the experiments of H. A. Kramers to the time inversion symmetry present in the Schrödinger equation [72].

where $\{d|\mathbf{s}\}$ are all the elements of \mathcal{R}/\mathcal{T} for which $d\mathbf{k} = -\mathbf{k} + \mathbf{G}_{\mathbf{g}}$, $g_{0\mathbf{k}}$ is the order of $\mathcal{G}_{0\mathbf{k}}$, and $\chi^{(\mathbf{k},\alpha)}(\{d|\mathbf{s}\}^2)$ is the character of the IRREP being tested. If the sum equals $g_{0\mathbf{k}}$, then there is not an additional degeneracy due to T , whereas if the sum is $-g_{0\mathbf{k}}$ or 0, then there is. This test, in the case of representations of the electromagnetic field, is equivalent to a test for the reality of the normal IRREPs.

Regardless of the outcome of the above test, if there is time reversal symmetry present then the spectrum at \mathbf{k} and $-\mathbf{k}$ are degenerate. The complication occurs if $-\mathbf{k}$ is already a member of the $\star\mathbf{k}$ and this degeneracy has already been captured by the normal IRREPs. In this case it is possible that additional degeneracies are formed between the normal IRREPs by the presence of time reversal symmetry. It is interesting to note that for the same Bravais lattice that electrons and photons may have different degeneracies due to time reversal symmetry. This is because of the spin of the electron.

3.5 Localized Defect Modes: Point Groups

Using group theoretical techniques one can use the symmetry of the optical cavity to categorize the eigenmodes of the electromagnetic field [77]. The optical microcavity of interest here is composed of a thin slab dielectric surrounded by air and patterned with a 2D hexagonal array of holes. A defect is created by changing the dielectric constant in a small region of space in hopes of trapping light within the defect region. This can be achieved in practice by varying the radius of the central hole, or by removing a hole entirely and varying the nearest neighbor holes. An illustration of the 3D cavity is shown in Figure 1.1. A cross-section of the cavity through the middle of the thin dielectric slab is shown schematically in Figure 4.8.

For a 2D photonic crystal (without the vertical waveguiding), the point group symmetry of the hexagonal photonic crystal is D_{6h} . The eigenmodes of the structure can be separated into TE and TM modes, as shown in the character table in Table 3.1. Focusing only on the TE modes, the point group symmetry of the system can be reduced to $C_{6v}=D_{6h}/\sigma_h$.

In the full 3D cavity the point group of the system is also D_{6h} ; however, the horizontal mirror plane, σ_h , lies in the middle of the dielectric slab. The eigenmodes of the system are characterized by TE-like and TM-like modes. TE-like modes are even under the mirror operation, whereas TM-like modes are odd. The cavity modes are not purely TE or TM polarized as in the 2D case. For both the 2D and 3D simulations, the defect modes can be classified by their TE-like or TM-like character and the irreducible representations (IRREPS) of the point group of the defect region and surrounding lattice.

The rules of group theory described above can be used quite successfully in describing the resonant modes of structures such as the photonic crystal defect cavity lasers studied in this thesis. A simple two step process may be employed to find approximate forms for localized optical modes of defects within periodic dielectric structures. For the patterned slab waveguide designs studied here, one begins with the guided modes of an unperturbed homogeneous slab waveguide. For a single mode waveguide the system reduces approximately to a two-dimensional system in which only the fundamental waveguide modes are of interest³⁹. In this case, the fundamental waveguide modes may be defined approximately by a scalar field, TE-like guided modes (with their electric field predominantly in the plane of the slab waveguide) being defined by B_z and TM-like guided modes being defined by E_z ⁴⁰. In what follows we concentrate solely on TE-like guided modes as it will be shown in chapter 4 that it is for these modes which a photonic band-gap forms.

In Figure 3.1 the reciprocal lattice vectors of a hexagonal Bravais lattice are shown. The primitive reciprocal lattice vectors are $\mathbf{b}_1 = (0, \frac{4\pi}{\sqrt{3}a})$, and $\mathbf{b}_2 = (\frac{2\pi}{a}, \frac{2\pi}{\sqrt{3}a})$. The high symmetry points of the IBZ are the six X -points,

³⁹Single-mode conditions depend on the wavelength of light, which in this case depends on the period of the patterning to be applied to the slab waveguide. It is thus the ratio of slab thickness to photonic crystal lattice (d/a) which determines whether or not the waveguide can be treated as an effective 2D system.

⁴⁰This approximation only works well in the middle of highly symmetric slab waveguides for the fundamental guided modes.

Table 3.1: D_{6h} character table.

$D_{6h} = C_{6v} \times \sigma_h$		E	C_2	$2C_3$	$2C_6$	$3\sigma_d$	$3\sigma_v$	$\{E$	C_2	$2C_3$	$2C_6$	$3\sigma_d$	$3\sigma_v\}$	$\times \sigma_h$
z	A_1^{TE}	1	1	1	1	1	1	1	1	1	1	1	1	
R_z	A_2^{TE}	1	1	1	1	-1	-1	1	1	1	1	-1	-1	
	B_1^{TE}	1	-1	1	-1	-1	1	1	-1	1	-1	-1	1	
	B_2^{TE}	1	-1	1	-1	1	-1	1	-1	1	-1	1	-1	
(x, y)	E_1^{TE}	2	-2	-1	1	0	0	2	-2	-1	1	0	0	
(R_x, R_y)	E_2^{TE}	2	2	-1	-1	0	0	2	2	-1	-1	0	0	
z	A_1^{TM}	1	1	1	1	1	1	-1	-1	-1	-1	-1	-1	
R_z	A_2^{TM}	1	1	1	1	-1	-1	-1	-1	-1	-1	1	1	
	B_1^{TM}	1	-1	1	-1	-1	1	-1	1	-1	1	1	-1	
	B_2^{TM}	1	-1	1	-1	1	-1	-1	1	-1	1	-1	1	
(x, y)	E_1^{TM}	2	-2	-1	1	0	0	-2	2	1	-1	0	0	
(R_x, R_y)	E_2^{TM}	2	2	-1	-1	0	0	-2	-2	1	1	0	0	

$$\{\pm(0, 1)k_X, \pm(\sqrt{3}/2, 1/2)k_X, \pm(\sqrt{3}/2, -1/2)k_X\}, \quad (3.93)$$

$$k_X = \frac{2\pi}{\sqrt{3}a}, \quad (3.94)$$

the six J -points,

$$\{\pm(1/2, \sqrt{3}/2)k_J, \pm(1/2, -\sqrt{3}/2)k_J, \pm(-1, 0)k_J\}, \quad (3.95)$$

$$k_J = \frac{4\pi}{3a}, \quad (3.96)$$

and the Γ -point=(0, 0). The six different (all degenerate) X and J points in the IBZ are labelled with an index i as shown in Figure 3.5. The point symmetry group of the group of the wave vector at the X , J , and Γ high symmetry points are C_{2v} , C_{3v} , and C_{6v} respectively. Character tables for these groups are given in Tables 3.2, 3.3, and 3.4.

Upon patterning the slab waveguide, coupling occurs between waveguide modes

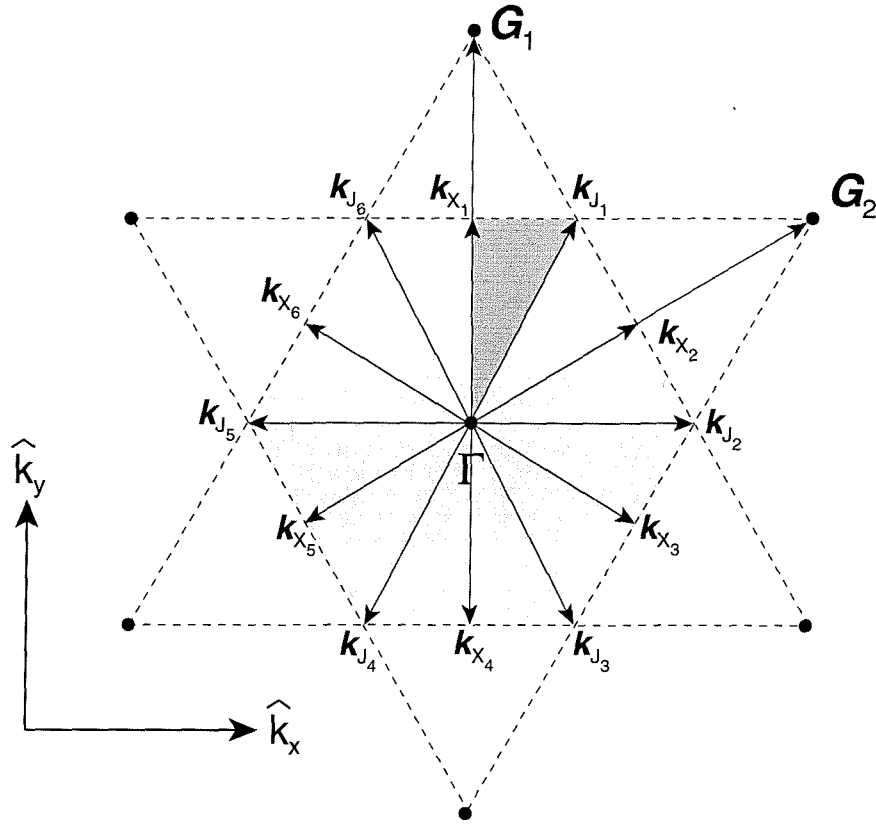


Figure 3.2: IBZ of the hexagonal lattice showing the indexing used to identify the different X and J points.

Table 3.2: C_{2v} character table.

$C_{2v}(2mm)$			E	C_2	σ_v	σ'_v
x^2, y^2, z^2	z	A_1	1	1	1	1
xy	R_z	A_2	1	1	-1	-1
xz	R_y, x	B_1	1	-1	1	-1
yz	R_x, y	B_2	1	-1	-1	1
		S_{X_1}	2	0	-2	0

Table 3.3: C_{3v} character table.

$C_{3v}(3m)$			E	$2C_3$	$3\sigma_d$
$x^2 + y^2, z^2$	z	A_1	1	1	1
	R_z	A_2	1	1	-1
$(x^2 - y^2, xy)$	(x, y)	E	2	-1	0
(xz, yz)	(R_x, R_y)				
		S_{J_1}	3	0	-1

Table 3.4: C_{6v} character table

$C_{6v}(6mm)$			E	C_2	$2C_3$	$2C_6$	$3\sigma_d$	$3\sigma_v$
$x^2 + y^2, z^2$	z	A_1	1	1	1	1	1	1
	R_z	A_2	1	1	1	1	-1	-1
		B_1	1	-1	1	-1	-1	1
		B_2	1	-1	1	-1	1	-1
(xz, yz)	$\{(x, y), (R_x, R_y)\}$	E_1	2	-2	-1	1	0	0
$(x^2 - y^2, xy)$		E_2	2	2	-1	-1	0	0
		S_{CB_X}	3	-3	0	0	1	-1
		S_{VB_J}	2	0	2	0	-2	0

with similar unperturbed frequencies and similar propagation constants modulo \mathbf{G} , where \mathbf{G} is a reciprocal lattice vector. Using group theory we can find simple expression for the eigenmodes of the patterned slab waveguide in terms of the unperturbed waveguide modes.

3.5.1 X-point

From Bloch's theorem (see eq. (3.82)) we know the eigenmodes at the X -point of a hexagonal photonic crystal must be the product of a periodic function and a plane wave with momentum \mathbf{k}_X . In the photonic crystal structures studied here, we are interested in wavelengths near the first order band-gap. These wavelengths correspond to the lowest frequency modes at the X -point which in the unperturbed waveguide have a frequency,

$$\omega_o^X \approx \frac{c}{n_{eff}} |\mathbf{k}_X| = \frac{c}{n_{eff}} \frac{2\pi}{\sqrt{3}a}, \quad (3.97)$$

where the guided mode has an effective index n_{eff} , and an approximate scalar field given by⁴¹, $\mathbf{B} = \hat{z}e^{-i\mathbf{k}_{X_1} \cdot \mathbf{r}}$. A symmetry basis for the IRREPs of the little group of \mathbf{k}_{X_1} ($\mathcal{G}_{\mathbf{k}_{X_1}}$) can be generated by applying all elements of the group of the wave vector at the X -point, $\mathcal{G}_{o\mathbf{k}_X} = C_{2v}$, to the seed vector \mathbf{k}_{X_1} :

$$X_1 = \begin{pmatrix} \mathbf{k}_{X_1} \\ -\mathbf{k}_{X_1} \end{pmatrix}, \quad (3.98)$$

where \mathbf{k}_{X_1} represents the magnetic field mode $\mathbf{B} = \hat{z}e^{-i\mathbf{k}_{X_1} \cdot \mathbf{r}}$. This method of obtaining the symmetry basis is equivalent to taking the unperturbed band diagram of the waveguide modes, folding it within the IBZ, and then constructing the basis from modes which lie on the same point in the folded band-diagram.

⁴¹More accurately a guided mode with propagation constant equal to \mathbf{k}_X .

X_1 must now be decomposed into the IRREP spaces of $\mathcal{G}_{\mathbf{k}_{X_1}}$, which is equivalent to decomposing them onto the IRREP spaces of $\mathcal{G}_{o\mathbf{k}_X}$. A matrix representation, S_{X_1} , of the transformation of the X_1 basis under the operations of C_{2v} is generated by using the transformation properties in reciprocal space of the plane wave \mathbf{k} -vectors. The character values of the S_{X_1} representation are shown in Table 3.2 from which one obtains $S_{X_1} = A_2 \oplus B_1$. Using the projection operator for the α IRREP [70],

$$\mathcal{P}_{ij}^\alpha = \frac{l_\alpha}{h} \sum_R D^\alpha(R)_{ij}^* S_{X_1}(R), \quad (3.99)$$

one can project X_1 onto the A_2 and B_1 spaces⁴². The degenerate symmetry basis of X_1 is thus found to split into two non-degenerate modes after patterning of the slab waveguide:

$$\mathbf{B}_{A_2}^{X_1} \propto \hat{z} \cos(\mathbf{k}_{X_1} \cdot \mathbf{r}), \quad (3.100)$$

$$\mathbf{B}_{B_1}^{X_1} \propto \hat{z} \sin(\mathbf{k}_{X_1} \cdot \mathbf{r}). \quad (3.101)$$

Considering that the dielectric structure, as defined here, has a low index air hole at the origin, then $\mathbf{B}_{A_2}^{X_1}$ correspond to the “valence” band mode and $\mathbf{B}_{B_1}^{X_1}$ to the “conduction” band mode. This follows as in general the maxima of the electric and magnetic field tend to be spatially offset from each other and the lower frequency modes tend to reside in regions of high dielectric constant [40].

We are not done yet as we must include all of modes of the $\star\mathbf{k}$ in order to fully define the modes at the X -point. The other two sets of modes can be generated from $(\mathbf{B}_{A_2}^{X_1}, \mathbf{B}_{B_1}^{X_1})$ by simply using the coset generators of the full point group, C_{6v} . The result is the following set of degenerate valence band modes,

⁴²Here $D^\alpha(R)$ is the representation of the α IRREP for the symmetry operation R and $S_{X_1}(R)$ is the representation of R on X_1 .

$$VB_{A_2}^X \propto \begin{pmatrix} \hat{z} \cos(\mathbf{k}_{X_1} \cdot \mathbf{r}) \\ \hat{z} \cos(\mathbf{k}_{X_2} \cdot \mathbf{r}) \\ \hat{z} \cos(\mathbf{k}_{X_3} \cdot \mathbf{r}) \end{pmatrix}, \quad (3.102)$$

and degenerate conduction band modes,

$$CB_{B_1}^X \propto \begin{pmatrix} \hat{z} \sin(\mathbf{k}_{X_1} \cdot \mathbf{r}) \\ \hat{z} \sin(\mathbf{k}_{X_2} \cdot \mathbf{r}) \\ \hat{z} \sin(\mathbf{k}_{X_3} \cdot \mathbf{r}) \end{pmatrix}, \quad (3.103)$$

at the X -point of a hexagonally patterned waveguide. These degenerate sets of modes will be used in what follows to generate approximate forms for localized modes which form when defects are introduced into the periodic photonic crystal.

3.5.2 J-point

A similar procedure may be performed in order to determine approximate forms for the TE-like valence and conduction band modes at the J -point of IBZ. At the J point,

$$\omega_o^J \approx \frac{c}{n_{eff}} |\mathbf{k}_J| = \frac{c}{n_{eff}} \frac{4\pi}{3a}, \quad (3.104)$$

for the lowest frequency unperturbed waveguide modes at the J point. The group of the wave vector at the J -point is C_{3v} . The symmetry basis for the little group at the J_1 -point can be determined just as in the previous section, however, using the seed vector \mathbf{k}_{J_1} :

$$J_1 = \begin{pmatrix} \mathbf{k}_{J_1} \\ \mathbf{k}_{J_3} \\ \mathbf{k}_{J_5} \end{pmatrix}, \quad (3.105)$$

where again \mathbf{k}_{J_i} is meant to represent the plane wave mode, $\mathbf{B} = \hat{z}e^{-i\mathbf{k}_{J_i}\cdot\mathbf{r}}$. The character of the representation (S_{J_1}) of J_1 on the C_{3v} symmetry group is given in Table 3.3. From the C_{3v} character table we get $S_{J_1} = A_2 \oplus E$. Using the projection operator on \mathbf{k}_{J_1} we get the following new basis functions for the IRREPs of A_2 and E :

$$\mathbf{B}_{A_2}^{J_1} \propto \hat{z}(e^{-i\mathbf{k}_{J_1}\cdot\mathbf{r}} + e^{-i\mathbf{k}_{J_3}\cdot\mathbf{r}} + e^{-i\mathbf{k}_{J_5}\cdot\mathbf{r}}), \quad (3.106)$$

$$\mathbf{B}_{E,1}^{J_1} \propto \hat{z}(e^{-i\mathbf{k}_{J_1}\cdot\mathbf{r}} + e^{-i\mathbf{k}_{J_3}\cdot\mathbf{r}} - 2e^{-i\mathbf{k}_{J_5}\cdot\mathbf{r}}), \quad (3.107)$$

$$\mathbf{B}_{E,2}^{J_1} \propto \hat{z}(e^{-i\mathbf{k}_{J_1}\cdot\mathbf{r}} - e^{-i\mathbf{k}_{J_3}\cdot\mathbf{r}}). \quad (3.108)$$

$\mathbf{B}_{A_2}^{J_1}$ has a maxima at the origin while $(\mathbf{B}_{E,1}^{J_1}, \mathbf{B}_{E,2}^{J_1})$ are zero. Using a similar argument to that in the previous section, the modes of the A_2 IRREP are valence band modes, lying lower in frequency than the IRREP E conduction band modes. The $\star\mathbf{k}_{J_1}$ also includes $(\mathbf{k}_{J_2}, \mathbf{k}_{J_4}, \mathbf{k}_{J_6})$. The additional valence band-edge and conduction band-edge modes can be generated by using the coset generator (C_6 rotation):

$$VB_{A_2}^J \propto \hat{z} \begin{pmatrix} e^{-i\mathbf{k}_{J_1}\cdot\mathbf{r}} + e^{-i\mathbf{k}_{J_3}\cdot\mathbf{r}} + e^{-i\mathbf{k}_{J_5}\cdot\mathbf{r}} \\ e^{-i\mathbf{k}_{J_2}\cdot\mathbf{r}} + e^{-i\mathbf{k}_{J_4}\cdot\mathbf{r}} + e^{-i\mathbf{k}_{J_6}\cdot\mathbf{r}} \end{pmatrix}, \quad (3.109)$$

$$CB_E^J \propto \hat{z} \begin{pmatrix} e^{-i\mathbf{k}_{J_1} \cdot \mathbf{r}} + e^{-i\mathbf{k}_{J_3} \cdot \mathbf{r}} - 2e^{-i\mathbf{k}_{J_5} \cdot \mathbf{r}} \\ e^{-i\mathbf{k}_{J_1} \cdot \mathbf{r}} - e^{-i\mathbf{k}_{J_3} \cdot \mathbf{r}} \\ e^{-i\mathbf{k}_{J_2} \cdot \mathbf{r}} + e^{-i\mathbf{k}_{J_4} \cdot \mathbf{r}} - 2e^{-i\mathbf{k}_{J_6} \cdot \mathbf{r}} \\ e^{-i\mathbf{k}_{J_2} \cdot \mathbf{r}} - e^{-i\mathbf{k}_{J_4} \cdot \mathbf{r}} \end{pmatrix}. \quad (3.110)$$

3.5.3 Conduction Band Donor Modes

By perturbing the dielectric constant in a small region of a periodic photonic crystal lattice, one mixes the Bloch modes of the lattice and localized defect modes can form. If the perturbation corresponds to a local increase in the dielectric constant, then the localized modes are formed predominantly from the conduction band modes, specifically the modes at the band-edge. This is a result of the fact that optical mode frequencies decrease with an increasing in the dielectric constant [40], thus the conduction band-edge modes are “pulled” into the band-gap of the photonic crystal near the defect resulting in a localized state. These type of localized modes will be termed donor modes in analogy to the electronic defect states in crystalline materials.

For the hexagonal lattice used in the laser cavities studied in this thesis, the minimum in the conduction band occurs at the X -point (see section 4.2 of chapter 4). Therefore, the appropriate symmetry basis to use for describing localized donor modes is the degenerate conduction band-edge modes of section 3.5.1, $CB_{B_1}^X$. The simplest defect is that of a single missing air hole in the photonic lattice. By removing a hole we have destroyed the translational symmetry of the photonic lattice and are left with the point group, C_{6v} .⁴³

The matrix representation of $CB_{B_1}^X$ under the operations of C_{6v} is labelled S_{CB_X} and its characters are shown in Table 3.4. From the C_{6v} character table we find that $S_{CB_X} = E_1 \oplus B_1$. Using the projection operators on $CB_{B_1}^X$, the basis functions for E_1 and B_1 look as follows:

⁴³Again, we focus only on the fundamental TE-like modes of the patterned slab waveguide which allows us to use C_{6v} as opposed to the full point group D_{6h} .

$$\mathbf{B}_{B_1}^d \propto \hat{z} \left(\sin(\mathbf{k}_{X_1} \cdot \mathbf{r}) - \sin(\mathbf{k}_{X_2} \cdot \mathbf{r}) + \sin(\mathbf{k}_{X_3} \cdot \mathbf{r}) \right), \quad (3.111)$$

$$\mathbf{B}_{E_{1,1}}^d \propto \hat{z} \left(\frac{5}{2} \sin(\mathbf{k}_{X_1} \cdot \mathbf{r}) + \sin(\mathbf{k}_{X_2} \cdot \mathbf{r}) - \sin(\mathbf{k}_{X_3} \cdot \mathbf{r}) \right), \quad (3.112)$$

$$\mathbf{B}_{E_{1,2}}^d \propto \hat{z} \left(\sin(\mathbf{k}_{X_2} \cdot \mathbf{r}) + \sin(\mathbf{k}_{X_3} \cdot \mathbf{r}) \right). \quad (3.113)$$

The B_1 donor mode transforms like a hexapole, whereas the degenerate E_1 modes transform as an (x, y) -dipole pair. The dipole pair provide a very good description of the deep donor pair of modes found using numerical FDTD simulations in chapter 4. $\mathbf{B}_{E_{1,1}}^d$ represents the y -dipole mode and $\mathbf{B}_{E_{1,2}}^d$ the x -dipole. Even the subtle difference in the in-plane radiation pattern of the (x, y) -dipole modes (see Figure 4.14) is contained within this simple description as can be seen by the lack of a third standing wave component in the y -dipole ($\mathbf{B}_{E_{1,2}}^d$) mode.

3.5.4 Valence Band Acceptor Modes

If instead of increasing the dielectric constant locally we had reduced it, by enlarging an air hole for instance, then instead of pulling the conduction band modes down into the photonic crystal band-gap we would have “pushed” valence band modes up into the band-gap. Modes localized to the defect region would then be formed predominantly from mixtures of Bloch modes from the valence band-edge. These type of defect modes are termed acceptor modes, again in analogy to the electronic states in a crystal. For the hexagonal lattice the maximum of the valence band occurs at the J -point (see Figure 4.3). As in the previous section the obvious symmetry basis to use to describe the acceptor modes is the degenerate valence band modes at the J -point generated in section 3.5.2, $VB_{A_2}^J$.

The simplest type of acceptor defect region consists of an enlargement of a single hole in the photonic lattice. This type of defect maintains the point group symmetry of the lattice, C_{6v} . The characters of the representation (S_{VB_J}) of $VB_{A_2}^J$ on C_{6v} is given in Table 3.4, from which the decomposition $S_{VB_J} = E_2 \oplus A_2$ is evident. Using

the projection operators the basis function of $VB_{A_2}^J$ are coupled together to form the following localized acceptor modes:

$$\mathbf{B}_{A_2}^a \propto \hat{z} \left(\cos(\mathbf{k}_{J_1} \cdot \mathbf{r}) + \cos(\mathbf{k}_{J_2} \cdot \mathbf{r}) + \cos(\mathbf{k}_{J_3} \cdot \mathbf{r}) \right), \quad (3.114)$$

$$\mathbf{B}_{B_2}^a \propto \hat{z} \left(\sin(\mathbf{k}_{J_1} \cdot \mathbf{r}) + \sin(\mathbf{k}_{J_3} \cdot \mathbf{r}) + \sin(\mathbf{k}_{J_5} \cdot \mathbf{r}) \right). \quad (3.115)$$

As will be seen in chapter 4 and 6, this simple formalism accurately predicts the type of localized modes which initially form, and provides a good description of the basic properties of the localized acceptor and donor modes found numerically and experimentally. Also, by using compatibility relations between IRREPs of different point groups, one can predict what splittings may occur under certain changes in the defect geometry. This is extremely helpful in labelling the resonant modes found experimentally as described in chapter 6.

Chapter 4 Numerical Electromagnetic Design of Photonic Crystal Defect Cavities

In this chapter numerical methods such as finite-difference time-domain [78] (FDTD) are used to design and accurately determine the properties of localized modes of defects within two-dimensional photonic crystal slab waveguides. Initially the guided modes of the unperturbed two-dimensionally patterned waveguide are analyzed in order to study the guided mode band-gap that forms. Three-dimensional FDTD is then used to study the radiation pattern, losses, and polarization of localized defect modes which form in defect cavities of various geometries. In the first part of this chapter the properties of the highly localized deep donor dipole-like modes are studied. In the second half of the chapter a more practical analysis is performed in which the fabrication limitations are included in the cavity design. This more careful analysis provides a clear understanding of many of the features seen in the photoluminescence measurements described in chapter 6.

4.1 Effective 2D Photonic Crystal Waveguide Analysis

In this section we analyze the in-plane properties of a 2D photonic crystal formed from a hexagonal pattern of air holes. This lattice has been shown to have a significant band-gap for TE (in-plane) polarized modes [40]. The lattice also has a significant filling fraction of material which will be shown to be important in the following sections. We begin the analysis with a 2D band-structure calculation to determine the dispersion properties of the lattice and its birefringence. The effects

of vertical guiding on the photonic crystal modes are approximated by replacing the slab material refractive index with an effective refractive index [64] of propagation for the fundamental guided slab mode.

The properties of the 2D hexagonal photonic crystal are determined by the inter-hole spacing, a , the ratio of the radius of the air holes to the spacing, r/a , and the refractive index of the material, n_{slab} . The ratio r/a affects the size of the TE and TM band-gaps; larger band-gaps for larger r/a . Also, as the r/a ratio is increased the frequencies of the photonic crystal modes tend to rise due to the larger air fraction and resulting lower average index [40]. In the 2D calculations we take r/a equal to 0.3, chosen conservatively to provide a reasonable TE mode band-gap while not reducing the material filling fraction too significantly.

The actual photonic crystal structures are fabricated in a 211 nm thick slab of InGaAsP material which has a refractive index of roughly 3.4 at a wavelength of $1.55\mu\text{m}$ [79]. Calculations of the fundamental TE and TM slab (no perforations) waveguide modes are shown in Figures 4.1 and 4.2. The slab waveguide effective index is 2.65 and 1.415 for the fundamental TE and TM guided mode of the half-wavelength thick slab, respectively. This effective index is used as the refractive index of the slab in order to approximate the effects of vertical guiding on the photonic crystal modes¹.

A dispersion diagram showing normalized frequency versus in-plane wave vector for TE and TM modes of the infinitely periodic, defect free, 2D photonic crystal is given in Figures 4.3 and 4.4, respectively. The band-structure calculation was performed using the plane-wave expansion method [80]. As Maxwell's equations scale with size, a normalized frequency, a/λ_o , is used, where λ_o is the wavelength in air. The band-diagrams show a frequency band-gap for TE polarized modes, but no gap for TM modes with this refractive index contrast and relatively small r/a . As a result, the TM modes, in general, will not be well localized by the photonic crystal.

In analogy to the electron energy bands in semiconductors, the terms “valence”

¹Of course the different photonic crystal modes will overlap the high index regions of the perforated slab differently. This, and polarization mixing, are neglected in the effective two-dimensional model.

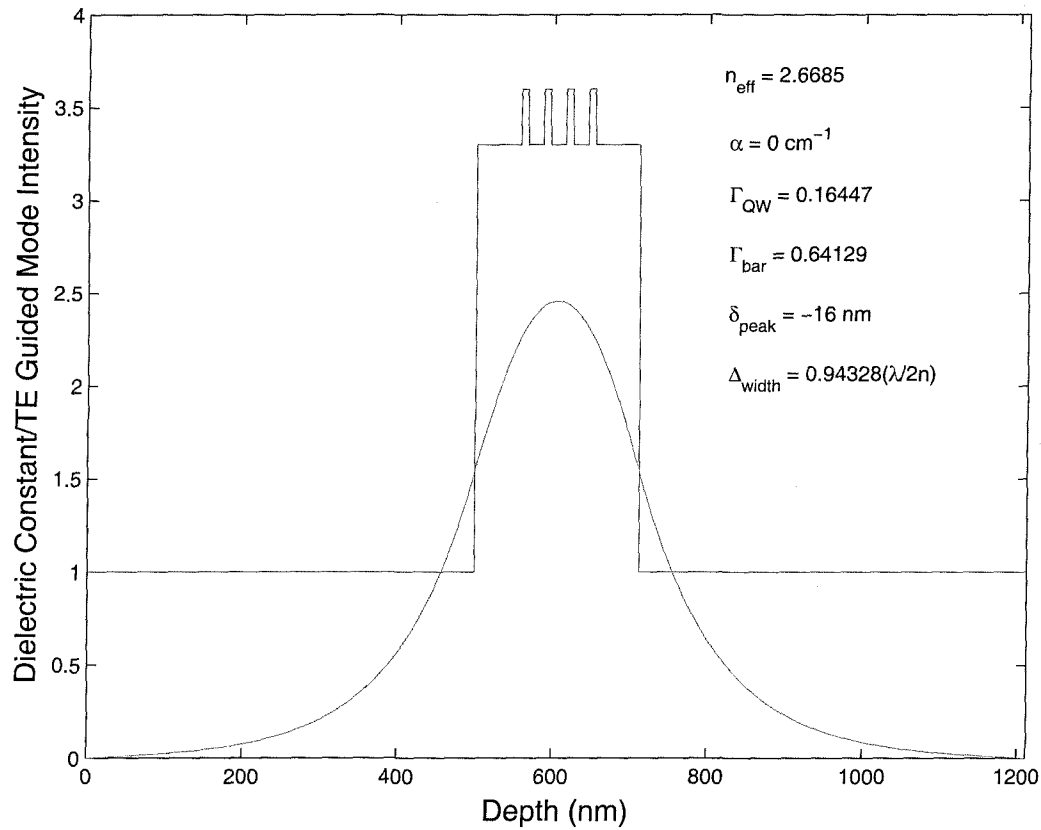


Figure 4.1: Intensity plot of the fundamental TE guided mode at $1.55 \mu\text{m}$ for a 211 nm dielectric slab of refractive index 3.4 surrounded by air cladding. The fundamental TE mode effective index (2.67) is used in the 2D bandstructure calculations for TE polarized light.

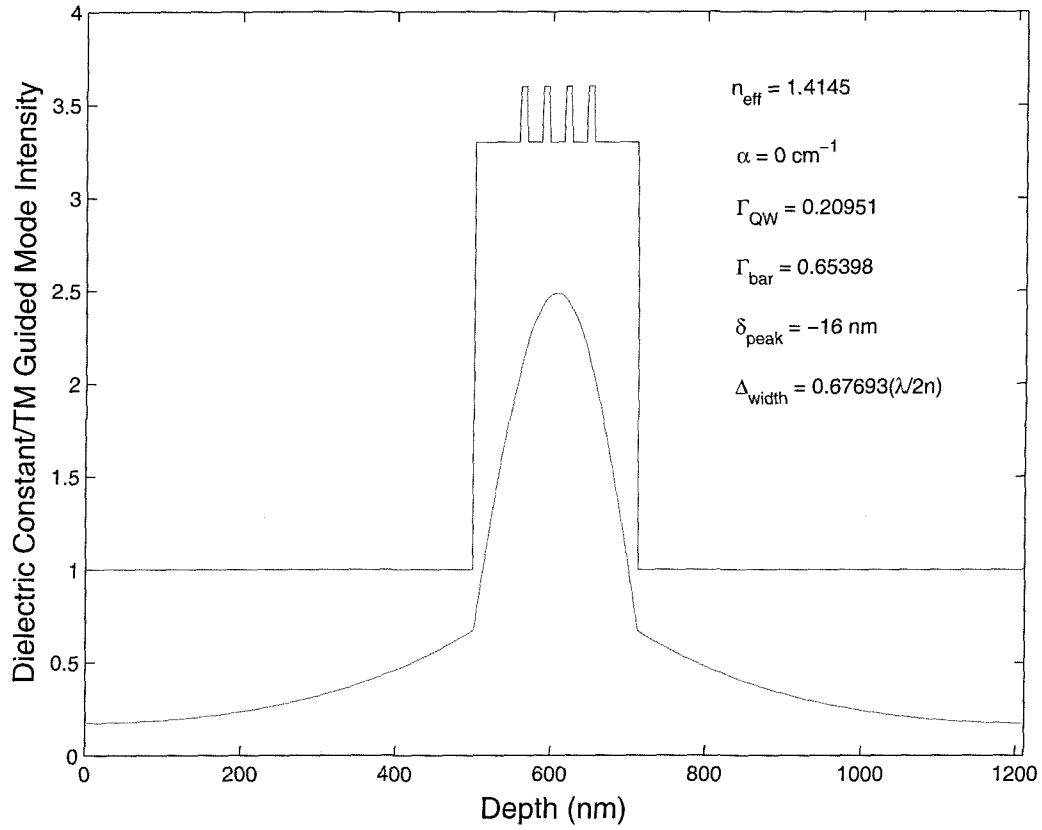


Figure 4.2: Intensity plot of the fundamental TM guided mode at $1.55 \mu\text{m}$ for a 211 nm dielectric slab of refractive index 3.4 surrounded by air cladding. The fundamental TM mode effective index (1.415) is used in 2D bandstructure calculations for TM polarized light.

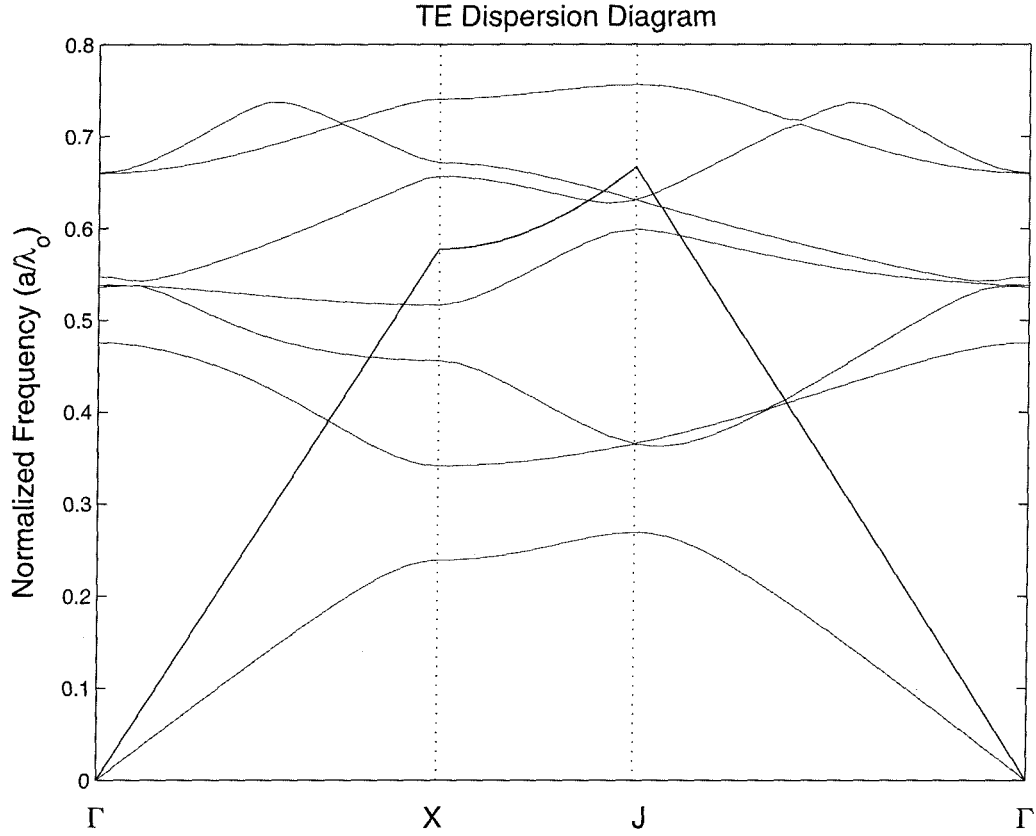


Figure 4.3: Band diagram for TE polarized light (E-field polarized in plane). The holes have a refractive index, $n_{air} = 1$. The dielectric has an index, $n_{eff}^{TE} = 2.65$, representing the fundamental TE mode effective index of an air clad 211 nm slab waveguide at a wavelength of $1.55 \mu m$. The radius of the holes is defined by the ratio $r/a=0.3$. The resulting in-plane TE band-gap extends between a normalized frequency, $\Delta\omega_{gap} = a/\lambda_o = 0.28 - 0.35$. The air (cladding) light line is also shown as a solid black line.

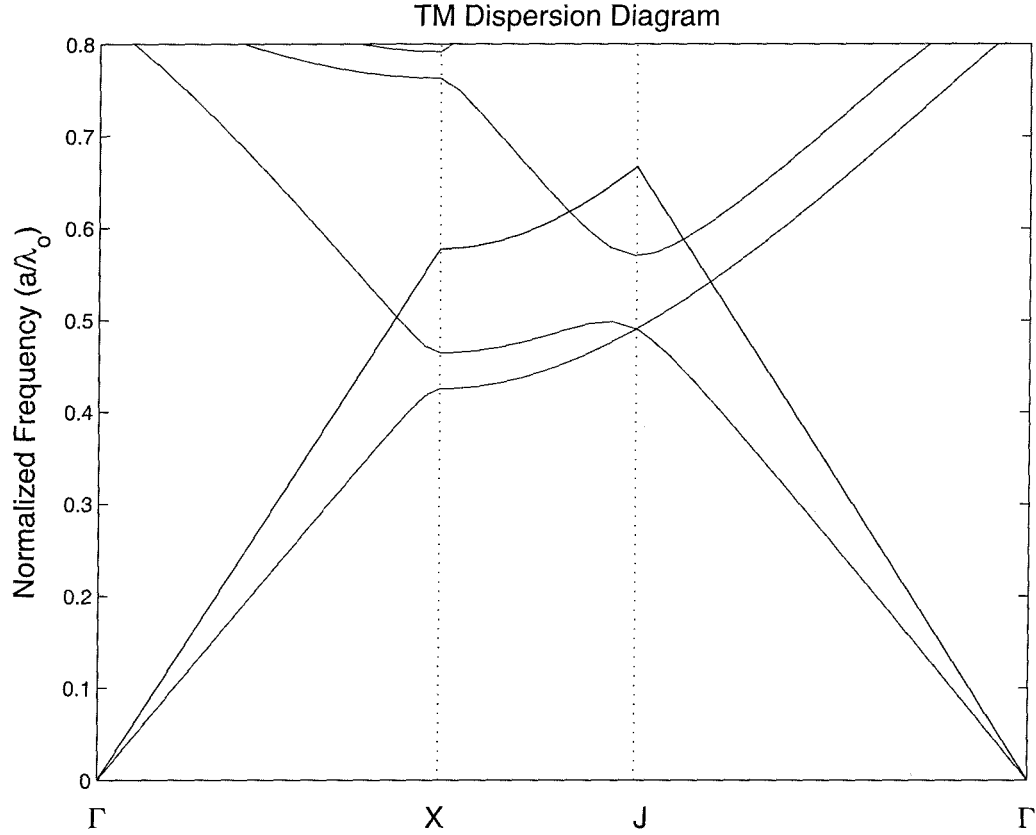


Figure 4.4: Band diagram for TM polarized light (E-field polarized in \hat{z} -direction). The dielectric has an index, $n_{eff}^{TM} = 1.415$, representing the fundamental TM mode effective index of an air clad 211 nm slab waveguide at a wavelength of $1.55 \mu m$. In this case the index contrast and r/a are not large enough to open a full 2D band-gap between the first (“valence”) and second (“conduction”) bands. The air (cladding) light line is also shown as a solid black line.

and “conduction” are used to describe the lower and upper frequency bands defining a photonic band-gap, respectively. The “valence” band-edge for the hexagonal lattice occurs at the J-point² and the conduction band-edge occurs at the X-point in reciprocal space. The symmetry of the band-edge points and the curvature of each band at the band-edge plays an important role in determining the types of modes which become localized to defects in the photonic lattice. This is discussed more fully in chapter 3.

4.2 3D FDTD Bandstructure Calculations of 2D Photonic Crystal Waveguide Structures

In the previous section the 2D photonic crystal was formed from infinitely long air holes in an infinitely thick dielectric slab. Here we shrink the dielectric slab to a thickness on the order of the wavelength of light, thus providing a high degree of localization in the vertical direction. The properties of the 2D photonic crystal are still determined by a , r/a , and n_{slab} , but now the finite slab thickness mixes TE and TM polarizations.

In the 3D structure one does not have purely TE or TM modes as in the effective 2D model, but rather TE-like and TM-like modes. The TE-like and TM-like modes are classified by how they transform under the horizontal mirror operation in the middle of the dielectric slab. TE-like modes are even under reflection and TM-like modes are odd. A 3D FDTD simulation is used to accurately model the finite slab photonic crystal waveguide. By applying appropriate Bloch boundary conditions over a unit cell of the photonic crystal, one may obtain the spectral response for a given wave vector. The peaks in the frequency spectrum give the eigenmodes of the photonic crystal at the k -vector determined by the boundary conditions. The interested reader is referred to the paper by Chan et al. [81] for further details. In

²See sub-section 3.5. The symmetries of the photonic crystal band-edge modes are described in chapter 3.

our case, the unit cell consists of an in-plane geometry given by the two-dimensional unit cell of the hexagonal lattice. In the \hat{z} -direction we do not have periodicity so a full description of the slab and surrounding air must be given. The Bloch boundary condition is applied to all four sides normal to plane of the slab, and Mur's absorbing boundary condition [82] is applied to the top boundary. For TE-like modes an even mirror reflection at the middle of the slab is applied, whereas for the TM-like modes an odd mirror symmetry is used. A plot of normalized frequency versus in-plane momentum for the even and odd modes is given in Figure 4.5. The effective 2D dispersion diagrams of the previous section correspond extremely well with the 3D band diagrams.

The regions above the dashed line in the band-diagrams correspond to frequencies above the cladding (air) light line. Modes of the slab are leaky in this region. Depending on the thickness of the dielectric slab there can be higher order guided modes. In this thesis the focus is on single-mode slab waveguides in which a photonic band-gap forms between the fundamental (0th order) "conduction" and "valence" band modes [23, 26]. From the TE-like band-structure of Figure 4.5, we see that the "conduction" band-edge is at the X point, and the "valence" band-edge is at the J point in the first Brillouin zone, just as in the 2D effective index simulations of the previous section. As described in chapter 3, the localized defect modes that are formed by increasing the dielectric constant of a central hole are predominately composed of Bloch modes of the "conduction" band near the band-edge. Owing to the relatively small r/a ratio used here, the "conduction" band-edge at the X point in Figure 1.2 is well below the air (cladding) light line. This is important in reducing the vertical losses of highly localized defect modes [29].

3D FDTD simulations are also used to study the variation of the fundamental TE-like band-gap with slab thickness. In Figure 4.6 we have plotted the "conduction" band-edge at the X point and the "valence" band-edge at the J point versus slab thickness for the fundamental TE-like guided modes. Also shown in this figure is the mid-gap frequency. A plot of the band-gap width is given in Figure 4.7. In these plots, the thickness of the dielectric slab, d , is in units of the inter-hole spacing, a .

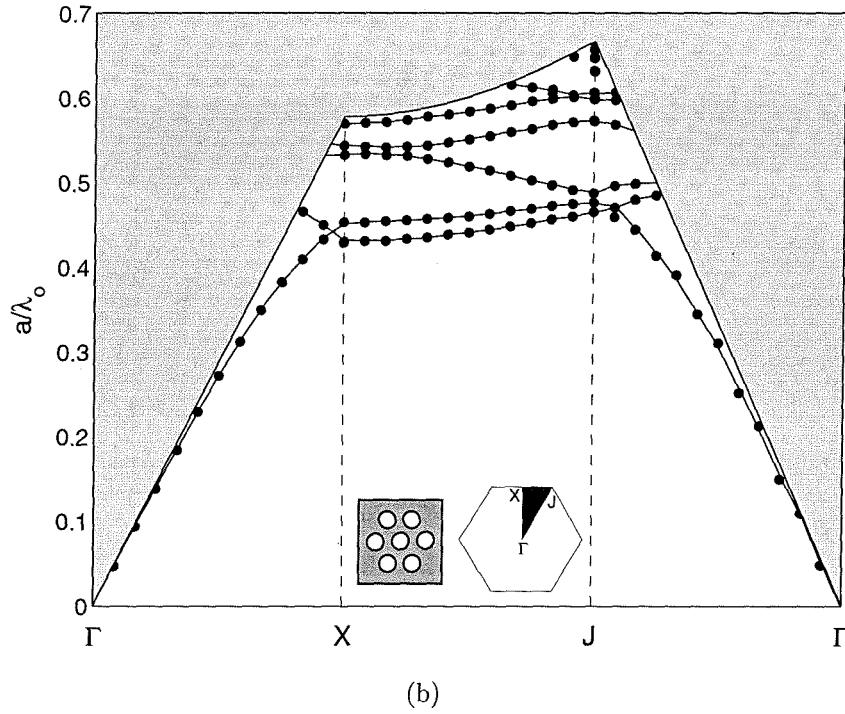
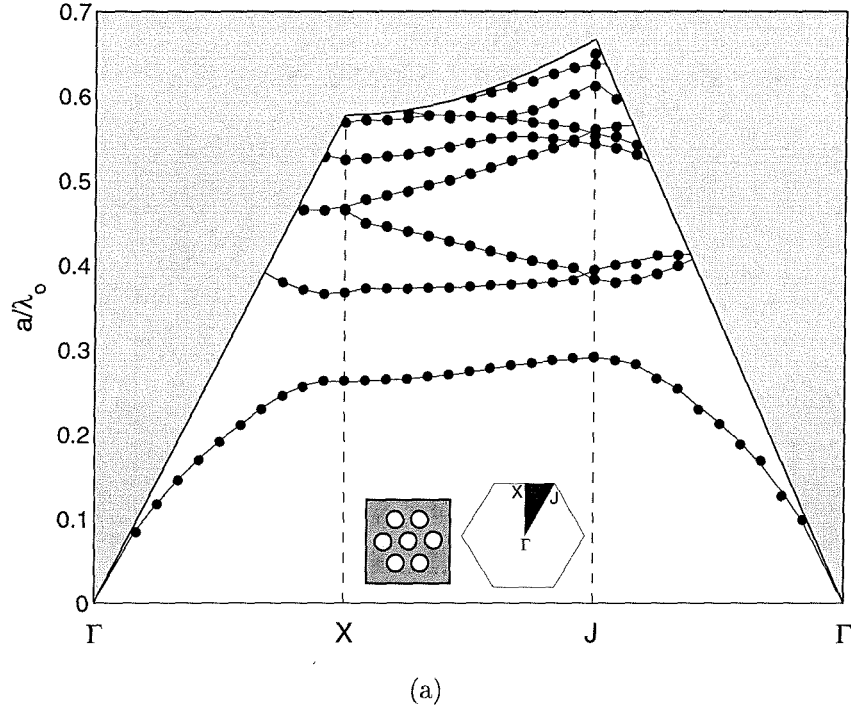


Figure 4.5: In-plane bandstructure of the triangular lattice of air holes in an optically thin high-index slab for (a) the TE-like (even) modes and (b) the TM-like (odd) modes. The parameters used in this calculation are: $r/a=0.32$, $d/a=0.409$, $n_{slab} = 3.4$, and $n_{clad} = 1$.

We see that the mid-gap frequency increases as the slab thickness is reduced due to increasing photon momentum in the \hat{z} -direction. The increase of the band-gap width with thinner dielectric slabs [24] seems at first to be counter-intuitive. However, a simple argument can be made by analogy to the frequency dispersion relation for a photon in a constant index material,

$$\left(\frac{\omega}{c}\right)^2 = \frac{1}{n^2}(k_{\parallel}^2 + k_{\perp}^2), \quad (4.1)$$

where n is the material refractive index, c the speed of light in vacuum, k_{\perp} is the photon momentum normal to the slab, and k_{\parallel} is the in-plane momentum (in this discussion fixed at the X or J point). The increase of the band-gap results from the concentration of the “conduction” band mode in the air holes and the “valence” band in the high index slab. The energy required for a given photon momentum is larger in the lower index material. Thus, as the slab becomes thinner and k_{\perp} increases, the “conduction” band frequency increases faster than the “valence” band, and the band-gap increases. For the range of slab thicknesses studied the TE-like in-plane guide mode photonic band-gap is defined by the fundamental guided mode “valence” and “conduction” bands. For larger slab thicknesses the higher-order guided modes of the photonic crystal waveguide (specifically the higher-order “valence band”) begin to overlap with the fundamental bands, thus reducing the effective in-plane band-gap. As will be discussed more thoroughly in the next section, although a large in-plane photonic band-gap is helpful in increasing the in-plane localization of defect states, a trade-off must be made in order to limit the vertical diffraction loss from the slab waveguide.

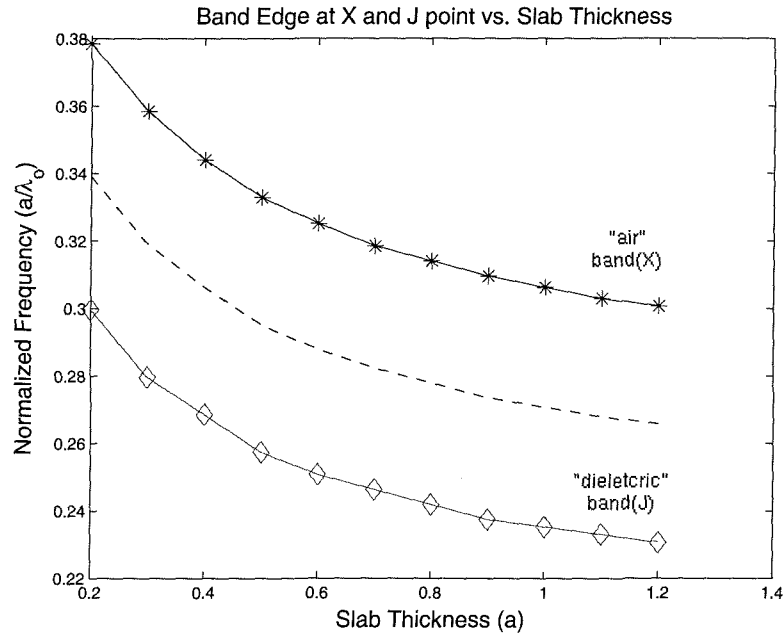


Figure 4.6: Plot of the “conduction” (“air”) and “valence” (“dielectric”) band-edges as a function of slab thickness. The mid-gap frequency is also plotted as a dashed line (- -).

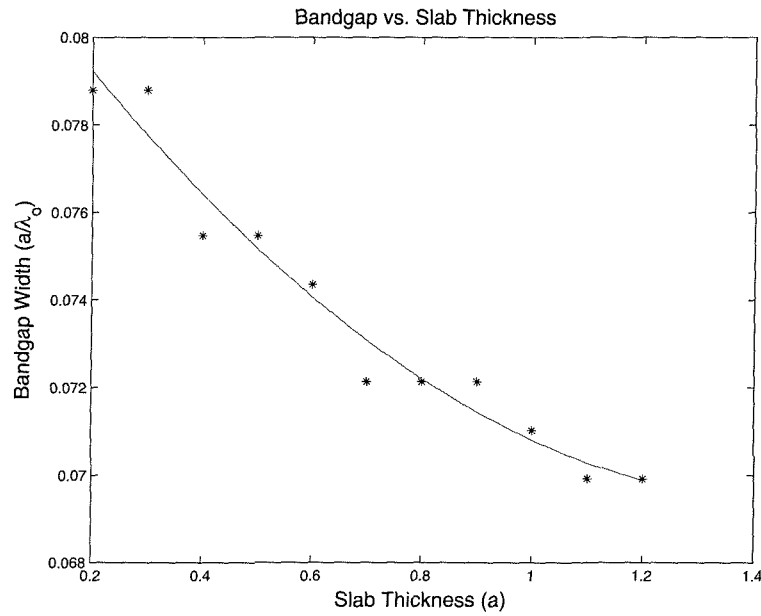


Figure 4.7: Plot of the frequency gap between the “conduction” and “valence” bands versus slab thickness.

4.3 3D FDTD Analysis of Localized Defect Resonances

We now introduce a defect into the photonic crystal and analyze the properties of the localized modes that develop. By analyzing the defect modes in three dimensions, we are able to evaluate the effectiveness of the vertical confinement for a finite thickness dielectric slab. The FDTD calculations are done for three different thicknesses of the slab, d : (i) $d = 0.8a$, (ii) $d = 0.4a$, and (iii) $d = 0.27a$. For frequencies in the band-gap of the photonic crystal, these thicknesses correspond to approximately λ , $\lambda/2$, and $3\lambda/8$, where λ is the wavelength of light in the slab.

To simulate the defect cavity the FDTD method is used with the computational mesh truncated by placing a non-reflecting absorber at all boundaries [83,84]. The computational mesh has a resolution of 15 points per inter-hole spacing, or equivalently 60 points per wavelength in each direction (at the defect resonance). As in the previous calculations the radius of the air holes is equal to $0.3a$. The number of periods of air holes surrounding the defect is three, and the absorbing boundary conditions are positioned as shown in Figure 4.8.

An initial TE polarized electric field is used to excite the TE-like modes of the defect structure. The initial field is then evolved in time using the FDTD method. A Fast-Fourier-Transform (FFT) is applied to the resulting time series of the field at a point of low symmetry in the cavity in order to pick out the resonance peaks. The field is then convolved in time with a bandpass filter to select out the defect modes [85]. In the following calculation the radius of the defect hole is kept constant at $0.3a$ while its refractive index is varied between 1.4 and 3.4. The upper defect refractive index value of 3.4 corresponds to the complete removal of a hole. For defect indices lower than 1.4, the optical mode is no longer well localized to the defect region with only three layers of holes surrounding the defect. With the chosen r/a and n_{slab} , and for the defect refractive index range 1.4-3.4, there is only one clear defect band that forms. A plot of the defect band frequency versus defect refractive index is given in Figure 4.9 for the three different slab thicknesses. For the slab thickness of $0.8a$, we did not

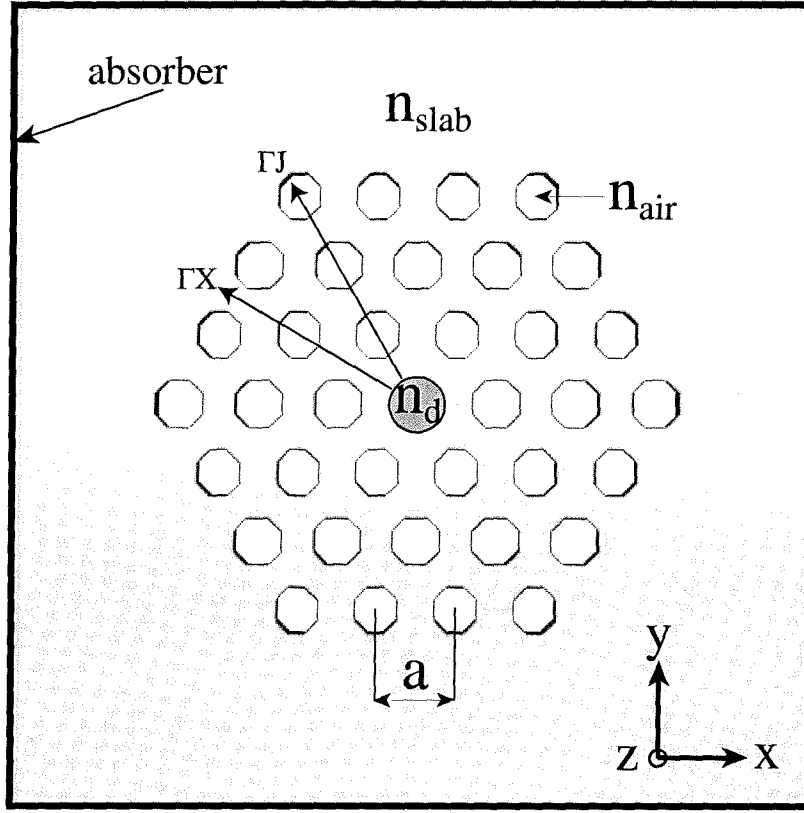


Figure 4.8: Schematic of a 2D slice through the middle of the patterned high index slab. The center hole has a larger refractive index than air, n_d , forming a defect in the hexagonal lattice of air holes.

plot the frequency of the defect mode for an index of 1.4 as the Q in this case was quite low, resulting in a large uncertainty in frequency.

The defect perturbation in this case is circular, and thus the symmetry of the defect cavity is the point group of the hexagonal lattice of air holes, C_{6v} . The modes can be labeled by the irreducible representations (IRREPS) of C_{6v} [77]. We have plotted the magnitude of the electric field of one of the modes of the defect band in Figure 4.10(a). The defect mode transforms like the y component of a vector (in-plane) under the point group operations of C_{6v} . We thus label it as an y -dipole mode. The character table of C_{6v} [70] shows that the y -dipole mode is a member of a doubly degenerate IRREP. This IRREP can be represented by a pair of basis functions that transform like (x, y) vector components. We have plotted the other

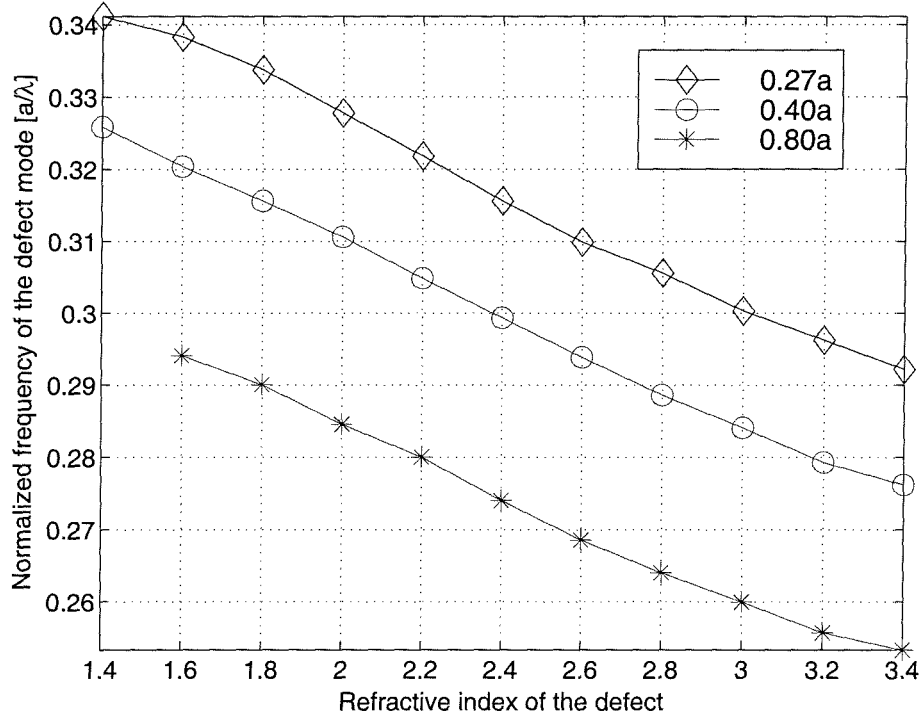


Figure 4.9: Plot of the normalized frequency versus defect refractive index of the degenerate defect mode. The radius of the defect hole was kept constant at $0.3a$ while the refractive index was varied.

defect mode, which we term the x -dipole mode, in Figure 4.10(b). To excite the y dipole mode we used an initial field with \hat{y} symmetry. Similarly, for the x -dipole mode we use an initial field with \hat{x} symmetry. The dipole modes are mainly TE polarized in the slab and have an anti-node in the center of the defect region. This is important in maximizing the overlap of the defect mode and the semiconductor active region, where we anticipate that electron and hole carrier densities will be much lower near the surfaces of the etched holes.

The in-plane symmetry of the defect modes allows us to apply the appropriate mirror conditions³ and reduce the computation size by one fourth. Since we are only interested in TE-like modes, we can also reduce the mesh size by a factor of two in the \hat{z} -direction by applying an appropriate mirror boundary condition at the middle

³The x and y dipole modes have different mirror conditions.

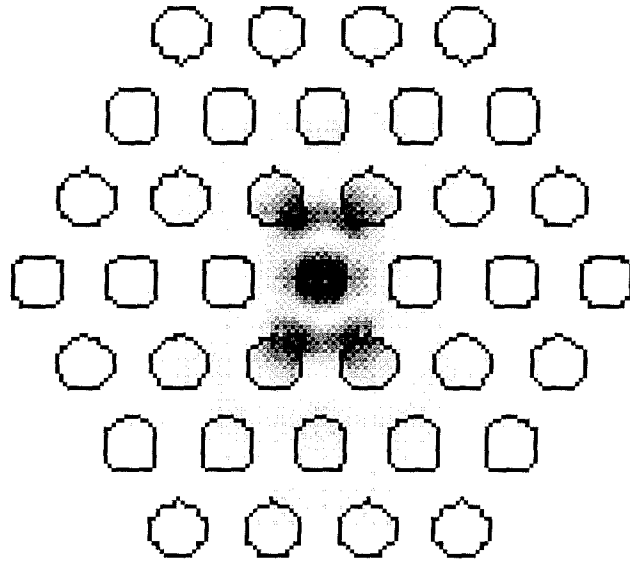
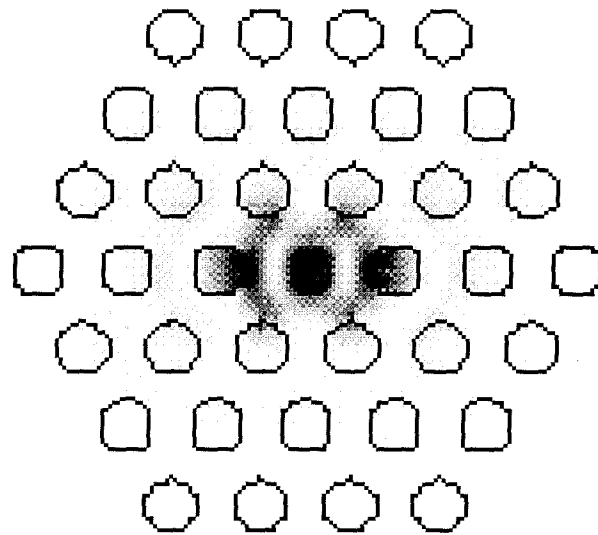
(a) x -dipole mode(b) y -dipole mode

Figure 4.10: 2D slice through the middle of the slab showing the x and y dipole mode electric field amplitudes (degenerate case).

of the slab. Using the reduced mesh, we calculated the quality factor of the x -dipole mode for the defect refractive index range 1.4 to 3.4. As the defect refractive index is changed, the dipole mode frequency sweeps across the band-gap as shown in Figure 4.9; thus we are able to obtain plots of the quality factor versus frequency.

Two different methods were used to calculate the quality factor of the cavity modes. The first method used was to measure the slope of the exponential decay of the energy of a given cavity mode [86]:

$$U(t) = U(0)e^{-t/\tau_{ph}} = U(0)e^{-(\omega_o t)/Q}, \quad (4.2)$$

where U is the energy in the mode, and we have used the relation,

$$Q \equiv \omega_o \tau_{ph}. \quad (4.3)$$

The photon lifetime of the cavity mode is τ_{ph} , and ω_o is the angular frequency. This method is useful for relatively low Q modes; however, for very high Q modes the slope is nearly zero and an alternate method is employed. The second method calculates the (cycled-averaged) power absorbed in the boundary, $P(t)$, and divides it by the energy in the cavity mode [66],

$$Q \equiv \frac{\omega_o U(t)}{P(t)} \quad (4.4)$$

We found little discrepancy between the two methods for the defect modes studied here due to the fact that the quality factors are not extremely large, and the modes are well localized. In the following plots we have chosen to display the quality factor of the defect modes calculated using the second method as this method enables one to separate out the radiation losses into different directions.

A plot of Q versus normalized frequency is given in Figure 4.11 for the three

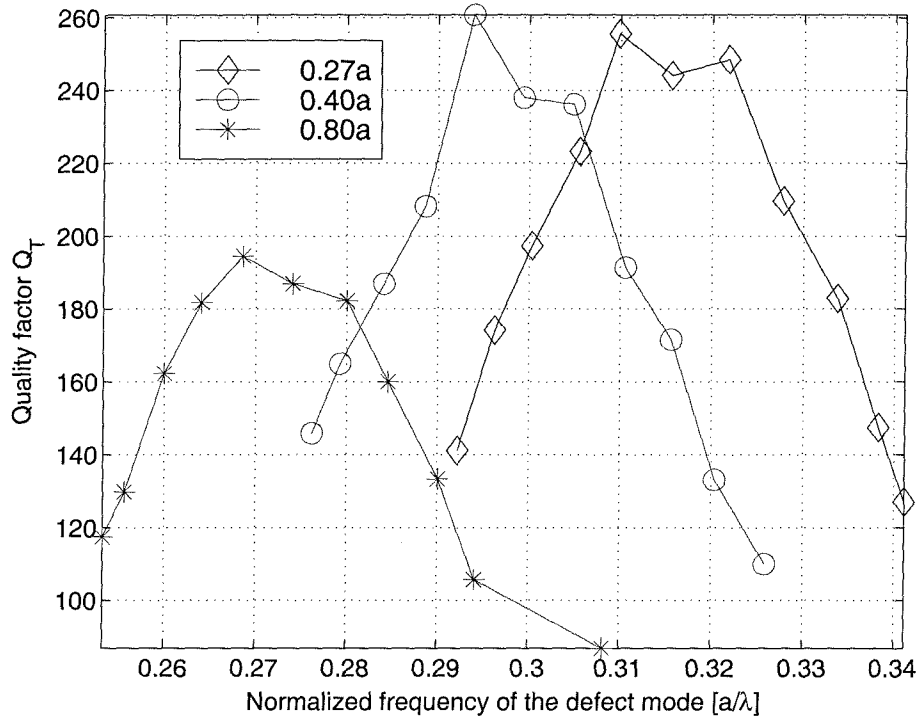


Figure 4.11: Plot of the quality factor versus normalized frequency of the x -dipole mode.

different slab thicknesses: $d = 0.8a$, $d = 0.4a$, and $d = 0.27a$. In Figure 4.14 plots of the electric field for the x and y dipole modes are shown highlighting the radiation pattern in the in-plane directions. Also plotted is the radiation pattern in the vertical direction of the x -dipole mode. From the field plots one can see that the guided in-plane radiation is highly directional and is well suited for coupling to waveguides for in-plane routing.

In order to establish the effectiveness of the vertical guiding, we plot in Figures 4.13 and 4.12 the effective vertical Q and in-plane Q , respectively, for the x -dipole mode. We define these *effective* quality factors as follows:

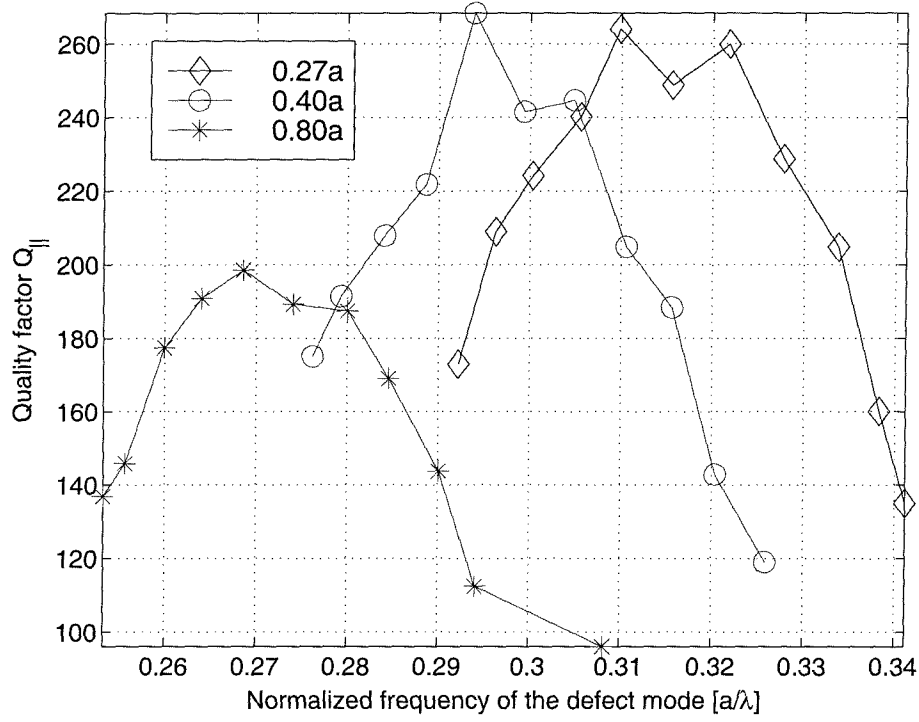


Figure 4.12: Plot of the effective in-plane quality factor, $Q_{||}$, versus normalized frequency.

$$\begin{aligned}
 \frac{\text{Total Power Lost to Boundary}}{\text{Total Energy Stored in Field}} &= \frac{P_T(t)}{U(t)} \\
 &= \omega_o \left(\frac{1}{Q_T} \right) \\
 &= \frac{P_{\perp}(t) + P_{||}(t)}{U(t)} \\
 &= \omega_o \left(\frac{1}{Q_{\perp}} + \frac{1}{Q_{||}} \right)
 \end{aligned} \tag{4.5}$$

where ω_o is the center frequency of the cavity mode, Q_T represents the total modal quality factor, Q_{\perp} is the effective vertical quality factor, and $Q_{||}$ is the effective in-plane quality factor. Q_{\perp} and $Q_{||}$ are calculated from the power lost to the absorber at the top and bottom of the structure (P_{\perp}), and the power lost to the absorber at the side walls ($P_{||}$), respectively.

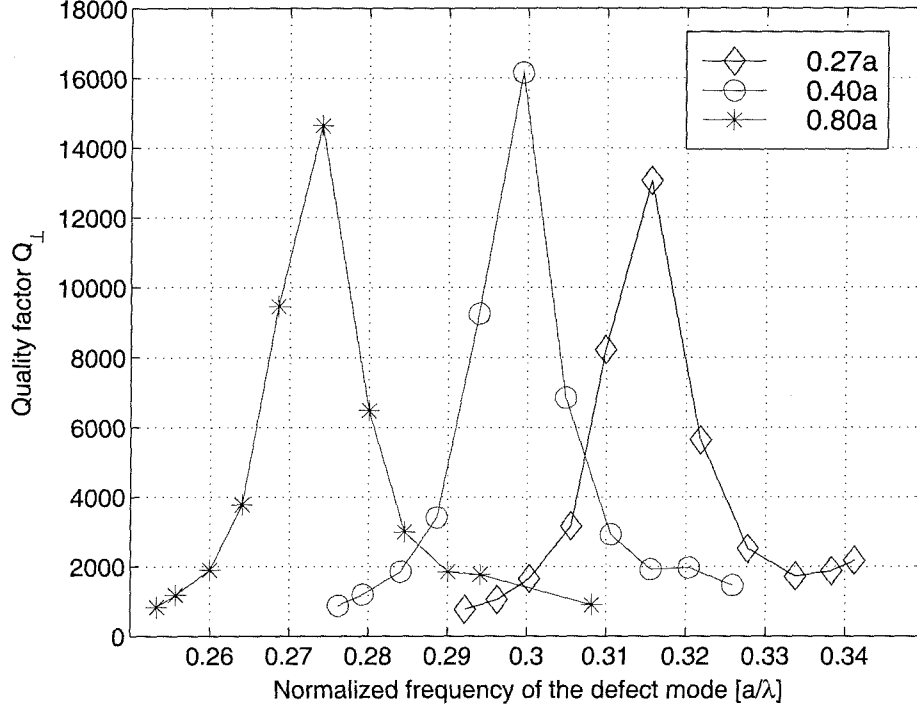
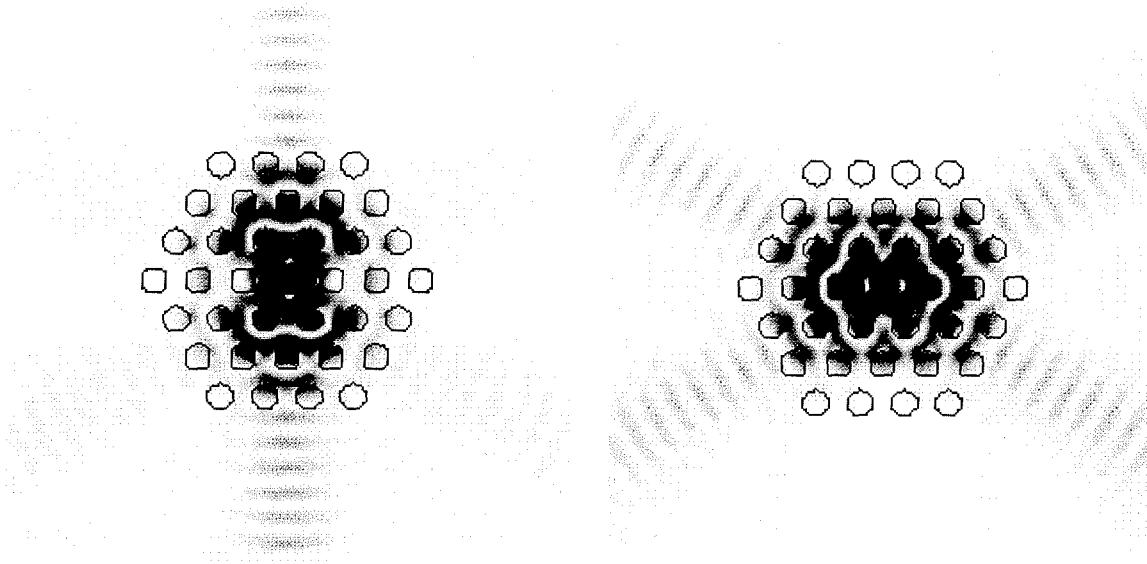


Figure 4.13: Plot of the effective quality factor in the vertical direction, Q_{\perp} , versus normalized frequency.

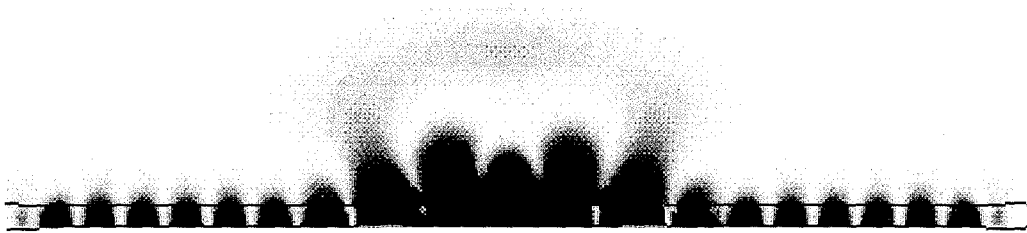
From the plots of the electric field intensity of the x and y dipole modes in Figure 4.14, we see that the fundamental k -component of the envelope of the defect modes is in the ΓX direction of the Brillouin zone. This coincides with the position of the “conduction” band-edge which is at the X-point. As shown in Figure 4.11, the total Q drops off as the defect mode frequency approaches either the “valence” or “conduction” band-edges as a result of the slower decay of the envelope into the photonic crystal and increased mirror losses. The relative heights of the peak effective in-plane quality factors for the different slab thicknesses is determined by the extent of the in-plane band-gap. As described in section 4.2, the thinnest slab, $d = 0.27a$, thus has the largest effective in-plane Q .

Since the “conduction” band is well below the light line at the X and J points of the Brillouin zone, one would expect the defect modes to have only a small amount of leakage in the vertical direction. As seen in the plots of Q_{\perp} versus frequency in Figure



(a) x -dipole mode: 2D horizontal slice shows guided in-plane radiation pattern.

(b) y -dipole mode: 2D horizontal slice shows guided in-plane radiation pattern.



(c) x -dipole mode: cross-section through the middle of the cavity along the \hat{y} -direction showing the point source-like radiation pattern of the defect in the vertical direction. Only the top half of the structure is plotted as the radiation is symmetric in the vertical direction.

Figure 4.14: In-plane radiation losses of the x and y dipole mode (degenerate case) are shown in (a) and (b), respectively. The vertical radiation pattern of the x -dipole mode is given in (c). In each plot the electric field amplitude has been saturated so as to highlight the losses.

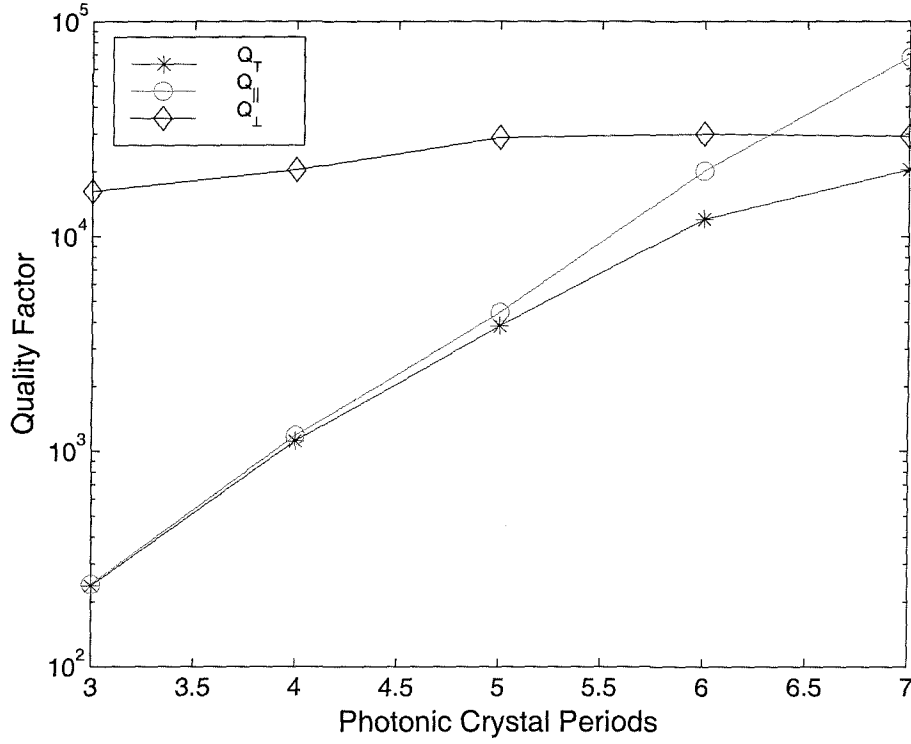


Figure 4.15: Plot of the different radiation loss components (Q_T , $Q_{||}$, and Q_{\perp}) of the x -dipole mode versus the number of periods of the photonic crystal surrounding the defect ($d = 0.4a$).

4.13, the effective vertical Q sharply peaks just below the center of the band-gap. The maximum Q_{\perp} is approximately 16,000 for the slab of thickness $0.4a$. This is much larger than the in-plane Q which is limited to 250 due to the small number of layers of photonic crystal. The modal loss in this case is dominated by in-plane radiation, and the microcavity is essentially an in-plane emitter. One can alter the device to be surface emitting by adding layers of the 2D photonic crystal. In fact, by changing the number of layers of holes surrounding the defect from 3 to 6, $Q_{||}$ can theoretically be increased well above Q_{\perp} , resulting in a total Q near 20,000 (see Figures 4.15 and 4.16). Realistically, the quality of the fabrication of the 2D photonic crystal will limit the obtainable in-plane Q . The optical cavity can also be designed to radiate in the vertical direction by adjusting the r/a ratio to shift the “conduction” band closer to light line.

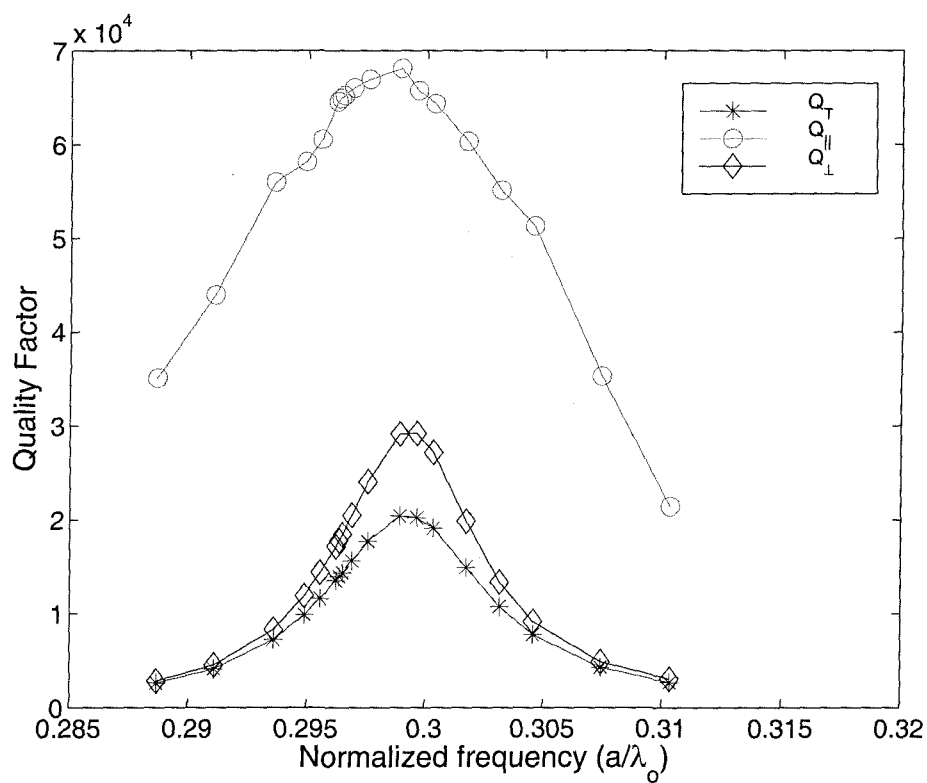


Figure 4.16: Plot of the quality factor versus normalized frequency of the x -dipole mode for a photonic crystal cavity with a seven period photonic crystal mirror surrounding the defect ($d = 0.4a$).

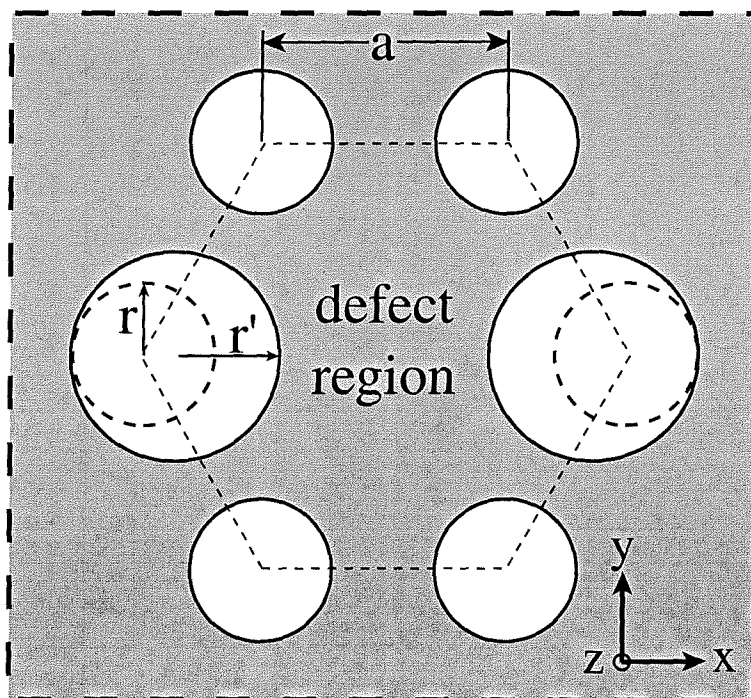
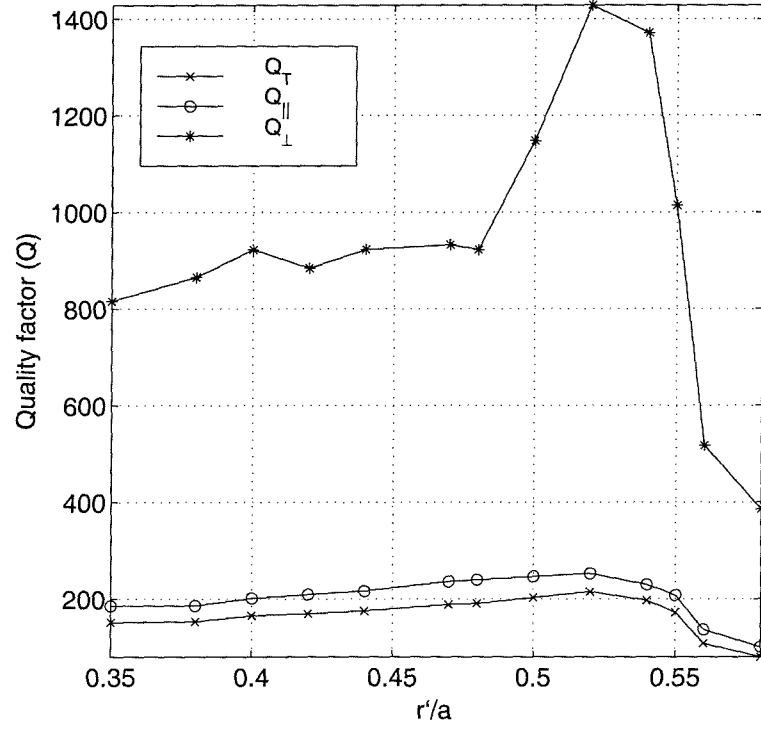


Figure 4.17: Cavity geometry for splitting of the dipole mode degeneracy. Only the nearest neighbor holes of the defect are shown. The two nearest holes in the \hat{x} direction have been enlarged. The central hole has been filled in and has a dielectric constant equal to that of the slab. Notice that the two enlarged holes have also been moved inwards towards the central hole so as to preserve the spacing between holes in the \hat{x} -direction.

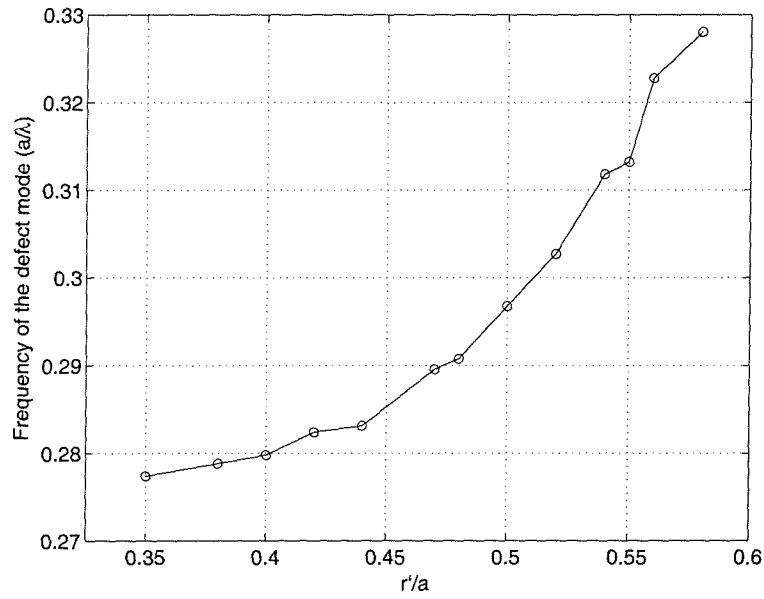
4.3.1 Degeneracy Splitting of the Dipole Modes

As pointed out in chapter 2, an important parameter of a laser cavity is the β factor. In the defect cavity analyzed in section 4.3 the localized defect modes which form are a pair of doubly degenerate dipole-like modes. Here we analyze the effect of creating a defect which is of lower symmetry than the hexagonal lattice, thereby splitting the dipole degeneracy. Since the y dipole mode is more extended in the \hat{x} -direction than the x -dipole, and vice versa, an obvious method of splitting the degeneracy would be to increase the nearest neighbor holes along the \hat{x} -axis. This has the effect of lowering the symmetry of the defect cavity to C_{2v} , which splits the (x, y) IRREP of C_{6v} into two non-degenerate IRREPS, thus splitting the x and y dipole modes.

An illustration of the modified cavity is given in Figure 4.17. The 3D FDTD



(a) Plot of the y -dipole mode Q as a function of r'/a .



(b) Plot of the normalized frequency versus r'/a .

Figure 4.18: Calculated Q and normalized frequency of the y -dipole as a function of the degeneracy-splitting defect, r'/a .

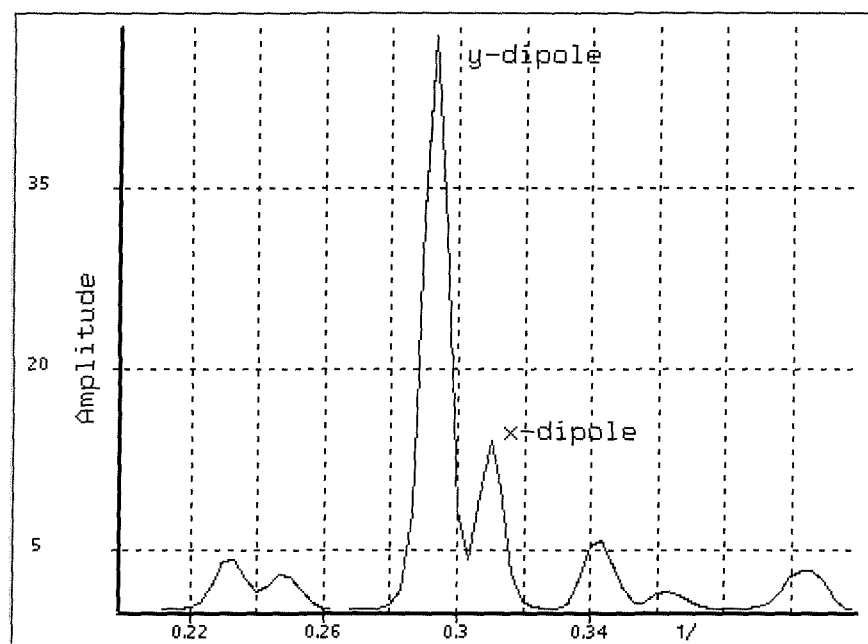


Figure 4.19: Fourier spectrum of an initial field chosen to excite both the x and y dipole modes. $r'/a = 0.35$ in this case. For larger r'/a ratios the splitting of the x and y dipoles is strong enough to push the y dipole frequency out of the band-gap. The y -dipole, on the other hand, is still highly localized and its frequency is only moderately changed [cf. Figure 4.18].

calculations are done for a slab thickness of $0.4a$. The radius of all holes, except the ones we explicitly modify, have $r/a = 0.3$. The refractive index of the defect hole is set to 3.4, which corresponds to removal of a single hole. Now, instead of varying the defect hole index, we vary the hole radius, r' , of the two nearest neighbor holes along the \hat{x} -axis, as marked on Figure 4.17. From a fabrication standpoint this is much more feasible, and does not require any patterning of the defect hole. Also as r' is increased the two holes are simultaneously moved towards the center defect. A plot of Q , Q_{\perp} , and Q_{\parallel} versus r'/a is given in Figure 4.18 for the x -dipole mode. From these plots we see that as the frequency of the x -dipole mode is increased, it eventually enters the “conduction” band and Q drops off significantly. The y -dipole is shifted much higher in frequency than the x -dipole as expected. The Fourier spectrum of the time evolved field for the structure with $r' = 0.35a$ is shown in Figure 4.19. At larger r'/a ratios the y -dipole mode is pushed completely out of the band-gap while the x -dipole frequency is only slightly shifted. The frequency separation between the x and y dipoles increases above 0.04 in normalized units for $r'/a > 0.4$. This corresponds to a wavelength separation of approximately 200nm, assuming the x -dipole is resonant at a wavelength of $1.55 \mu\text{m}$. The linewidth of the spontaneous emission from quantum-wells at this wavelength is roughly 200nm wide [34], thus, the mode splitting forces the y -dipole out of the inhomogeneously broadened emission linewidth, creating a single mode cavity ($\beta \approx 1$).

4.4 FDTD Simulation of Reduced Symmetry Defect Cavities

In the previous section general characteristics of the polarization, emission pattern, and loss rate of the dipole-like defect modes were established. These are ideal defect cavities, free of fabrication error and difficult to realize in practice. Realistic structures have etch roughness, undesirable and unintentioned lithographic defects, and many other ailments. In this section we analyze several types of defect cavities which correspond more closely to the actual photonic crystal cavities measured in chapter 6. These simulations allow us to predict the formation of shallow and deep acceptor modes. These acceptor modes can also be well localized and, as we will see in chapter 6, play a significant role in the emission spectra of defect cavity lasers.

4.4.1 Symmetric (S) Cavity

The simplest cavity geometry that can be readily implemented is that of a single missing hole (schematically shown in Figure 4.20). A FDTD simulation frequency spectra in which an initial localized source field is used to “interrogate” the symmetric cavity is shown in Figure 4.21. The cavity geometry is chosen to lie somewhere in the middle of the range of cavities that were fabricated and tested in chapter 6.

Near the center of the band-gap are deep donor-like modes similar to the modes described in the previous section. There also weak resonances which lie within the valence band and the conduction band. These resonances correspond to low-Q delocalized modes which weakly reflect off of the interface between the patterned and unpatterned regions of the slab waveguide at the cavity edge⁴.

The filtered resonant mode patterns are shown in Table 4.1. In order to reduce calculation time and to choose a preferred basis, the modes were filtered using a pair

⁴One may think of the surrounding unpatterned waveguide as a patterned waveguide with zero hole radius. The hexagonally shaped patterned area then forms a defect region itself. In this case the “defect” corresponds to a locally decreased average refractive index. This tends to form acceptor type modes as discussed in chapter 3.

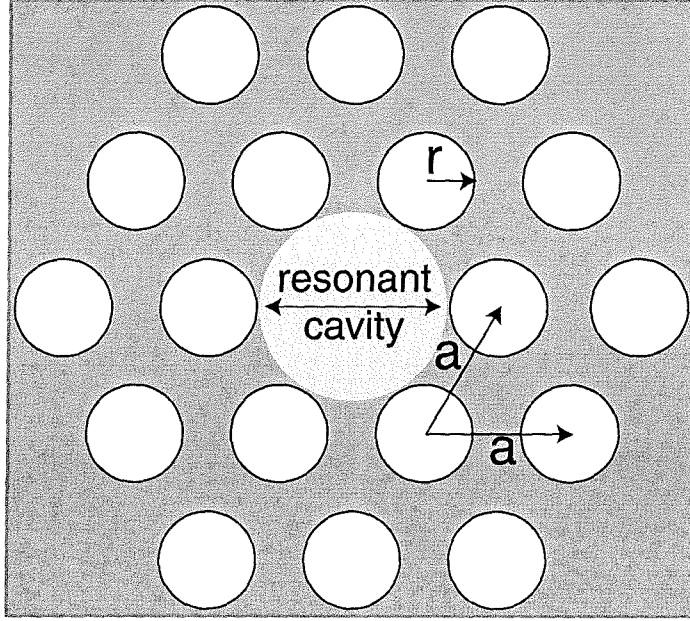


Figure 4.20: Schematic of a symmetric defect cavity with a single hole removed.

of mirror planes (σ_x, σ_y) and are classified according to the IRREPs of C_{2v} . This helps in separating degenerate or nearly degenerate cavity modes, and also helps relate these resonant modes to the resonant modes in the X -split and Y -split cavities described below. A table comparing the properties of the different resonant modes of the symmetric cavity is given in Table 4.2.

One of the most detrimental problems faced in the fabrication process of the photonic crystal cavities is the large size and non-uniformity of the holes which can be created. As described in chapter 5, the defect cavities are formed using e-beam lithography to define the pattern of the two-dimensional array of air holes. This is followed by an HCl etch to undercut the perforated waveguide. This process results in slightly larger holes at the center of the defect cavity than at the perimeter. A linear grading of the hole radius of 10% is quite common. A FDTD simulation of the resonant mode spectra for a defect cavity with a central missing hole along with linear grade in r/a (from the center outwards) of 0.38-0.34 is shown in Figure 4.22.

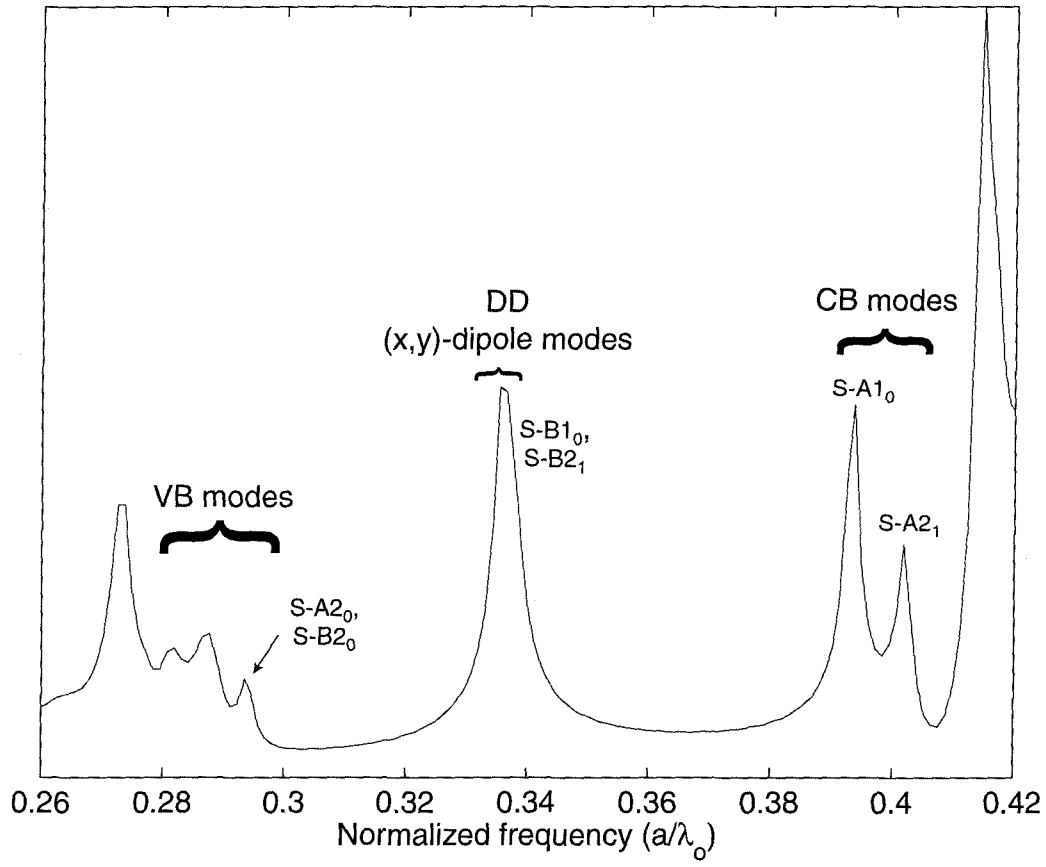


Figure 4.21: FDTD simulation of the resonant modes in a symmetric defect cavity ($r/a = 0.34$, $d/a = 0.409$, $n_{slab} = 3.4$, $p = 5$).

Table 4.1: Magnetic field amplitude patterns of the resonant modes in a symmetric cavity ($r/a = 0.34$, $d/a = 0.409$, $n_{slab} = 3.4$, $p = 5$).

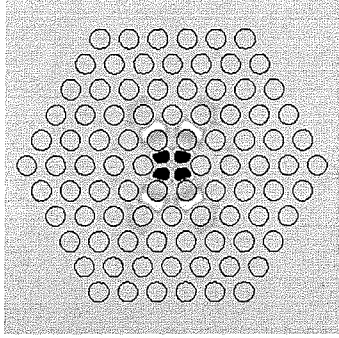
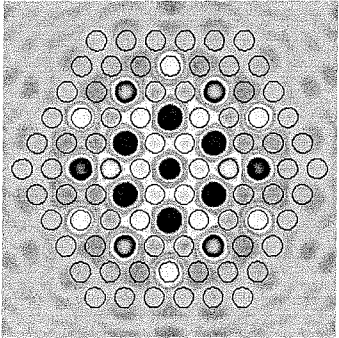
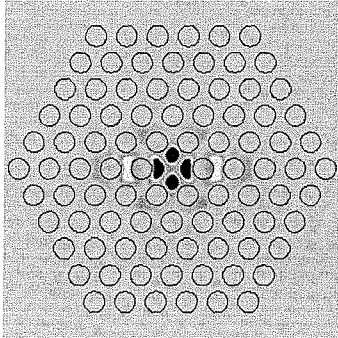
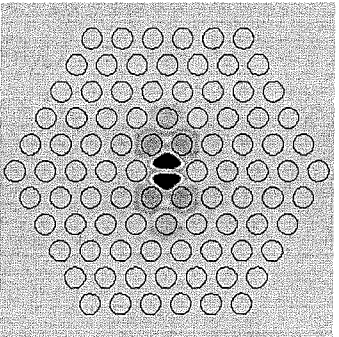
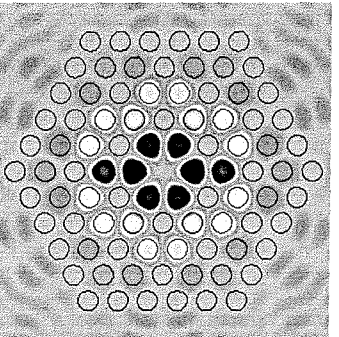
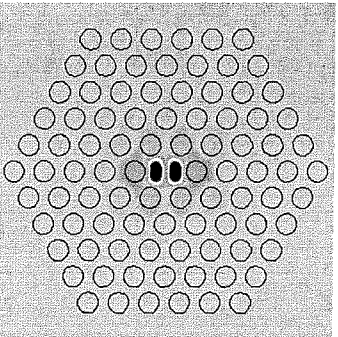
A1 (+, +)	S-A1 ₀	
		
A2 (-, -)	S-A2 ₀	S-A2 ₁
		
B1 (-, +)	S-B1 ₀	
		
B2 (+, -)	S-B2 ₀	S-B2 ₁
		

Table 4.2: Symmetric cavity resonant mode characteristics ($r/a = 0.34$, $d/a = 0.409$, $n_{slab} = 3.4$, $p = 5$).

Label	Group	Transformation Char.	ω_n	$Q_{ }$	Q_{\perp}	V_{eff}
S-A1 ₀	CB	quadrapole ($x^2 - y^2$)	0.393	860	330	n/a
S-A2 ₀	VB	($-$, $-$)	0.293	150	1e4	n/a
S-A2 ₁	CB	quadrapole (xy)	0.401	850	350	n/a
S-B1 ₀	DD	dipole (\mathbf{x})	0.339	1180	150	2.7
S-B2 ₀	VB	($+$, $-$)	0.294	166	1800	n/a
S-B2 ₁	DD	dipole (\mathbf{y})	0.336	1370	180	2.7

The spectra clearly shows the addition of a shallow acceptor resonance peak above the valence band-edge. In fact the resonance peak contains two nearly degenerate modes (S-A2₀, S-B2₀), the field patterns of which are plotted in Table 4.3. These are the type of modes predicted for shallow acceptors using the group theory formalism of chapter 3.

The properties of these shallow acceptor modes are listed in Table 4.4 for various gradings of the hole radius. The S-B2₀ mode is slightly higher in frequency than S-A2₀ and as a result is slightly deeper within the band-gap. For this reason S-B2₀ is more localized in-plane and has a significantly larger Q-value. Owing to its low vertical and in-plane loss, the S-B2₀ mode is found to lase in the defect cavities tested in chapter 6.

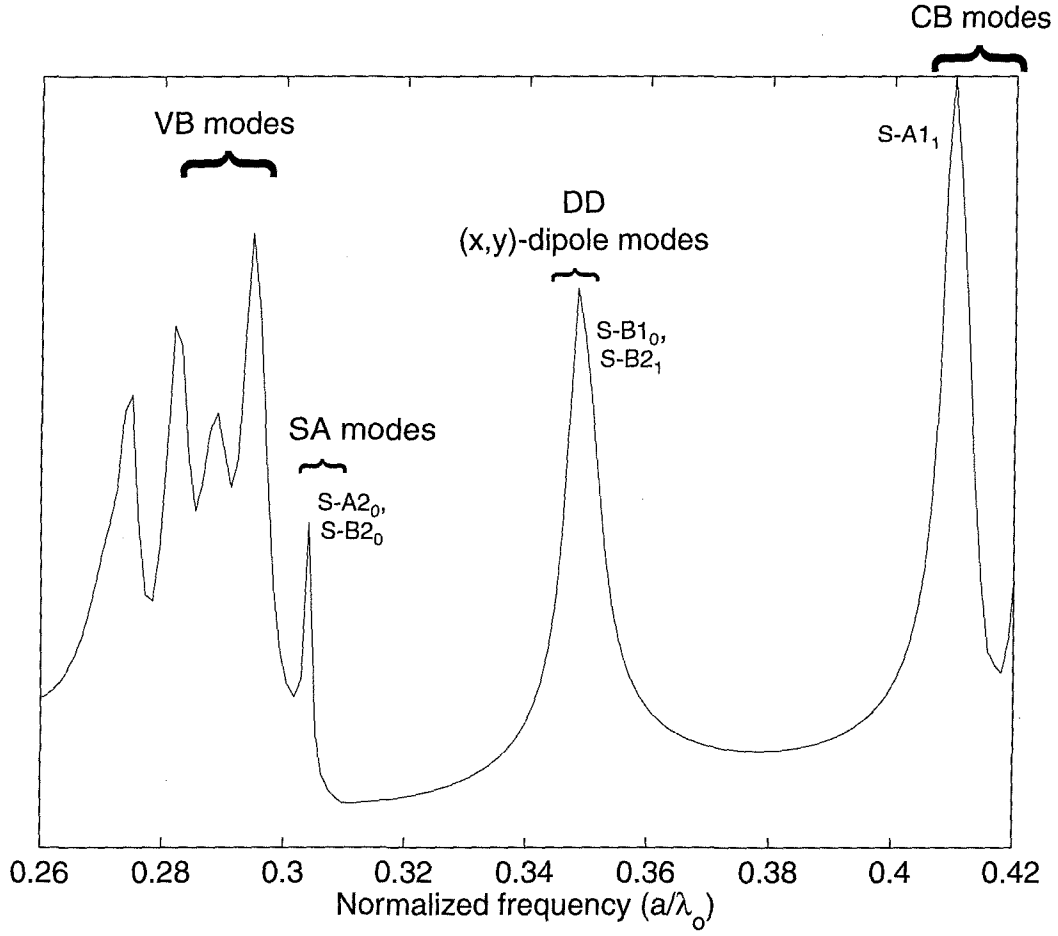


Figure 4.22: FDTD simulation of the resonant modes in a symmetric (S) defect cavity with r/a graded (center outwards) from 0.38 – 0.34 ($d/a = 0.409$, $n_{slab} = 3.4$, $p = 5$).

Table 4.3: Field amplitudes of the SA modes of a symmetric cavity with r/a linearly graded from 0.38 – 0.34 ($d/a = 0.409$, $n_{slab} = 3.4$, $p = 8$).

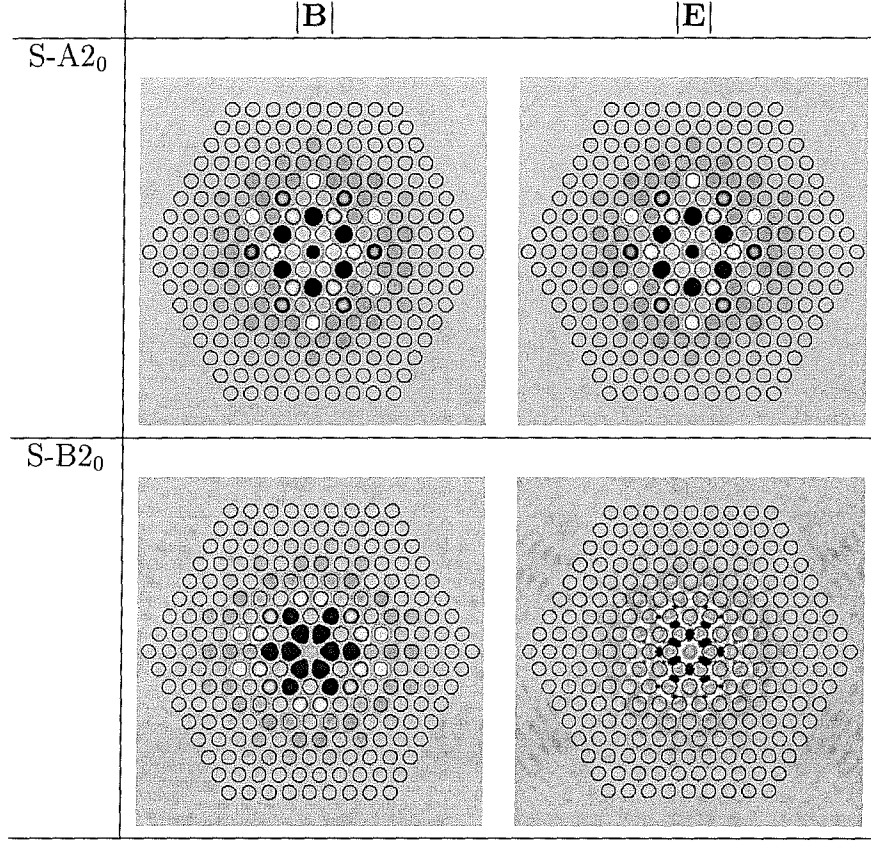


Table 4.4: Characteristics of shallow acceptor modes in a symmetric cavity with different gradings of the hole radius ($d/a = 0.409$, $n_{slab} = 3.4$, $p = 8$).

	fixed r/a (0.34)				$r/a = 0.36$ for 6 n.n.				r/a graded (0.38 – 0.34)			
Label	ω_n	$Q_{ }$	Q_{\perp}	V_{eff}	ω_n	$Q_{ }$	Q_{\perp}	V_{eff}	ω_n	$Q_{ }$	Q_{\perp}	V_{eff}
S-A ₂₀	0.293	150	1e4	n/a	0.297	740	2.9e4	45	0.307	4800	1.0e4	17.6
S-B ₂₀	0.294	166	1800	n/a	0.298	1170	3.4e4	16.7	0.309	8800	6.4e4	12

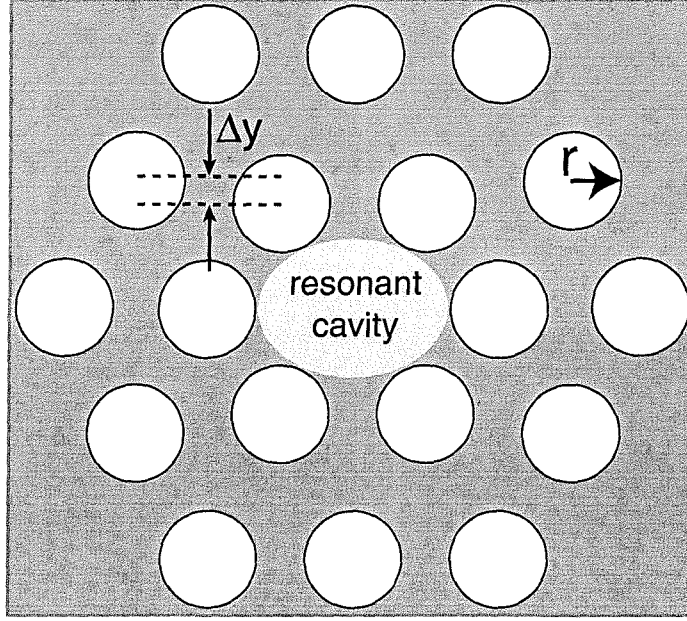


Figure 4.23: Schematic of an X-split defect cavity. The degree of splitting is measured by Δy , the distance which the four nearest neighbors on top and bottom of the defect region are moved together.

4.4.2 X-Split (X) Cavity

Another type of defect cavity that was fabricated and tested is shown in Figure 4.23. In this cavity the four air holes on top and bottom of the central missing hole are moved inwards a distance Δy . In the fabricated structures $\Delta y \sim 0.15a \sim 75$ nm. This reduces the defect symmetry from C_{6v} to C_{2v} and splits the degenerate (x, y) -dipole modes. A FDTD spectra is plotted in Figure 4.24.

The deep donor (x, y) -dipole modes are seen to split as expected, the x -dipole being higher in frequency. There is also the introduction of two shallow acceptor modes, S-A₂₀ and S-B₂₀. These are the same modes as those found in a symmetric cavity with enlarged central holes. The magnetic field amplitudes of the different resonant modes of the X-split cavity are shown in Table 4.5. The frequency, Q-factor, and effective mode volume are also given in Table 4.6.

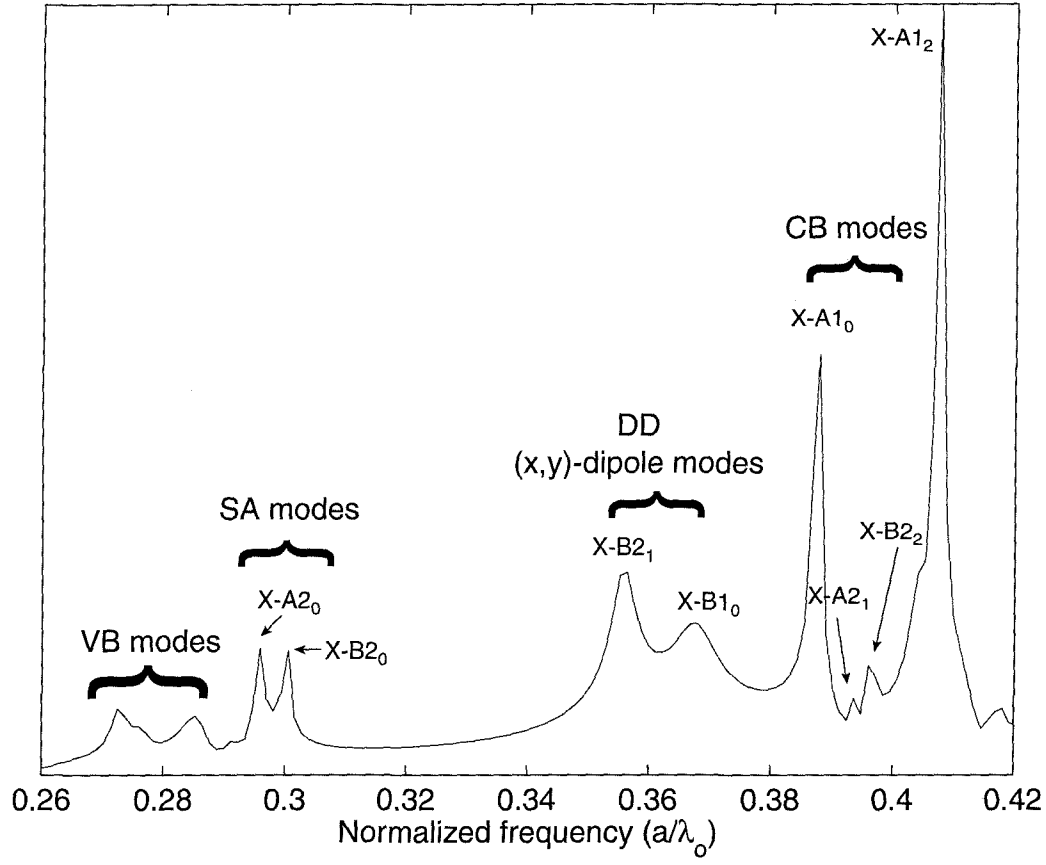


Figure 4.24: FDTD simulation of the resonant modes in an X-split defect cavity with $r/a = 0.34$, $d/a = 0.409$, $n_{slab} = 3.4$, and $\Delta y = 0.15a$.

Table 4.5: Magnetic field (amplitude) patterns of the resonant modes in an X-split cavity ($r/a = 0.34$, $d/a = 0.409$, $n_{slab} = 3.4$, $\Delta y = 0.15a$, $p = 5$).

A1 (+, +)	S-A1 ₀	S-A1 ₁	
A2 (-, -)	S-A2 ₀	S-A2 ₁	
B1 (-, +)	S-B1 ₀		
B2 (+, -)	S-B2 ₀	S-B2 ₁	S-B2 ₂

Table 4.6: X-split cavity resonant mode characteristics ($r/a = 0.34$, $d/a = 0.409$, $n_{slab} = 3.4$, $\Delta y = 0.15a$, $p = 5$).

Label	Group	Transformation Char.	ω_n	$Q_{ }$	Q_{\perp}	V_{eff}
S-A1 ₀	CB	quadrupole ($x^2 - y^2$)	0.388	2000	1000	n/a
S-A1 ₁	CB	(+, +)	0.408	1000	1100	n/a
S-A2 ₀	SA	(-, -)	0.297	962 ^a	3680 ^a	9.7
S-A2 ₁	CB	(-, -)	0.393	1900	650	n/a
S-B1 ₀	DD	dipole (x)	0.366	400	60	3.2
S-B2 ₀	SA	(+, -)	0.300	3970 ^a	1740 ^a	5.5
S-B2 ₁	DD	dipole (y)	0.355	650	100	2.5
S-B2 ₂	CB	(+, -)	0.395	2000	650	n/a

^a $p = 8$.

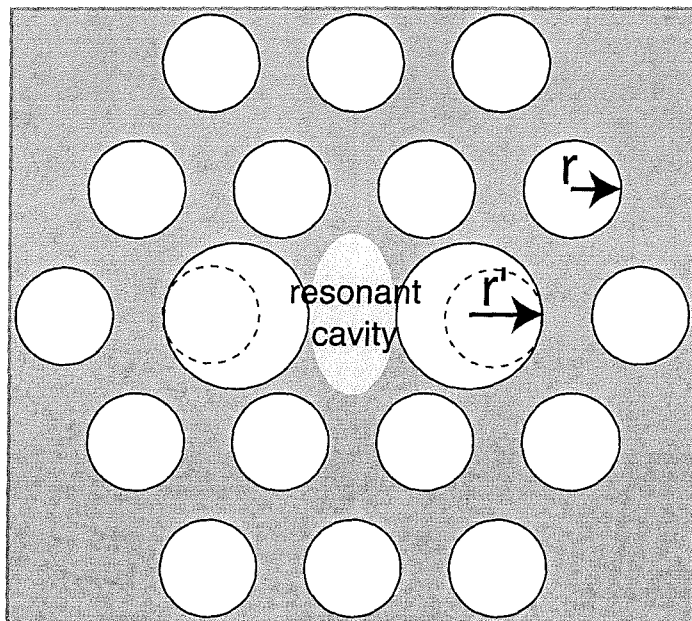


Figure 4.25: Schematic of a Y-split defect cavity. The degree of splitting is measured by r'/r , the scaling factor of the radius of the two nearest neighbor holes along the \hat{x} -direction.

4.4.3 Y-Split (Y) Cavity

The Y-split cavities have already been described in sub-section 4.3.1. Unlike the X-split cavities, the Y-split cavity tends to shrink the cavity horizontally. The two nearest neighbor holes on either side of the central missing hole along the ΓJ direction are enlarged and moved slightly inwards. The cavities studied here use hole enlargements which are quite significant and result in a much stronger perturbation of the cavity than in the X-split case. An illustration of the Y-split cavity is shown in Figure 4.25.

A FDTD simulation showing the mode spectra of a Y-split cavity with the two nearest neighbor holes enlarged by 150% is shown in Figure 4.26. There are now at least four different localized modes within the band-gap. The two enlarged holes act as centers for acceptor modes which gives rise to the two deep acceptor (DA) modes in the spectra. There is a SA mode present as well. The splitting of the (x, y) -dipole

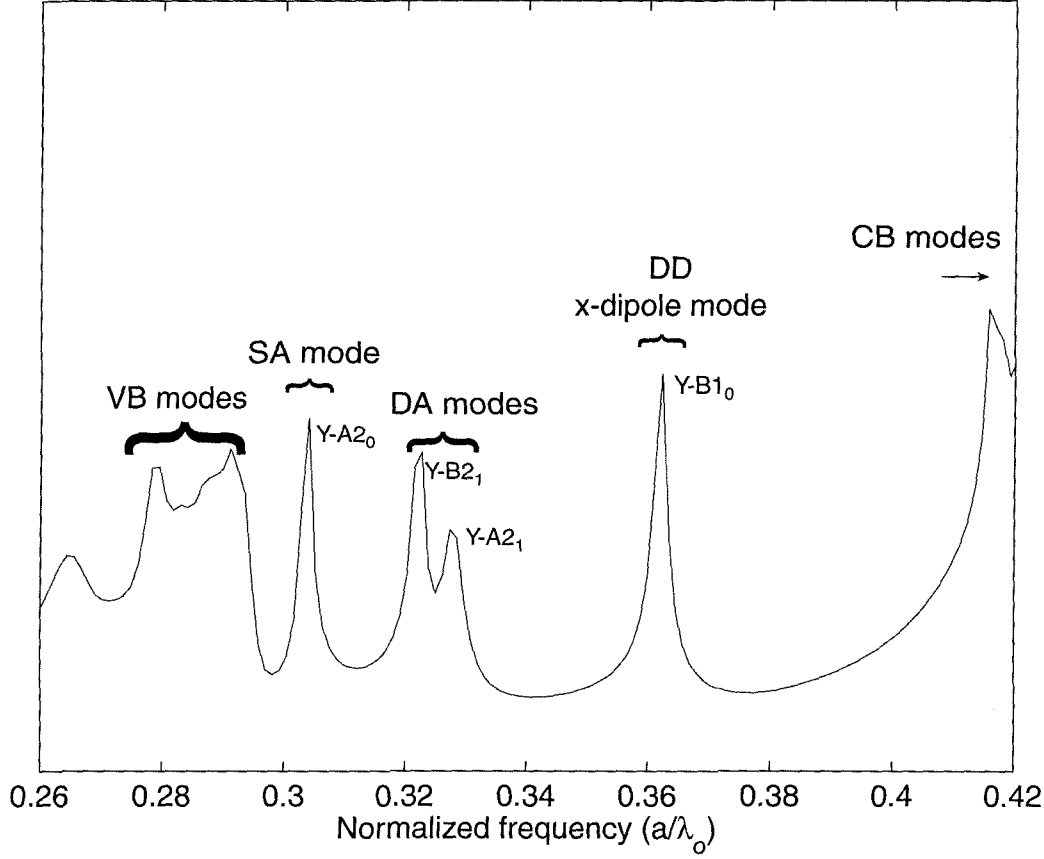


Figure 4.26: FDTD simulation of the resonant modes in a Y-split defect cavity with $r/a = 0.34$, $r'/a = 0.51$, $d/a = 0.409$, and $n_{slab} = 3.4$.

modes is so strong in this case that the y -dipole mode is completely pushed out of the band-gap and only the x -dipole mode remains.

The magnetic field amplitudes of the various localized defect modes of the Y -split cavity are shown in Table 4.7. It is interesting to note that the DA modes are as well localized as the DD dipole-like mode. Table 4.8 shows the Q and effective mode volume of the Y -split defect modes. The low Q values of the DA modes and the x -dipole mode are due to the large size of the splitting holes⁵.

⁵These hole sizes are somewhat exaggerated and the Q values somewhat pessimistic in comparison to some of the defect cavities tested in section 6.4.

Table 4.7: Field amplitude patterns of the resonant modes in a Y-split cavity ($r/a = 0.34$, $r'/a = 0.51$, $d/a = 0.409$, $n_{slab} = 3.4$, $p = 8$).

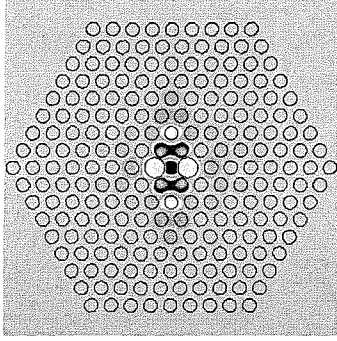
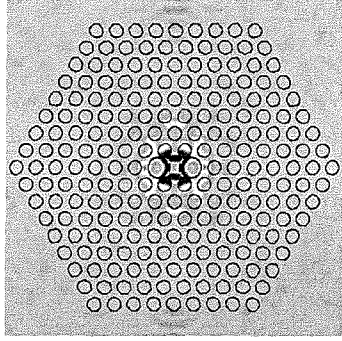
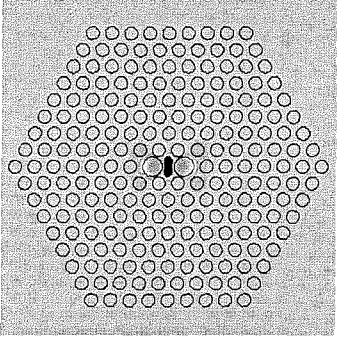
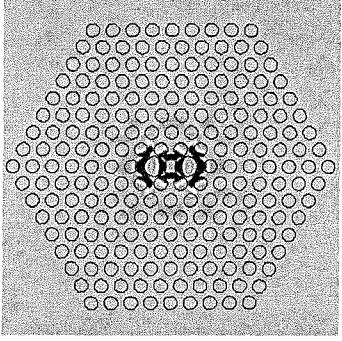
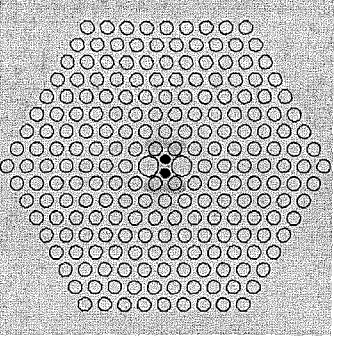
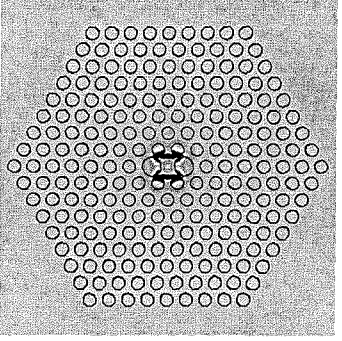
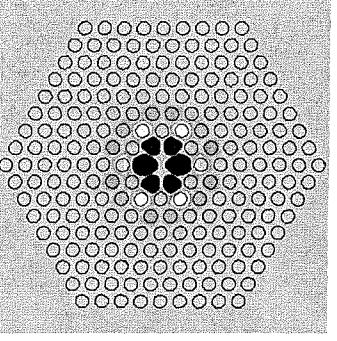
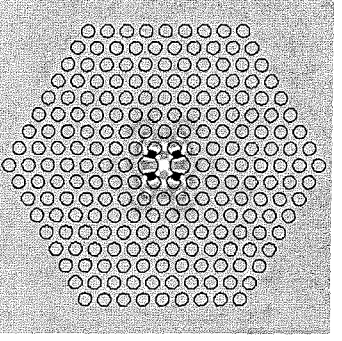
	$ \mathbf{B} $	$ \mathbf{E} $
A2 $(-, -)$	S-A2 ₀	
		
A2 $(-, -)$	S-A2 ₁	
		
B1 $(-, +)$	S-B1 ₀	
		
B2 $(+, -)$	S-B2 ₀	
		

Table 4.8: Y-split cavity resonant mode characteristics ($r/a = 0.34$, $r'/a=0.51$, $d/a = 0.409$, $n_{slab} = 3.4$, $p = 8$).

Label	Group	Transformation Char.	ω_n	$Q_{ }$	Q_{\perp}	V_{eff}
S-A2 ₀	SA	(-, -)	0.304	2140	350	2.8
S-A2 ₁	DA	(-, -)	0.328	690	130	2.2
S-B1 ₀	DD	dipole (x)	0.362	2110	235	2.8
S-B2 ₀	DA	(+, -)	0.322	2170	230	2.9

Chapter 5 Fabrication

One of the simplest and most elegant designs for a high-Q semiconductor optical microcavity is that of the microdisk laser [6, 34]. Processing of the microdisk cavity is straightforward and involves little more than optical lithography and selective wet etching. These cavities consist of an optically thin disk (approx. half-wavelength thick) with a pedestal in the middle for support. Light is strongly guided in the vertical direction by the high-index slab and whispers around the edge of the disk as it circulates. In the photonic crystal defect cavity, the smooth outer disk surface is replaced with a two-dimensional photonic crystal mirror. Although the physical process by which the microdisk and the photonic crystal cavity trap light is very different, the choice of material epitaxy and many of the fabrication steps are similar.

The photonic crystal defect cavity lasers were fabricated in the InGaAsP-InP material system. The choice of this material system was threefold. Firstly, the emission wavelength of InGaAsP MQW structures is in the 1500 nm wavelength band which is important in the fiber-optic telecommunication industry. The long wavelength also increases the size of the photonic crystal, reducing the lithographic and etching tolerances. Finally, this material system has a relatively slow surface recombination velocity [13, 64] which is critical due to the large surface to volume ratio of etched photonic crystal structures.

Metalorganic chemical vapor deposition (MOCVD) [87] was used to grow the laser structure on an indium phosphide (InP) substrate¹. A schematic of the epitaxy is shown in Figure 5.1. Optical gain is provided by four 0.85% compressively strained quaternary QWs [88, 89] designed for a peak emission wavelength of 1.55 μm at room temperature. The barriers are also quaternary with a room temperature band-gap of 1.22 μm . Cladding material (57.5 nm) identical to the barriers is placed on top

¹Growth of this laser material was done by In Kim in the research group of Dan Dapkus at the University of Southern California.

50nm InP cap	
211nm {	57.5nm InGaAsP
	9nm InGaAsP QW (+0.85%) X 4
	20nm InGaAsP barrier ($E_g=1.22\mu\text{m}$) X 3
	57.5nm InGaAsP ($E_g=1.22\mu\text{m}$)
664nm InP buffer layer	
20nm InGaAs etch stop	
InP substrate	

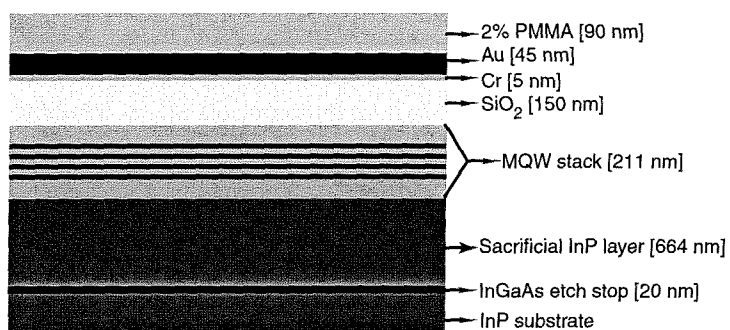
Figure 5.1: InGaAsP-InP epitaxy for the defect lasers. The active region consists of four 0.85% compressively strained InGaAsP quantum-wells. The InP buffer layer is used as a sacrificial layer which is removed by a selective HCl etch in order to free the membrane from the substrate. The total thickness of the membrane after processing is 211 nm.

and bottom of the active region to isolate the QWs further from the surface and to increase the final waveguide thickness. A sacrificial InP (664 nm) layer is grown beneath the QWs and cladding which is subsequently removed in order to free the membrane. A thin InGaAs etch stop layer is grown just below the sacrificial InP layer.

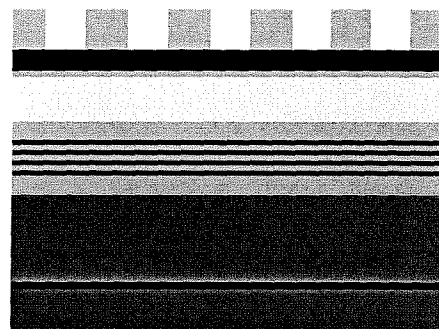
In the fabrication of the photonic crystal cavities, a three-step lithography process² was used in order to create a sturdy etch mask. Initially, masking layers consisting of a Cr/Au (5 nm/45 nm) metal layer followed by a SiO₂ or Si₃N₄ dielectric layer (150 nm) were deposited on the InGaAsP wafer surface. The Cr/Au metal layers provide a selective etch mask for a reactive ion etch of the dielectric layer. The Cr acts as an adhesion layer between the Au and the dielectric layer³. Following the surface mask deposition, the wafer was cleaved up into samples roughly 5 mm on a side, and the samples were then put in a dry box for storage. The final mask layer, a 90-100 nm (post soft-bake) layer of electron sensitive 2% polymethyl methacrylate (PMMA) electron-beam resist, was spun on at 3500 rpm for 45 s. The sample was placed on a hot plate at 150 °C for 20 min. to soft-bake the PMMA.

²One step electron beam lithography, 2 steps mask amplification.

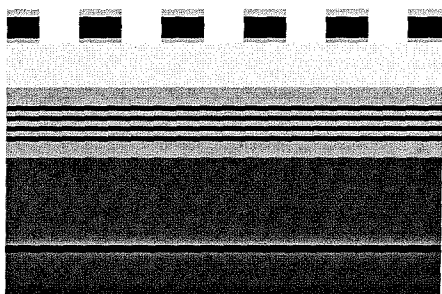
³Care must be taken not to oxidize the Cr as it will be difficult to mill the resulting oxide in the



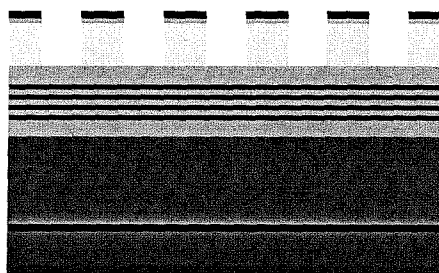
(a) Deposition of Cr/Au/SiO₂/PMMA surface mask.



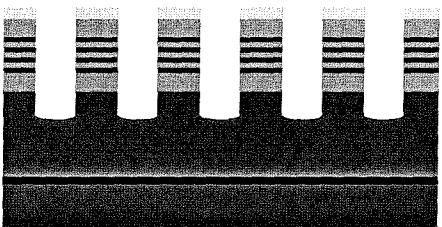
(b) 2D patterning of PMMA using electron-beam lithography.



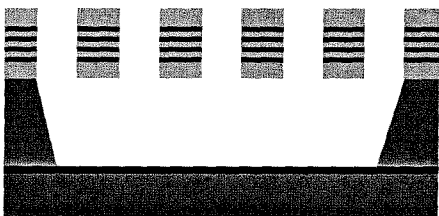
(c) Ar⁺ ion beam milling of metal layers.



(d) C₂F₆ RIE etch of SiO₂ layer.



(e) CAIBE etch of InGaAsP waveguide layer.



(f) HCl:H₂O (4:1) wet etch to release the perforated InGaAsP membrane.

Figure 5.2: Suspended membrane photonic crystal waveguide processing steps.

A diagram illustrating the fabrication sequence is shown in Figure 5.2. Patterning of the PMMA was performed using a modified Hitachi S-4500 II cold cathode field emission scanning electron microscope (SEM). A beam current (as measured by a Faraday cup on the sample stage) of 30 pA, an accelerating voltage of 30 kV, and a working distance of 6 mm were used throughout. Adjustments to the electron beam exposure were made coarsely by changing the pixel density⁴ and more finely by adjusting the rastering speed of the electron beam (exposure/pixel). The overall scale of a pattern was adjusted by varying the magnification setting of the SEM. In this way a single template pattern can be used to generate photonic crystals with varying lattice spacing as well as porosity. A 200 μm x 200 μm square pattern (“check box”) was also beam-written in close proximity to the photonic crystal patterns. After each etch step, the “check box” patterns were profiled using a Dektak profilometer in order to calibrate etch durations and to quickly determine any changes in the processing conditions.

The beam-written pattern was developed using a mixture of 99% 2-Ethoxyethanol ($\text{C}_2\text{H}_5\text{OCH}_2\text{CH}_2\text{OH}$) and Methanol (CH_3OH) in a 3:7 ratio at room temperature. Typical development times were on the order of 30 s (15-45 s), dependent upon the exposure used. After development the sample was placed in an isopropyl alcohol (IPA) rinse for approximately 7 s and then dried with a high purity nitrogen spray.

With the initial pattern written into the PMMA resist, the first step in mask amplification was performed with an Ar^+ ion beam which transferred the pattern into the Cr/Au layers. The ion beam was generated using a Kaufman-type ion source (with a collimating grid) placed 25 cm from the sample. The Ar partial pressure was maintained at $\sim 2 \times 10^{-4}$ Torr using a mass flow controller to regulate the flow rate. Milling was performed with a specimen current density of $\sim 250 \mu\text{A}/\text{cm}^2$ and a beam voltage of 1000 V. Under these conditions the mill rates of PMMA, Au, and Cr are ~ 20 , 40, and 5 nm/min., respectively. After milling the sample for ~ 3 min., it

mask amplification step.

⁴Adjustments in pixel density and rastering speed of the beam were done in software. The software was written by Oliver Dial while he was an undergrad at Caltech.

was then visually inspected with a high power microscope and the check boxes were profiled. By placing a bright fiber-optic light source at a low angle relative to the sample, an estimate of the lattice spacing of the photonic crystal could be made by visual inspection of the color of the diffracted light. This is particularly useful for III-V semiconductor photonic crystals in the 1500 nm band as the lattice spacing is in the 400-600 nm range.

After the visual inspection, the sample was placed in a C_2F_6 reactive ion etch (RIE) which etches the pattern into the SiO_2 or Si_3N_4 dielectric layer. The flow rate of C_2F_6 was fixed at 20 sccm using a mass flow controller. The partial pressure inside the chamber was set to 35 mTorr by adjusting the position of the gate valve between the chamber and the diffusion pump. An RF generator and matching network were used to supply 60 W of RF power (1-2 W reflected power) during the RIE process. The DC bias voltage under these conditions was ~ 370 V. Prior to etching the sample, an O_2 plasma etch was performed (40 sccm, 120 mTorr, 150 W, 30 min.) to pre-treat the chamber. The sample was then placed in the chamber and a 5-6 minute C_2F_6 etch was performed⁵. This completed the mask amplification steps.

The final dry etching step was a chemically⁶ assisted ion beam etch (CAIBE) [10] used to transfer the pattern through the MQW active region and into the sacrificial InP layer. In addition to the Ar ion beam source described above, a 1/16" nozzle was used to produce a focused Cl_2 jet (flux ~ 20 sccm) in close proximity to, and directed at, the sample surface. The sample was mounted with thermal paste on a sample stage equipped with a heating element and water cooling lines for control of the sample stage temperature. For etching of InP based materials a high ion beam current density ($J_b \sim 800 \mu A/cm^2$) and energy (1500 eV) are used with no active cooling or heating of the sample stage. Under these conditions a delicate balance between chemical etching and physical sputtering is struck producing a good mask-semiconductor etch selectivity, highly anisotropic etch profile, as well as smooth etch surfaces (see Figure 5.3). In other work [90], where much lower beam current

⁵RIE etch rate of Au ~ 4 nm/min. under these conditions.

⁶An Ar ion beam is used along with Cl_2 gas.

densities, beam voltages, and reactive gas flux was used, sample heating to $> 200\text{ }^{\circ}\text{C}$ was required to increase the chemical reactivity of the InP surface and to remove the non-volatile InCl_x reaction product. In our case, although still most likely dominated by physical sputtering, the large current density of high energy Ar ions [91] and the high Cl_2 concentration at the sample surface⁷ resulted in a good mask-semiconductor etch selectivity, highly anisotropic etch profile, as well as smooth etch surfaces (see Figure 5.3). With the 150 nm SiO_2 dielectric surface mask etch rates of 350 nm/min. through holes of 300 nm in diameter were possible in the InGaAsP-InP epitaxy shown in Figure 5.1⁸. The Si_3N_4 layer was found to be a slightly less robust mask, but could be used without the Cr adhesion layer.

Once the dry etching was completed, the remains of the surface mask were removed using a buffered oxide etch. The perforated waveguide was then undercut by placing the sample in a $\text{HCl}:\text{H}_2\text{O}$ (4:1) solution at room temperature. The diluted HCL solution was stirred with a magnetic stirring rod at a rate of 180 rpm. HCl etches InP at a much faster rate than the InGaAsP layers in the waveguide region of the epitaxy in Figure 5.1 providing a high degree of selectivity [92]. One drawback of the HCl etch, however, is the strong crystallographic dependence of the etch rate of InP [93–96]. HCl etches more slowly the In rich (111) crystal planes of InP⁹ thus resulting in a direction dependent etch rate. Owing to this crystallographic etch rate dependence, the final etch geometry formed from a planar template is strongly dependent upon the geometry (concave, convex, crystallographic orientation) of the surface mask used [96]. This has been used to positive ends in the fabrication of InGaAsP based edge-emitting lasers [97,98] where the orientation of the laser stripe mask influences the resulting etched mesa profile¹⁰.

In the formation of the undercut waveguide structures, the InGaAsP waveguide

⁷There is also the possibility that the direct dissociation of Cl_2 into Cl^+ by the Ar^+ beam plays a significant role under these conditions, thus increasing the chemical etching of the InP.

⁸Etch rate varies strongly with the percentage of P in the epitaxial layers, decreasing for higher P mole fraction.

⁹The In rich (111) crystal planes are denoted as $\{111\}\text{In}$ or $\{111\}\text{A}$. The P rich (111) crystal planes are much more reactive and are denoted as $\{111\}\text{P}$ or $\{111\}\text{B}$.

¹⁰This was for planar lithography done on (100) InP, similar to the material used to fabricate the lasers tested in this thesis work.

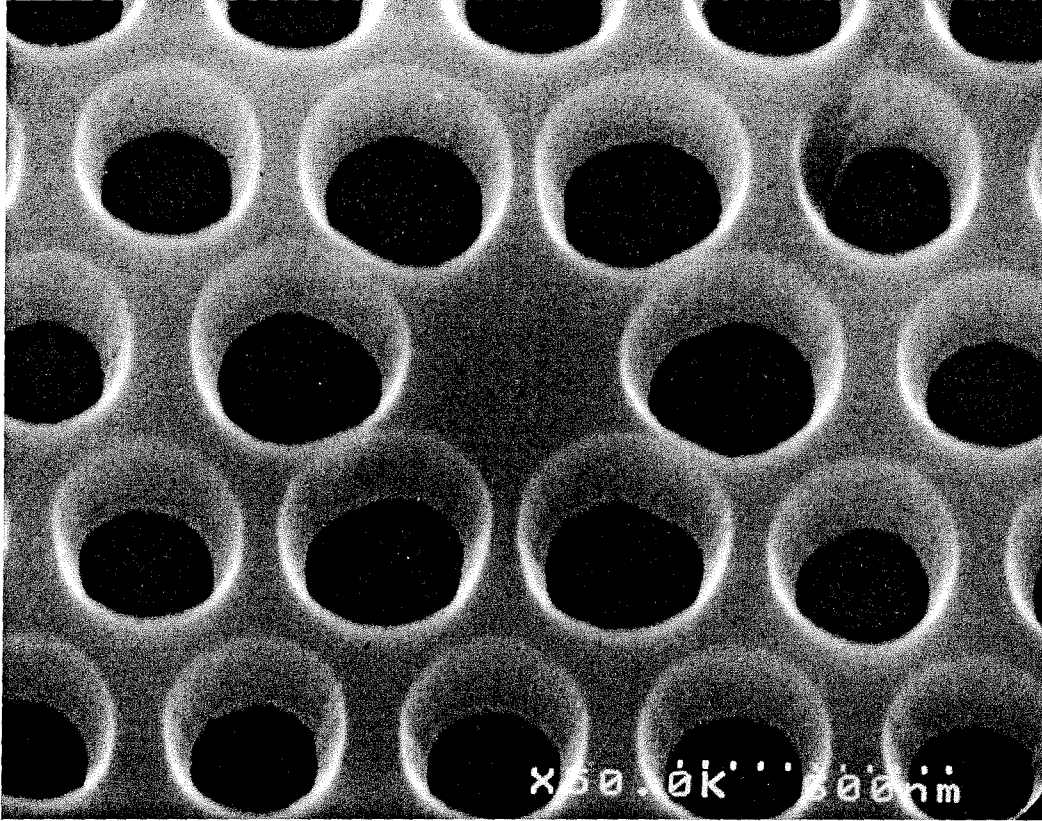


Figure 5.3: SEM micrograph of a defect cavity taken at an angle of 30° . After the HCl etch the etched surfaces appear smooth down to a scale of 5 nm (SEM resolution). The sidewalls of the holes are sloped at 10° from vertical, which can be reduced by optimizing the temperature and gas flow during the chemically-assisted ion-beam etch.

layer above the InP plays the role of an etch mask. For devices designed for the 1500 nm band, the hexagonal array of cylindrical holes have an approximate radius of 150 nm and lattice spacing of 500 nm. The HCl solution enters through the etched holes in the InGaAsP waveguide layer and selectively removes the underlying InP material. In order to completely undercut the perforated waveguide layer, the HCl solution must etch laterally to connect adjacent holes. For convex mask shapes (openings), as in this case, the etch shape is determined by the slowest etch planes [92], which here are the $\{111\}$ In planes. The shape of the HCl wet etch is illustrated in Figure 5.4 for different cross-sectional planes. SEM images of a partially undercut structure are shown in Figure 5.5, in which the crystallographic dependent nature of the HCl etch is evident. The angles of the etch surfaces in Figure 5.5(a) and (b) are roughly 55° and 125° from the surface plane, corresponding to the angles of $\{111\}$ In crystal planes. Complete under-cutting of the photonic crystal waveguide is contingent upon the overlapping of these crystal planes between adjacent holes. This puts additional constraints on the depth of the CAIBE etch into the sacrificial InP layer, as well as the filling fraction¹¹, lattice spacing, and the orientation of the photonic crystal pattern with respect to the InP crystal axes.

In Figure 5.6 the importance of the orientation of the photonic crystal is highlighted. In Figure 5.6(a) the ΓJ direction of the hexagonal photonic crystal lattice is aligned with the $[01\bar{1}]$ direction of the InP lattice, and in Figure 5.6(b) ΓX is aligned along $[01\bar{1}]$. In Figure 5.6(a) long “V grooves” form, resulting in ridges which are connected to the bottom side of the InGaAsP waveguide layer, whereas in Figure 5.6(b) isolated “V groove” pits form. Experimentally, it was found that under-cutting of the perforated waveguide proceeded much more quickly for the alignment shown in Figure 5.6(b). Etch times varied from 5-15 minutes at room temperature and were extremely dependent upon the CAIBE etch depth and r/a ratio of the photonic crystal. The InGaAs layer provided an etch stop for the HCl wet etch, yielding a smooth

¹¹The two-dimensional filling fraction, f , of the photonic crystal structure can be defined as the fractional area taken up by the air holes in the plane of the slab waveguide, and is equal to $2\pi/\sqrt{3}(r/a)^2$ for a hexagonal lattice. The shortest distance between etched holes (openings in the wet etch mask) is then $d_{min} = a(1 - 2(r/a))$.

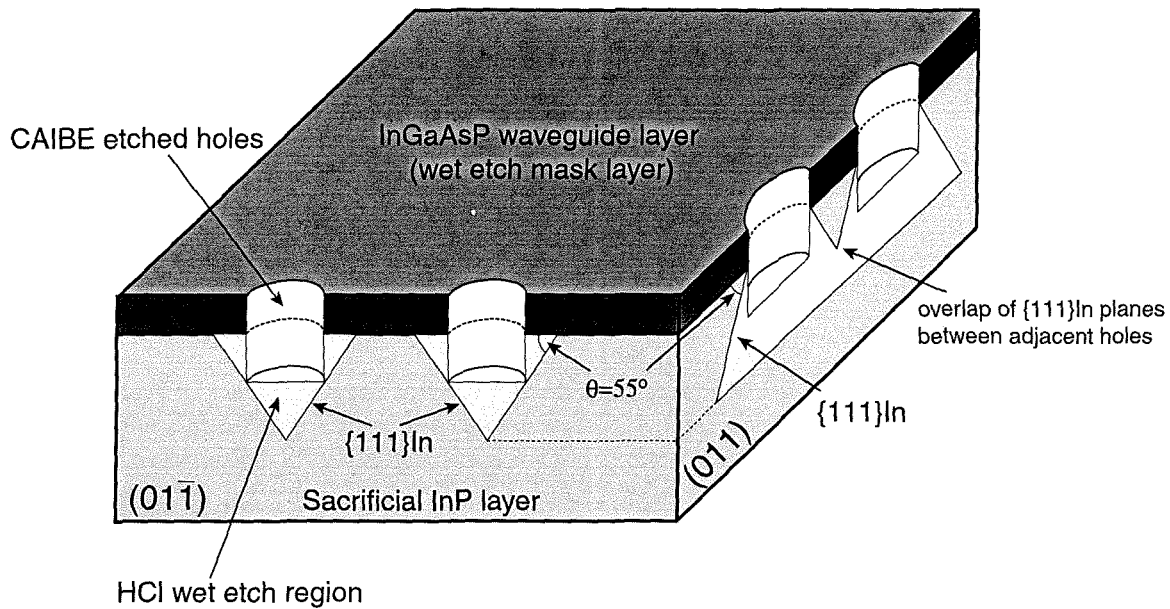


Figure 5.4: Illustration of the shape of the etch pits resulting from the crystallographic dependence of the HCl wet etch. Notice that the size of the “V-grooves” formed are dependent upon the depth of the CAIBE etch.

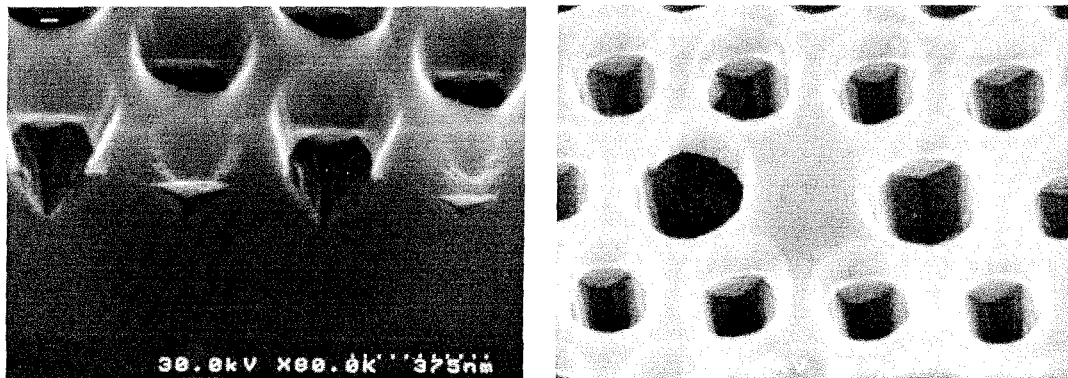


Figure 5.5: SEM images of a partially undercut photonic crystal waveguide structure showing the formation of $\{111\}\text{In}$ crystal plane facets. A cross-section in the $(01\bar{1})$ plane is shown in (a), and a top view (30° tilt) is shown in (b).

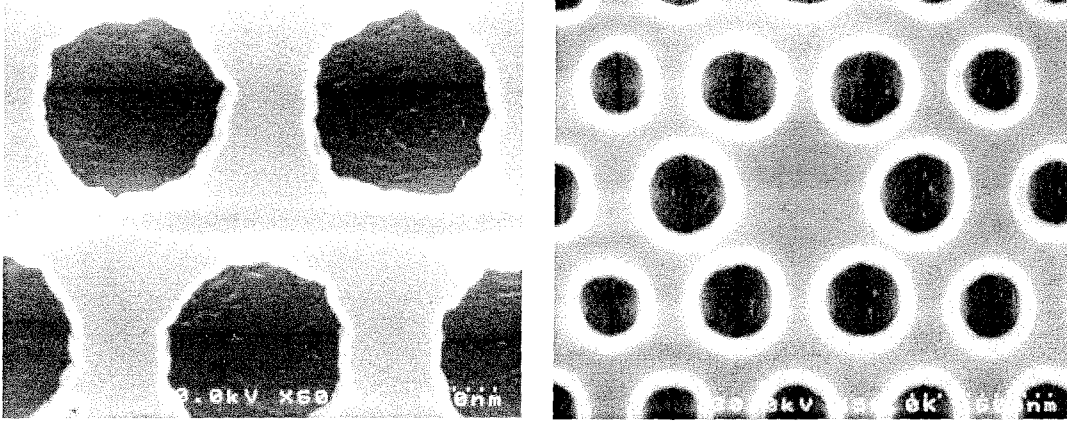


Figure 5.6: SEM images of the wet etch structure formed from photonic crystal patterns with different orientations relative to the InP crystal lattice. In (a) the ΓJ direction of the hexagonal photonic crystal lattice is aligned with the $[01\bar{1}]$ direction of the InP lattice. In (b) the ΓX direction is aligned with the $[01\bar{1}]$ direction.

bottom interface.

Scanning electron microscope (SEM) images of a fully processed defect cavity are shown in Figures 5.7 and 5.8. The resulting undercut membrane is 211 nm thick and approximately $8\ \mu\text{m}$ across. The lattice spacing (a) and the hole radius (r) of the defect cavity is approximately 500 nm and 160 nm, respectively¹². For cavities larger than 10-15 μm in diameter, the undercut membrane collapses during processing. Optical interference patterns in a Normarski differential microscope indicate that even for the defect cavities tested in chapter 6 a slight bowing of the perforated membrane is present.

Although unforeseen prior to device testing, the HCl wet etch step resulted in a number of subtle structural properties important to device performance. One of the limitations of the HCl etch was a restriction of the porosity of the photonic crystal cavities which could be undercut. For the etch depths obtainable with the CAIBE conditions described above ($\sim 350\ \text{nm}$), we found there to be a lower limit value of

¹²At these dimensions a forbidden frequency band-gap opens up for the TE-like (or even) guided modes of the thin membrane which encompasses the 1500 nm emission band of the InGaAsP QWs.

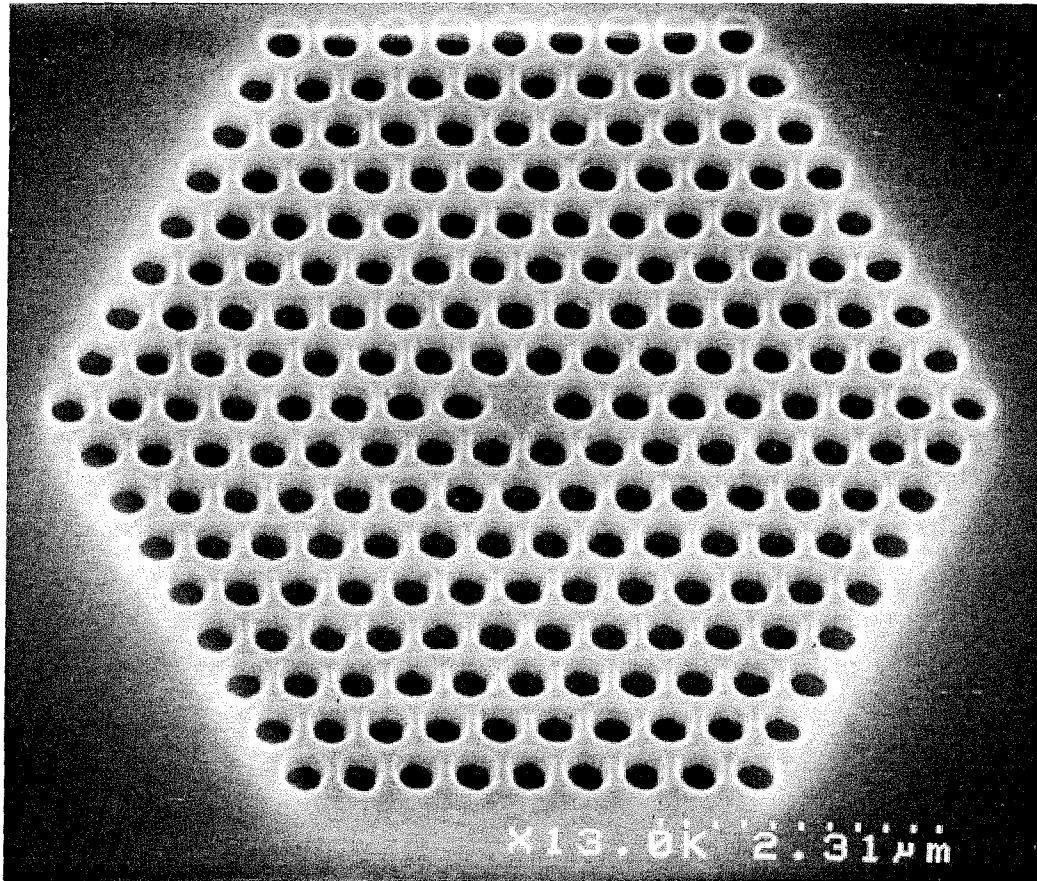


Figure 5.7: Top view of a microfabricated 2D hexagonal array of air holes with a single central hole missing. The inter-hole spacing, a , is 500nm, and the radius of the holes are approximately 160nm.

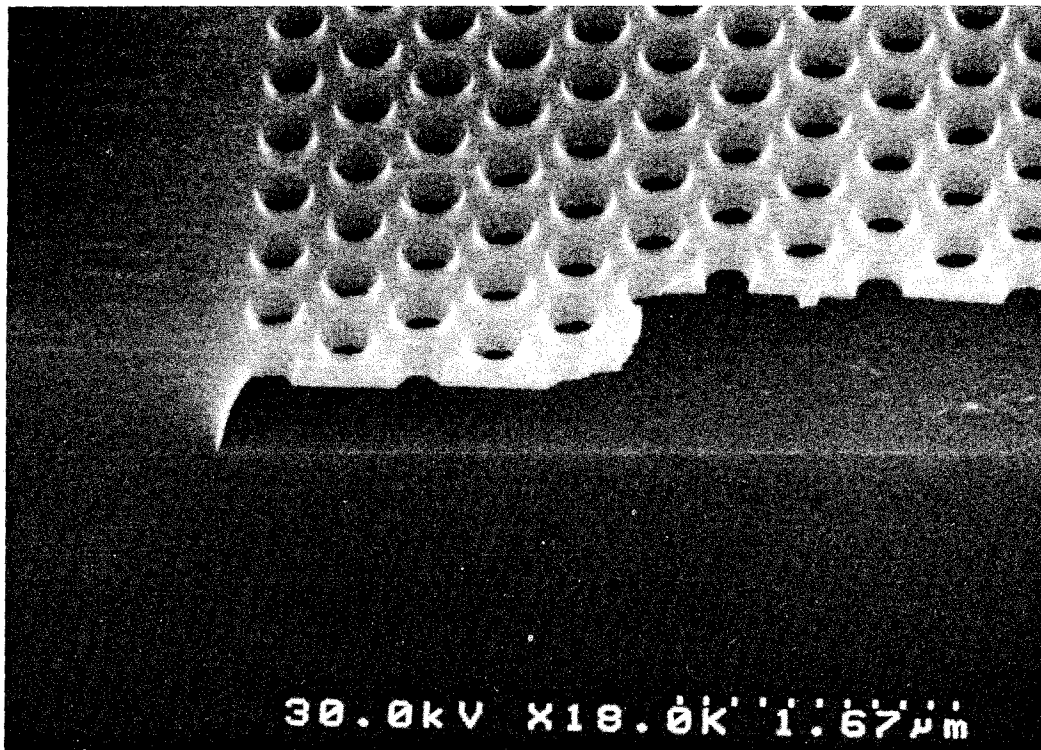


Figure 5.8: Cross-section through the patterned membrane structure. The slab is 211 nm thick after processing. The use of an InGaAs etch stop layer results in a smooth bottom interface below the membrane. For membranes larger than $10\ \mu\text{m}$ a significant bowing occurs and for devices greater than $15\ \mu\text{m}$ the membrane collapses onto the InGaAs etch stop layer.

r/a that could be obtained. For the 1500 nm band photonic crystal structures this value was approximately 0.32. This has a significant impact on the vertical losses of the defect cavities and the largest obtainable Q value as described in section 4.3 of chapter 4.

Also, as with any ion beam etch, damage can be incurred which is detrimental to the optical and electrical performance of semiconductor opto-electronic devices such as the laser [99,100]. The post-CAIBE wet etch removes a layer of 10-20 nm thickness from the potentially damaged etched sidewalls during the under-cutting. This tends to reduce the surface recombination velocity and the non-radiative current associated with surface recombination.

Finally, due to proximity effects during the e-beam lithography, the holes near the center of the photonic crystal cavity had a slightly larger radius than holes near the perimeter. The difference in hole sizes at the center and perimeter of the photonic crystal mirror was further increased by the HCl wet etch. Under-cutting of the cavities started in the center of the pattern (see Figure 5.9) and then slowly proceeded outwards. The central holes, being more open to attack by the HCl, were enlarged even further in comparison to the holes at the perimeter¹³. Holes in the center of the photonic crystal pattern were typically 5-10% larger than in the perimeter, depending on the e-beam dose and severity of proximity effects in the lithography. The grading of the photonic crystal hole radius creates an extended defect region resulting in localized shallow acceptor (SA) modes theoretically predicted in sub-section 4.4.1 and experimentally measured in section 6.1.

¹³Although HCl is a highly selective etch, etching of the active InGaAsP layer still occurred and proceeded at an increased rate when exposed more fully after under-cutting.

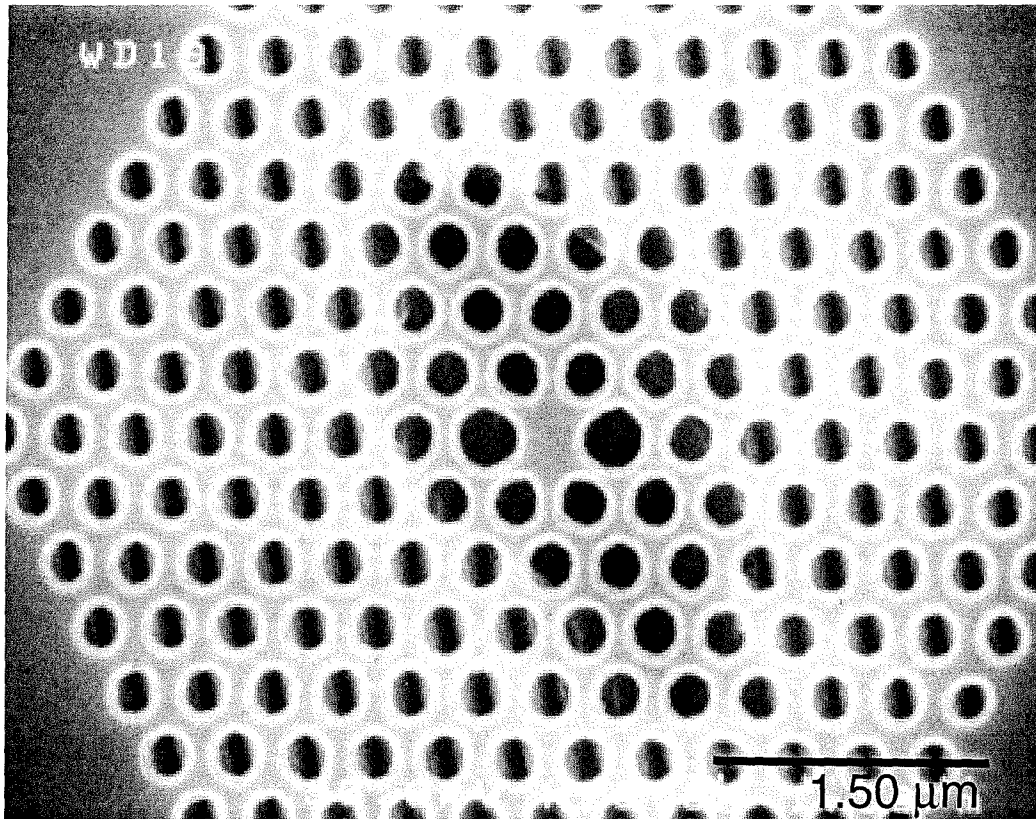


Figure 5.9: SEM image showing how the under-cutting of the patterned waveguide proceeds from the center, where the holes are largest, towards the edge of the patterned area.

Chapter 6 Photoluminescence Measurements

Characterization of the photonic crystal defect cavities was performed by optically pumping the multi-quantum-well InGaAsP layers within the waveguiding layer of the cavity. As described earlier, light emission from the quantum-wells has a wavelength in the 1500 nm band at room temperature. By locally exciting a defect cavity and analyzing the resulting 1500 nm emission, one can determine the internal resonant mode structure of the cavity. The defect cavity acts as a filter, modifying the spectral, spatial, and polarization properties of the emitted light from the quantum-wells. Subtle changes in the symmetry, lattice constant, and porosity of the defect cavity have a significant impact upon the cavity resonances. By fabricating and testing a wide variety of defect cavity geometries, the spectral “puzzle” can be pieced together and resonant modes can be classified and related to the theoretically calculated cavity modes of chapter 4.

In each of the measurements described below, a large array of defect cavities was fabricated with varying lattice spacings and hole sizes in order to cover a wide range of wavelengths of the defect mode resonance. Each of the defect cavities consists of eight periods of the photonic crystal surrounding a single removed hole in the center. With this number of periods of the photonic crystal mirror, the defect modes theoretically emit quite strongly in the vertical direction due to the high index contrast of the photonic crystal and the resulting small leakage of light in-plane. This allows for light to be collected from the top of the sample.

The samples were mounted on an X-Y-Z stage and the defect cavities were optically pumped from above at an angle normal to the sample surface. A high numerical aperture, long working distance 100X objective lens was used to both image the defect cavities and to focus the optical pump beam. An 830 nm semiconductor laser diode

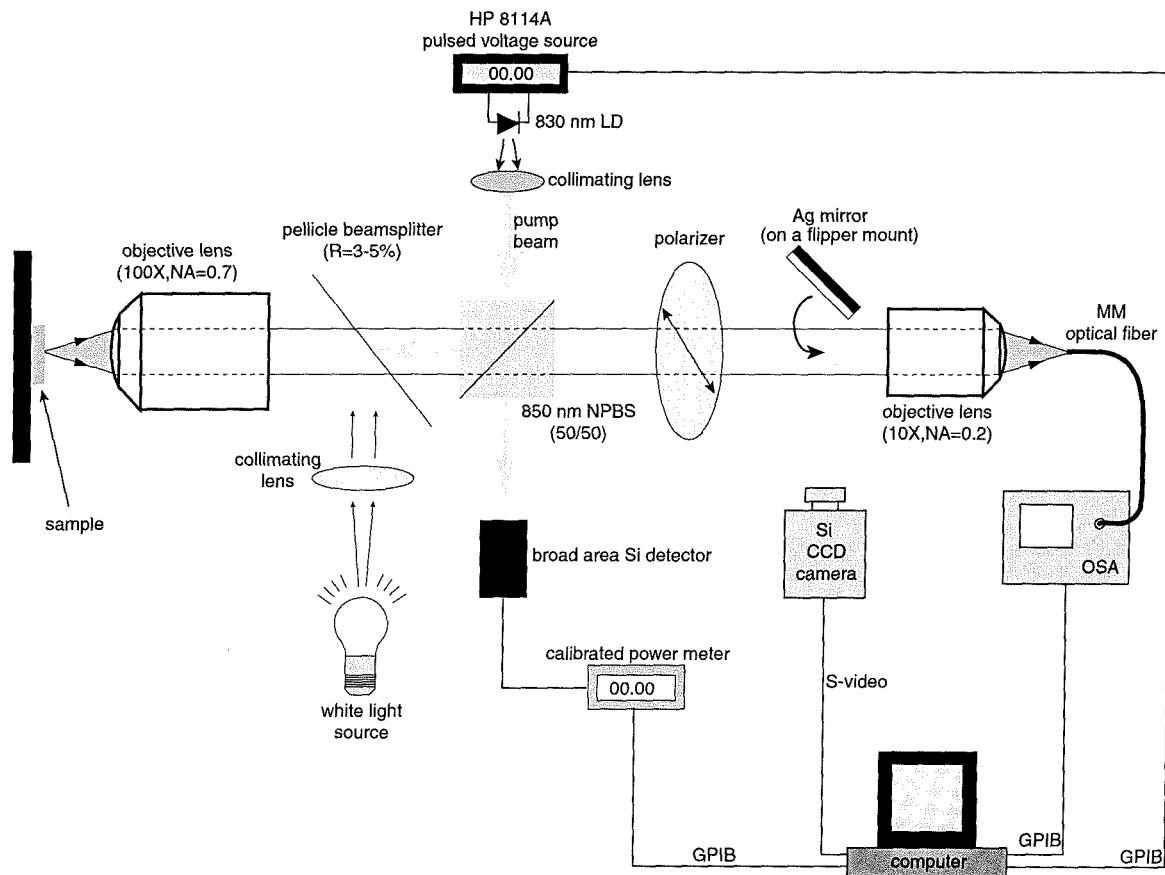


Figure 6.1: Photoluminescence measurement set-up used to characterize the photonic crystal defect cavities.

was used as the pump source in this experiment. The photoluminescence (PL) was also collected by the objective lens and then fed into an optical spectrum analyzer. A GaAs filter was placed just before the optical spectrum analyzer to separate the pump from PL. The spot size of the beam on the sample surface could be adjusted down to $1\ \mu\text{m}$; however, optimization of the intensity of the collected light depended on the spatial extent and profile of the resonant mode being analyzed. A schematic of the photoluminescence set-up is shown in Figure 6.1.

With the pump beam focused to a $4\ \mu\text{m}$ spot, the PL was first measured from an unprocessed area on a sample which contained several arrays of defect cavities. In Figure 6.2 the PL spectra is shown for various duty cycles and pump powers. At low pump powers (bottom plot) the emission is peaked at $1545\ \text{nm}$ which corresponds to

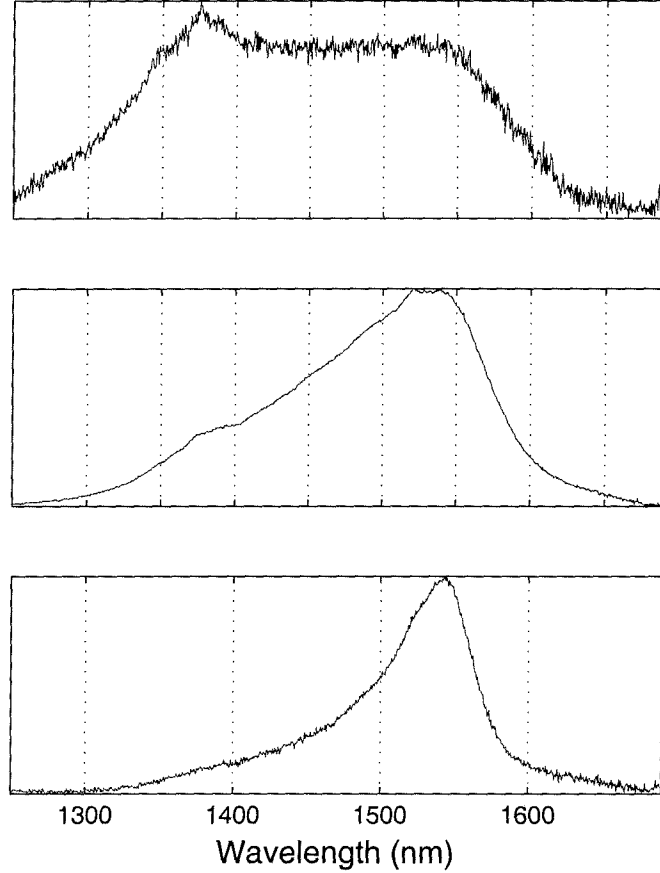


Figure 6.2: PL from an unprocessed area is shown for three different pumping conditions ($4\ \mu\text{m}$ pump spot size). The bottom plot corresponds to $20\ \mu\text{W}$ CW pumping. In the middle plot the peak pump power is $170\ \mu\text{W}$ with a 50% duty cycle. The PL in the top plot was taken using 10 ns pulses with a $3\ \mu\text{s}$ period at a peak pump power of 7 mW (duty cycle $\sim 0.3\%$).

the first energy level in the QWs. As the pump power is increased (middle plot), a peak in the emission spectrum appears at 1380 nm corresponding to the second level in the QWs. The top plot was obtained using similar pumping conditions as those used to obtain lasing in the defect cavities (10 ns pulses, 0.3% duty cycle). The PL is very broad in this case due to heating and band filling, providing almost a 400 nm wide emission range over which the photonic crystal cavities can be characterized.

6.1 S-Defect Cavity

The first cavity geometry tested was that of a symmetric cavity (S) with a central hole removed. The symmetric defect cavity retains the point symmetries of the lattice which is D_{6h} . As shown in chapter 4, there are theoretically no localized resonant modes for the odd or TM-like states of the defect cavities owing to the lack of a guided mode band-gap. A band-gap does form for the fundamental even modes of the perforated waveguide, and these modes are predominantly TE-like within the waveguide core. The point symmetry group reduces to C_{6v} for the even modes. The localized defect modes can then be classified as IRREPS of C_{6v} (see table 3.4).

The PL from the defect cavities is markedly different than that from the unprocessed areas. The emission spectrum from a symmetric defect cavity with a lattice spacing of 525 nm is shown in Figure 6.3. The emission can be seen to be strongly frustrated except for two peaks. The broad shorter wavelength peak at 1425 nm corresponds to spontaneous emission from the degenerate deep donor (DD) dipole-like modes. The narrow longer wavelength peak at 1580 nm is the more extended shallow acceptor (SA) mode laser line.

Spectra from several defect cavities with lattice spacing ranging from 570 nm to 480 nm ($r/a \sim 0.325$) is shown in Figure 6.4(a). By plotting the emission spectra versus normalized frequency as in Figure 6.4(b) we can piece together the different spectra and cover the entire guided mode photonic band-gap of the perforated waveguide. The guided mode band-gap is seen to extend from a normalized frequency of nearly 0.30 all the way to a normalized frequency of 0.42, where the SA and SD resonance peaks are used as approximate positions of the valence and conduction bands, respectively. This corresponds to a fractional band-gap ($\Delta\omega_n/\omega_n$) of nearly 30%. The slight shifts in normalized frequency of the DD dipole modes is a result of the difference in normalized slab thickness, d/a , for the three devices (see section 6.2).

At room temperature, lasing was limited to the SA mode due to its higher Q-factor as discussed in chapter 4. The lasing threshold of the defect modes was a function

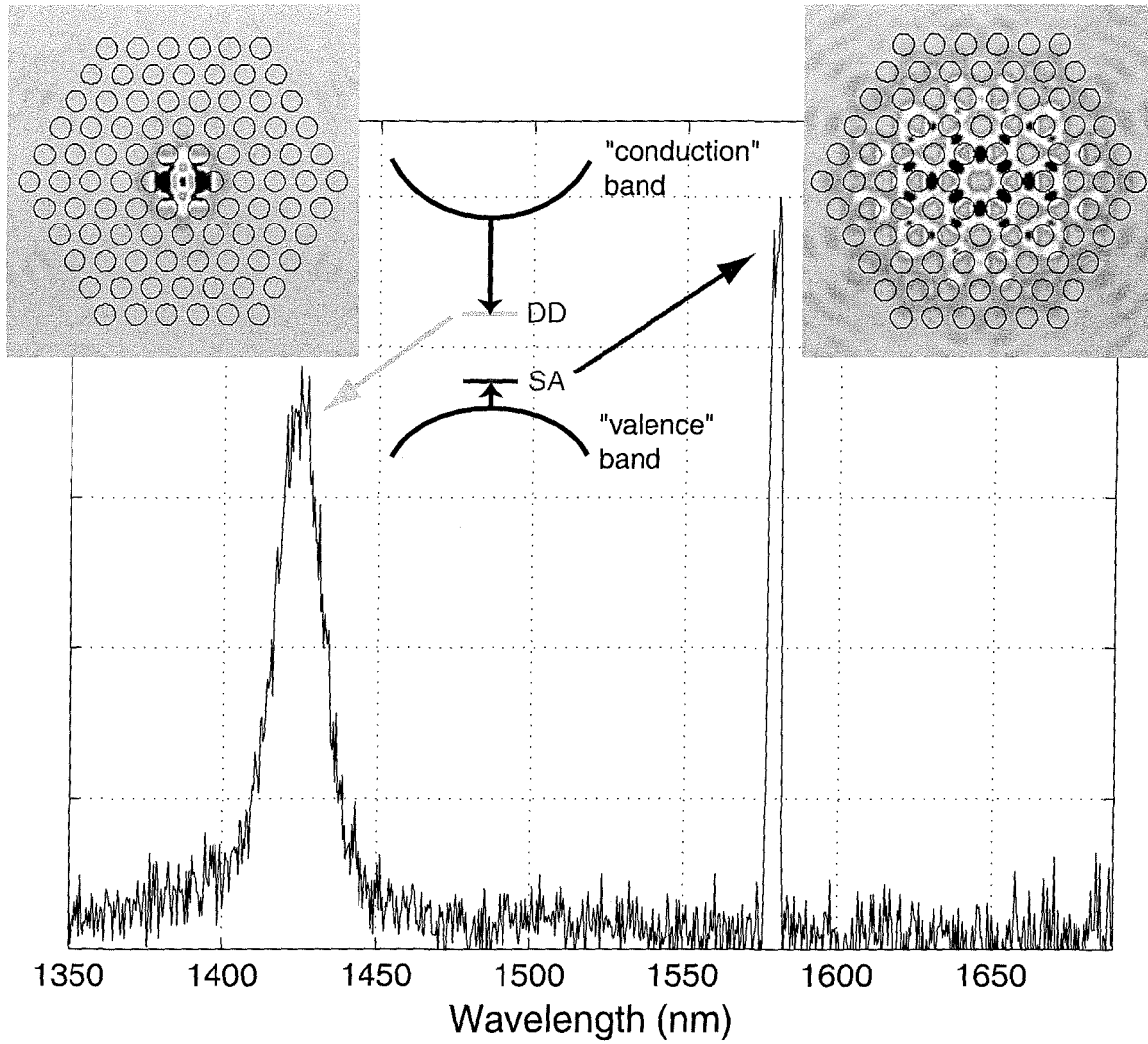
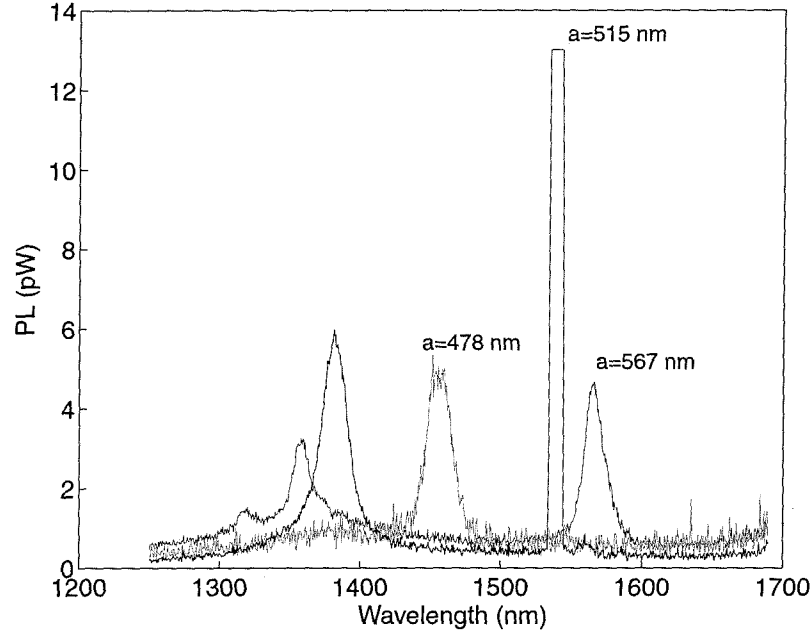
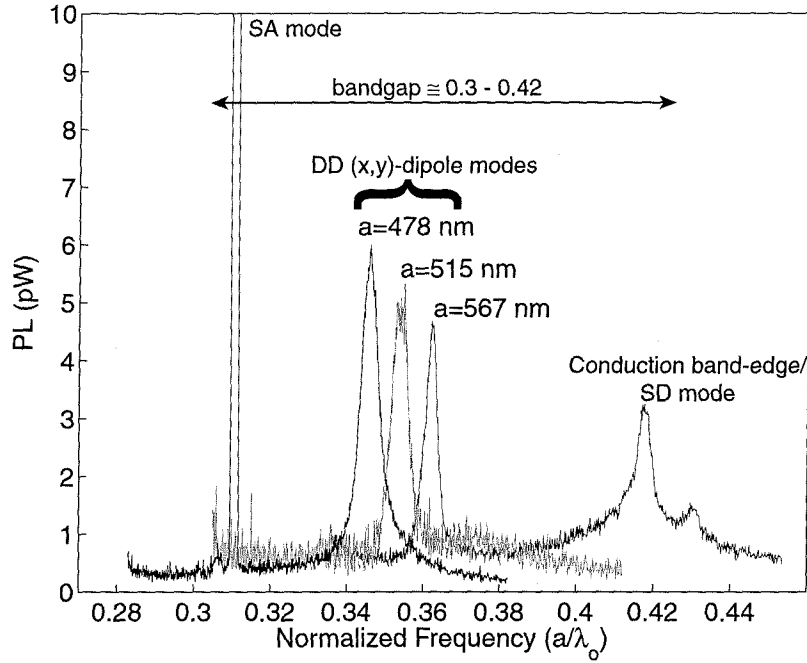


Figure 6.3: Near-threshold photoluminescence from a symmetric defect cavity with $a = 515$ nm, $r/a \approx 0.34$, and $d/a = 0.409$. The two resonance peaks correspond to the degenerate DD S-B₁₀ and S-B₂₁ modes (x,y dipole-like modes, respectively), and the SA S-B₂₀ cavity mode.



(a) Emission vs. wavelength



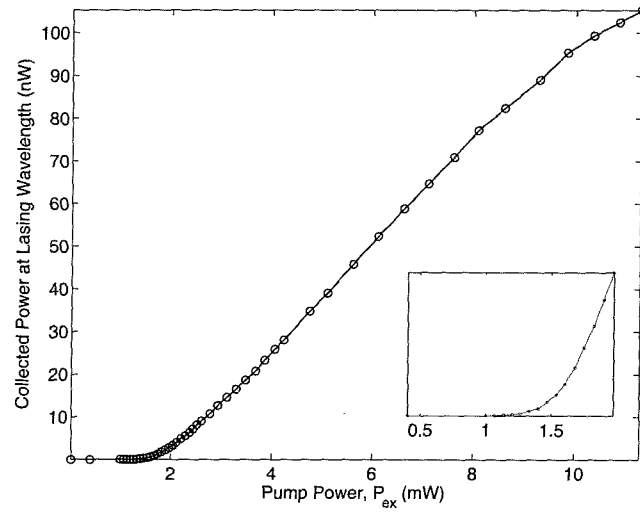
(b) Emission vs. normalized frequency

Figure 6.4: PL from a series of S defect cavities with lattice spacing equal to 570, 515, and 480 nm ($d/a = 0.3721 - 0.4416$). The porosity of the cavities were nearly identical (as measured by SEM) with an r/a ratio of 0.325.

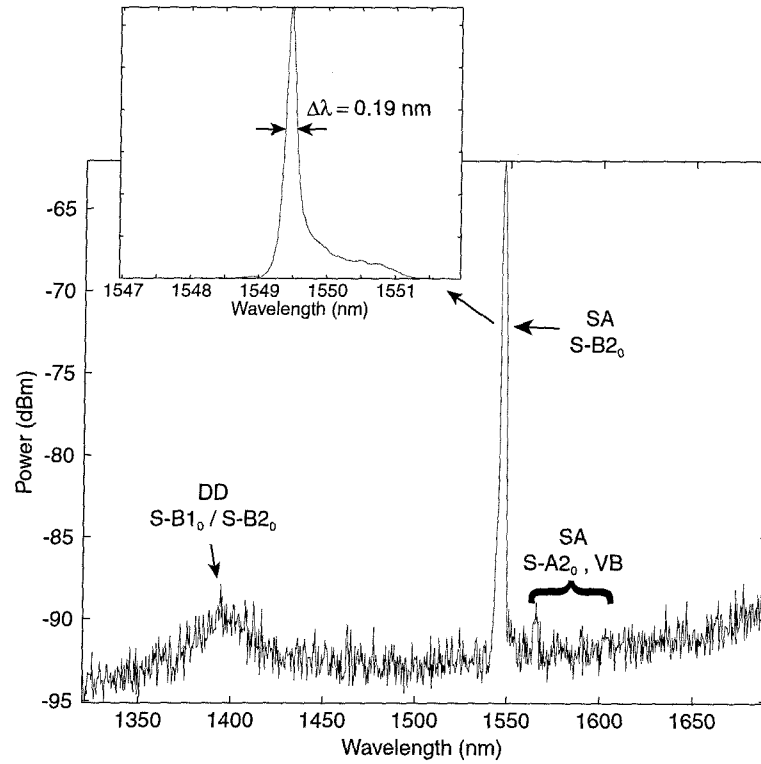
of the position and size of the pump beam. This can be attributed to the fact that the QWs in the photonic crystal mirror surrounding the defect are absorbing if not pumped to transparency. If the pump beam spot size only extends over a few lattice periods surrounding the defect region then absorption in the 2D photonic crystal mirror will limit the Q of the defect cavity modes, resulting in an increased laser threshold. As the pump is de-focused and the spot size increases to cover more of the defect cavity, the intensity in the center of the cavity decreases to a point where the threshold pump power begins to rise again. For the SA defect modes a spot size of approximately $4\text{ }\mu\text{m}$ consistently provided the lowest lasing threshold.

A plot of the collected power versus the pump power (L-L) for a symmetric defect cavity exhibiting low threshold pump power is shown in Figure 6.5(a). The laser remains single mode over the entire pumping range of this plot. The external threshold pump power (peak) is approximately 1.5 mW, from which we estimate an absorbed power of $500\text{ }\mu\text{W}$ ($\sim 3.1\text{ kW/cm}^2$). The laser line becomes linearly polarized (measured in the plane of the slab) above threshold. The fiber coupled average power from some of the defect laser cavities is as high as 4 nW, which corresponds to an approximate peak power of $1\text{ }\mu\text{W}$. This is roughly 30dB above the DD resonance peak (Figure 6.5(b)). Lasing action occurred for duty cycles up to 1% (30 ns pulses); however, threshold pump powers were significantly increased due to heating in the membrane. The relatively large threshold powers are most likely a result of the poor heat sinking of the membrane cavity. Non-radiative Auger recombination exponentially increases with temperature and is especially problematic in small band-gap materials such as InGaAsP [101].

The linewidth of the SA (S-B₂₀) defect mode narrows from 1.1 nm just below threshold ($Q \sim 1500$) to 0.15 nm at twice threshold. An estimate of the Q of a resonant mode can be made by measuring the linewidth of the resonance at transparency. From an approximate absorbed threshold pump power of $500\text{ }\mu\text{W}$, the threshold carrier density within the defect cavity is estimated to be three times the transparency carrier density (see Figure 6.7(b)). For the lowest threshold devices



(a) Plot of the collected power at the lasing wavelength versus input pump power (peak external value).



(b) Photoluminescence spectra of SA S-B₂₀ lasing line. External peak pump power is 9.26 mW (110 μ W average).

Figure 6.5: SA S-B₂₀ laser mode in a symmetric defect cavity with dimensions $a = 515$ nm, $r/a = 0.351$, and $d/a = 0.409$.

the average detected power was too small¹ to make accurate linewidth measurements near the transparency pumping level. For several of the higher threshold devices, however, linewidths of ~ 2.5 nm were measured at pump levels which were 2.5 times below threshold. This corresponds to an approximate Q value of 600 for the higher threshold S-B2₀ defect modes, consistent with the FDTD calculated values of chapter 4.

To get an estimate of the influence of non-radiative recombination on the lasing threshold in the photonic crystal defect cavities a model relating excited state carrier density in the active region to optical pumping power is needed. A simple rate equation² for the excited state carrier density in the quantum-well, taking into account surface recombination at the etched surfaces of the photonic crystal and Auger recombination, can be used to relate the pumping rate of electrons into the quantum-well to the steady state carrier density:

$$\Lambda_e = AN + BN^2 + CN^3. \quad (6.1)$$

Λ_e is the electron pump rate into the quantum-well active region, N is the carrier density, and A , B , and C are the surface recombination coefficient, spontaneous emission coefficient, and Auger recombination coefficient, respectively.

The effective electron current reaching the quantum-well active region is proportional to the number of absorbed photons per unit time,

$$\Lambda_e = \frac{1}{V_a} \eta_i \eta_{abs} \frac{\Lambda}{\hbar \omega_p}. \quad (6.2)$$

¹Due to the temperature sensitivity of the membrane cavities duty cycles much above 1% significantly reduced the PL.

²This model assumes that surface recombination can be modeled as a single particle process linear in carrier density, spontaneous emission is quadratic in carrier density (electron density \approx hole density), and that Auger recombination is a three particle process proportional to the carrier density cubed.

In eq. (6.2), Λ is the incident optical pump power at angular frequency ω_p , V_a is the volume which is being pumped, η_i is the efficiency of the pumping into the quantum-well states, and η_{abs} is the absorption efficiency of the incident pump beam.

The density of carriers required for lasing is determined by the amount of gain needed to compensate the modal loss:

$$\Gamma_{xy}\Gamma_z g_{o,th}^t = \gamma_{ph}, \quad (6.3)$$

where $g_{o,th}^t$ is the temporal material gain per unit time, γ_{ph} is the modal loss rate, and Γ_{xy} and Γ_z are the in-plane and vertical confinement factors of the defect mode with the active region, respectively. The temporal material gain can be related to the carrier density through the differential gain:

$$g_o^t = (N - N_o)g'v_g, \quad (6.4)$$

where N_o is the transparency carrier density, g' is the per unit length differential gain, and v_g is the group velocity. Solving for the threshold carrier density in eq. (6.3) yields,

$$N_{th} \approx N_o + \frac{\gamma_{ph}}{g'v_g\Gamma_{xy}\Gamma_z}. \quad (6.5)$$

Substituting the threshold value for carrier density into eq. (6.1) one now has a relation between the required pump power needed to reach threshold and the cavity Q.

Based upon this model, a theoretical estimate of the threshold pump power versus defect mode Q-factor for active regions of 1,2,3, and 4 quantum-wells is shown in Figure 6.6. The values of the parameters used in the calculation are given in Table 6.1. For the defect cavities studied in this work we are most likely operating in the

low-Q regime (500-1500) of the threshold curve in Figure 6.6. The lowest thresholds are consequently obtained, in theory, for the largest number of quantum-wells, four. The threshold pump powers for the four quantum-well devices are in the range of a milliwatt for Q values near 10^3 , consistent with the experimentally measured threshold powers. A breakdown of the non-radiative and radiative threshold currents for the four quantum-well device is shown in Figure 6.7(a). In the low-Q regime Auger recombination and surface recombination dominate the radiative spontaneous emission current. In fact, owing to the poor thermal heat-sinking of the suspended membrane, the Auger recombination current is most likely underestimated as the calculations are based upon room temperature values for the Auger coefficient.

Table 6.1: Parameters used to estimate the threshold pump power of localized defect modes in the MQW InGaAsP perforated membrane.

Param.	Description	Value/Relation
Λ	optical pump power	Watts
d	slab waveguide thickness	211 nm
t_{QW}	QW thickness	9 nm
n_{QW}	# of QWs in waveguide	[1,2,3,4]
Γ_z	QW vert. confinement factor	[0.0663,0.1308,0.1909,0.2467] ^a
Γ_{xy}	lateral mode confinement factor	1
λ_{PL}	emission wavelength	1500 nm
λ_p	pump wavelength	830 nm
γ_{ph}	cavity photon loss rate	ω_{PL}/Q [s ⁻¹]
N	carrier density	$N(\Lambda)$ [cm ⁻³]
N_{tr}	transparency carrier density	1e18 cm ⁻³ ^b
g	differential gain	2.5e-16 cm ² ^b
g_o^s	spatial material gain	$(N - N_{tr})g'$ [cm ⁻¹]
v_g	waveguide group vel. in gain meas.	$c/n_g \approx 1e10$ cm/s ^c
g_o^t	temporal material gain	$g_o^s v_g$ [s ⁻¹]
v_s	surface recomb. velocity	5e3 cm/s ^d
B	radiative coeff.	0.24e-10 cm ³ /s ^b
C	Auger coeff.	3.0e-29 cm ⁶ /s ^b
R_p	pump radius	1.5 μ m
r	hole radius	160 nm
a	lattice spacing	515 nm
f_a	fractional area intercepting beam	0.61
A_a	in-plane active region area	$\pi R_p^2 f_a$ [cm ²]
V_a	active region volume	$A_a t_{QW} n_{QW}$ [cm ³]
n_h	number of etched holes pumped	~ 36
a_s	active region etched surface area	$n_h(\pi r^2)$ [cm ²]
δ_a	active region surface-to-volume ratio	a_s/V_a [cm ⁻¹]
A	surface recomb. coeff.	$\delta_a v_s$ [s ⁻¹]
R	reflectivity of InGaAsP surface	0.30
p_{abs}	FP-like absorption factor	$(1 - R)(1 - e^{-\alpha d})/(1 - R e^{-\alpha d})$
η_{abs}	pump absorption efficiency	$\sim f_a p_{abs}(1 + R(1 - p_{abs})) = 0.29$
η_i	internal pumping efficiency	1 (optically pumped)

^a Calculated using slab waveguide mode profile.

^b From Ref. [89].

^c Typical effective index of a single-mode waveguide assumed.

^d From ref. [64].

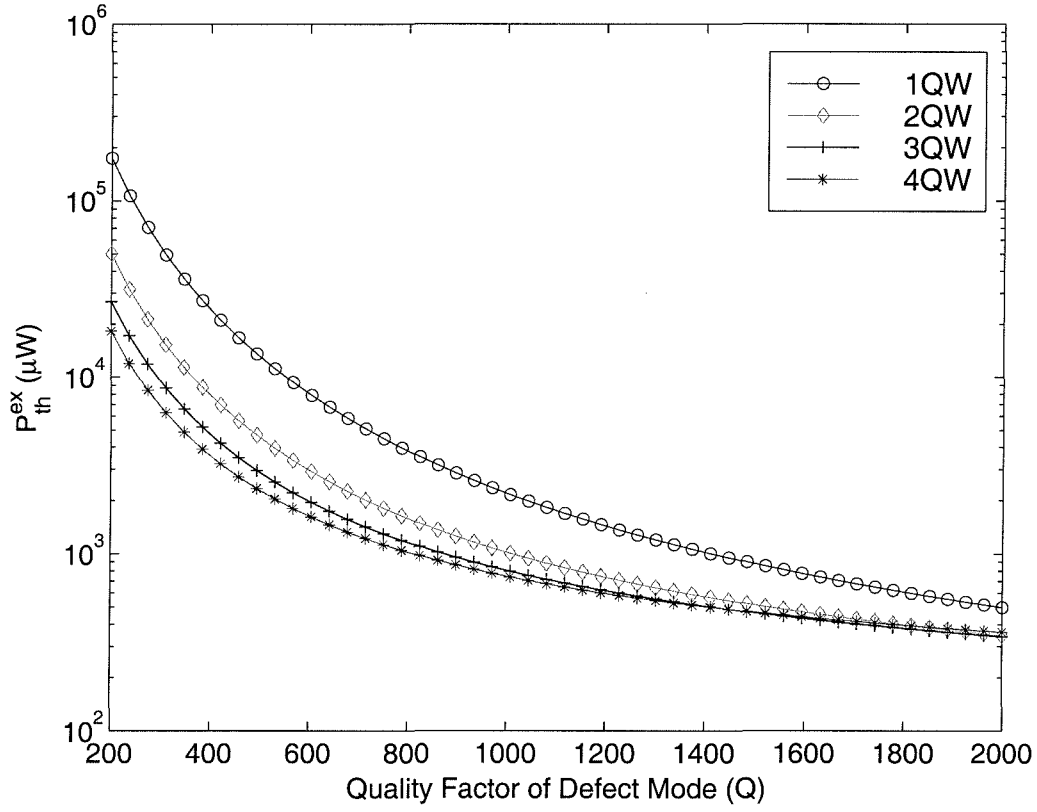
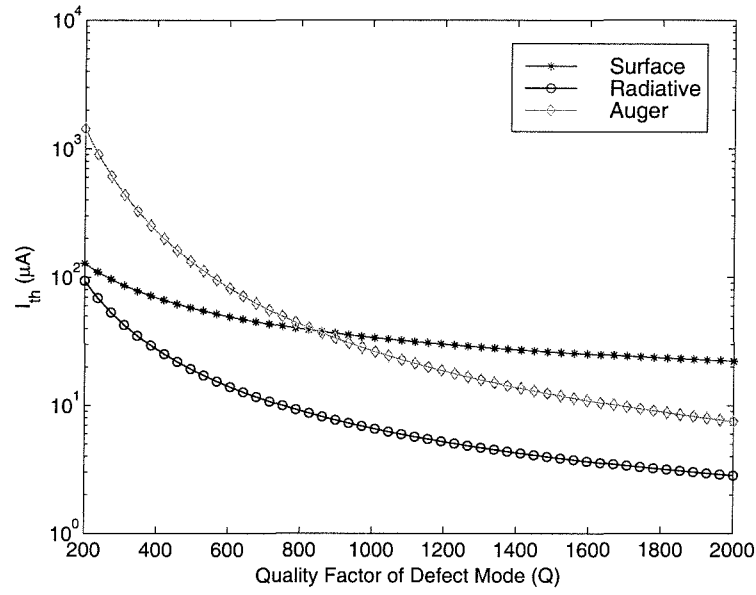
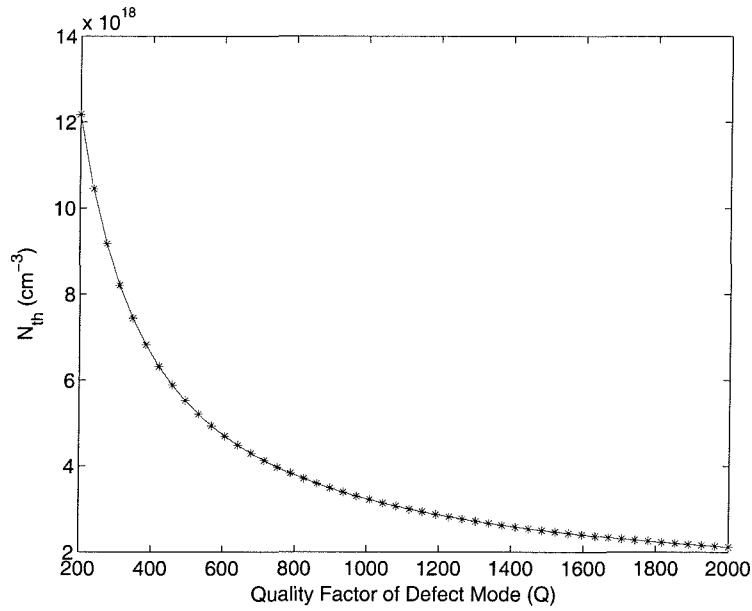


Figure 6.6: Estimated external lasing threshold optical pump power vs. mode Q for 1,2,3, and 4 QW active regions at room temperature using parameters in Table 6.1.



(a) Auger, surface recombination, and radiative current components at threshold.



(b) Threshold carrier density.

Figure 6.7: Estimated threshold current and carrier density vs. mode Q for a four QW active region at room temperature (see Table 6.1).

6.2 Lithographic Wavelength Tuning

As mentioned in the introduction, one of the important features of the 2D photonic crystal defect cavity is the ability to control, through planar lithography, the wavelength, emission direction, and polarization of the lasing mode. The combination of high device density and lithographically controllable light emission make this technology interesting for a variety of laser/detector array applications such as beam-steering, beam-shaping, and multi-wavelength optical signal processing. In this section lithographic techniques are used to produce a high-density multi-wavelength 2D laser array of photonic crystal defect cavities. This experiment serves to determine both the wavelength tuning characteristics of the defect cavity lasers, as well as the accuracy and limitations of the fabrication process.

Wavelength Tuning Parameters

The two-dimensional photonic crystal cavities used in the laser array have a symmetric defect region (S-type). As discussed in sub-section 4.4.1, a number of high Q cavity modes form within the frequency band-gap of the photonic crystal host. These cavity modes are highly sensitive to the local cavity geometry as well as the surrounding photonic crystal environment. In the host photonic crystals studied here there are three geometric tuning parameters: lattice spacing a , hole radius r , and slab thickness d . In order to understand the tuning affects of the photonic crystal geometry on the cavity modes, it is most convenient to normalize all structural parameters to the inter-hole spacing, a . The photonic crystal slab is then described by its normalized hole radius, r/a , and its normalized slab thickness, d/a . Due to the scaling properties of Maxwell's equations a normalized eigen-frequency can also be defined:

$$\omega^n = \frac{a\omega}{2\pi c} = \frac{a}{\lambda_o}, \quad (6.6)$$

where ω is the angular frequency, c is the speed of light, λ_o is the wavelength in

vacuum, and the superscript n denotes normalized frequency. For fixed r/a and d/a the wavelength simply scales with lattice spacing.

Since the waveguide thickness of the laser cavities is fixed in our experiment, the ratio d/a will vary with lattice spacing. The effects of vertical waveguiding on the photonic crystal slab modes can be approximated by separating the in-plane and vertical components of momentum,

$$\omega^2 \approx \omega_{2D}^2 + \left(\frac{c}{n_{eff}^z} \right)^2 k_z^2, \quad (6.7)$$

where ω_{2D} is the mode frequency in the 2D case (in-plane curvature only), $k_z \equiv 2\pi/\lambda_z$ represents the curvature due to the vertical guiding, and n_{eff}^z is an effective index determined by the field pattern of the 2D mode and its overlap with dielectric material. For the fundamental vertically guided modes of the photonic crystal slab, assuming strong confinement, $\lambda_z \approx 2d$. The frequency of a mode in the photonic crystal waveguide, after normalization using eq. (6.6), can then be written as

$$\omega^n \approx \sqrt{(\omega_{2D}^n)^2 + \left(\frac{1}{2n_{eff}^z} \right)^2 \left(\frac{d}{a} \right)^{-2}}. \quad (6.8)$$

Thus for fixed r/a and fixed d the normalized frequency increases with increasing lattice spacing and the wavelength varies sub-linearly with lattice spacing.

The variation of the mode frequency with r/a is more complicated; however, intuitively as r/a increases the mode frequency will also increase due to the reduced filling fraction of high dielectric material [40]. In the experiment described below all three parameters a , d/a , and r/a are varied in the laser cavities in order to tune the wavelength of the modes of the single defect photonic crystal cavities.

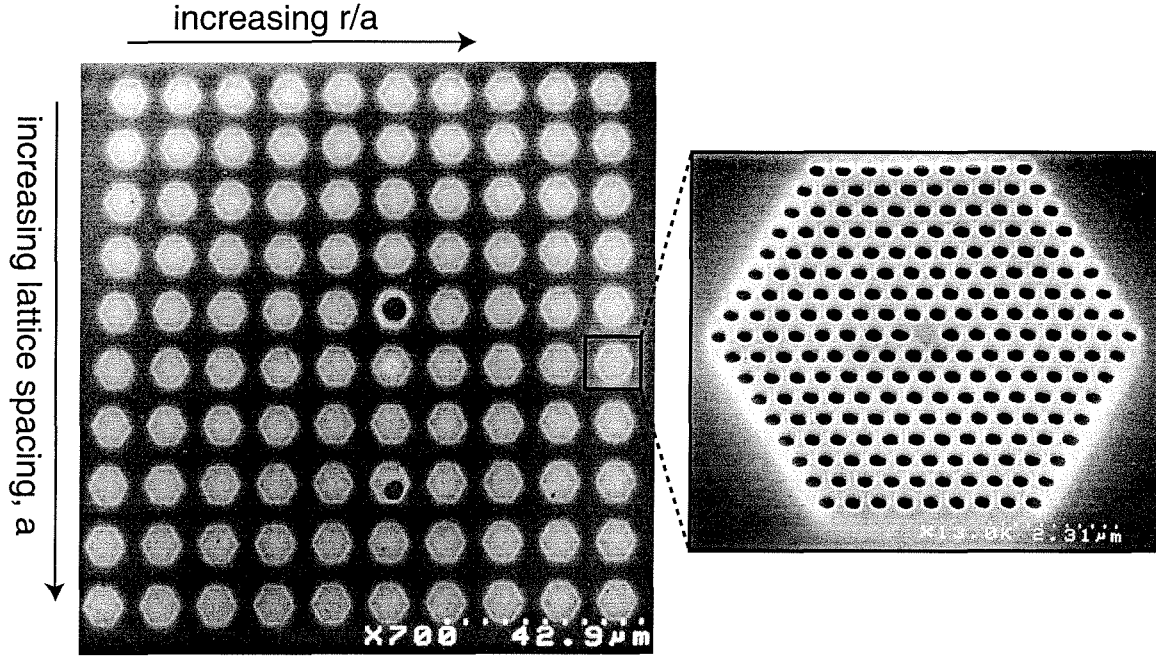


Figure 6.8: SEM micrograph of the photonic crystal laser array. The lattice spacing varies with row number, and the hole radius varies with column number. An expanded view of an individual defect cavity is also shown on the right.

Laser Array Characteristics

An array of S-type defect cavities was fabricated with varying lattice spacings and hole sizes in order to cover a wide range of wavelengths of the defect mode resonance. A scanning electron microscope image of the laser array is shown in Figure 6.8. The patterned membrane diameter varied with the lattice spacing but was on average $8\mu\text{m}$, and the devices were spaced by $10\mu\text{m}$. The defect cavity lattice spacing was varied from 564 nm down to 470 nm , and for each different lattice spacing a series of devices with r/a ratios between 0.30 and 0.40 were fabricated.

The sample was mounted on an X-Y-Z stage and the defect cavities were optically pumped from above at an angle normal to the sample surface. Similar to previous measurements, an 830 nm semiconductor laser diode was used as the pump source. A $100\times$ objective lens was also used to focus the pump beam to a $4\mu\text{m}$ spot as well as to collect the photoluminescence (PL). Lasing was single-mode for each cavity

tested, and only occurred off of the longer wavelength S-B₂₀ mode resonance peak at room temperature. This is due to the weak localization and extended nature of the SA mode which results in less vertical diffraction loss and a theoretical Q which is five times that of the strongly localized DD modes. The lasing threshold pump powers were in the 1.5-3 mW range (external peak pump power), and typical peak fiber coupled output power from the defect laser cavities was about 0.5 μ W. Heating in the undercut membrane limited lasing action to pump pulses shorter than 30 ns (duty cycle < 1%) at room temperature.

A plot of the spectra of a series of defect lasers with lattice spacing fixed at 490 nm and varying hole radius is shown in Figure 6.9. The longer wavelength laser line is roughly 30 dB above the shorter wavelength DD resonance peak. The lasing wavelength tunes between 1520 nm and 1580 nm with an inter-wavelength spacing of 10 nm as the r/a ratio is varied from 0.38 to 0.32. This corresponds to a change in diameter of the air holes of 5 nm from device to device³. The DD resonance peak is also seen to tune with r/a as expected.

A series of measurements were also performed on defect cavities with r/a fixed at 0.38 and varying lattice spacings. The defect lasing peak was successfully tuned from 1500 nm to 1625 nm with a wavelength spacing of roughly 30 nm. For devices with lattice spacings above 530 nm lasing action did not occur as the SA mode is tuned out of the gain bandwidth of the active material. A plot of the wavelength of the SA mode laser peak and DD mode peak versus lattice spacing is shown in Figure 6.10. The normalized frequency is seen to decrease with increasing d/a as predicted by eq. (6.8). Finite-difference time-domain (FDTD) simulations of the tuning of the cavity modes were also performed and are shown as solid curves in Figure 6.10.

³The limit of our lithography system.

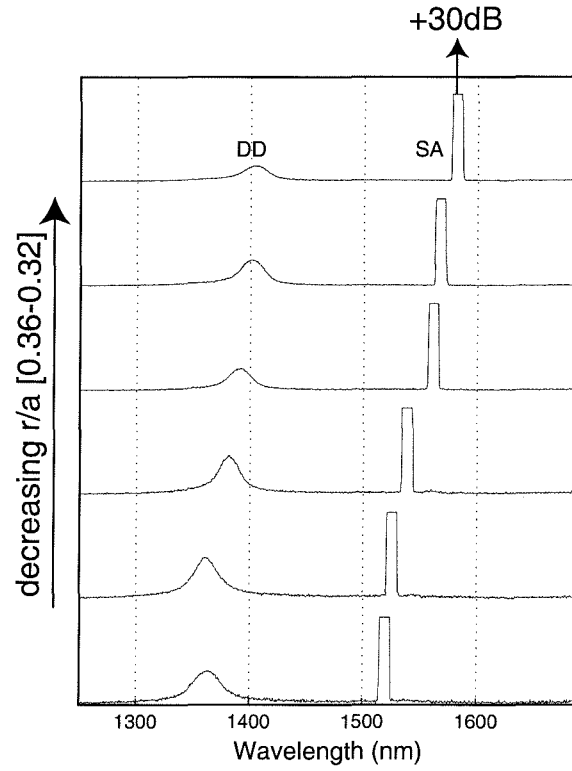


Figure 6.9: Tuning of the laser wavelength versus r/a . The lattice spacing in this case is fixed at 490 nm, while the radius of the air holes is tuned from 165 nm to 150 nm [$r/a = 0.38 - 0.32$].

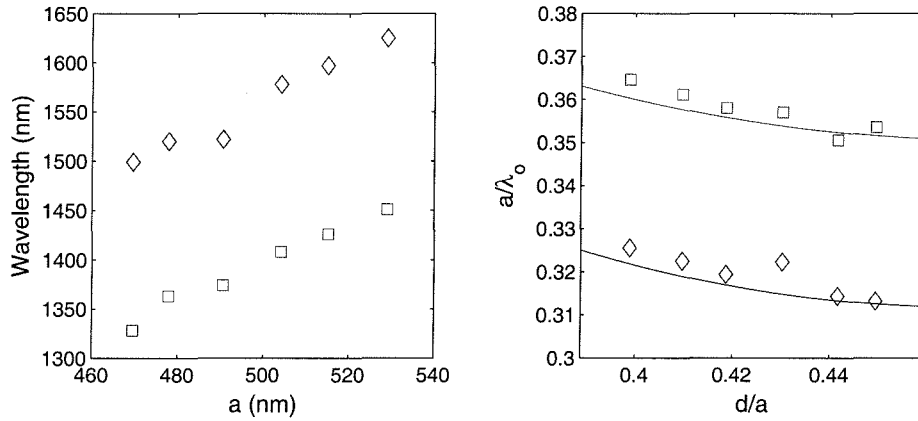


Figure 6.10: Plot of the SA laser peak (\diamond) and the DD peak (\square) for different photonic crystal lattice spacings. On the left the wavelength is plotted versus lattice spacing, and on the right the normalized frequency is plotted versus the normalized slab thickness. The solid lines correspond to FDTD simulations of the DD and SA cavity mode tuning.

6.3 X-Defect Cavity

As described in sub-section 4.4.2, by introducing defects with a symmetry lower than that of the host photonic crystal, the resonant mode structure can be substantially altered. In an X -split cavity the symmetry is reduced to C_{2v} by moving four nearest neighbor holes towards the central defect. Photoluminescence from an X -split cavity is shown in Figure 6.11. Two very interesting features are present. First, the deep donor modes near 1350 nm are seen to split into two distinct peaks separated by ~ 30 nm⁴. Second, there are two SA peaks split by ~ 15 nm at a wavelength of 1550 nm. Comparing these measurements with the simulations in Figure 4.24, the resonant peaks can be labelled as in Figure 6.11. The normalized frequency of resonant peaks in the PL are 5 – 10% larger than the FDTD simulation predictions due to the larger porosity of the fabricated structures.

As in the symmetric cavity of the previous section, the only modes to lase were the SA modes at room temperature. The power within each of the SA laser modes was strongly dependent upon the spatial profile of the pump beam. Each of the SA laser modes could be independently switched on by optimizing the pump beam profile. A plot of the collected lasing power versus pump power for the X-B₂₀ and X-A₂₀ SA modes are shown in Figures 6.12 and 6.13, respectively. Consistent with the cavity quality factor predictions of FDTD simulations, the shorter wavelength X-B₂₀ SA mode has a slightly lower threshold than the X-A₂₀ mode. This result was found to be generally true for a large number of tested devices, and is a result of the greater depth within the band-gap of the X-B₂₀ mode.

⁴The two peaks have also broadened as expected from the FDTD simulation of chapter 4.

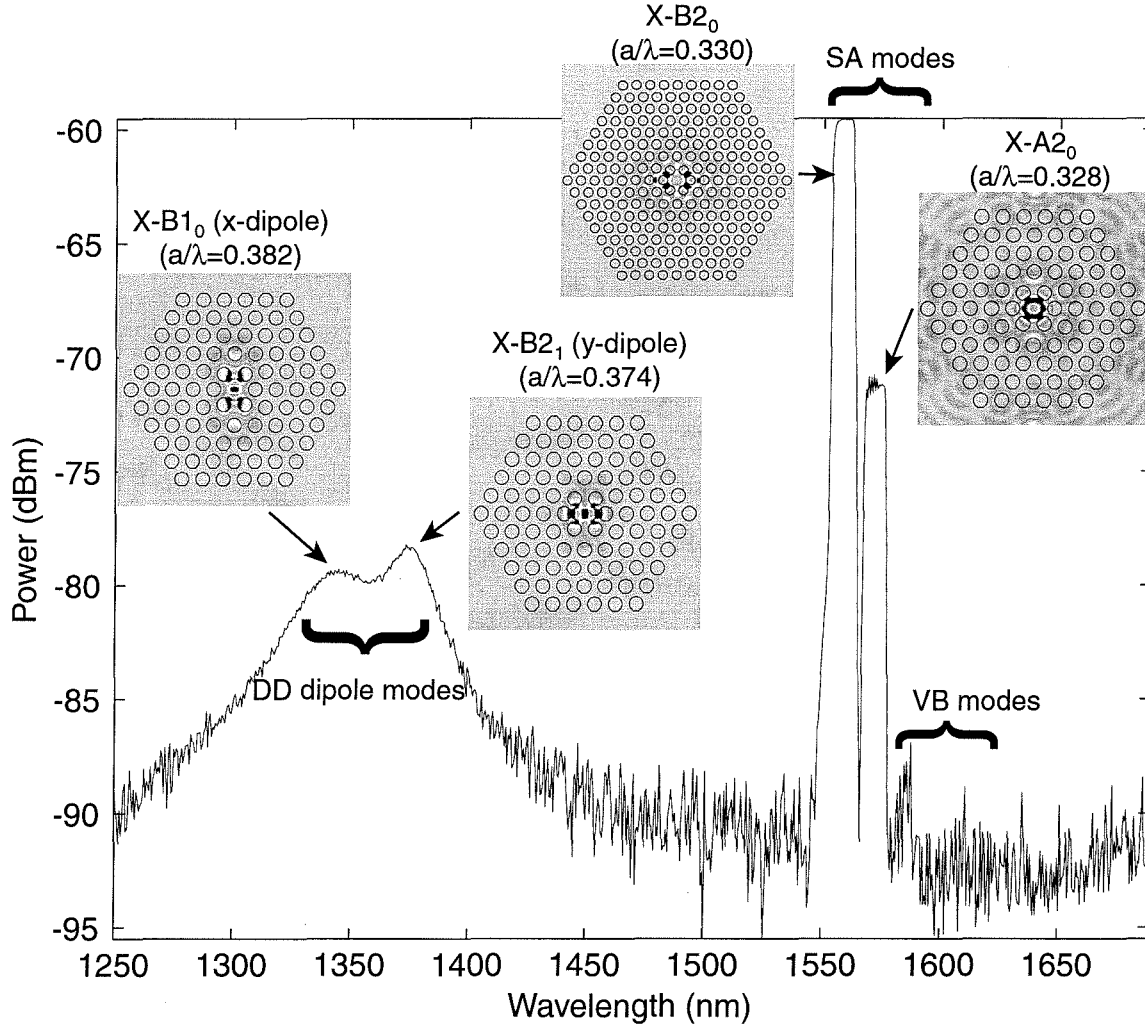


Figure 6.11: Photoluminescence spectra from an X-split defect cavity with $a = 515$ nm, $r/a = 0.35$, $\Delta y = 0.05a$, and $d/a = 0.409$. The peak external pump power is 7.16 mW with pulses of width 10 ns and a pulse period of 3 μ s.

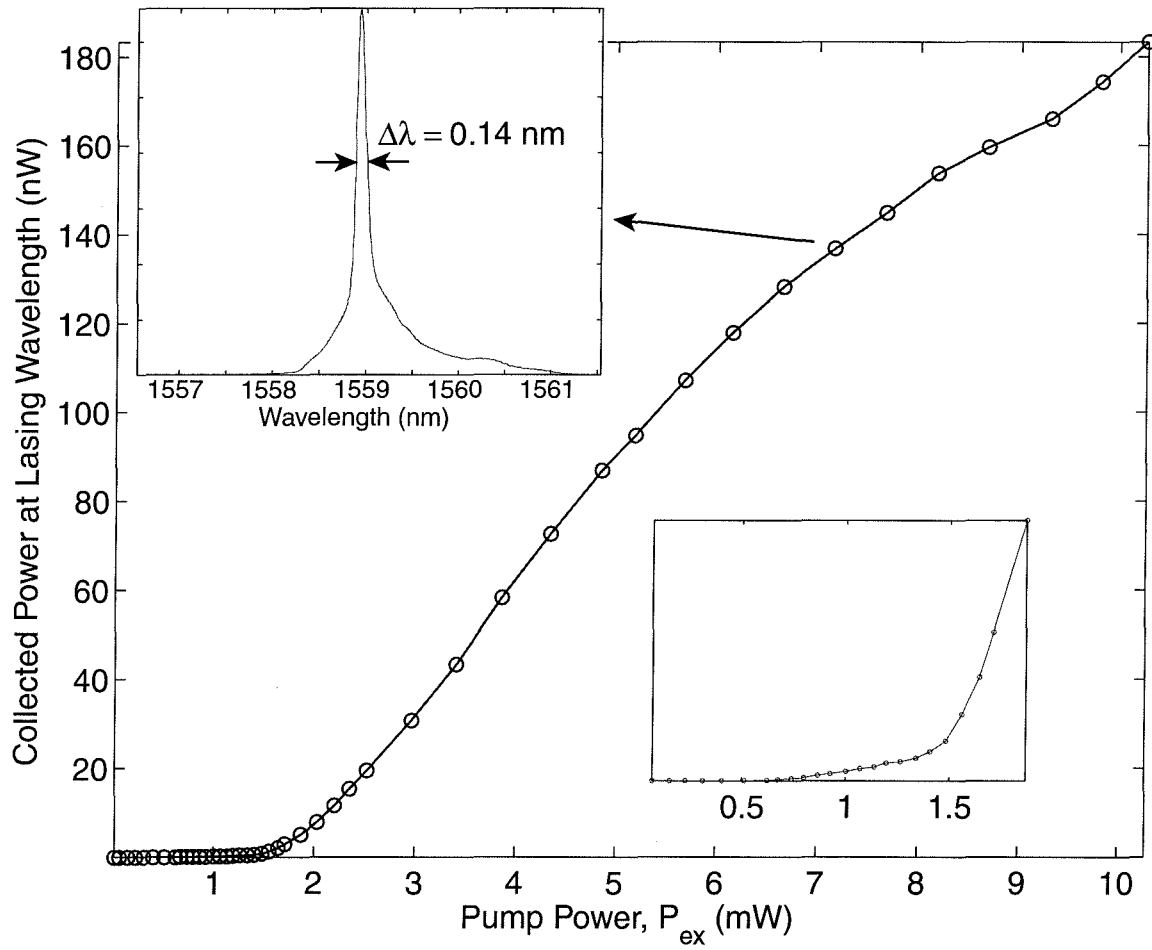


Figure 6.12: Plot of the peak collected power at the wavelength of the SA X-B₂₀ defect mode wavelength (1560 nm) vs. external peak pump power (10 ns pulses with 3% duty cycle).

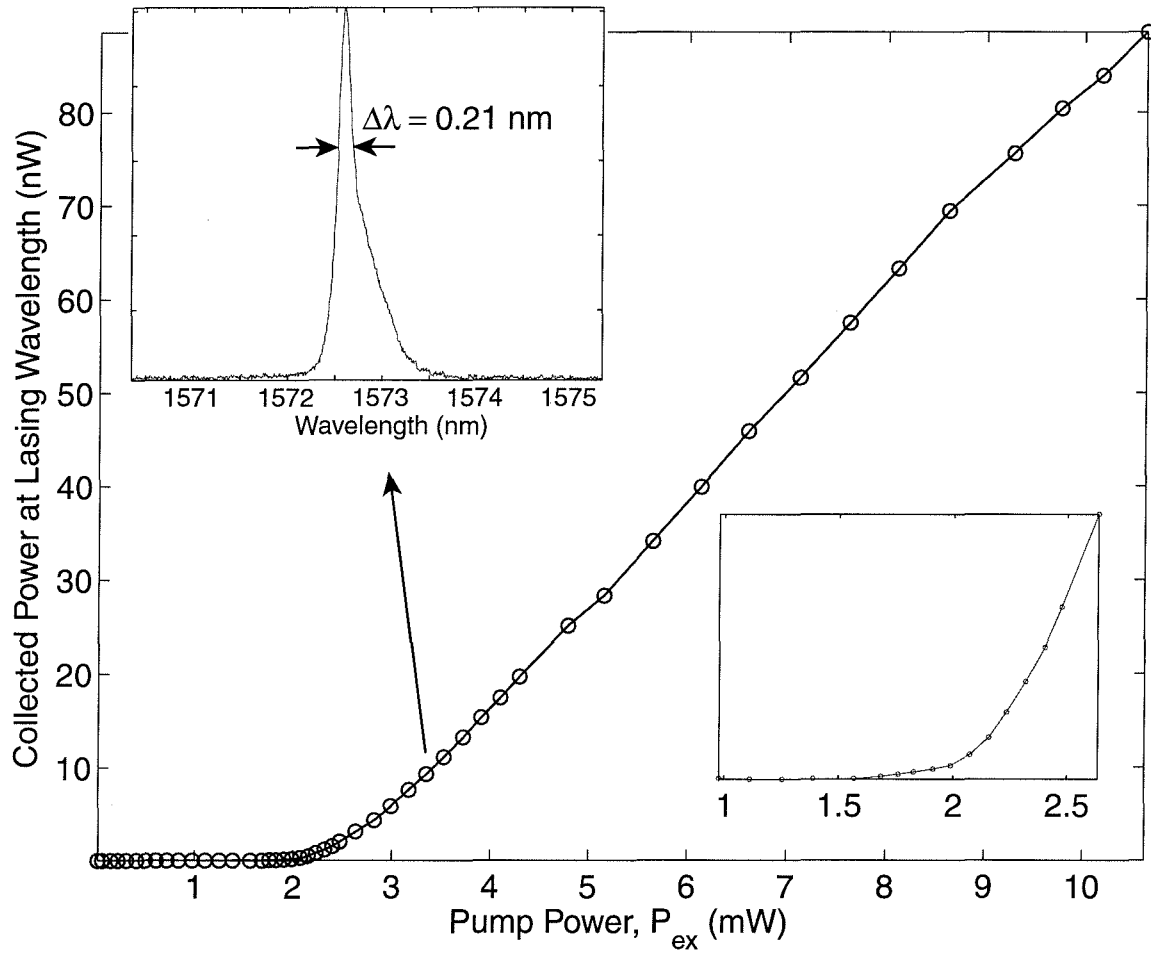


Figure 6.13: Plot of the peak collected power at the wavelength of the SA X-A₂₀ defect mode wavelength (1573 nm) vs. external peak pump power (10 ns pulses with 3% duty cycle).

6.4 Y-Defect Cavity

The Y-split cavity spectra is the most complex of all the defect cavity geometries tested. This is not completely unexpected as the Y-split cavity, in effect, is composed of three different defect cavities. The standard missing central hole defect is now accompanied by two enlarged holes on either side of the central missing hole, which tend to create localized acceptor type states. All three of the defects are coupled to form a wide variety of different defect modes. A photoluminescence spectra from a typical Y-split cavity is shown in Figure 6.14. There are now a total of at least four different localized discrete mode peaks. The DD dipole-like modes are split, and the remaining single peak at 1350 nm corresponding to the x -dipole mode (see section 6.5). Two deep acceptor (DA) modes are now present in the spectrum near the middle of the band-gap (Y-A₂₁ and Y-B₂₀). Another SA mode (Y-A₂₀) is also present along with a slew of modes near the valence band-edge. Again, as in the X-split cavity mode, normalized frequencies are slightly larger in the measured PL spectra than in the FDTD simulations due to the increased hole size in the fabricated structure. The frequency spacing between modes, however, matched that of simulations extremely well for the devices tested.

Pulsed lasing action was obtained at room temperature for all of the DA and SA modes of the Y-split cavity. By modifying the spatial profile of the pump beam to match a given mode it was possible to selectively obtain lasing in a single mode peak. Figure 6.15 shows the PL spectra for different pump beam profiles. The laser line spectra of the SA Y-A₂₀ mode for a relatively diffuse pump beam (profile “A”) is shown in Figure 6.16. The spectra also includes several peaks in the VB edge. L-L curves for the two DA modes are shown in Figures 6.17 and 6.18. The threshold pump power for the DA modes was slightly larger than that of the SA modes of the symmetric and X-split cavities, as well as the Y-A₂₀ mode of the Y-split cavity. This is not surprising as the DA modes are highly localized, and for the relatively large porosity of the fabricated devices there is significant vertical diffraction loss.

The DD x -dipole mode did not lase at room temperature in any of the cavities

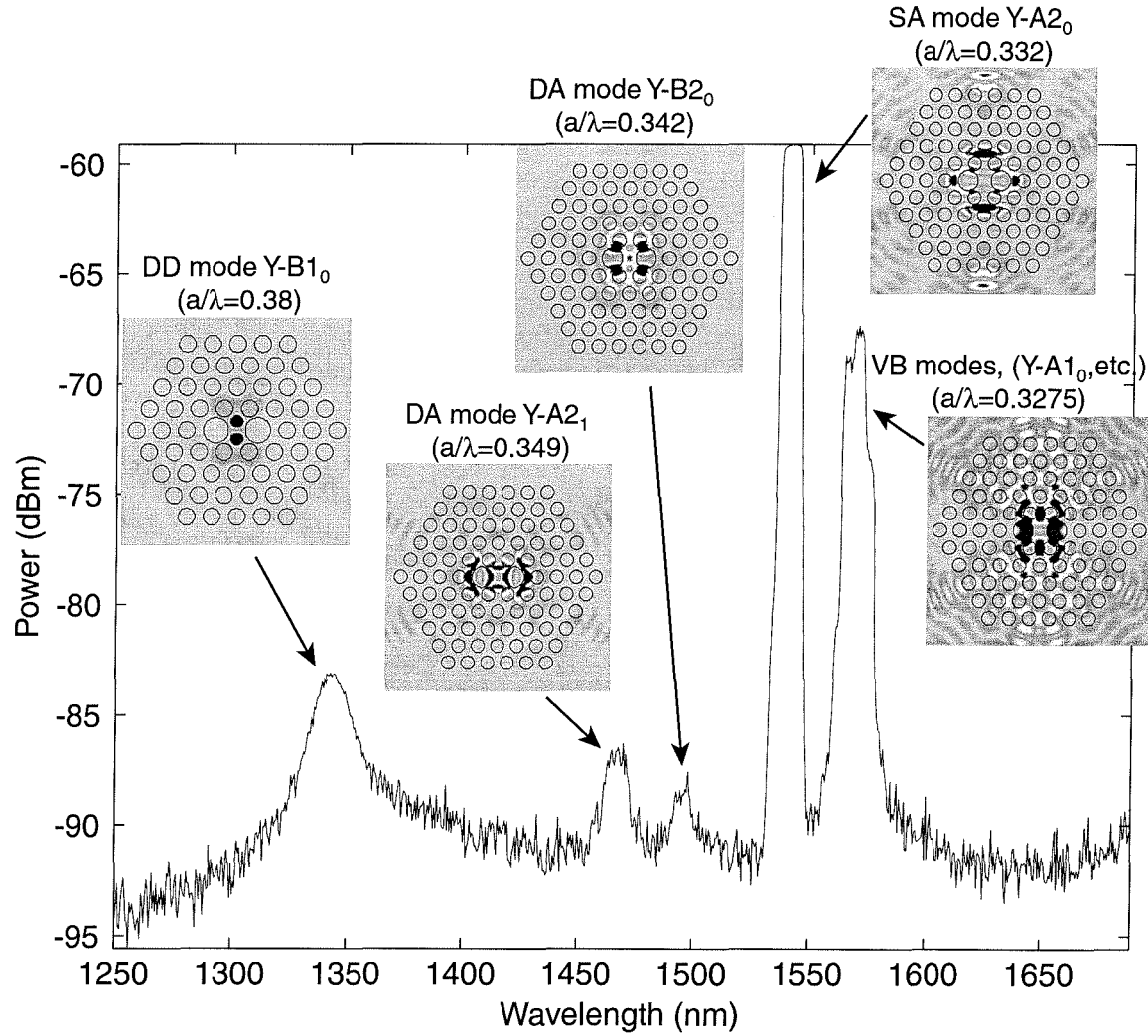


Figure 6.14: Photoluminescence spectra from a Y-split defect cavity with $a = 515$ nm, $r/a = 0.35$, $r'/a = 0.52$, and $d/a = 0.409$. The peak external pump power is 7.16 mW with pulses of width 10 ns and a pulse period of 3 μ s.

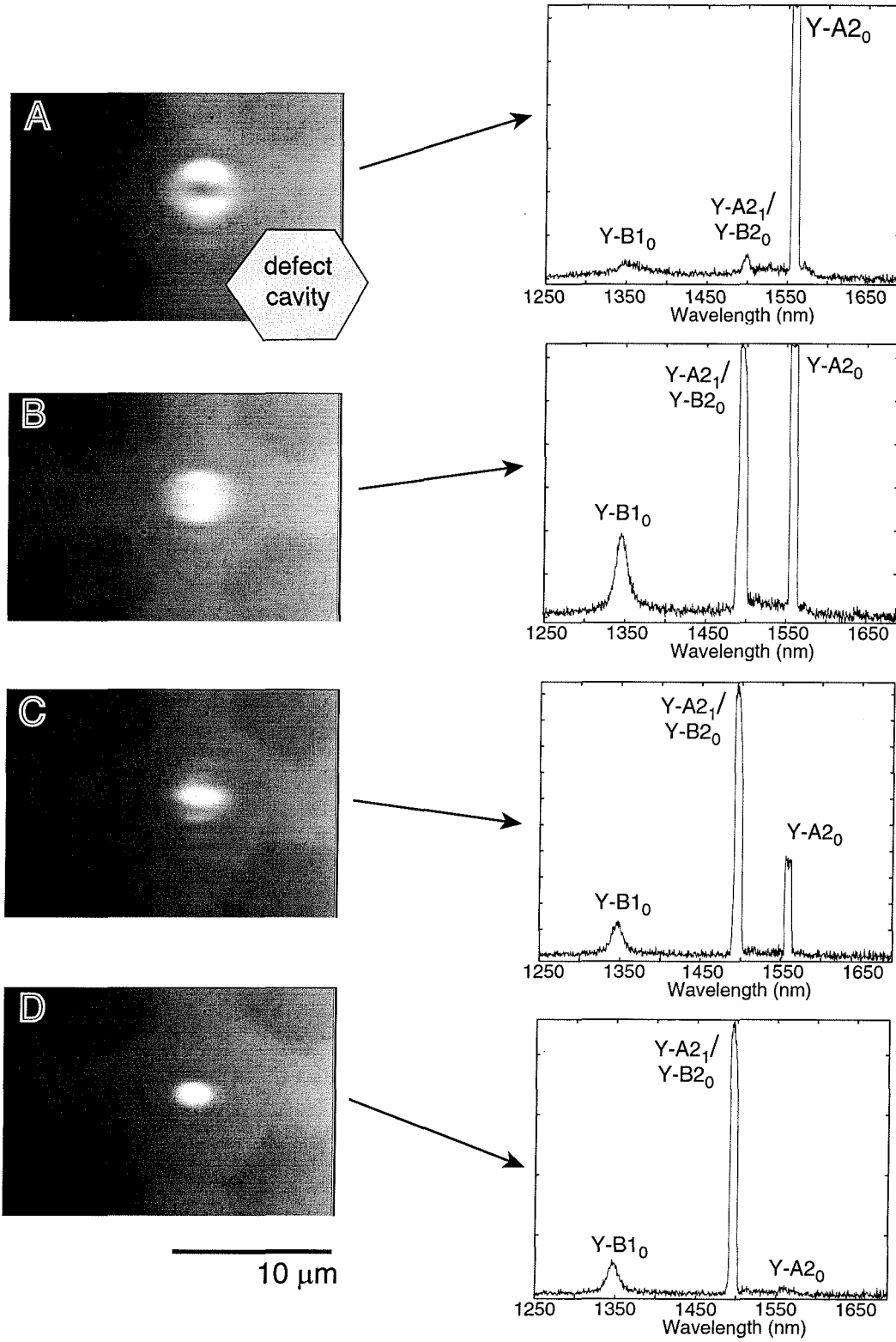


Figure 6.15: Selective mode excitation with varying pump beam profile in a Y-split cavity ($a = 490$ nm, $r/a = 0.315$, $r'/a = 0.45$, $d/a = 0.409$).

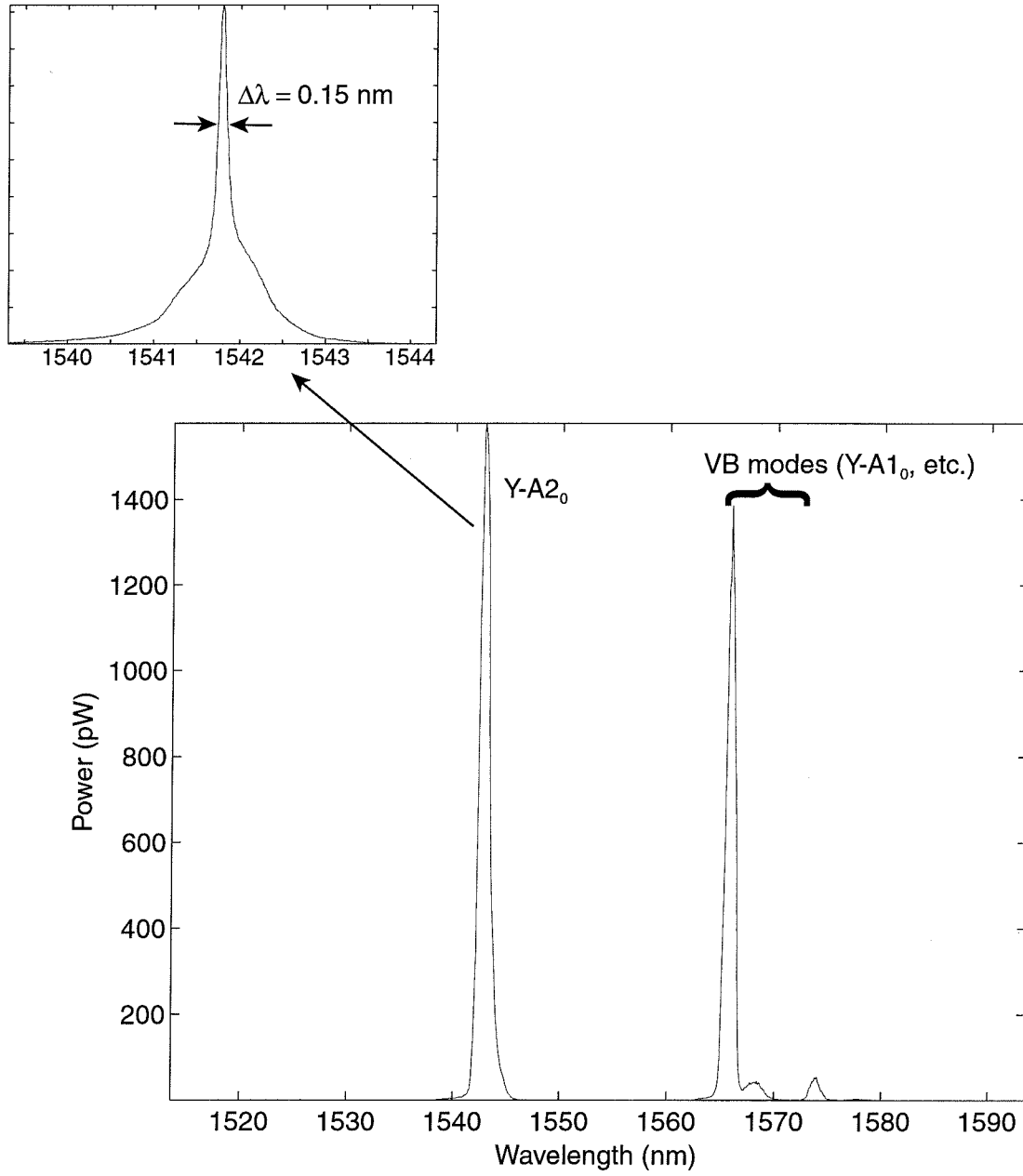


Figure 6.16: $Y-A1_0$ (VB) and $Y-A2_0$ lasing lines in the Y-split defect cavity of Figure 6.14. The peak external pump power is 4.3 mW with pulses of width 10 ns and a pulse period of 3 μ s.

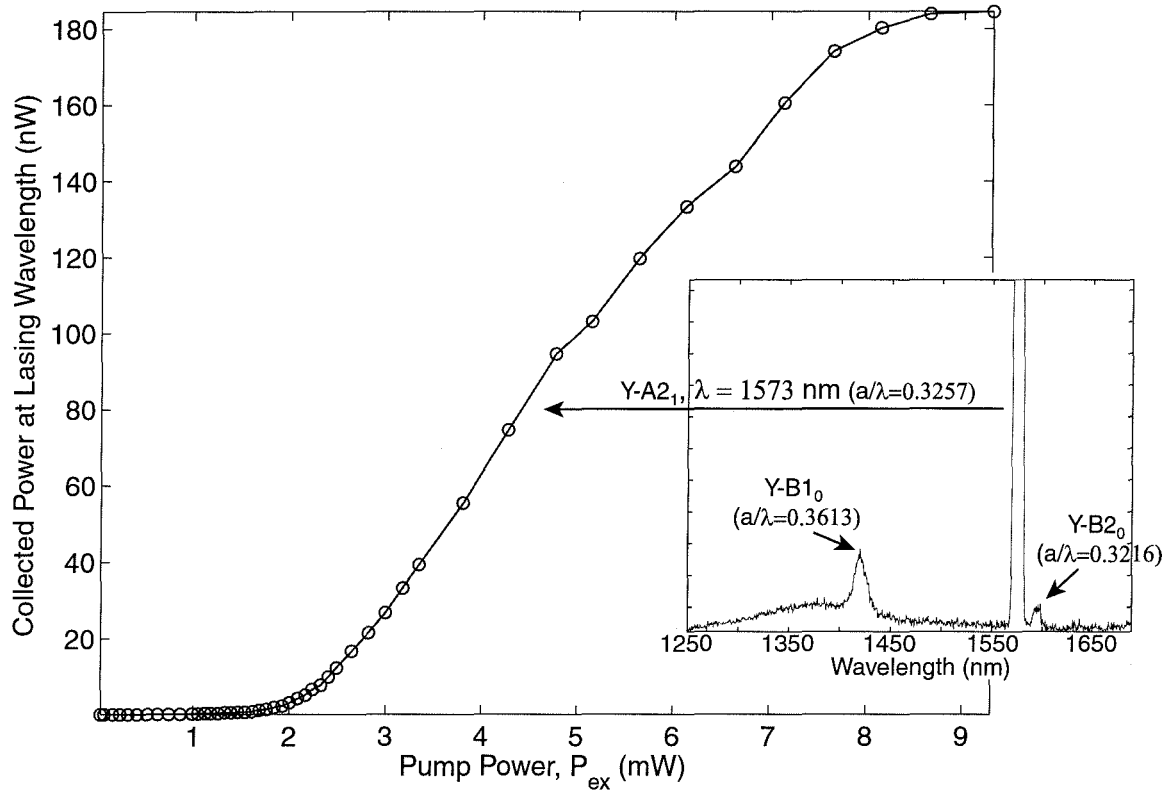


Figure 6.17: Light-in vs. Light-out curve for a localized DA Y-A₂₁ mode. The Y-split defect cavity has dimensions: $a = 515$ nm, $r/a = 0.316$, $r'/a = 0.45$, and $d/a = 0.409$.

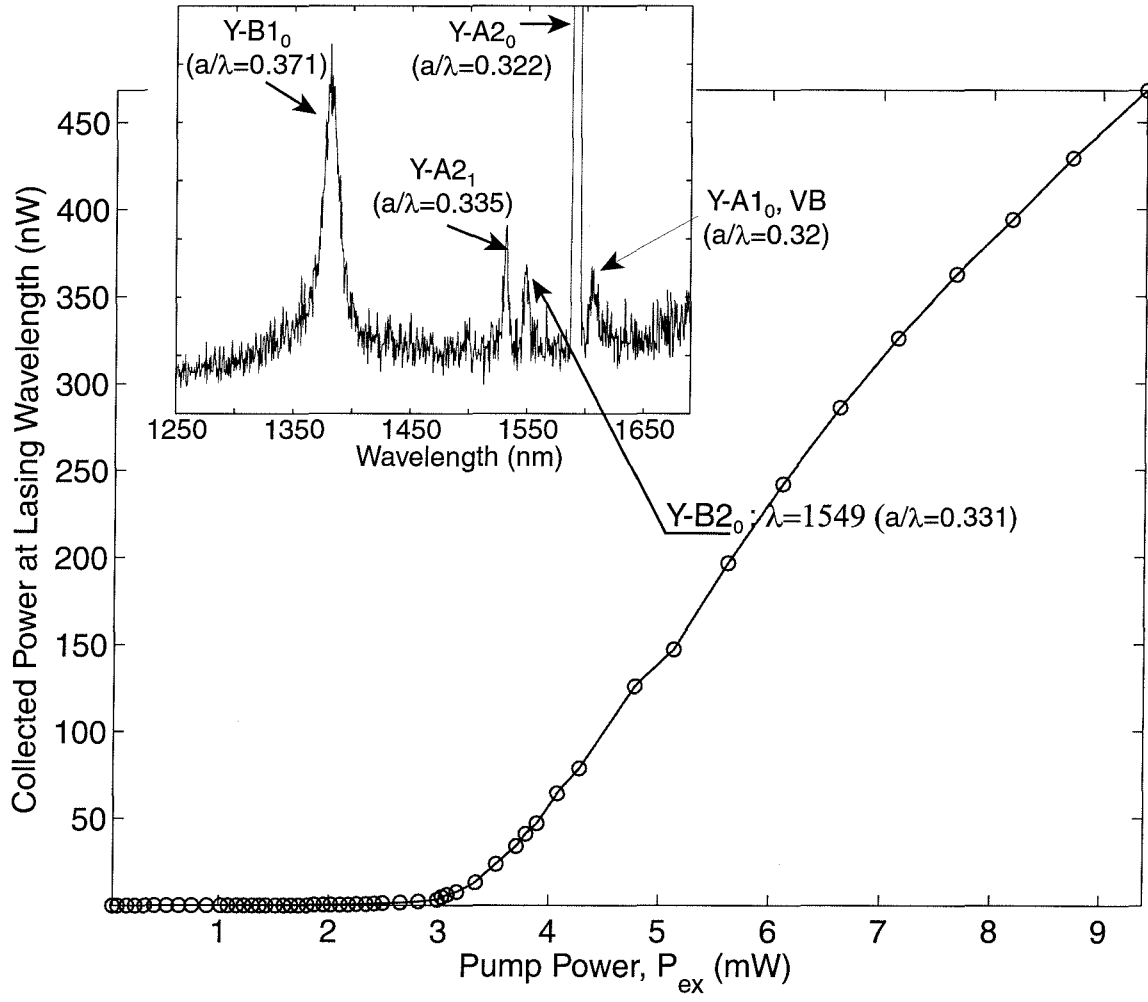


Figure 6.18: Light-in vs. Light-out curve for a localized DA Y-B2₀ mode. The Y-split defect cavity has dimensions: $a = 515$ nm, $r/a = 0.325$, $r'/a = 0.50$, and $d/a = 0.409$.

tested. This is rather surprising as the Q-factor of the x -dipole mode is theoretically comparable to that of the DA modes. One explanation is that for the devices tested the lattice spacing was limited to 545 nm and below. For this lattice spacing range the x -dipole wavelength is short of the room temperature gain peak near 1550 nm. Once the devices are cooled, the gain peak shifts to shorter wavelengths and better overlaps with the x -dipole mode. In section 6.6 lasing from the x -dipole mode is shown to occur at temperatures below 150 K.

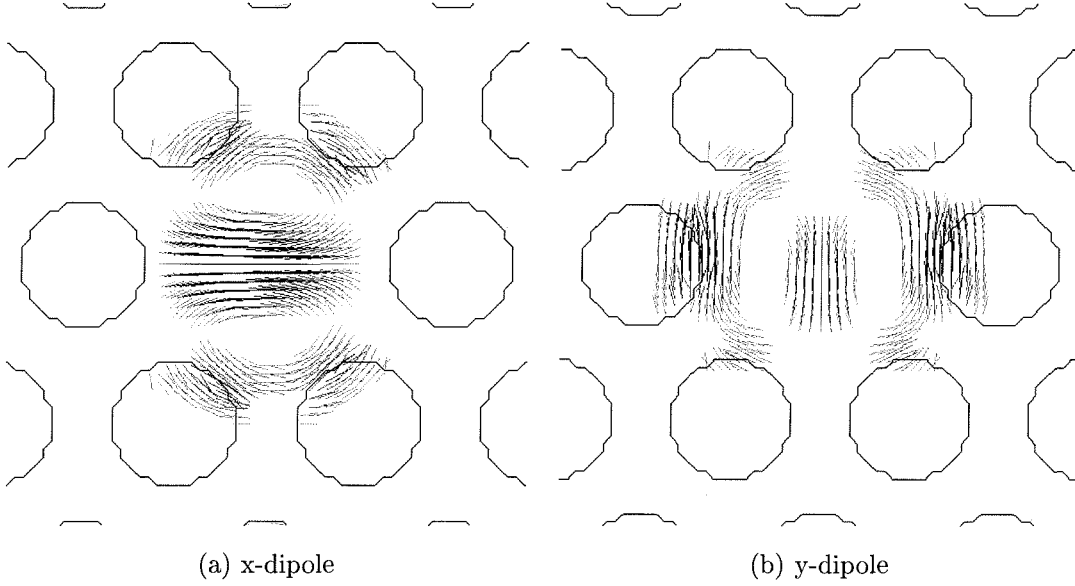


Figure 6.19: Electric field patterns of the (x,y) dipole modes in the middle of the slab waveguide.

6.5 Polarization of (x,y) Dipole Modes

Although the label “ x and y dipole” for the deep donor modes is based upon the symmetry of the modes, owing to the small scale of the photonic crystal defect cavities, the field patterns of the deep donor modes strongly resemble that of an oscillating electric dipole. A vector plot of the \mathbf{E} -field of the x and y dipole modes in the plane of the slab is shown in Figure 6.19. The strong polarization discrimination between the modes is interesting technologically for polarization selective filters and sources; however, one simple application is in the spectroscopic classification of modes in the photoluminescence spectra of different cavity symmetries.

In this experiment a polarizer was placed in the beam path after the collimating lens as shown in Figure 6.1. In this position the polarizer is sensitive to the far-field polarization in the plane of the defect cavities. As shown in Figure 6.20, two orthogonal angles of the polarizer, labelled PX and PY , were chosen to correspond to the linear polarization directions of the deep donor modes when projected on the

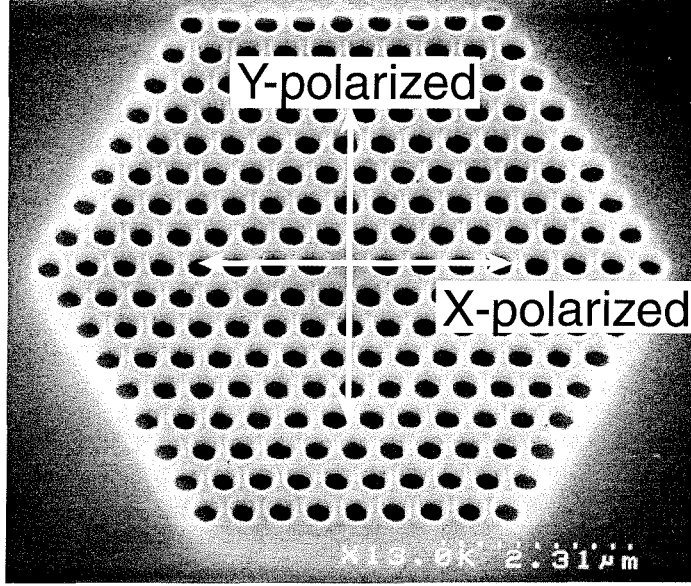


Figure 6.20: PX and PY polarizer angle projected on the top surface of a defect cavity as mounted in the PL set-up.

sample surface.

The defect cavities were fabricated in sets of three: one symmetric S -cavity, one X -split cavity, and one Y -split cavity. Each of the different cavities within the triplet was designed to have the same lattice spacing and nominal hole radius. A lattice spacing of approximately 550 nm was found to provide the best overlap between the deep donor modes of all three cavities and the quantum-well emission.

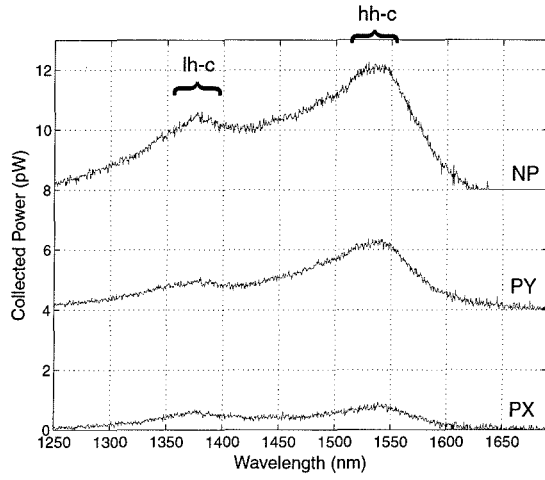
In Figure 6.21(a) the polarized PL from an unprocessed region on the sample is shown for reference. The two peaks in the unprocessed spectra correspond to the hh-c and lh-c band transitions in the quantum-well. The PL from the symmetric cavity with the polarizer removed from the beam path (Figure 6.21(b)) has a single resonance near 1550 nm. This resonance peak contains energy in both the PX and PY polarizations. The two polarization peaks are nearly degenerate with a 2-3 nm splitting, consistent with the degeneracy of the (x,y) -dipole modes in a symmetric cavity.

The PL from the X -split cavity with no polarizer (NP) has two peaks which were previously labelled as the (x,y) -dipole modes in section 6.3. Each of the peaks is

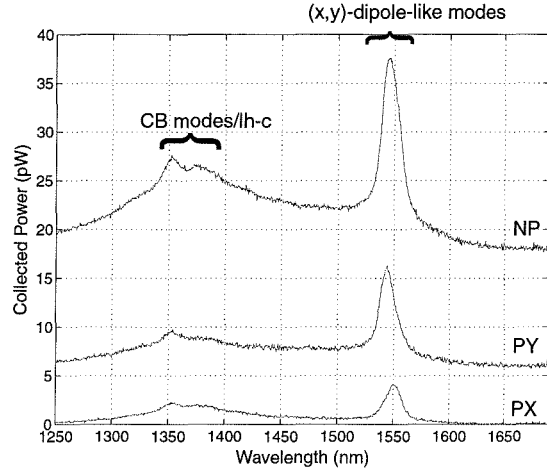
seen to be nearly completely polarized, the long wavelength peak along PY and the short wavelength peak along PX . This is consistent with the fact that for the X -split cavity the x -dipole mode has a higher frequency than the y -dipole mode.

The PL from the Y -split cavity has only a single peak which is nearly completely polarized along PX . This is also consistent with the labelling of section 6.4. It also matches the FDTD simulations very well, in which the dipole modes were strongly split and only the x -dipole remained in the band-gap.

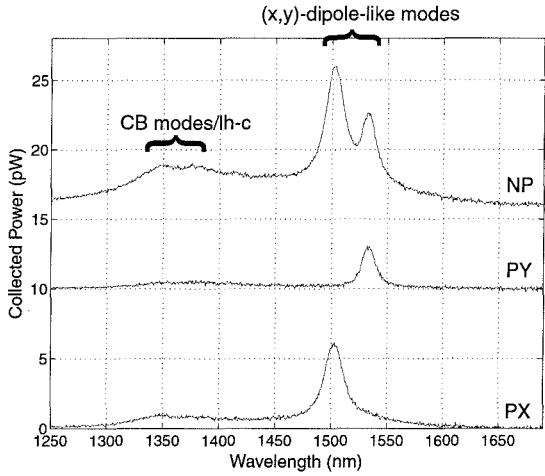
The strong polarization signature, even sub-threshold, of the (x, y) -dipole modes provided a reference point for classifying other resonant modes in the PL spectra of the different cavities studied in the previous few sections. Determining the absolute frequency of the deep donor dipole modes for different cavity geometries also provided a measure of the accuracy of the FDTD simulations, establishing a strong tie between the experimental measurements and the theoretical calculations.



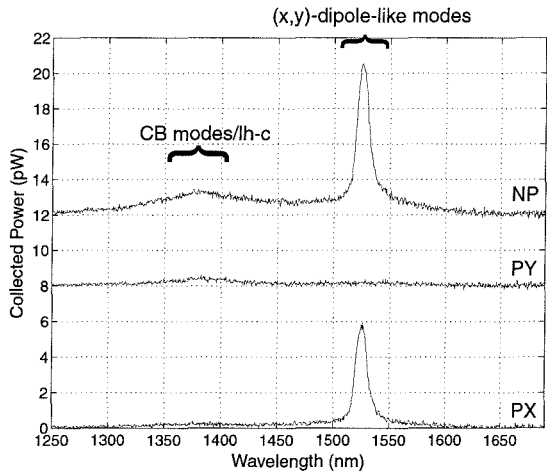
(a) Unprocessed



(b) Symmetric cavity



(c) X-split cavity



(d) Y-split cavity

Figure 6.21: Polarization filtered (no polarizer (NP), X-polarized (PX), and Y-polarized (PY)) photoluminescence spectra for the three cavity geometries (S, X, Y) showing the polarization characteristics of the deep donor modes.

6.6 Low Temperature Lasing of the X-Dipole Mode

The relatively large r/a ratio of the fabricated photonic crystal cavities⁵ precluded room temperature lasing of the highly localized deep donor states in the previous few sections. Vertical diffraction losses associated with the porosity of the resulting perforated membrane results in diminished dipole-mode quality factors. The high-gain needed to obtain lasing of these modes requires larger pump powers, which in room temperature surroundings causes the membrane cavity to heat up significantly. In order to combat the thermal roll over of the gain in the defect cavities, the sample is cooled to cryogenic temperatures in this section.

Measurements were performed on the Y -split cavities as the Q -factor of the x -dipole mode of these structures is both theoretically and experimentally larger than the degenerate dipole modes of the S -type cavities⁶. As described in sub-section 4.4.3, in this laser cavity the symmetry is lowered by increasing the radius of two nearest neighbor holes along the \hat{x} direction (Figure 5.7). This results in a single mode optical cavity, in which only the x -dipole mode is well localized. The magnitude of the electric field of the x -dipole mode, calculated using FDTD, is plotted (Figure 6.23). The polarization of this mode is predominantly TE inside the high-index slab.

A scanning electron microscope (SEM) micrograph shows a top view of one of the fabricated Y -split microcavities (Figure 6.22). The dimensions of the laser cavity (as measured from the SEM micrograph) are: $a = 515nm$, $r = 180nm$, $r' = 240nm$, and $d = 210nm$, where r' is the radius of the enlarged holes used to split the dipole mode degeneracy.

Simulations of this cavity, with $n_{slab} = 3.4$, give an estimate of 250 for the quality factor (Q), and a normalized frequency a/λ_o of 0.34 for the x -dipole mode. The effective modal volume is approximately 2.5 cubic half-wavelengths ($2.5(\lambda/2n_{slab})^3$). For a lattice spacing of 515 nm the above normalized values correspond to a resonance

⁵A result of the HCl wet etch constraints described in chapter 5.

⁶This is strictly only true for symmetric cavities in which a single hole is removed and no other changes are made. Of course, if the six nearest neighbor holes are adjusted in size, the Q can be increased significantly without breaking the symmetry of the cavity.

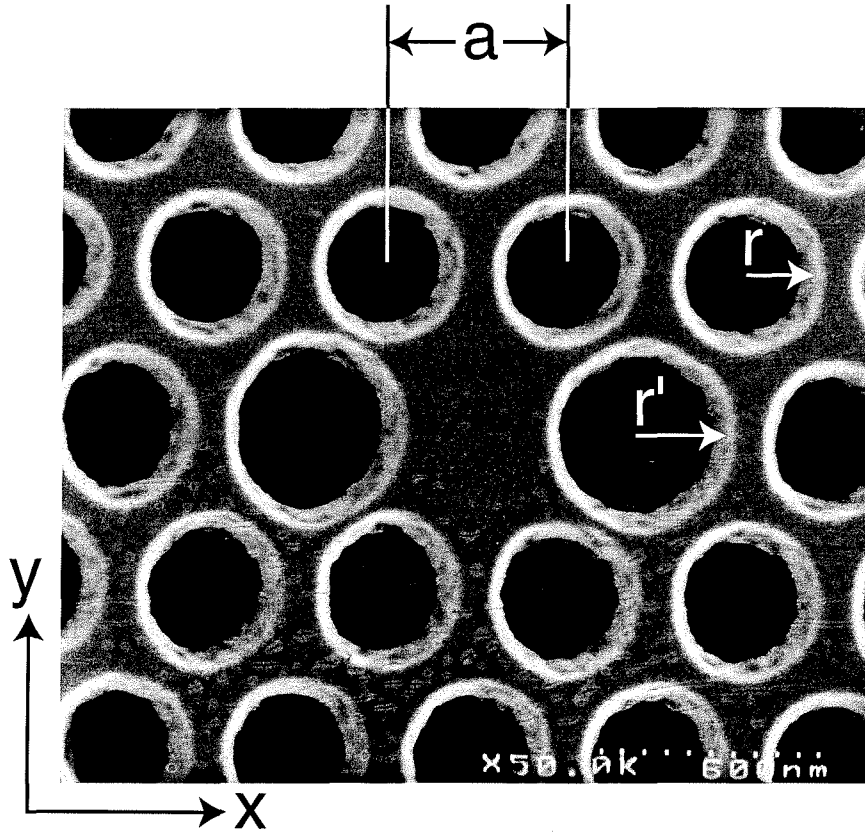


Figure 6.22: Top view of a microfabricated Y-split cavity. The inter-hole spacing is 515 nm, and the radius of the holes are approximately 180 nm. The two enlarged holes, which are used to split the dipole mode degeneracy, have a radius of 240 nm. The InGaAsP membrane is 220 nm in thickness.

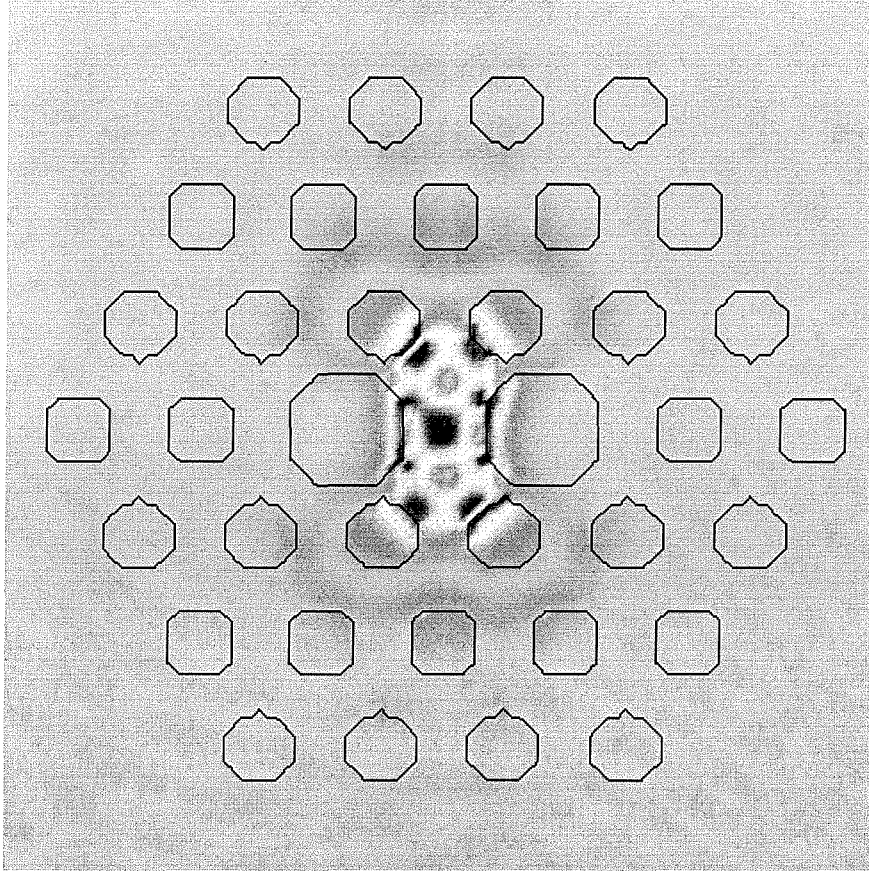


Figure 6.23: 2D slice through the middle of the slab showing the electric field amplitude of the x -dipole mode. The defect mode has a large overlap with the gain region due to the anti-node at the center of the defect. The enlarged air holes serve two functions: the first is to tune the x -dipole mode frequency so as to maximize the Q ; the second is to push the y -dipole mode frequency out of the band-gap of the photonic crystal resulting in a single mode cavity.

peak wavelength of 1509 nm and a modal volume of $0.03 \mu\text{m}^3$. Simulations of the radiation pattern of the x -dipole mode show that nearly all the power is emitted vertically. This is due to the large number of periods of the photonic crystal surrounding the defect region, and the large r/a ratio in the actual fabricated structure.

The sample was placed in a liquid Helium cryostat⁷ with a large transparent window and a minimum sample working distance of 5-6 mm. A 20X (0.35 NA) ultra-long working distance Mitutoyo objective lens was used to image, pump, and

⁷Oxford Instruments Microstat^{He}.

collect the photoluminescence from the defect cavities. As described earlier, the defect cavities were pumped from above at normal incidence with a 830 nm laser diode. The spot-size of the pump beam on the sample surface was roughly $6\text{ }\mu\text{m}$ as estimated using a CCD camera. Temperature was monitored and actively stabilized. An hour settling time was required at each temperature set-point in order to allow the contractions in the cold finger assembly to stabilize. Alignment of the pump beam to the desired defect cavity was performed by imaging the front sample surface using a white-light source. The microcavities are fabricated with 8 periods of the photonic crystal surrounding the defect, resulting in an undercut region of approximately $8\text{ }\mu\text{m}$ in diameter. The cavity mode, by comparison, is effectively localized to a diameter of approximately $0.5\text{ }\mu\text{m}$ ⁸.

An array of defect cavities was fabricated with varying lattice spacings and porosities in order to cover a wide wavelength range. This is necessary as the spontaneous emission peak (and consequently the gain peak) shifts with temperature from 1550 nm at room temperature all the way down to 1420 nm at 4 K. Measurements were made at 180 K, 143 K, and 77 K. At each temperature a number of defect cavities were scanned in order to establish which resonance peak belonged to the x -dipole mode. Defect cavities with x -dipole mode resonances aligned with the spontaneous emission peak⁹ were then more carefully tested. A variety of pumping conditions were used by varying pulse widths, duty-cycles, and pump beam profiles. Initial measurements at 180 K resulted in linewidth narrowing from 7 nm down to 1.5 nm due to increased gain experienced by the x -dipole mode; however, lasing action as characterized by a “knee” in the Light-in vs. Light-out (L-L) curve was not observed¹⁰.

Only at temperatures of 143 K or below was pulsed lasing action of the deep donor x -dipole mode observed. To avoid heating in the defect cavity pump pulses of 10ns were used with a pulse period of 250 ns. A spectrum of the laser line above threshold

⁸Using the standard definition of effective mode volume derived in sub-section 2.3.4.

⁹In actuality cavities with x -dipole mode wavelengths slightly red shifted from the spontaneous emission peak were focused on in order to better align with the gain peak.

¹⁰This highlights the difficulty in estimating the cold-cavity Q from linewidth measurements in an active structure.

is shown (Figure 6.24) for a substrate temperature of 143 K. The lasing wavelength is 1504 nm, very close to the theoretically predicted value for the x -dipole mode. The spontaneous emission well below threshold (inset of Figure 6.24) is a combination of emission from the defect cavity and emission from the surrounding unprocessed area excited by the tail of the pump beam¹¹. The broad shorter wavelength peak at 1460 nm (blue shifted due to the lower temperature of the substrate) corresponds to emission from unprocessed material surrounding the defect cavity. The narrow longer wavelength peak is the defect mode resonance. The emission from the undercut microcavity, which is at a higher temperature than the substrate, is red shifted and much broader as is evident by the long wavelength tail in the emission spectra. The linewidth of the defect laser narrows dramatically from 7 nm ($Q = 250$) below threshold to 2 Å above threshold (resolution limited). An L-L (light out vs. light in) curve of the collected power at the lasing wavelength versus pump power (Figure 6.25) shows an external threshold pump power of 6.75 mW.

The large threshold pump power is a result of the low Q value (250) of the defect mode, poor thermal heat-sinking of the floating membrane, and inefficient optical pumping (the pump beam is more than 30 times larger in area than the defect mode itself). Also, although this microcavity theoretically has a near unity spontaneous emission factor [41] (β), the L-L plot shows a distinct slope change at threshold. This is in part due to the relatively high temperature of the undercut membrane and high carrier density near threshold, which results in a much larger non-radiative Auger recombination rate, and subsequent low radiative efficiency below threshold. The laser cavity described here is not optimal, however, and by tailoring the ratio of r/a and r'/a the Q can theoretically be increased, which would significantly lower pump threshold values and increase the device operating temperature. Continuous-wave operation at room temperature, however, will ultimately require better heat sinking of the membrane [34, 102] through wafer bonding to low-index substrates or the use

¹¹In the room temperature measurements the spot-size was much smaller and the tail of the pump beam did not overlap as strongly with unprocessed areas adjacent to the cavity. For the low temperature measurements, the pump beam is focused through a cryostat window and the resulting spot size is not as small.

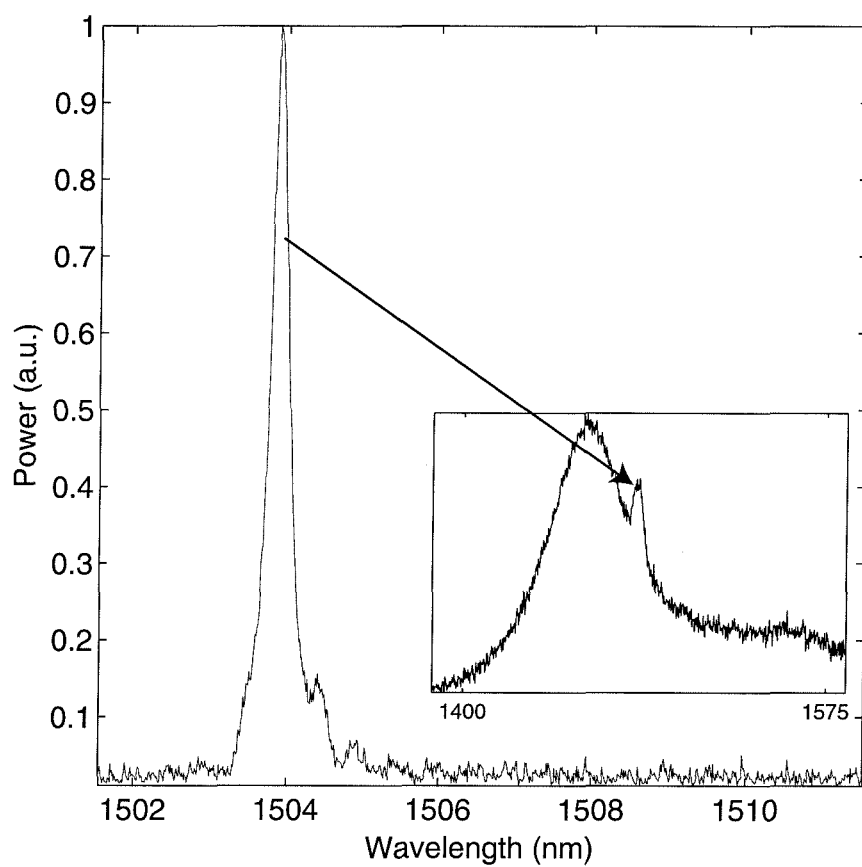


Figure 6.24: Spectrum of the laser line just above threshold. The linewidth is approximately 0.2nm, limited by the resolution of the spectrometer. The spontaneous emission well below threshold is shown in the inset.

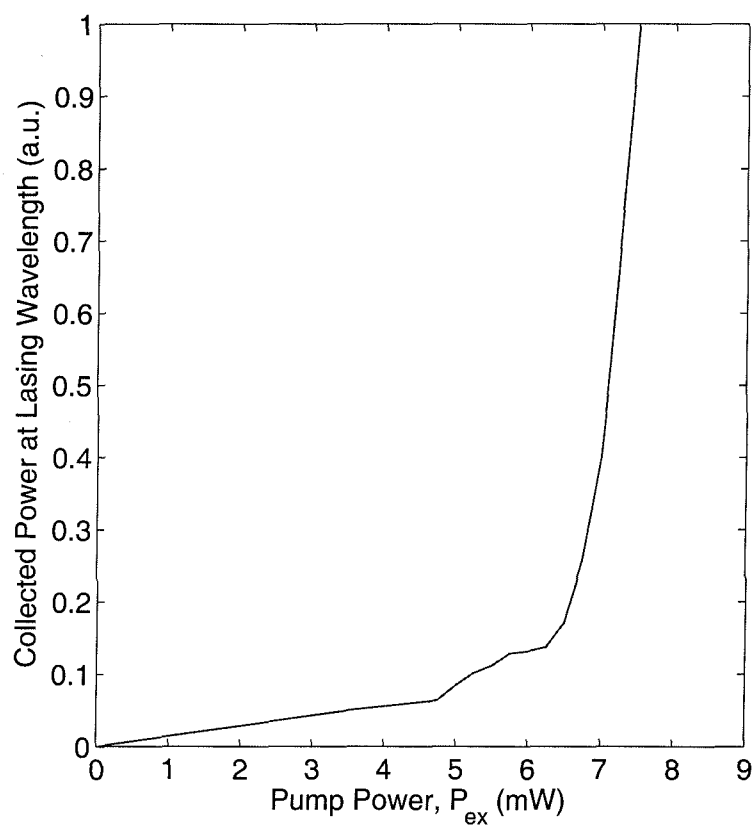


Figure 6.25: L-L curve showing the power at the laser wavelength versus the incident pump power. The sample was cooled to 143K and pumped with 10 ns pulses (4% duty cycle).

of a bottom DBR mirror.

Chapter 7 Summary

Optical nanocavities supporting resonant modes with volumes as small as $2(\lambda/2n)^3$ were created by intentionally introducing local defect regions into two-dimensional photonic crystals formed using microfabrication techniques. Optical pumping of an InGaAsP MQW active region embedded in the photonic crystal was used to investigate the properties of these tiny resonators.

The symmetries and mode structure of different defect cavities were studied using group theoretical techniques. As well, finite-difference time-domain electromagnetic simulations were used to study optical loss mechanisms of the cavities, and to estimate the required geometry to align the cavity resonances to the 1500 nm emission band of the InGaAsP MQWs.

Fabrication of the defect cavities was performed using e-beam lithography, anisotropic ion-beam etching, and wet chemical etching. By lithographically adjusting the local defect geometry a variety of donor and acceptor type resonant modes could be generated. In symmetric cavities which retain the C_{6v} symmetry of the host hexagonal lattice, the dominate modes were a pair of degenerate dipole-like donor modes. In the actual fabricated devices, shallow acceptor modes also formed due to a slight grading in the radius of the air holes from the center of the cavity pattern to the perimeter. Splitting of the degenerate dipole-like modes was seen for defect cavities with C_{2v} symmetry. In the X -split cavities there was weak splitting of the dipole modes as well as the introduction of two new shallow acceptor modes. The Y -split cavities demonstrated strong splitting of the dipole-like modes, pushing the y -dipole mode completely out of the band-gap. In enlarging two of the holes in the Y -split cavity, two highly localized deep acceptor modes were also created.

Lithography was also used to scale the in-plane lattice parameter, a , of the photonic crystal and create a multi-wavelength two-dimensional laser array. The wavelength was tunable over a 125 nm range from 1500 nm to 1625 nm with a 10 nm

resolution. The tuning of the wavelength was sub-linear with respect to a due to the changing normalized waveguide thickness d/a .

Lasing action in these cavities was limited to low duty-cycle pulsed operation at room temperature due to the poor heat-sinking present in the undercut membrane structures. Limitations in the fabrication of the photonic crystal cavities also resulted in increased vertical diffraction loss of the localized modes which severely degraded the Q-factor of these modes. As a result, lasing from the highly localized dipole-like modes was only possible at reduced temperatures (< 150 K).

The lowest threshold laser modes were the shallow acceptor (SA) modes of the symmetric defect cavity. Pump threshold values as low as 1.5 mW external power, or approximately 500 μ W absorbed power, were obtained. The quality factor of the SA modes of the low threshold devices was estimated at close to 2,000. In direct contrast to the highly localized modes, the Q-factors of the SA modes were limited by in-plane loss.

Bibliography

- [1] E. M. Purcell, “Spontaneous emission probabilities at radio frequencies,” *Phys. Rev.* **69**, 681 (1946).
- [2] J. C. Slater, *Microwave Electronics* (Dover, New York, NY, 1969).
- [3] L. Brillouin, *Wave Propagation in Periodic Structures*, 2nd ed. (Dover Publications, Inc., Mineola, NY, 1953).
- [4] D. Kleppner, “Inhibited Spontaneous Emission,” *Phys. Rev. Lett.* **47**, 233–236 (1981).
- [5] E. Yablonovitch, “Inhibited Spontaneous Emission in Solid-State Physics and Electronics,” *Phys. Rev. Lett.* **58**, 2059–2062 (1987).
- [6] S. L. McCall, P. M. Platzman, R. Dalichaouch, D. Smith, and S. Schultz, “Microwave Propagation in Two-Dimensional Dielectric Lattices,” *Phys. Rev. Lett.* **67**, 2017–2020 (1991).
- [7] E. Yablonovitch, T. J. Gmitter, R. D. Meade, A. M. Rappe, K. D. Brommer, and J. D. Joannopoulos, “Donor and acceptor modes in photonic band-structure,” *Phys. Rev. Lett.* **67**, 3380–3383 (1991).
- [8] P. Yeh, A. Yariv, and E. Marom, “Theory of Bragg fiber,” *J. Opt. Soc. Am. B* **9**, 1196–1201 (1978).
- [9] H. A. Harris and C. V. Shank, “Antisymmetric taper of distributed feedback lasers,” *IEEE J. Quan. Elec.* **15**, 532–540 (1976).
- [10] G. A. Lincoln, M. W. Geis, S. Pang, and N. N. Efremow, “Large area ion beam assisted etching of GaAs with high etch rates and controlled anisotropy,” *J. Vac. S. Tech. B* **1**, 1043–1046 (1983).

- [11] C. C. Cheng, A. Scherer, V. Arbet-Engels, and E. Yablonovitch, "Lithographic band gap tuning in photonic band gap crystals," *J. Vac. S. Tech. B* **14**, 4110–4114 (1996).
- [12] T. Krauss, Y. P. Song, S. Thoms, C. D. W. Wilkinson, and R. M. D. L. Rue, "Fabrication of 2-D photonic bandgap structures in GaAs/AlGaAs," *IEE Elec. Lett.* **30**, 1444–1446 (1994).
- [13] T. Baba and T. Matsuzaki, "Fabrication and Photoluminescence of GaInAsP/InP 2D Photonic Crystals," *Jap. J. Appl. Phys. 1* **35**, 1348–1352 (1996).
- [14] O. Painter, R. Lee, A. Yariv, A. Scherer, and J. O'Brien, "Photonic bandgap membrane microresonator," In *Integrated Photonics Research*, OSA Technical Digest Series **4**, 221–223 (Optical Society of America, Washington, D.C., 1998).
- [15] H. Benisty *et al.*, "Optical and Confinement Properties of Two-Dimensional Photonic Crystals," *J. Lightwave Tech.* **17**, 2063–2077 (1999).
- [16] T. Hamano, H. Hirayama, and Y. Aoyagi, "Optical characterization of GaAs 2D photonic bandgap crystal fabricated by selective MOVPE," In *Conference on Lasers and Electro-Optics*, OSA Technical Digest Series **11**, 528–529 (Optical Society of America, Washington, D.C., 1997).
- [17] S. Noda, N. Yamamoto, M. Imada, and H. Kobayashi, "Alignment and Stacking of Semiconductor Photonic Bandgaps by Wafer-Fusion," *J. Lightwave Tech.* **17**, 1948–1955 (1999).
- [18] S.-Y. Lin, E. Chow, V. Hietala, P. R. Villeneuve, and J. D. Joannopoulos, "Experimental Demonstration of Guiding and Bending of Electromagnetic Waves in a Photonic Crystal," *Science* **282**, 274–276 (1998).
- [19] H. Kosaka, T. Kawashima, A. Tomita, M. Notomi, T. Tamamura, T. Sato, and S. Kawakami, "Superprism phenomena in photonic crystals," *Phys. Rev. B* **58**, 10096–10099 (1998).

- [20] G. Feiertag *et al.*, “Fabrication of photonic crystals by deep x-ray lithography,” *Appl. Phys. Lett.* **71**, 1441–1443 (1997).
- [21] K. Inoue, M. Wada, K. Sakoda, M. Hayashi, T. Fukushima, and A. Yamanaka, “Near-infrared photonic band gap of two-dimensional triangular air-rod lattices as revealed by transmittance measurement,” *Phys. Rev. B* **53**, 1010–1013 (1996).
- [22] S. John and K. Busch, “Photonic Bandgap Formation and Tunability in Certain Self-Organizing Systems,” *J. Lightwave Tech.* **17**, 1931–1943 (1999).
- [23] D. M. Atkin, P. S. J. Russell, T. A. Birks, and P. J. Roberts, “Photonic band structure of guided Bloch modes in high index films fully etched through with periodic microstructure,” *J. Mod. Opt.* **43**, 1035–1053 (1996).
- [24] P. S. J. Russell, D. M. Atkin, and T. A. Birks, in *Microcavities and Photonic Bandgaps* (Kluwer Academic Publishers, The Netherlands, 1996), pp. 203–218.
- [25] P. S. J. Russell and T. A. Birks, “Hamiltonian Optics of Nonuniform Photonic Crystals,” *J. Lightwave Tech.* **17**, 1982–1988 (1999).
- [26] S. G. Johnson, S. Fan, P. R. Villeneuve, J. D. Joannopoulos, and L. A. Kolodziejaki, “Guided modes in photonic crystal slabs,” *Phys. Rev. B* **60**, 5751–5758 (1999).
- [27] O. Painter, J. Vučković, and A. Scherer, “Defect Modes of a Two-Dimensional Photonic Crystal in an Optically Thin Dielectric Slab,” *J. Opt. Soc. Am. B* **16**, 275–285 (1999).
- [28] M. Boroditsky, R. Vrijen, T. F. Krauss, R. Coccioli, R. Bhat, and E. Yablonovitch, “Spontaneous Emission and Purcell Enhancement from Thin-Film 2-D Photonic Crystals,” *J. Lightwave Tech.* **17**, 2096–2112 (1999).

- [29] S. Fan, P. R. Villeneuve, J. D. Joannopoulos, and E. F. Schubert, "High Extraction Efficiency of Spontaneous Emission from Slabs of Photonic Crystals," *Phys. Rev. Lett.* **78**, 3294–3297 (1997).
- [30] H. Kosaka, T. Kawashima, A. Tomita, M. Notomi, T. Tamamura, T. Sato, and S. Kawakami, "Photonic crystals for micro lightwave circuits using wavelength-dependant angular beam steering," *Appl. Phys. Lett.* **74**, 1370–1372 (1999).
- [31] O. Painter, R. K. Lee, A. Yariv, A. Scherer, J. D. O'Brien, P. D. Dapkus, and I. Kim, "Two-Dimensional Photonic Band-Gap Defect Mode Laser," *Science* **284**, 1819–1824 (1999).
- [32] J. L. Jewell, J. P. Harbison, A. Scherer, Y. H. Lee, and L. T. Florez, "Vertical-Cavity Surface-Emitting Lasers: Design, Growth, Fabrication, Characterization," *IEEE J. Quan. Elec.* **27**, 1332–1346 (1991).
- [33] S. L. McCall, A. F. J. Levi, R. E. Slusher, S. J. Pearton, and R. A. Logan, "Whispering-gallery mode lasers," *Appl. Phys. Lett.* **60**, 289–291 (1992).
- [34] A. F. J. Levi, S. L. McCall, S. J. Pearton, and R. A. Logan, "Room Temperature Operation of Submicrometre Radius Disk Laser," *IEE Elec. Lett.* **29**, 1666–1667 (1993).
- [35] D. Y. Chu and S.-T. Ho, "Spontaneous emission from excitons in cylindrical dielectric waveguides and the spontaneous-emission factor of microcavity ring lasers," *J. Opt. Soc. Am. B* **10**, 381–390 (1993).
- [36] L. Rayleigh, "The Problem of the Whispering Gallery," *Philosophical Magazine* **20**, 1001–1004 (1910).
- [37] J. S. Foresi, P. R. Villeneuve, J. Ferrera, E. R. Thoen, G. Steinmeyer, S. Fan, J. D. Joannopoulos, L. C. Kimerling, H. I. Smith, and E. P. Ippen, "Photonic-Bandgap microcavities in optical waveguides," *Nature* **390**, 143–145 (1997).

- [38] J. P. Zhang, D. Y. Chu, S. L. Wu, W. G. Bi, R. C. Tiberio, R. M. Joseph, A. Taflove, C. W. Tu, and S. T. Ho, “Nanofabrication of 1-D Photonic Bandgap Structures Along a Photonic Wire,” *IEEE Photonics Tech. Lett.* **8**, 491–493 (1996).
- [39] T. F. Krauss, B. Vögele, C. R. Stanley, and R. M. D. L. Rue, “Waveguide Microcavity Based on Photonic Microstructures,” *IEEE Photonics Tech. Lett.* **9**, 176–178 (1997).
- [40] J. D. Joannopoulos, R. D. Meade, and J. N. Winn, *Photonic Crystals* (Princeton University Press, Princeton, New Jersey, 1995).
- [41] J. Vučković, O. Painter, Y. Xu, A. Yariv, and A. Scherer, “FDTD Calculation of the Spontaneous Emission Coupling Factor in Optical Microcavities,” *IEEE J. Quan. Elec.* **35**, 1168–1175 (1999).
- [42] L. A. Graham, D. L. Huffaker, and D. G. Deppe, “Spontaneous lifetime control in a native-oxide-apertured microcavity,” *Appl. Phys. Lett.* **74**, 2408–2410 (1999).
- [43] Y. Yamamoto and S. Machida, “Microcavity semiconductor laser with enhanced spontaneous emission,” *Phys. Rev. A* **44**, 657–668 (1991).
- [44] H. Yokoyama, “Physics and Device Application of Optical Microcavities,” *Science* **256**, 66–70 (1992).
- [45] T. Yoshie, C. C. Cheng, and A. Scherer, “Two-dimensional photonic crystals in GaN,” In *1998 IEEE 16th International Semiconductor Laser Conference*, (IEEE, Nara, Japan, 1998).
- [46] H. Gießen, J. D. Berger, G. Mohs, P. Meystre, and S. F. Yelin, “Cavity-modified spontaneous emission: From Rabi oscillations to exponential decay,” *Phys. Rev. A* **53**, 2816–2821 (1996).

- [47] W. W. Chow, S. W. Koch, and M. S. III, *Semiconductor-Laser Physics* (Springer-Verlag, New York, 1994).
- [48] W. Vogel and D.-G. Welsch, *Lectures on Quantum Optics* (Akademie Verlag GmbH, Berlin, Federal Republic of Germany, 1994).
- [49] I. H. Deutsch, J. C. Garrison, and E. M. Wright, "Excess noise in gain-guided amplifiers," *J. Opt. Soc. Am. B* **8**, 1244–1251 (1991).
- [50] P. W. Milonni, *The Quantum Vacuum*, 2nd ed. (John Wiley & Sons, Inc., New York, NY, 1995).
- [51] J. J. Sakurai, *Advanced Quantum Mechanics* (Addison-Wesley Publishing Company, Inc., New York, NY, 1967).
- [52] C. Kittel, *The Quantum Theory of Solids*, 2nd revised printing ed. (John Wiley & Sons, Inc., New York, NY, 1987).
- [53] K. Petermann, "Calculated Spontaneous Emission Factor for Double-Heterostructure Injection Lasers with Gain-Induced Waveguiding," *IEEE J. Quan. Elec.* **15**, 566–570 (1979).
- [54] A. E. Siegman, "ORTHOGONALITY PROPERTIES OF OPTICAL RESONATOR EIGENMODES," *Opt. Commun.* **31**, 369–373 (1979).
- [55] A. Yariv and S. Margalit, "On Spontaneous Emission Into Guided Modes with Curved Wavefronts," *IEEE J. Quan. Elec.* **18**, 1831–1832 (1982).
- [56] A. W. Snyder and J. D. Love, *Optical Waveguide Theory* (Chapman and Hall, New York, NY, 1983).
- [57] A. E. Siegman, *Lasers* (University Science Books, New York, NY, 1986).
- [58] N. W. Ashcroft and N. D. Mermin, *Solid State Physics* (Saunders College Publishing, New York, NY, 1976).

- [59] S. W. Corzine, R.-H. Yan, and L. A. Coldren, in *Quantum Well Lasers* (Academic Press, Inc., San Diego, CA, 1993), pp. 17–96.
- [60] J. Shah, *Ultrafast Spectroscopy of Semiconductors and Semiconductor Nanostructures*, *Springer Series in Solid-State Sciences* (Springer, New York, NY, 1996).
- [61] L. Allen and J. Eberly, *Optical Resonance and Two-Level Atoms* (Dover Publications, Inc., Mineola, NY, 1987).
- [62] K. J. Vahala, Ph.D. thesis, California Institute of Technology, 1985.
- [63] A. Yariv, *Quantum Electronics*, 3rd ed. (John Wiley & Sons, New York, NY, 1989).
- [64] L. A. Coldren and S. W. Corzine, *Diode Lasers and Photonic Integrated Circuits* (John Wiley & Sons, Inc., New York, NY, 1995).
- [65] M. E. Peskin and D. V. Schroeder, *An Introduction to Quantum Field Theory* (Addison-Wesley Publishing Company, New York, NY, 1997).
- [66] J. D. Jackson, *Classical Electrodynamics*, 2nd ed. (John Wiley & Sons, Inc., New York, NY, 1975).
- [67] E. M. Purcell, *Electricity and Magnetism*, Vol. 2 of *Berkeley Physics Course* (McGraw-Hill, Inc., New York, 1985).
- [68] B. Schutz, *Geometrical methods of mathematical physics* (Cambridge University Press, New York, NY, 1980).
- [69] W. Ludwig and C. Falter, *Symmetries in Physics: Group Theory Applied to Physical Problems*, No. 64 in *Springer-Verlag Series in Solid-State Sciences*, 2nd ed. (Springer-Verlag, New York, NY, 1996).
- [70] M. Tinkham, *Group Theory and Quantum Mechanics*, *International Series in Pure and Applied Physics* (McGraw-Hill, Inc., New York, NY, 1964).

- [71] S. F. Savitt, *Time's Arrows Today: Recent Physical and Philosophical Work on the Direction of Time* (Cambridge University Press, New York, NY, 1997).
- [72] E. P. Wigner, *Group Theory and Its Applications to the Quantum Mechanics of Atomic Spectra*, Vol. 5 of *Pure and Applied Physics* (Academic Press Inc., New York, NY, 1960).
- [73] M. Kaku, *Quantum Field Theory: A Modern Introduction* (Oxford University Press, New York, NY, 1993).
- [74] J. J. Sakurai, *Modern Quantum Mechanics*, revised ed. (Springer, New York, NY, 1994).
- [75] J. D. Bjorken and S. D. Drell, *Relativistic Quantum Fields, International Series in Pure and Applied Physics* (McGraw-Hill, Inc., New York, NY, 1965).
- [76] T. Inui, Y. Tanabe, and Y. Onodera, *Group Theory and Its Applications in Physics*, No. 78 in *Springer-Verlag Series in Solid-State Sciences* (Springer-Verlag, New York, NY, 1996).
- [77] K. Sakoda, "Symmetry, degeneracy, and uncoupled modes in two-dimensional photonic crystals," *Phys. Rev. B* **52**, 7982–7986 (1995).
- [78] K. S. Yee, "Numerical solution of boundary value problems involving Maxwell's equations in isotropic media," *IEEE Trans. Antennas Propag.* **14**, 302–307 (1966).
- [79] S. Adachi, "Material parameters of $In_{1-x}Ga_xAs_yP_{1-y}$ and related binaries," *J. Appl. Phys.* **53**, 8775–8792 (1982).
- [80] M. Plihal and A. A. Maradudin, "Photonic band structure of two-dimensional systems: The triangular lattice," *Phys. Rev. B* **44**, 8565–8571 (1991).
- [81] C. T. Chan, Q. L. Yu, and K. M. Ho, "Order-N spectral method for electromagnetic waves," *Phys. Rev. B* **51**, 16635–16642 (1995).

- [82] G. Mur, "Asorbing Boundary Conditions for the Finite-Difference Approximation of the Time-Domain Electromagnetic-Field Equations," IEEE Transactions on Electromagnetic Compatibility **23**, 377–382 (1981).
- [83] K. Chamberlain and L. Gordon, "Modeling Good Conductors Using the Finite-Difference, Time-Domain Technique," IEEE Transaction on Electromagnetic Compatibility **37**, 210–216 (1995).
- [84] B. D'Urso, O. Painter, J. O'Brien, T. Tombrello, A. Scherer, and A. Yariv, "Modal reflectivity in finite-depth two-dimensional photonic-crystal microcavities," J. Opt. Soc. Am. B **15**, 1155–1159 (1998).
- [85] D. H. Choi and W. J. R. Hoefer, "The Finite-Difference-Time-Domain Method and its Application to Eigenvalue Problems," IEEE Transactions on Microwave Theory and Techniques **34**, 1464–1469 (1986).
- [86] A. Yariv, *Optical Electronics*, 4th ed. (Saunders College Publishing, a division of Holt, Rinehart and Winston, Inc., Orlando, Florida, 1991).
- [87] Stringellow, *Organometallic Vapor-Phase Epitaxy*, 2nd ed. (Academic Press, San Diego, CA, 1999).
- [88] I. Kim, D. G. Chang, and P. D. Dapkus, "Growth of InGaAsP in a stagnation flow vertical reactor using TBA and TBP," J. Cryst. Growth **119**, 138–143 (1988).
- [89] Y. Zou, J. S. Osinski, P. Grodzinski, P. D. Dapkus, W. Rideout, W. F. Sharfman, and F. D. Crawford, "Experimental Verification of Strain Benefits in 1.5 μ m Semiconductor Lasers by Carrier Lifetime and Gain Measurements," IEEE Photonics Tech. Lett. **4**, 1315–1318 (1992).
- [90] C. Youtsey, R. Grundbacher, R. Panepucci, and I. Adesida, "Characterization of chemically assisted ion beam etching of InP," J. Vac. S. Tech. B **12**, 3317–3321 (1994).

- [91] J. Daleiden, K. Eisele, R. Keller, G. Vollrath, F. Fiedler, and J. D. Ralston, "InGaAsP/InP 1.55- μ m lasers with chemically assisted ion beam-etched facets," *Optical and Quantum Electronics* **28**, 527–532 (1996).
- [92] P. Mounaix, P. Delobelle, X. Mélique, L. Bornier, and D. Lippens, "Micromachining and mechanical properties of GaInAs/InP microcantilevers," *Materials Science and Engineering B* **51**, 258–262 (1998).
- [93] S. Adachi and H. Kawaguchi, "Chemical Etching Characteristics of (001)InP," *J. Electrochem. Soc.* **128**, 1342–1349 (1981).
- [94] P. H. L. Notten, "The etching of InP in HCl Solutions: A Chemical Mechanism," *J. Electrochem. Soc.* **131**, 2641–2644 (1984).
- [95] S. das neves and M.-A. D. Paoli, "A Quantitative Study of Chemical Etching of InP," *J. Electrochem. Soc.* **140**, 2599–2603 (1993).
- [96] M. Chahoud, H.-H. Wehmann, and A. Schlachetzki, "Etching simulation of convex and mixed InP and Si structures," *Sensors and Actuators A* **69**, 251–258 (1998).
- [97] R. Y. Fang, D. Bertone, G. Morello, and M. Meliga, "Eaves Structures on (001) InP and InP/InGaAsP/InP Heterostructures," *J. Electrochem. Soc.* **144**, 3940–3945 (1997).
- [98] D. T. C. Huo, M. F. Yan, J. Wynn, and D. P. Wilt, "Preferential Etching of InGaAsP/InP Using Low Temperature Bromine/Methanol for Planar Buried Heterostructure Lasers," *J. Electrochem. Soc.* **136**, 1828–1830 (1989).
- [99] A. Scherer, H. G. Craighead, M. L. Roukes, and J. P. Harbison, "Electrical damage induced by ion beam etching of GaAs," *J. Vac. S. Tech. B* **6**, 277–279 (1988).
- [100] M. Tamura, T. Ando, N. Nunoya, S. Tamura, S. Arai, and G. U. Bacher, "Estimation of Sidewall Nonradiative recombination in GaInAsP/InP Wire Struc-

tures Fabricated by Low Energy Electron-Cyclotron-Resonance reactive-Ion-Beam-Etching,” Jap. J. Appl. Phys. 1 **37**, 3576–3584 (1998).

- [101] G. P. Agrawal and N. K. Dutta, *Semiconductor Lasers* (Van Nostrand Reinhold, New York, NY, 1993).
- [102] S. M. K. Thiyagarajan, A. F. J. Levi, C. K. Lin, I. Kim, P. D. Dapkus, and S. J. Pearton, “Continuous room-temperature operation of optically pumped InGaAs/InGaAsP microdisk lasers,” IEE Elec. Lett. **34**, 2333–2334 (1998).